

UNIVERSITÉ DE STRASBOURG

ÉCOLE DOCTORALE DES SCIENCES CHIMIQUES

Laboratoire de Biophotonique et Pharmacologie – UMR 7021

THÈSE présentée par :

Fei LIU

soutenue le : 16 Juin 2022

pour obtenir le grade de : **Docteur de l'université de Strasbourg**

Discipline/ Spécialité : Chimie biologique et thérapeutique

***In situ* reactions in lipid nanostructures
for bioimaging and therapy**

THÈSE dirigée par :

M. KLYMCHENKO Andrey

DR1 CNRS, Université de Strasbourg

M. ANTON Nicolas

Maître de conférences, l'EPST Inserm 1260

RAPPORTEURS :

Mme. MURA Simona

Maître de conférences, l'EPST Institut Galien Paris-Saclay

M. ROUX Stéphane

Professeur, l'EPST Institut UTINAM

AUTRES MEMBRES DU JURY :

M. BASTIAT Guillaume

Maître de conférences CNRS, MINT Inserm U1066

M. ZUBER Guy

DR2 CNRS, l'EPST UMR7242

Acknowledgments

Firstly, I would like to thank the jury members, Dr. Simona Mura, Pr. Stéphane Roux, Dr. Guillaume Bastiat, and Dr. Guy Zuber for kindly accepting our request to evaluate this work. I feel honored to be evaluated by leading experts in the chemistry and pharmaceutical fields.

This thesis work has been an important part of my life. The thesis cannot be done without the kindness and help of numerous people. My strongest gratitude goes to my supervisor Dr. Andrey Klymchenko. Supervising me has not been easy for him. He has been a guide through my whole Ph.D. journey, not only a guide with an immense source of knowledge and enlightened ideas but also a teacher and friend providing me tremendous support and motivation. Many thanks for his guidance during my research and thesis writing. Also, I admire his ability to maintain everything in order in such a big lab. It must not have been easy for him to always be patient and to respond to even tiny complaints and sort things out resulting in a good working environment for everyone. I feel extremely fortunate to have him as my supervisor, with his passionate attitude toward projects, unique perspective in observing and explaining seemingly “bad” results, his positive attitude in dealing with tough conditions, and his patience. I could not imagine a better supervisor than him.

I would also like to thank my co-supervisor, Nicolas Anton, for recommending me to this lab and for his continuous support, guidance, and help. Without him, I would never have had a chance to be in this lab and even start my Ph.D.

Although the journey went through difficulties of Covid pandemic situation, setbacks in experiments and research work, the current and previous members of the Nanochemistry and Bioimaging group (Laboratory of Bioimaging and Pathologies, UMR7021) always provided me with a warm environment and helped me to look to the positive side of life. Not every research group is like this. It is an international group consisting of people from India, Korea, Ukraine, Italy, Portugal, Greece, and France. For me, as the only Chinese student in the group, it is really interesting to interact with them about different cultures and more importantly, food! Most of them are excellent chefs, providing delicious cakes and native specialties, which, refills me again and again with energy to continue my research work. I would like to give my thanks to many present and former members of the lab. Elisabete for your sunshine personality, the cheerleader of the lab;

Lucie, Paraskevi, and Nina for your delicious cakes; Rémi for our nice discussions; Lazar and Antoine for always being so friendly; Deep for always considering others; Dima for our wonderful cooperation; Redouane for teaching me how to formulate nano-emulsions the first day I arrived; Adarsh for teaching me how to use microscope; Caterina for drawing so many cute cartoons to make the lab lively; Anila for always willing to help people in need; Tanushree for being a good office neighbor; Kyong, Sylvie and Sophie for your smile and always being so friendly.

Our lab is very lucky to have Dr. Philippe Chabert who is usually the first person whom a newcomer encounter. Thank you, Philippe, for welcoming newcomers and navigating us in the French system. And also for helping me with translating the summary of the thesis. And I will always miss your delicious fruit cakes, and the time spent with you chatting about delicious French food and fruits; Dr. Jurga Valanciunaite for drawing the front page graphical abstract for our article published in Chemical Science; Dr. Andreas Reisch for discussions; Dr. Mayeul Collot for your humorous personality, your jokes always magically lightened up a gloomy day! I am very thankful to present and former secretaries, Ingrid Barthel and Marlyse Wernet for their incredible efficient administrative work and willingness to help! I am also thankful to some members in other labs. Dr. Nicolas Humbert for always helping with technical problems; Dr. Bertrand Vernay, and Dr. Romain Vauchelles for giving me a lesson in the ImageJ and providing me with valuable plugins and techniques for processing and analyzing microscopy images, which saved me a lot of time and energy. Members of the Pacsi platform also helped me in my experiments. Thank you, Dr. Delphine Garnier and Dr. Estefania Oliva for your efforts to maintain the NMR and Mass analysis platform to continue our analysis work. Special thanks to Delphine Garnier, for kindly helping me to do an urgent mass analysis during her pregnancy!

Many thanks to our numerous collaborators, namely Dr. Jacky Goetz, Dr Olivier Lefebvre, Pr. Valérie Schini-Kerth and Dr. Chrystelle Po. I was delighted to work on cross-disciplinary projects and to broaden my point of view on my projects.

In my overseas journey I also was lucky to be accompanied by many kind Chinese friends who kept curing my homesickness. Thank you Shuangqi Tang and Xinyue Wang for welcoming me on the first day I arrived and for your efforts in organizing lots of memorable gatherings and dinners. Thank you Ye Yuan for your generous offerings of lots of essential cooking devices; And Taozhi

Ye and Junjie Lin for our outings. I cannot imagine how lonely and homesick I would be without your company. This experience will forever engrave in my mind.

I also would like to mention the outings organized by SUAPS, which offers ski outings on the price students can afford. I had a chance to meet a lot of students who love skiing. Thank you, Gauthier, Celine, Raphene, Diego, Maryna, Mary, and Paul for accompanying me during the enjoyable ski week!

Finally, I would like to acknowledge financial support from CSC (China Scholarship Council) for supporting my living expenses in France. I also would like to thank the research funds from the European Research Council ERC Consolidator grant BrightSens 648528 and institutional funds from INSERM, CNRS and University of Strasbourg.

Contents

Acknowledgments.....	1
Contents.....	4
List of Abbreviations	6
Aim of Ph.D. thesis.....	8
1-PART 1. Bibliographical overview	10
1.1- Drug delivery by nanomaterials.....	10
1.1.2- Principle of targeted delivery	10
1.1.3- Nanoparticles used in drug delivery	14
1.2- Dye-loaded nano-emulsions	25
1.2.1- Nano-emulsions	25
1.2.2- Preparation of dye-loaded nano-emulsions	25
1.2.3- Dyes and dye-loaded NEs	29
1.2.4- Surface modification of NEs.....	37
1.2.5- Biological applications of fluorescent NEs.....	38
1.2.6-Targeted imaging with dye-loaded NEs.....	49
1.3- Dynamic covalent chemistry.....	53
1.3.1- Requirements for Dynamic Covalent Bonds (DCB).....	53
1.3.2- Catalysis for dynamic covalent bonds	54
1.3.3- Different dynamic covalent reactions types.....	54
1.3.4- Applications of dynamic covalent bonds.....	59
1.3.5- Drug delivery.....	63
2- PART 2. Results and Discussions.....	69
2.1- Drug-Sponge Lipid Nanocarriers for <i>in Situ</i> Cargo Loading and Release Using Dynamic Covalent Chemistry (Article 1)	70
Article 1	72
2.2- Functional nanoemulsion based on reversible imine bonds for controlled cargo delivery and capture (Article 2 – manuscript).....	105
Article 2 – Manuscript.....	107
2.3- Preparation of functionalized nanoemulsion by <i>in situ</i> covalent chemistry and exploring the potential for tumor targeting applications (Article 3 – manuscript)	137
Article 3 – manuscript.....	139

2.4- Dynamic covalent chemistry in live cells for organelle targeting and enhanced photodynamic action (Article 4).....	161
Article 4	163
3-PART 3. Conclusions and Perspectives	206
4- PART 4. Materials and Methods	211
4.1- Materials.....	211
4.2- Methods.....	212
4.2.1- Synthesis and chemical characterization.....	212
4.2.2- Instruments.....	221
4.2.3- Preparation of NEs.....	222
4.2.4- pH dependent cargo release.....	225
4.2.5- In situ reaction study	226
4.2.6- Preparing of Antibody NEs (for chapter 2.3)	228
4.2.7- Cell experiments	231
4.2.8- Experiment with adipose tissue from chicken skin	239
4.2.9- <i>In vivo</i> mice experiments (for chapter 2.1).....	240
References	242
List of Publications	256
List of Conferences.....	257

List of Abbreviations

Cy	Cyanine dyes
Chol-M	Cholesterol modified
DLS	Dynamic light scattering
DOPC	1,2-Dioleoyl-sn-glycero-3phosphocholine
DOX	Doxorubicin
EPR	Enhanced permeation and retention
FRET	Förster or fluorescence resonance energy transfer
FBS	Foetal bovin serum
F888	49-Dioctylamino-3-octyloxyfavone
ICG	Indocyanine Green dyes
LipoHD	Lipophilic hydrazide
LipoAmine	Lipophilic amine
LUVs	Large unilamellar vesicles
LD-HZ	Lipid droplet targeting hydrazide
MCT	Medium-chain triglycerides
Mito-HZ	Mitochondria targeting hydrazide
MRI	Magnetic resonance imaging
NR668	Lipophilic Nile red
NRK	Nile Red ketone
NR	Nile Red dyes
NIR	Near-infrared
NPs	Nanoparticles
NCs	Nanocarriers
NEs	Nano-emulsions
PEG	Poly(ethylene glycol)
PDT	Photodynamic therapy
PBS	Phosphate-buffered saline
PM-HZ	Plasma membrane targeting hydrazide
PA	push-pull pyrene dye

QY	Quantum yield
QDs	Quantum Dots
ROS	Reactive oxygen species
SLN	Solid Lipid NCs
TLC	Thin layer chromatography
TPB	Tetraphenylborate
HPLC	High performance liquid chromatography
RGD	The tripeptide Arg-Gly-Asp

Aim of Ph.D. thesis

The range of techniques and systems used to deliver therapeutics is expanding rapidly. The introduction of dynamic covalent chemistry has been exploited by researchers to seek better methods achieving the purpose of drug-specific targeting and delivery. The application of dynamic covalent chemistry in drug delivery is still at its beginning, and the future holds bright promise for further innovation.

My Ph.D. project aims to investigate novel ways of applying dynamic covalent chemistry in the field of drug delivery. To be specific, four continuous points are listed as follows:

✍ To develop a concept of a drug sponge based on lipid NEs. In this concept, lipophilic hydrazide inside the oil core can form *in situ* dynamic hydrazone bonds with cargo-ketone compounds and thus will enable *in situ* capture and release of active cargo at the cellular and animal level. We aimed to obtain NEs stable under neutral pH, whilst releasing intact cargo (drug or dye) under low pH, characteristic for the tumor microenvironment. On the other hand, the capacity of NEs to capture active molecules opens the route to detoxification of tissues from drugs/toxins.

✍ The extension of the drug-sponge concept using imine dynamic covalent chemistry. In this case, a lipophilic reactive capture molecule bearing amine group inside NEs enables *in situ* capture and release of aldehyde cargoes (dyes and drugs).

✍ Using *in situ* chemistry inside NEs, to develop a method for functionalization of NEs with targeting ligands, such as antibodies, and apply them further for specific targeting of tumors.

✍ Using dynamic covalent chemistry to target free ketone drugs or dyes to different cell organelles and to study their induced photo-toxicity behavior (photodynamic effect). We exploited dynamic covalent chemistry to target drugs and dyes to specific parts of cells. We aimed to develop ligand-bearing hydrazide groups that specifically accumulate at the cell surface and organelles (lipid droplets and mitochondria). These ligands were designed to form reversible hydrazone bonds with targeted molecules in lipid structures of the cells, thus ensuring “dynamic covalent targeting”.

Exploring and developing these techniques could help to overcome the difficulties in drug loading, obtaining surface-modified NEs, targeting the drug to the specific site in its native form, and propose an innovative strategy for drug capture *in situ* for tissue detoxification.

1-PART 1. Bibliographical overview

1.1- Drug delivery by nanomaterials

1.1.2- Principle of targeted delivery

Targeted drug delivery system refers to the transfer of drugs only to the area that requires pharmaceutical treatment excluding the parts of innocent tissues, cells, or organelles. The system is intended to increase the drug concentration in areas requiring treatment, while reducing the drug concentration in unintended areas, thus reducing side effects on one hand and increasing the therapeutic effect on the other hand.

1.1.2.1- First-order targeting

First-order targeting is also named as passive targeting. On this level of targeting, size of nanocarrier (NCs) is usually carefully controlled around 100 nm for the purpose of spontaneous accumulating nanocarriers specifically to targeted tumor areas, where the vasculature is generally leaky, with a dysfunctional lymphatic system^[1,2]. Therefore, it allows easy access for molecules and nanoobjects, such as drugs, liposomes and NPs entering tumorous tissues (Figure 1.1A)^[3]. In contrast, tight junctions of endothelial cells contained within normal tissue do not allow the transport of delivered therapeutics across them (Figure 1.1B). This phenomenon named “enhanced permeation and retention” (EPR) effect is discovered by Yasuhiro Matsumura *et.al.* in 1986^[4]. EPR was also described in the study by Sugahara *et al.*, which suggested that NPs accumulate tumors more efficiently than small molecule drugs^[5]. The EPR effect had been properly characterized by an increased accumulation of particles with size in the range of 100 to 200 nm in tumors versus in normal tissues. This phenomenon is beneficial for applying nanocarriers to delivering drugs to tumors.

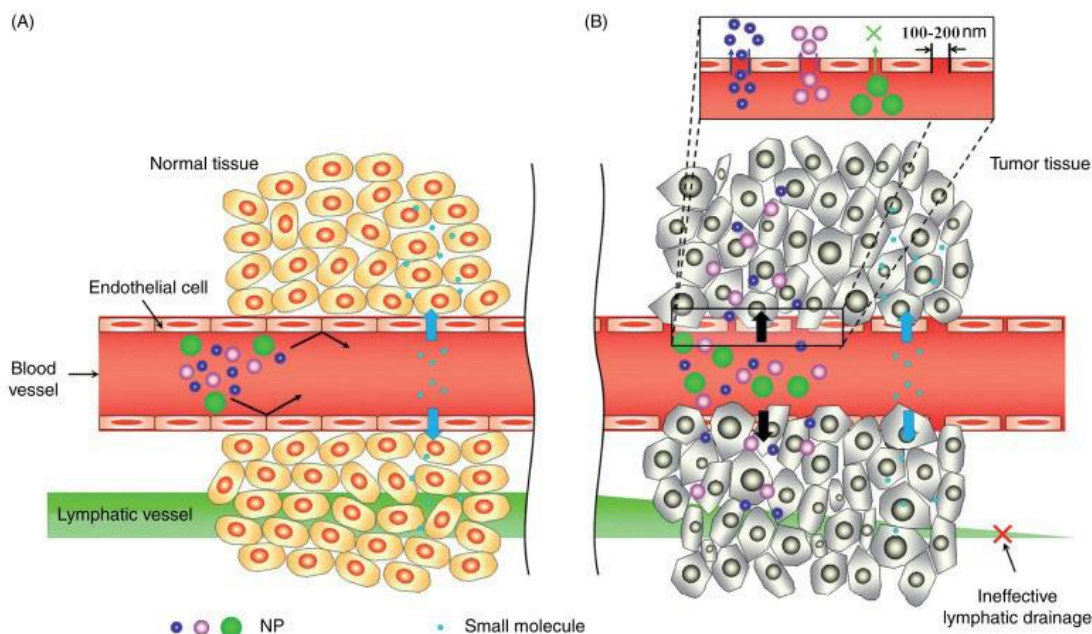


Figure 1.1. Scheme showing differential uptake of NPs and small molecules based on their size across (A) normal and (B) cancerous tissues. Adapted from ref [3].

1.1.2.2- Second-order targeting

Second-order targeting or active targeting refers to the selective delivery of drugs to specific cell types such as tumor cells avoiding normal cells. It is essential for drugs or theranostics (combining therapeutics and imaging) agents to be delivered specifically to the areas of interest while avoiding healthy tissues, thus enhancing the therapeutic efficiency and reducing the side effects. Thus, significantly increase the quantity of drug delivered to the target cells and tissues compared to a free drug or passively targeted systems. Most studies on this level of targeting referred to drug targeting with the use of nanocarriers (NCs), taking the advantage of their feasibility for surface modification and drug encapsulation. After the passive targeting process, NCs assemble to the region of interest (e.g. tumor region). The drug targeting efficiency could further increase by active targeting at this level. The most common way to achieve this purpose is by modifying the NCs surfaces with ligands binding to receptors over-expressed on the surface tumor cells (showed in Figure 1.2). Drugs are easier to penetrate the surface of cancer cells when loaded in NCs with targeting ligands. This phenomenon was firstly observed by Leserman *et al.* using liposomes grafted with antibodies^[6], in another research, functional nano-emulsions (NEs) were designed

with a low molecular weight antibody, scFv-Fc TEG4-2C (37 KDa) enabled direct MRI imaging of atherosclerosis in mice models^[7]. A variety of ligands were developed as NCs-surface modifiers, including folic acid, different peptides, and proteins including antibodies^[8,9]. Among the classical ligands, folic acid (FA) could specifically bind to the folate receptor (FAR) which is abundant in the tumor microenvironment (TME)^[10]. FA was bound either through the synthesis of FA-drug conjugates^[11] or through FA-grafting onto NCs^[12,13] promoting their endocytosis in cancer cells. RGD peptide was found to bind $\alpha_v\beta_3$ integrin^[14]. F3 peptide and aminopeptidase N (CD 13) were found to bind to nucleolin receptors expressed on angiogenic endothelial cells in the TME, both directed by Asn-Gly-Arg (NGR) peptide^[15–17]. Moreover, transferrin is a ligand that targets transferrin receptors (TfR) or nicotinic acetylcholine receptors rich in the environment of brain tumors^[18]. In the meantime, several antibodies for specific receptors were successfully produced and studied both *in vitro* and *in vivo*^[19–21]. In particular, trastuzimab and cetuximab have been popular antibodies for targeting drugs and NCs^[22,23]. Various NCs systems were developed for grafting of the targeting ligands, for instance, nanoparticles^[24], micelles^[25], dendrimers^[26–28].

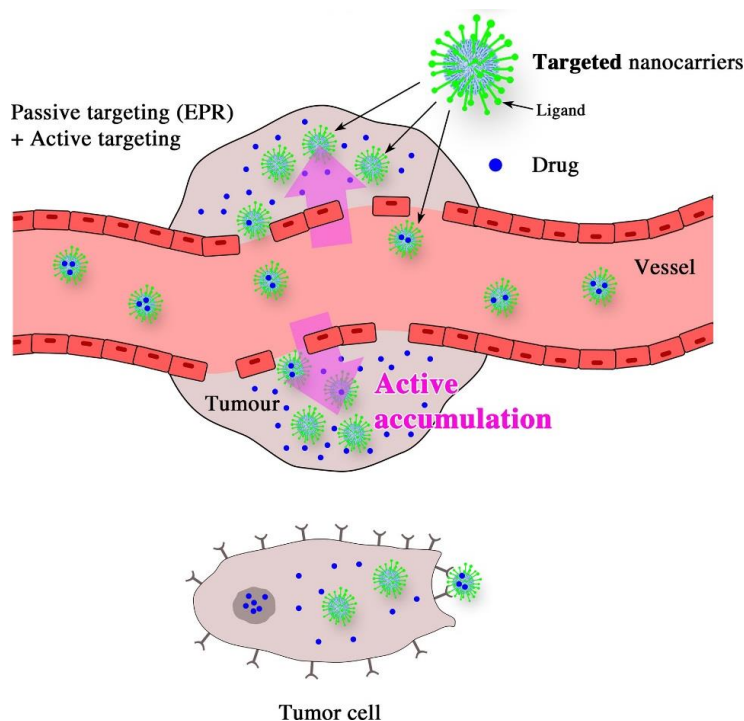


Figure 1.2. Scheme illustrating the passive targeting (EPR) and the active targeting into a tumor. Adapted from ref ^[29].

1.1.2.3- Third-order targeting

This level of targeting is generally related to drug targeting to subcellular structures (organelles). Organelle can play their functions and form a network of organelle interactions (such as mitochondria-lysosome, mitochondria-lipid droplets, lysosome-autophagosome, etc.) to participate in cellular functions cellular homeostasis in various diseases such as cancer, osteoarthritis, non-alcoholic fatty liver, and neurodegenerative diseases. Drug development using organelle as targets has become a hot anti-tumor research topic. For instance, numerous works proved that in tumors areas mitochondria provide the vast majority of adenosine triphosphate via the oxidative phosphorylation system and function gatekeepers for apoptosis and inflammation and as storage compartments for metabolites (e.g., calcium, lipids, and protons). Multiple targeting methods were also developed for organelle targeting. These include biological conjugation of NCs, fluorophores, drugs to biological compounds, for example, oligosaccharides, peptides, lipids, and drugs or chemical conjugation to synthesized anchors^[30–34]. Due to the diverse properties and microenvironments of different organelles, a variety of targeting ligands could be designed for the purpose of targeting molecules to specific organelles^[30]. Different targeting ligands were chemically designed regarding specific characteristics of different organelles. For instance, the membrane potential in mitochondria remains stable at around -180 to -200 mV across their lipid bilayer for channel pumps and oxidation functionality. This uniquely high negative charge does not exist in other organelles. As a result, lipophilic cations could be designed for mitochondria targeting^[35]. Many lipophilic cations were designed for this purpose, including triphenylphosphonium (TPP), Flupirtine rhodamine 123, anthracyclins, and MKT-077^[36]. For the plasma membrane targeting that maintains a membrane potential from ~ -3 to ~ -90 mV, due to the bilayer lipid structure, usually, a hydrophobic alkyl chain (to attach) along with sulfonate group (to prevent internalization) was used. Golgi contains a Golgi protein cyclooxygenase-2 (COX-2) inhibitor named SC-558, a phenylsulfonamide fragment is used as the functional group that binds in pockets filled with COX-2 complexes^[37,38]. Therefore, phenylsulfonamide moiety is expected to serve as a promising Golgi anchor^[39]. For nuclear targeting, cationic polymers were used to deliver DNA to the nucleus^[40]. For lysosome targeting, due to the reversible protonation at physiological pH, N-Alkylmorpholin moiety is usually used for lysosome targeting. For endoplasmic reticulum (ER) targeting, propyl chloride^[30,41] and pentafluorophenyl amide^[42–44]

were reported as efficient ligands. For lipid droplet targeting, due to the neutral electrical potential and lipophilic nature, its targeting moiety was usually nonionic lipophilic alkane chains. It is worth mentioning that our group developed a family of lipid droplets targeting dyes ranging from yellow to near-infrared (NIR)^[45].

1.1.3- Nanoparticles used in drug delivery

Nanoparticles are regarded as novel and increasingly used nanoscale material applied in drug delivery for diagnosis, controlled delivery of therapeutics, and so on. Different types of NPs have been used in drug delivery: (i) polymeric NCs, (ii) lipid-based NCs and (iii) inorganic NCs. The following sections refer to the description of some of them.

1.1.3.1- Polymeric nanocarriers

Polymeric NCs involved polymeric NPs, polymeric micelles, dendrimers, and polymeric hydrogels.

1.1.3.1.1- Polymeric nanoparticles

Polymeric NPs systems, benefiting from bio-friendly properties such as high biodegradability and biocompatibility, are regarded as efficient tools for drug delivery in controlled and targeted ways. For the EPR effect, it is optimal to use these particles with a diameter ranging from 100 to 200 nm. A variety of polymers usually biodegradable have been commonly used for the formation of these polymeric NCs, for example, poly (D, L-lactic acid) (PLA), poly (ϵ -caprolactone) (PCL), poly (D, L-lactic-*co*-glycolic acid) (PLGA). These polymers could also form copolymers with each other, or block polymers such as poly(ethylene glycol) (PEG) or d- α -tocopheryl polyethylene glycol 1000 succinate (TPGS), *etc.* to improve the hydrophilic property^[46]. Besides this, polymers based on some polysaccharides, for instance, chitosan, pectin, alginate, *etc.* are also regarded as materials for the formation of polymeric NPs^[47,48]. It is also interesting to mention that some polymers are capable to target cancer cells, for example, hyaluronic acid and chondroitin sulfate can target cancer cells where CD44 is over-expressed^[49,50].

1.1.3.1.2 Polymeric micelles

Polymeric micelles refer to micelles formed during the self-assembly process of amphiphilic polymers at high concentration (above the critical micellar concentration) amphiphilic polymers^[51]. These micelles are usually formed from non-consistently linked di or tri block conjugations of hydrophilic and lipophilic blocks^[52,53] (Figure 1.3). Usually, drugs were encapsulated in the lipophilic core of the micelle, while the hydrophilic shell provides good solubility of the micelle in aqueous environment^[48].

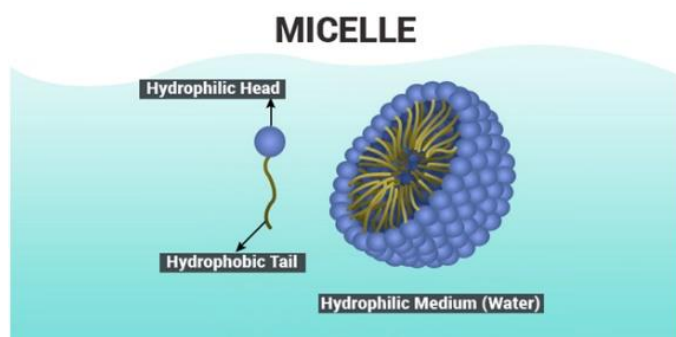


Figure 1.3. Illustration of polymeric micelle architecture. Adapted from ref ^[53].

1.1.3.1.3- Dendrimers

Dendrimers are different from conventional polymer NPs composed of a covalent assembly of multiple small polymer molecules. Dendrimers refer to single macromolecules (Mw ranging from 5000 to 500,000 Da) with highly branched three-dimensional (3D) nanoscopic structure and homogeneous distribution (low PDI)^[54] (Figure 1.4). At present, dendrimers for drug delivery are built upon the chemical reaction from some basic compounds, for instance, polyglycerol, polyamidoamine (PAMAM), polyetherhydroxylamine (PEHAM), melamine, polyester amine (PEA), polypropylene imine(PPI), and poly-L-lysine^[55]. The types of dendrimers are defined from the number of repeated branched units ranging from around 1 for the premier generation (G1) to G10 (around 10 units). By conjugating hydrophilic moieties to the dendrimer surface, the water solubility of dendrimers could be dramatically improved, thus increasing the chance of adopting it as drug carriers.

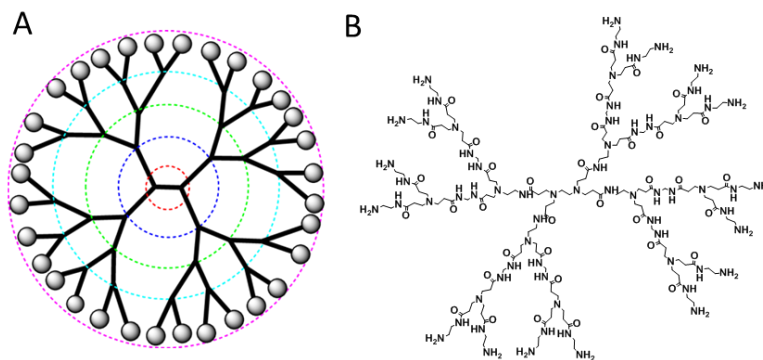


Figure 1.4. (A) Illustration of architecture of G2 dendrimers. (B) PAMAM G2 chemical structure Adapted from ref ^[56].

1.1.3.1.4- Polymeric hydrogels

Polymeric hydrogels refer to cross-linked (by physical entanglements) lipophobic polymer networks with high integrity having high compatibility to the aqueous bio-environment and capable of sustainable local release of a drug. These characteristics made it a good candidate for drug delivery^[57,58].

Some drugs could be covalently linked to a polymeric macromolecular carrier *via* degradable bonds^[59,60], which involved the use of different kinds of functional groups for covalent reaction such as disulfide, adipic dihydrazide, succinic anhydride, *etc.*^[61].

1.1.3.2- Lipid-based nanocarriers

Lipid nanoparticles (LNPs) are the name used for a family of NPs composed of lipids. Lipid-based drug delivery systems include liposomes, nano-emulsions (NEs, see a dedicated chapter 1.2-below), and solid lipid NPs. These LNPs can transport hydrophobic and hydrophilic molecules, display very low or no toxicity, and increase the time of drug action due to prolonged half-life and a controlled release of the drug^[62]. These systems have also demonstrated their considerable potential in enhancing the biocompatibility of drugs^[63].

They are common candidates as NCs in the field of drug delivery, bio-imaging, drug discovery, and so on. It is worth mentioning that LNPs became more widely known in late 2020, for the reason that some COVID-19 vaccines based on RNA technology use PEGylated lipid NPs as delivery vehicle to carry fragile mRNA strands (including both the Moderna and the Pfizer–

BioNTech COVID-19 vaccines). Lipid NPs having organic cores are classified based on their physical state: solid lipid NPs (SLNPs) and nano-emulsions (NEs). SLNPs have a solid lipid core because they are composed of lipids remaining in the solid state at room temperature^[64–66]. Non-ionic or ionic surfactants are used as the stabilization agents for their surface. Although the solid core renders SLNPs relatively stable, the fabrication of dye-loaded SLNPs is challenging, because the solid lipid can form orientated crystalline domains that gradually expel encapsulated material to the particle surface^[67]. On the other hand, NEs are dispersion of two immiscible liquids, oil in water (O/W) or water in oil (W/O) in form of nano-droplets, which are stabilized by an amphiphilic surfactant, with a diameter below 300 nm^[68–70]. NEs can be also in form of double^[71] and multiple layer emulsions^[72].

1.1.3.2.1- Liposomes

Liposomes are self-assembling systems consisting of a bilayer lipid membrane surrounding an aqueous interior compartment^[73] (Figure 1.5A). They are usually composed of natural biodegradable compounds, such as phospholipids (Figure 1.5B) and cholesterol. Surface modification with some groups for adding stealth properties (with PEG) and targeting ability (folic acid, aptamers, sialic acid, *etc.*) is also possible^[74].

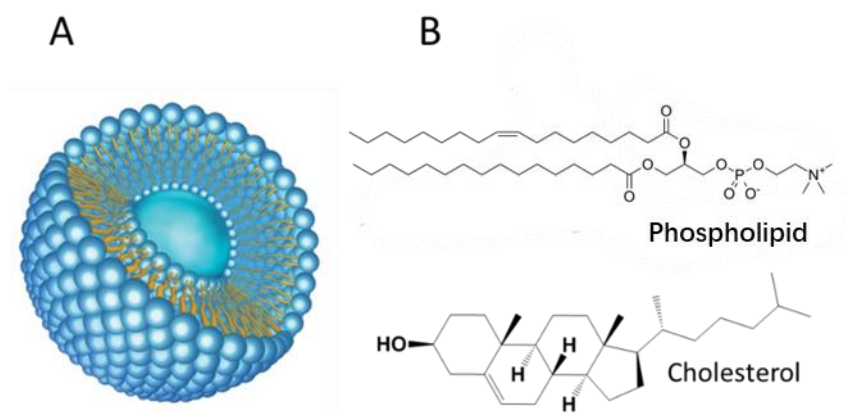


Figure 1.5. (A) Illustration of liposome architecture; (B) Structure of one phospholipid named 1-Oleoyl-2-palmitoyl-phosphatidylcholine (PC) and cholesterol (Chol).

1.1.3.2.2- Solid lipid nanoparticles

Solid lipid nanoparticles are consisted of solid lipids and surfactants. Solid lipids, *e.g.*, glyceryl monostearate, stearic acid, cholesterol, tristearin, *etc.*, are stabilized by a surfactant layer for colloidal stability in water. Due to the better stability in comparison to liquid core-based NEs, it is one of the most widely used NCs in drug delivery systems^[75]. These NPs are capable to pass through the cell membrane by recruiting P-glycoprotein transporter^[76,77]. A study indicated better and selective *in vitro* cytotoxicity of a drug named aloe-emodin when encapsulated inside solid lipid NPs. This nanoparticle showed strong affinity to two types of human cancer cell lines, while low non-specific attachment to a type of healthy tissue cell line. Resulting stronger toxicity and specificity to tumors compared to native aloe-emodin^[78].

1.1.3.3- Inorganic nanocarriers

Inorganic NCs is another type of NPs used for drug delivery. This family of NCs consists of gold NPs, magnetic nanomaterials, carbon nanotubes, nano-silica, and quantum dots^[79,80].

1.1.3.3.1- Gold nanoparticles

Gold nanoparticles (AuNPs) are particles with an Au core coated with a polymer surface^[81,82]. They are easy to synthesize and with good biocompatibility. Their surface can be functionalized with different ligands for targeting, imaging, and therapy (Figure 1.6). A lot of studies suggested they are good candidates as NCs^[83,84]. As an example, a study using apigenin encapsulated in gold NPs showed selective *in vitro* toxicity towards epidermoid squamous carcinoma (A431) and human cervical squamous cell carcinoma (SiHa) cells while demonstrating no specific toxicity toward a normal cell line named HaCat^[85]. In a recent study, AuNPs decorated with phospholipid modified with folic acid, showed increased accumulation in the Hela cells^[86].

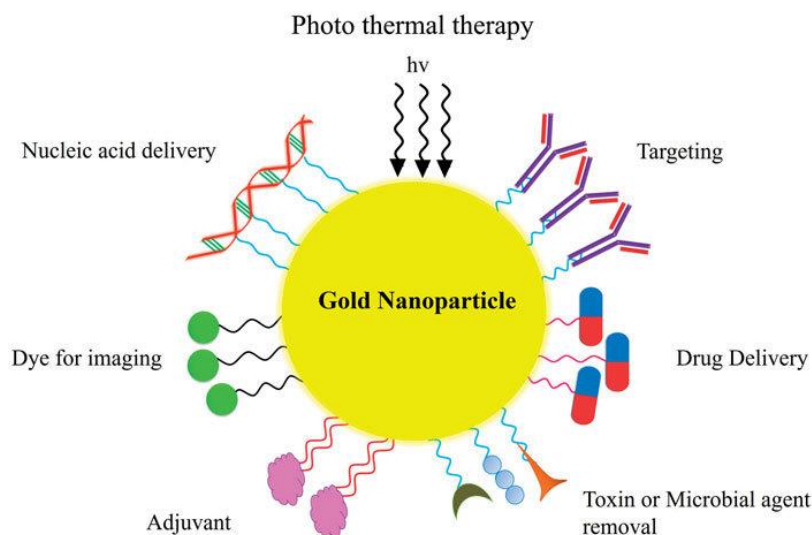


Figure 1.6. Illustration of the different surface coating of gold nanoparticles for targeting, drug delivery, and other. Adapted from ref [82].

1.1.3.3.2- Carbon nanotubes

Carbon nanotubes are composed of one or more sheets of carbon atoms rolling upon themselves. They usually have a diameter of around a few nanometers and a length up to 100 nm. Graphene is the basic material for the preparation of carbon nanotubes. Due to this fact, carbon nanotubes usually have special properties such as high electrical and thermal conductivity and extremely high tensile strength. There exist two classes of carbon nanotubes, namely, single-walled carbon nanotubes (SWNTs) and multi-walled nanotubes (MWNTs)^[87] (Figure 1.7). Carbon nanotubes have also been explored for drug delivery^[88]. With suitable chemical modification, these nanotubes based on carbon atoms could have good solubility in water and increased biocompatibility^[89].

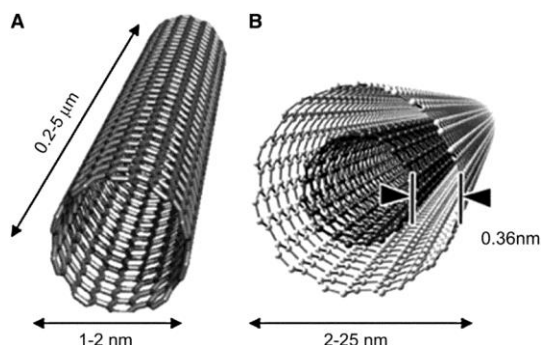


Figure 1.7. Conceptual diagram of single-walled carbon nanotube (SWCNT) (A) and multi-walled carbon nanotube (MWCNT) (B) showing typical dimensions of length, width, and separation distance between graphene layers in MWCNTs. Adapted from ref [87].

1.1.3.3.3- Magnetic nanoparticles

Magnetic nanoparticles are a class of NPs that can be manipulated using magnetic fields. Some of their characteristics such as small size and magnetic properties render them good candidates for drug delivery^[90]. Several methods have been explored to make them efficient drug carriers (Figure 1.8). Recently, curcumin magnetic NPs were synthesized to improve the biocompatibility and efficacy of the drug^[91]. The drug presented 2.5 folds of loading capacity in serum compared with its native form. Through the modification of the surface with various target ligands, the particle could have targeting capability^[92]. In this study, the authors, besides using a targeting agent for tumor targeting, also applied an external magnetic field for better targeting to tumor areas as well as for reducing non-specific effects to normal tissues. The xenograft mouse model also showed a better capacity for suppressing tumor growth and prolonged mice lifespan with administration of drug-loaded magnetic NPs with grafting compared to without.

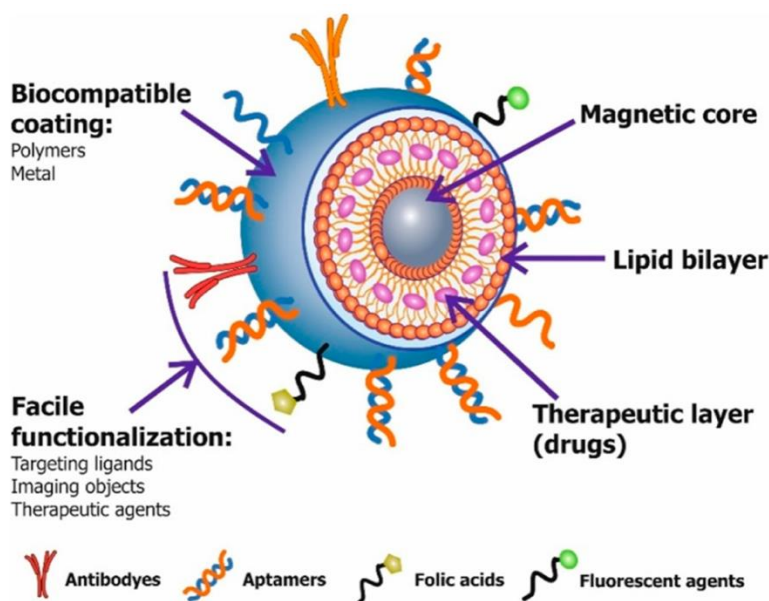


Figure 1.8. Illustration of a multifunctional magnetic nanoparticle structure with different types of coatings, target ligands and imaging agents. Adapted from ref ^[92].

1.1.3.3.4- Silica nanoparticles

Silica nanoparticles are a class of NPs made from silicon materials and their oxides. These NPs have the advantage of easy surface modification and low toxicity. Additionally, the materials for the formation of silica NPs are abundant in nature. Thus, silica nanoparticles are regarded as excellent candidates for drug delivery^[93]. Broadly, there are two different types of silica NPs,

namely, nonporous (solid) and mesoporous silica NPs (pore size: 2–50 nm) (Figure 1.9). The porous characteristics of the mesoporous silica NPs have a larger surface area and lower density, rendering them promising NPs for drug delivery^[94].

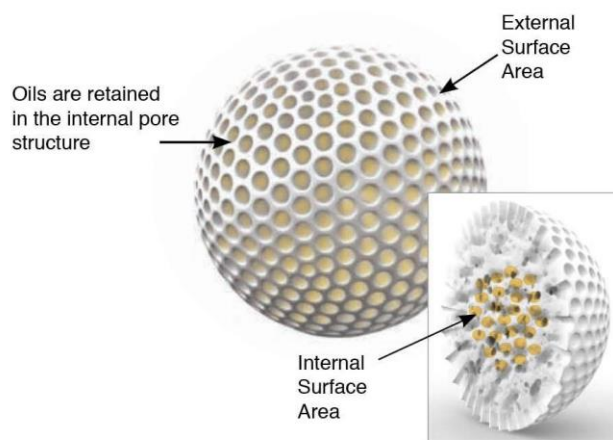


Figure 1.9. Illustration of mesoporous silica nanoparticle structure. Adapted from ref ^[95].

1.1.3.4- Stimuli-responsive nanocarriers

Amongst some ideal characteristics (stability, biocompatibility, reduced leakage during transit) of NPs mentioned above, stimuli-responsive NCs are mostly studied for targeted drug delivery. These NCs are responsive to various external factors, such as ultrasound^[96,97], heat^[98–100], magnetism^[101,102], light^[103–105], pH^[106] and ionic strength^[107]. Thus, drugs loaded in these NCs are triggered to be released under suitable conditions, which leads to improved targeting and control (Figure 1.10). For example, superparamagnetic iron oxide NPs could be combined with polymeric NCs^[108] or lipids^[109] to form a controlled drug delivery system that is responsive to the external magnetic field. It is worth mentioning that multiple stimuli could in most cases be merged on one NCs system. For instance, Chen *et al.* developed a multi-stimuli-responsive Au/Fe₃O₄ polymer NCs that are responding to magnetic field for localization as well as absorbing in infrared region for controlled release. The system is developed for use in NIR-triggered chemo-photothermal therapy^[110].

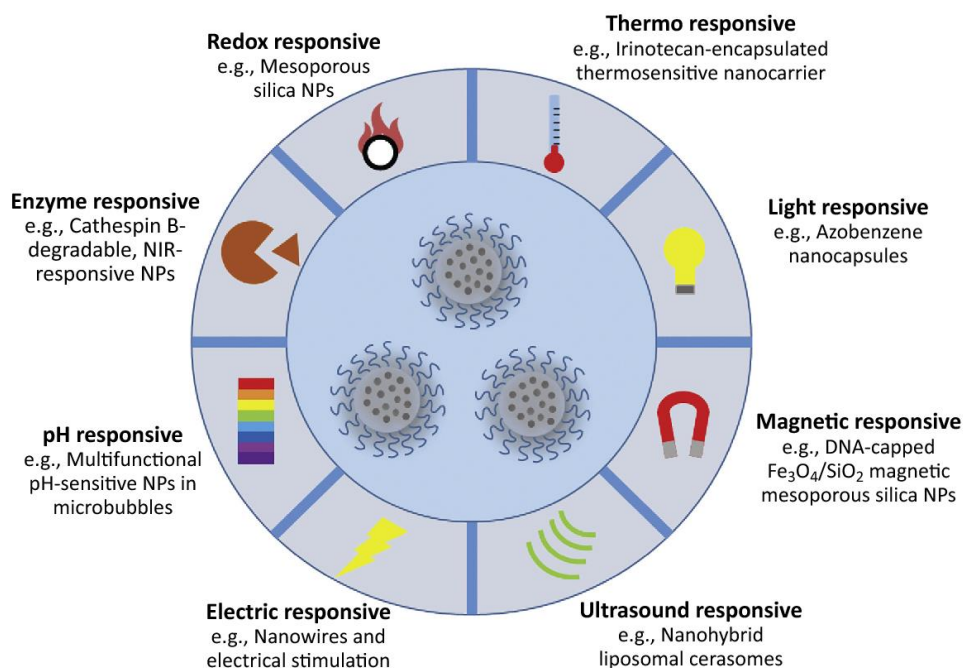


Figure 1.10. Schematic overview of eight different types of stimuli applied in the design of stimuli-responsive NCs for drug delivery. Adapted from ref ^[111].

1.1.3.5- Nanoparticles for *in situ* uptake

Conventionally, NPs are used as carriers for drug delivery. However, some researches showed that NPs could also be used as extraction agents to extract toxins or oxidants from media, which makes them potential candidates for dialysis, de-pollution, and detox. As an example, Chen *et al.* developed a cross-linked cationic surfactant nanoparticles (micelles) capable of removing nutrients of anionic species (CrO_4^{2-} , SO_4^{2-} , HPO_4^{2-} , NO_3^- , Br^- , NO_2^- , Cl^- , HCO_3^- , H_2PO_4^- , and F^-) found in natural water for de-pollution applications^[112] (Figure 1.11). In Figure 1.11, phosphate is presented in blue in the presence of a colorimetric indicator. Suspension of nanoparticles as extraction agents was placed within dialysis membranes and exchanged anionic species with 100 mL of Wabash River water (polluted by phosphate). Judging from the blue color intensity changes of the solution before and after the dialysis process, it is obvious that the phosphate was extracted by nanoparticles inside of the dialysis membrane (Figure 1.11).

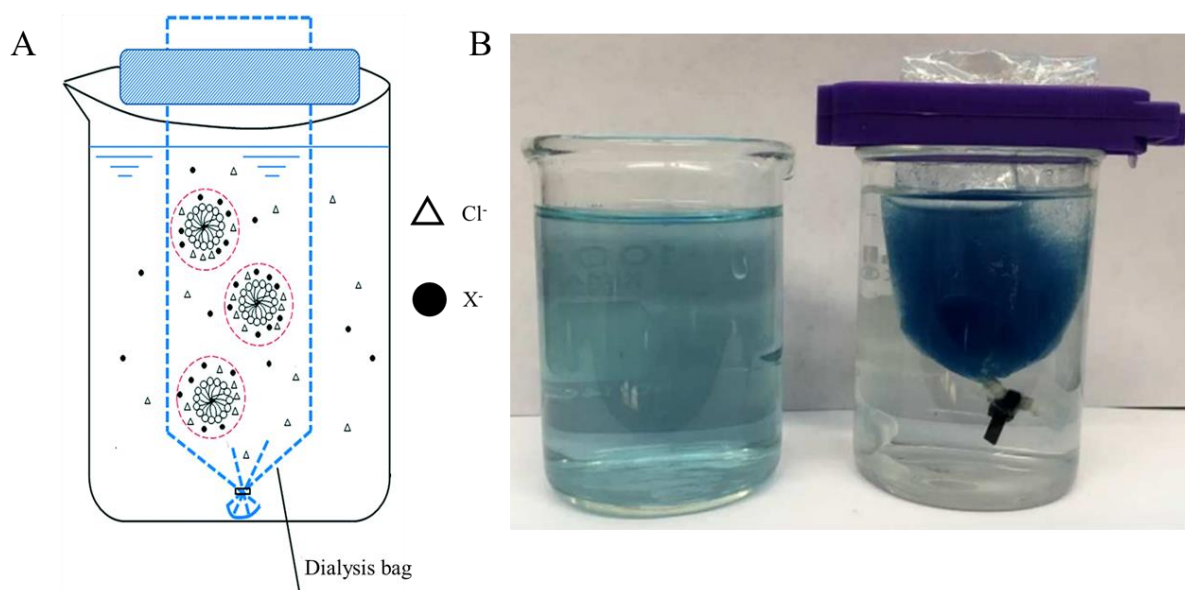


Figure 1.11. (A) Anion extraction illustration and (B) Wabash River water, before and after dialysis with QASE NPs. Adapted from ref^[112].

Yukio *et al.* designed a porous silica nanoparticle for scavenging oxygen species in dialysate to reduce oxidative stress. The study exploited dynamic covalent chemistry to conjugate reactive oxygen species (ROS) scavenger called nitroxide radical to silica nanoparticle with surfactant surface^[113]. The functional silica NPs (SiRNP) showed the ability to decrease concentration of uremic toxins *in vivo* (Figure 1.12).

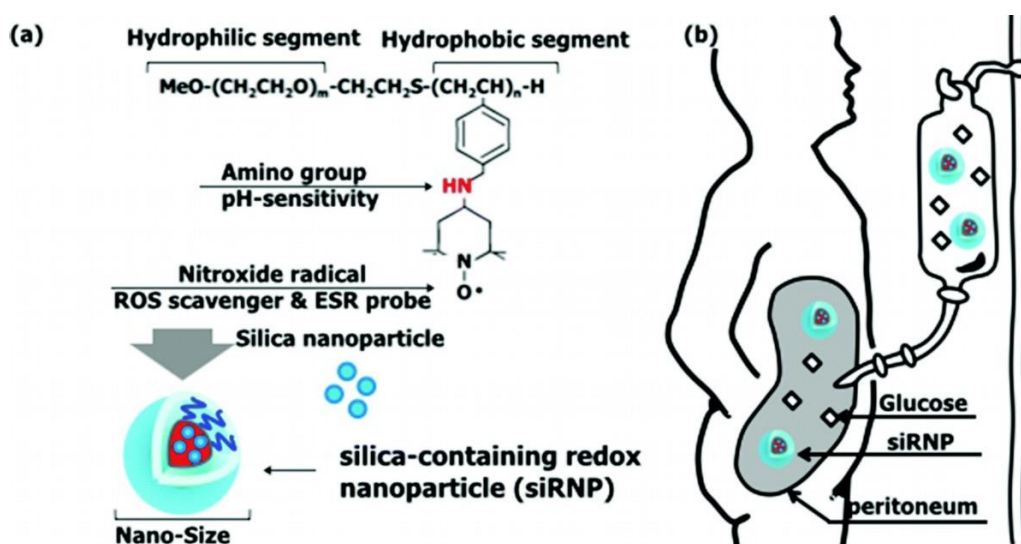


Figure 1.12. Schematic illustration of silica-containing redox NPs (siRNPs). (a) Structure of siRNPs and (b) application of siRNPs for peritoneal dialysis. Adapted from ref^[113].

In another research, a magnetic nanoparticle (MAHD) was developed based on the Fe_3O_4 host carrier, and bovine serum albumin (BSA) was conjugated on it for extraction purposes^[114]. Model experiments indicated a dramatic increase in both the removal rate and the overall removal efficiency of MAHD compared to conventional magnetic nanoparticles without BSA (HD). A more thoroughly investigated field is nanoparticle used as “cellular nanosponges” for the extraction of biological components such as chemical toxicant, bacterial toxins, and harmful antibodies^[115]. Usually, nanoparticles were coated with cell-membrane with specific decoys for bio-components. For example, Chen *et al.* designed a cell-membrane-cloaked oil nanosponges by covering olive oil core with red blood cell (RBC) membrane, the nanosponge could soak up toxicants through physical partition and specifically absorb and neutralize toxicants through biological binding^[116]. Nevertheless, nanoparticles use for toxin uptake is still a novel field of research.

1.2- Dye-loaded nano-emulsions

1.2.1- Nano-emulsions

Nano-emulsions emerged in the past decade as a promising delivery platform, due to their long-term stability, low toxicity, high encapsulation efficiency, capacity for rapid large scale production and biocompatibility properties^[70,117–121]. Importantly, they can be built from components generally recognized as safe (GRAS) and usually, FDA approved^[122]. They can be formulated easily using nonionic surfactants conferring a high surface density of PEG, which ensures their stealth properties concerning the immune and reticular-endothelial system^[123–126], resulting in increased circulation time in blood^[127]. On the other hand, oil core is a perfect reservoir for solubilizing lipophilic guest molecules at high concentrations, in particular, organic dyes to formulate fluorescent NEs.

Another attractive feature of NEs with oily cores is that they are analogs of particles naturally present in the body, such as intracellular lipid droplets, and low-density lipoproteins (LDLs). Lipid droplets are cellular organelles that regulate the storage and metabolism of lipids, which are found in almost every eukaryotic cell, and are particularly abundant in adipose tissues^[128,129]. Lipid droplets are also a storage for cholesterol and acylglycerols, required for biomembrane formation and maintenance. On the other hand, LDLs are lipid core-protein shell NPs naturally present in the blood and ensure solubilization and transport of lipophilic molecules like cholesterol. LDLs can be considered a drug NCs and have already raised interest in nanomedicine^[130,131]. Therefore, NEs emerge as bio-mimicking “green” NCs, with strong potential as a future safe scaffold for the preparation of contrast imaging agents and nanomedicines. In this review, we will focus on NEs as NCs of fluorescent dyes, their fabrication, properties as well as bioimaging and biomedical applications.

1.2.2- Preparation of dye-loaded nano-emulsions

1.2.2.1- Components of NEs: Oil

We can use a broad range of oils, natural or synthetic in the formulation of NEs. However, biocompatible oil phases from the vegetable origin are preferred, such as re-esterified fractions

derived from soybean oil^[132–135], sesame oil^[135], cottonseed oil^[136], sunflower oil^[137], coconut oil^[138], rice bran oil (see examples in Figure 1.13A)^[139]. A major limiting factor to use natural oils of vegetal origin is their instability. The relatively high content of unsaturated esters in linseed oil makes it susceptible to polymerization reactions when exposed to air^[140]. D- α -Tocopherol (vitamin E) family has also been extensively used as a carrier in NEs^[141–144]. Oleic acid and ethyl oleate have also been used in oral, topical and parenteral NEs^[145,146]. Alternatively, synthetic oils are also widely used, which include long-chain triglycerides (LCT), medium-chain triglycerides (MCT) or short-chain triglycerides (SCT). Depending on their chain lengths they are used either alone or in combination to formulate NEs. Among them; MCT (*e.g.* Labrafac[®] WL) is one of the most common synthetic oils used for formulation of NEs. Solubility of encapsulated compounds (drugs or dyes) in the oil phase is an important factor to consider when choosing the oils used in NEs formulation.

1.2.2.2- Components of NEs: Surfactant

Surfactants are essential for formulation of NEs, because they reduce the interfacial tension and prevent nano-droplets from aggregation. During the formulation process, they rapidly adsorb at oil-water interface of the newly formed droplets, providing stabilization to NEs by steric and/or electrostatic forces. For that purpose, nonionic surfactants are widely used. They present the advantage to decorate the droplets with a PEG layer, which strongly stabilize the droplets. Some of them, like ricinoleate PEG-35 amphiphile (*e.g.* Kolliphor[®] ELP) are parenteral grade molecules, used in clinical formulations with a variety of oils^[68]. Other similar non-ionic surfactants were also employed: Tween 20, 40, 60 and 80 (Polyoxyethylene sorbitan monolaurate)^[147–149], Span 20, 40, 60 and 80 (Sorbitan monolaurate)^[150,151] and Kolliphor[®] HS-15 (polyoxyethylene-660-hydroxystearate) (see examples in Figure 1.13B)^[152]. In addition, common surfactants of different chemical nature can be also used for NEs preparation: poloxamers (also known as Pluronic)^[153], amphiphilic proteins like casein^[154,155], lactoglobulin^[156], polysaccharides (*e.g.*, gums, starch derivatives)^[157] and PEG containing block copolymers^[158]. Ionic surfactants have also been used for preparation of NEs, like for instance, sodium dodecyl sulfate and docusate sodium salt (AOT)^[159,160].

Importantly, natural lipids also mentioned as emulsifying agents. In particular, phospholipids, like phosphatidylcholine (lecithin, Figure 1.13B) bearing a zwitterionic head group^[161], and their PEGylated analogues, have been extensively used for preparation of NEs. In case of saturated lipids, their monolayer at the surface was hypothesized to be present in gel (solid) phase, so that these NEs droplets were also called nanocapsules^[162,163]. Cholesterol, a natural molecule used for stabilization of liposomes, can also be used for similar purpose in NEs formulations^[164]. Ultimately, in a biomimetic approach, lipid membranes from blood cells have also been used to stabilize NEs for *in vivo* applications^[165].

In addition to the formulation of simple oil nano-droplets structures, several literature reports proposed modifications to control their surface properties: for example, the addition of a small amount of amphiphilic polyelectrolytes in the formulation, such as PMAO (poly(maleic anhydride-alt-1-octadecene)), results in the decoration of the droplets interface with carboxylic acid functional groups^[166]. An approach based on layer-by-layer (LbL) assembly onto the droplet surface has also been proposed^[167].

1.2.2.3- General principles of NEs preparation

Owing to the large interfacial area developed at the water/oil interface of NEs, they are present in a metastable state. Interfacial area indeed involves a high Gibbs free energy (ΔG) of the system according to the equation $\Delta G = \sigma \Delta F - T \Delta S$ ^[168], where ΔF is the change of the surface area of interface, ΔF is the increase of interfacial area, σ is interfacial tension at the boundary between the internal phase of NEs and the dispersion medium, T is the temperature and ΔS is the change of entropy^[169]. The higher G_f , the higher the system instability, and this is due to the interfacial energy created (ΔA). Therefore, the main challenges in the preparation of emulsions include control of the stability and the need to decrease surface tension as well as the need to supply some energy to increase interfacial area during the formulation.

In the case of macro-emulsions (diameter higher than micrometer), the stability issue is very important to consider. On the other hand, in the case of NEs (below 300 nm), droplets are so small that, even if G_f is much higher, droplets are stabilized because of their size range, that prevents the effect of gravitation (*i.e.* droplets are Brownian particles that do not cream). In addition, nano-

droplets do not flocculate for steric reasons^[170,171]. Stability is in fact one of the main interesting features of nano-emulsions compared to other lipid-based NCs.

NEs can be prepared by either high energy or low energy methods^[120]. Indeed, the huge interface can be created by supplying a large amount of energy^[169] but also by physico-chemical (low energy) methods, so-called *spontaneous emulsification*^[172], which takes benefit of the physicochemical properties of the nonionic surfactants to break-up the oil phase into nano-droplets. The spontaneous nano-emulsification method follows very simple processes, where an aqueous phase is added to a homogenized mixture of oil with the surfactants under intensive stirring (Figure 1.13C). This process is usually with temperature control, which depends on both oil and surfactant. The simplicity of this formulation method makes it especially attractive, allowing rapid production and industrial scale-up.

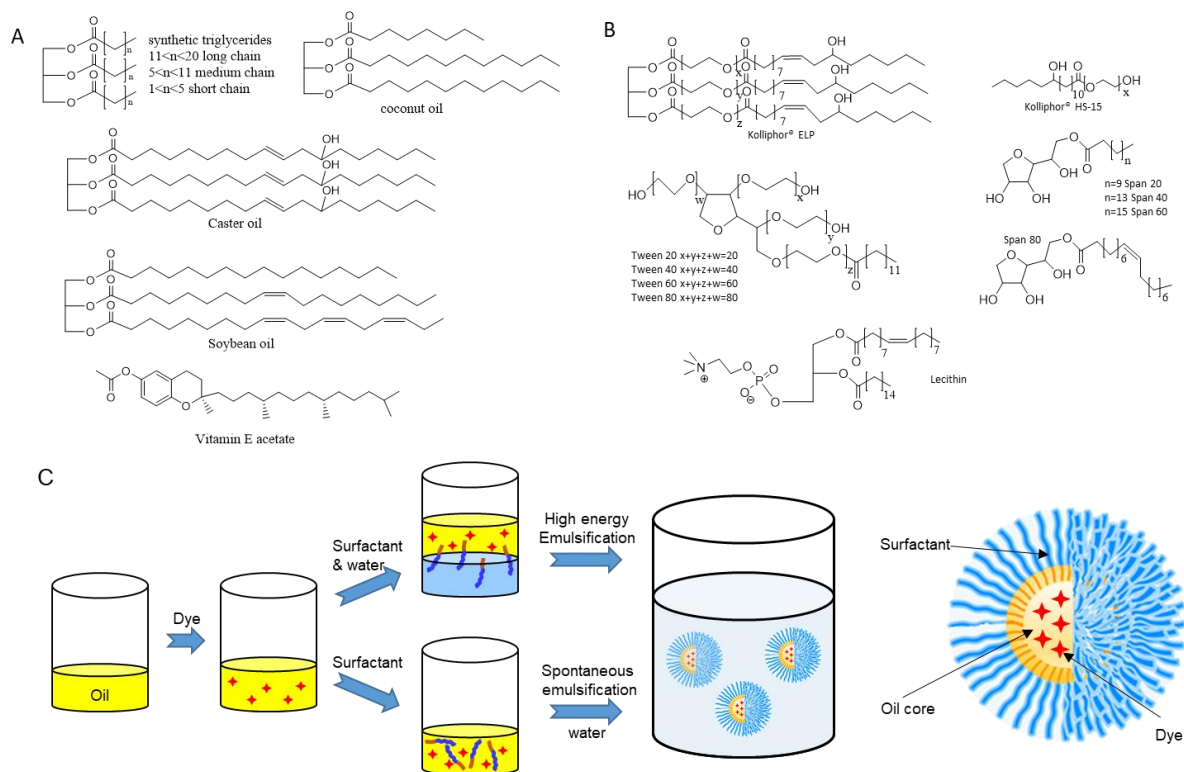


Figure 1.13. Structure of typical oil (A) and surfactant (B) used in NEs formulation, (C) General procedure for dye loaded NEs formation.

1.2.3- Dyes and dye-loaded NEs

Although the dye-loaded NPs have been intensively studied^[173–176], the research on dye-loaded NEs is still in its infancy. The goal of a successful formulation of dye-loaded NEs is a high and efficient loading, high particle brightness and stability with minimal dye leakage. Indeed, the dye leakage diminishes the brightness of fluorescent NEs, but increases the background because of the leaked dyes. Dyes inside NEs generally loaded by non-covalent methods, which means that the non-polar oil environment of NEs physically entrapped the dye. In this method, dyes are dissolved in the oil before the process of NEs formation^[177]. In some cases, the nano-emulsification process needs to be adapted to prevent dye degradation, for example by modulating the temperature or changing the type of surfactant^[178,179]. In cases when dyes have limited solubility in oil, an organic solvent is concomitantly used with dyes, surfactant, and oil^[180]. It is then evaporated before the nano-emulsification^[181]. While the dye solubility in oil is improved due to the amphiphiles (surfactants).

1.2.3.1- Dyes for NEs

The key to prepare dye-loaded NEs is proper selection/design of the encapsulated dyes, in order to achieve high solubility in oil, efficient dye loading and high brightness. There already existed variety of dyes for loading NEs (Figure 1.14). There also exist several strategies for dye encapsulation into NEs, which are aimed to improve dye solubility in oil. The most common and efficient approach is covalent modification of dyes with lipophilic chains^[123,182]. Indeed, practically all examples of dyes for NEs loading bear alkyl chains (Figure 1.14). Increase in the dye lipophilicity has several positive effects. First, it improves dye solubility in oil and thus enables efficient loading of dyes and ensures long term stability of NEs without dye precipitation^[123,182]. Second, higher lipophilicity will shift the water/oil partition towards the oil core, which inhibit the dye leakage, commonly observed for NEs^[123,178,179]. Finally, the dye could be chemically grafted to the components of NEs, such as oil or surfactant molecules^[183]. The second approach, which is applied to charged dyes (like cyanines) is the use of bulky hydrophobic counter-ions^[178,179].

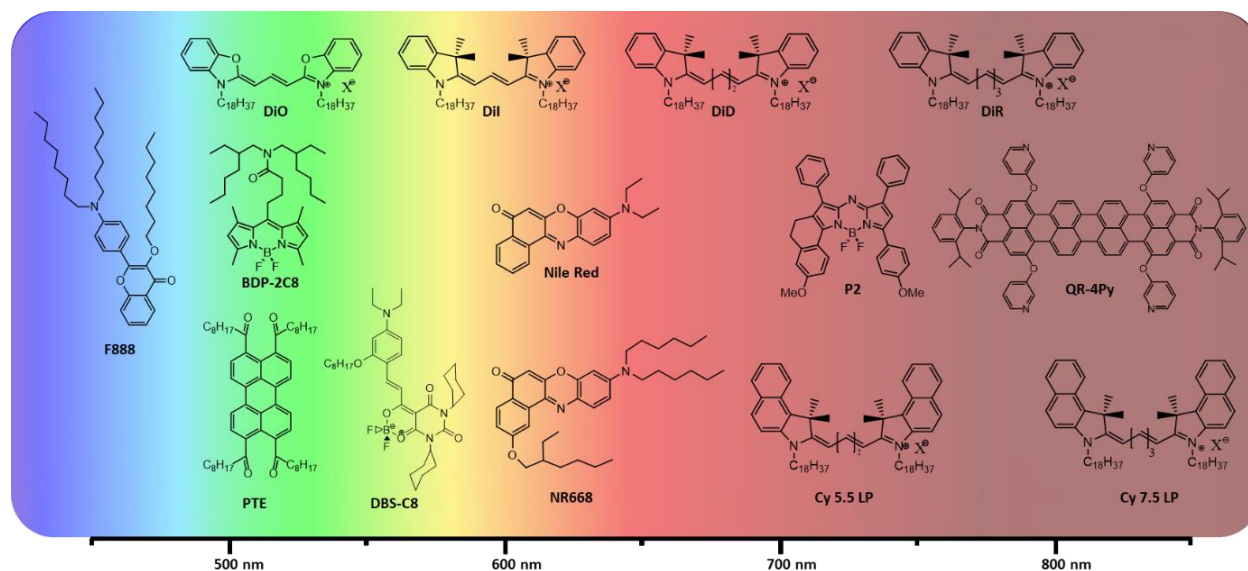


Figure 1.14. Examples of fluorescent lipophilic dyes used for preparation of dye-loaded lipid NEs organized by their emission wavelength in oil. (X^- is counter-ion, inorganic anion or tetraphenylborate).

1.2.3.2- Challenges in dye-loaded nano-emulsions

1.2.3.2.1- Brightness of dye-loaded nano-emulsions

Brightness of dye loaded NEs is crucial for bioimaging applications because it is directly relevant in obtaining images with high resolution. High brightness of dye-loaded NEs is beneficial for the quality of image obtained, because stronger capacity of NEs to emit intense fluorescence light could result higher signal-to-noise ratio of the image and the temporal and special resolution of the imaging. In general, the brightness (B) of a NE droplet is defined by the equation applied to any dye-loaded nanoparticle^[176]: $B = n \times \epsilon \times QY$, where n is the number of fluorophores loaded in the oily core, ϵ and QY correspond to the extinction coefficient and fluorescence quantum yield of the loaded dye inside NE particle. In the search for brighter dye-loaded NEs, there exist three different ways to improve the brightness of dye-loaded NEs based on this equation. The first way is to increase the number of loaded dyes, which is to increase the n in the equation. Increase the size of NEs is one way to achieve this, because the larger volume of NEs corresponds to larger n for the same dye concentration. Second way is to increase in the dye concentration inside NEs. In achieving this purpose, firstly, dye with good solubility in oil is required. As mentioned above, one way is to modify dyes with lipophilic groups. Long alkyl chains have been used by Texier *et*

al. to improve the optical properties of lipid NEs loaded with cationic cyanine dyes DiD and DiR^[180]. Either of them were encapsulated into NEs with encapsulation efficiency of 99% to reach dye concentration of 3.9 mM in oil core, without any observed fluorescence self-quenching. An increase in the fluorescence quantum yield Φ from 0.28 to 0.38 and fluorescence lifetimes τ from 1.0 to 1.8 ns were observed for DiD inside NEs vs. organic solvent. Authors observed similar tendency observed for DiR: Φ increased from 0.13 to 0.25, while τ increased from 0.57 to 1.1 ns. These effects assigned to the fact that oil core is more viscous compared to the organic solvent. Having 350 dyes per particle, the brightness of DiD-loaded particles scored up to $1.6 \times 10^7 \text{ M}^{-1} \text{ cm}^{-1}$ ^[184], this brightness are even higher than the reported highest values for QDs ($\sim 4 \times 10^6 \text{ M}^{-1} \text{ cm}^{-1}$)^[185], dye-loaded silica NPs ($\sim 2 \times 10^6 \text{ M}^{-1} \text{ cm}^{-1}$)^[186] and polymeric micelles ($\sim 5 \times 10^5 \text{ M}^{-1} \text{ cm}^{-1}$)^[187].

When dyes are loaded at high concentration, a fundamental problem of aggregation caused quenching (ACQ) arise due to the close proximity of the encapsulated fluorophores^[176]. In our previous studies, we showed that Nile Red and NR688, self-quenched at high concentrations inside the oil core, indicating that its planar structure favors dye aggregation at high concentrations^[123]. Dye aggregation can also result in the destabilization of NEs and sometimes in dye precipitation^[123]. Therefore, we should avoid ACQ as much as possible. Our group developed two ways to prevent ACQ behavior in dye-loaded NEs. One way is by incorporating bulky lipophilic groups, for example, 3-alkoxychromone derivative F888 (Figure 1.14), which bears bulky groups to prevent direct π - π stacking showed a remarkable resistance to ACQ even at very high dye loading, showing up to 78% fluorescence QY at 10 wt% loading in the oil core^[123]. Another way is by using bulky hydrophobic counter-ions in cases of encapsulation cationic dyes. For instance, DiD and DiR bearing long alkyl chains used for loading into NEs^[180], they are prone to form self-quenched π -stacked structures (H-aggregates) at high concentration^[188], which are responsible for strong ACQ. After replacing their small hydrophilic counter-ion (i.e. perchlorate, iodide, etc) with bulky hydrophobic counter-ions^[178,189]. The ion pair of cationic cyanine dye DiI (same dye family as DiD and DiR) with tetraphenylborate TPB (DiI-TPB, Figure 1.15), showed >40-fold improved solubility in labrafac, allowing dye loading up to 8 wt %^[178]. It was remarkable that even at 8 wt% DiI-TPB loading only negligible dye aggregation was observed judging from the optical absorption measurements of the dye-loaded NEs. Only 3.5-fold decrease in NEs quantum yield was observed by increasing the dye

concentration by 80-fold (from 0.1 to 8 wt%). This led to the increase of estimated particle brightness 23-fold ($80/3.5$) compared to the NEs with of 0.1 % dye loading. The obtained 90 nm NEs encapsulating ~12000 dyes per droplet showed a quantum yield of 0.14, which corresponded to theoretical brightness $B = 2.5 \times 10^8 \text{ M}^{-1} \text{ cm}^{-1}$. This value was close to that obtained experimentally ($B = 8.0 \times 10^7 \text{ M}^{-1} \text{ cm}^{-1}$) by single-particle microscopy with reference particles (FluoSpheres™) of known brightness. The latter value was >100-fold brighter than quantum dots of similar emission wavelength with quantum yield of ~0.5 and extinction coefficient at the long-wavelength maximum of $\sim 1 \times 10^6$ ($B \sim 5.0 \times 10^5 \text{ M}^{-1} \text{ cm}^{-1}$).

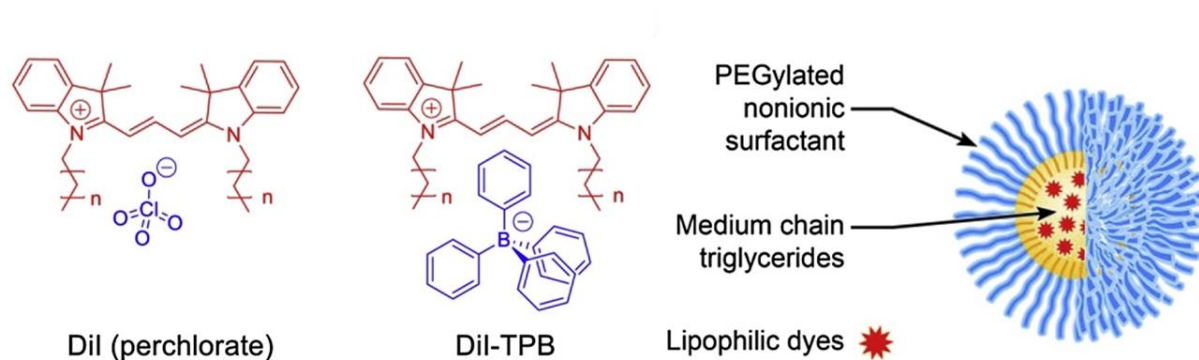


Figure 1.15. Chemical structures of DiI perchlorate and DiI-TPB and schematic presentation of a nano-droplet encapsulating them. Adapted from ref ^[178].

Brightness of dye-loaded NEs is also closely associated with the characteristics of dye itself, notably its extinction coefficient and quantum yield. A lot of research have been done in the past few years on the developing of novel dyes with improved brightness characteristics^[190], although the efforts to design bright dyes specially for NEs are still limited. Earlier, Zybrev *et al.*^[191] introduced the dioxaborine barbituryl moiety and then Kovtun *et al.* designed new fluorophores based on dioxaborine complexes and indolenine moieties^[192–194]. By combining these design approaches, we recently reported a series of fluorophores called StatoMerocyanines. They are composed of an indolenine moiety and a bulky barbiturate rigidified by a dioxaborine complex, which are ultrabright in oil and used as lipid droplet markers in cellular and tissue imaging^[45]. They displayed remarkable high molar extinction coefficients (up to $390\,000 \text{ M}^{-1} \text{ cm}^{-1}$) and quantum yields up to 100%. However, the dye compatible with common 488 nm excitation (SMCy3) showed modest quantum yield of 0.25 and extinction coefficient of $87,300 \text{ M}^{-1} \text{ cm}^{-1}$. Therefore, the indolenine group replaced with aniline unit yielding new fluorophores called

dioxaborine barbituryl styryl dyes (DBS) and incorporating long alkyl chain (DBS-C₈, Figure 1.16). This dye showed a good molar extinction coefficient of 120 000 M⁻¹ cm⁻¹ (two times higher than Nile Red) and an increased quantum yield of 0.98 (similar to Nile Red)^[144]. The brightness of DBS fluorophores in oil was enhanced due to their viscosity^[144], a phenomenon similar to that observed earlier by Texier et al using cyanines^[180]. The developed DBS dyes showed highest brightness (quantum yield and molar extinction coefficient) in castor oil (with the highest viscosity) compared with other oils (e.g. MCT and VEA)^[195,196].

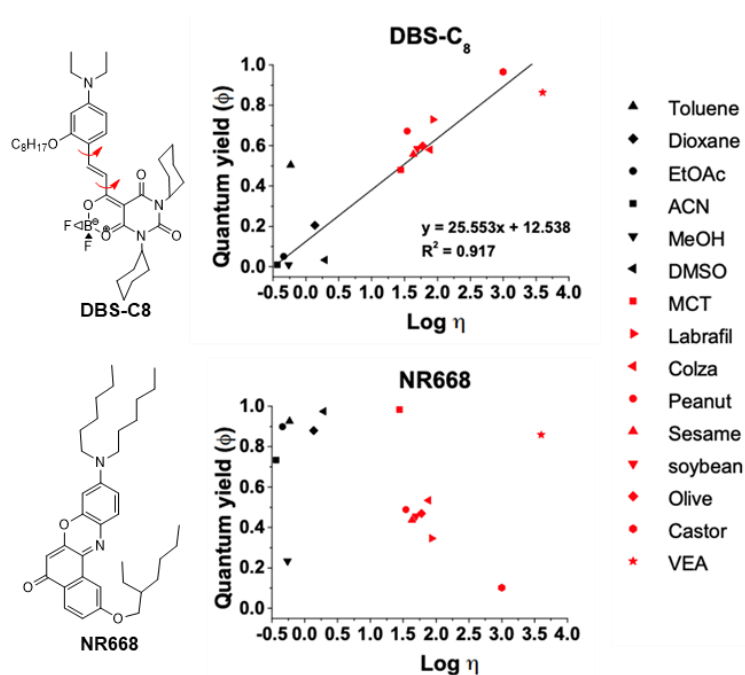


Figure 1.16. Correlation of the fluorescence quantum yield of DBS dyes and NR668 with the viscosity of the media. η is the solvent viscosity expressed in mPa.s. Red arrows show rotational freedom in DBS-C₈ dye, responsible to viscosity effect. Adapted from ref ^[144].

1.2.3.2.2- Photostability

High photostability of dye-loaded NEs is almost as important as brightness for high-quality fluorescence imaging, because it defines the number of photons emitted by the system before complete photobleaching. Photobleaching, which is a loss of fluorescence intensity (brightness) over time on continuous exposure to light, is a common problem of organic dyes. It is a common problem for cellular microscopy experiments when the same region of cells repeatedly imaged. In the study of Gravier *et al.*^[184] the increase in the DiD concentration from 1.2 to 4 mM, increased

in the photobleaching rate by 63 %. However, further increasing the concentration to 10 mM decreased the photobleaching rate to the same as 1.2 mM. The first phenomenon was attributed to photoproduct oxidized radicals that could react with neighboring fluorophore. By increasing the dye concentration, the bleaching reaction should be faster when the dye concentration is below dye self-quenching concentration. However, after the dye loading concentration reached the self-quenching value, dye would form aggregates, thus lower down the concentration of reactive dye species concentration, leads to a higher resistance to photobleaching.

In addition to photo-degradation of encapsulated dyes, intense light irradiation can directly affect the stability of dye-loaded NEs^[103]. Indeed, our earlier studies with NEs loaded with NR688 dye showed that strong irradiation for a few seconds can not only induce photo-degradation of the dye, but also its effective release into biological environment. The effect found to be oxygen-dependent, indicating that that some photochemical degradation of the NEs and/or dye could trigger dye release of NEs. This originally unwanted phenomenon was then applied for a light-controlled release of NEs cargos in cells and in zebrafish embryo^[103].

1.2.3.2.3- Stability and cargo release

When the dyes are non-covalently encapsulated inside NCs, they may undergo a leakage that depends on both dye and nanoparticle platform^[197]. As mentioned above, it is important to prevent the dye leakage, because it decreases the particle brightness, but increases the background signal caused by the released dyes. Therefore, the leakage lowers the imaging contrast obtained with the dye-loaded NEs and can be a source of important artifacts^[123]. Unlike solid lipid particles, due to the liquid nature of dye loaded NEs, dye are more prone to leakage issues^[198,199].

Characterization of dye release from hydrophobic reservoir of NEs and NPs is challenging using classical methods, such as dialysis^[200,201]. The point is that hydrophobic cargo is poorly soluble in water, so that in the conditions of dialysis in pure water, NEs would produce false impression of good stability. Unfortunately, the use of acceptor media containing organic solvents (like ethanol and isopropanol) is not compatible with NEs because they can destabilize the nano-droplets. Moreover, dialysis is difficult to realize in the presence of serum, as serum particles are much larger than dialysis membrane and could alter its function. Analysis of particle size is very useful to understand stability, although dye leakage is not always associated with changes in the particle size and measurements of particle size in complex biological systems is prone to artifacts.

Methods exploiting light absorption and fluorescence of the encapsulated dyes can help to understand the problem of dye leakage and NEs stability. The simplest approach uses optical spectroscopy, where the dye aggregation or leakage can lead to changes in the absorption and emission wavelengths^[202–205]. One of the most powerful methods to understand particle integrity is Förster resonance energy transfer (FRET). Since short donor-acceptor distances are required for the efficient FRET (2–10 nm), one should achieve mM concentrations of dyes to realize FRET inside the nano-droplets. This means that we can use the efficiency of FRET as the tool to monitor the concentration of dyes loaded in the NEs and thus dye leakage behavior. This approach was successfully used for variety of NPs in order to understand their stability and the cargo leakage in solution and directly in small animals: polymeric NPs^[206], conjugates with quantum dots^[207], and dye-loaded lipid NPs^[208]. When using this technique, the FRET pair should be carefully chosen in order to have good overlap between emission band of the donor and the absorption band of the acceptor, while keeping donor and acceptor emission bands well separated to avoid their overlap^[209]. A complementary approach to study stability of fluorescent NPs is Fluorescence correlation spectroscopy (FCS), a well-known technique in biophysics^[210] and materials science^[211] that allows to study *in situ* diffusion of emissive species. Similar to DLS, it can provide information about the hydrodynamic diameter. Moreover, we can use it *in situ* in biological media, including serum, which is challenging for DLS. Therefore, it was successfully used to study interactions of NPs with serum proteins and formation of protein corona of NPs^[176,212]. The unique feature of FCS is that it can provide information about brightness and the number of emissive species. The two parameters are directly linked to the stability of NPs, because once the fluorescent cargo is released into recipient media (*e.g.* serum), the number of emissive species increases while their brightness decreases^[123,201].

In our early studies, we focused on the development of stable non-leaking dye-loaded NEs based on Nile Red^[123]. To ensure proper loading and stability against dye leakage, parent Nile Red functionalized with three hydrophobic alkane chains (NR668, Figure 1.17C). Then, using FRET and FCS techniques, we compared stability of NEs loaded with NR668 *vs* the parent analogue: Nile Red. To design FRET NEs, they were loaded with a FRET donor dye F888 (Figure 1.17C), which is blue dye also bearing three lipophilic chains and its emission showed good spectral overlap with the absorption of Nile Red dyes. Efficient FRET could be achieved at 0.5 wt.% loading of both donor (F888) and acceptor (Nile Red or NR668) (Figure 1.17B). Then incubation

in serum revealed that FRET NEs based on Nile Red acceptor lost their FRET signal already after 3 min of incubation, whereas only minor release for NEs loaded with NR668 after 6 h at 37 °C (Figure 1.17C). This result indicated that lipophilic version of Nile Red, NR668, had stronger stability against leakage than Nile Red. The stability of NEs was then studied by FCS through monitoring the brightness and number of the emissive species in the serum media^[123]. In this case, Nile Red-loaded NEs showed rapid increase in the number of emissive species and drop of the particle brightness already after 5 min of incubation in serum, whereas these parameters were relatively stable for NR668 cargo. These FCS results correlated well the FRET data, confirming the importance of lipophilic alkyl chains in the stability of NEs^[123]. Another interesting application of FRET with NEs was to monitor their formation process. Sanchez Gaytan *et al.*^[213] used a micro-flow-homogenizer to mix basic components to form NEs along with two lipophilic dyes, DiO and DiI, upon NEs formulation, the FRET pair was encapsulated into the oil core, triggering FRET (Figure 1.17E). As the NEs formed, authors observed an increase in the acceptor fluorescence intensity and decrease in the donor fluorescence intensity, so that the color changed from the green to red (Figure 1.17F, G).

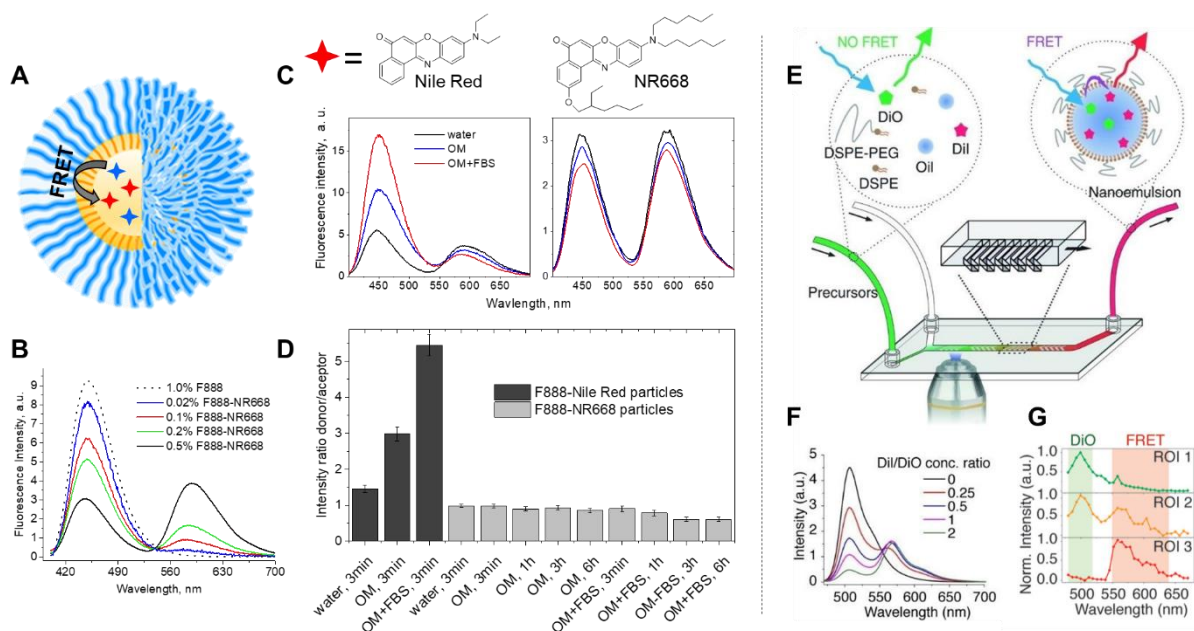


Figure 1.17. (A) Schematic presentation of FRET NEs. (B) Fluorescence spectra of FRET NEs at different concentrations of donor (F888) and acceptor (NR668). (C) Investigation by FRET of the dye release from NEs in different media: water, Opti-MEM (OM) and Opti-MEM with 10 vol.% FBS (OM+FBS). (D) FRET quantification as the fluorescence intensity ratio between the

maximum of the donor (450 nm) and acceptor (590 nm). (E) Schematic illustration of the microfluidic setup to study formation of NEs by FRET. (F) Emission spectra of NEs containing different DiI/DiO concentration ratios, excited at 458 nm. (G) Emission spectra recorded inside microfluidic device at indicated ROIs: ROI 1 corresponds to the organic phase; ROI 2 lies at the periphery of the solutions mixing area, and the ROI 3 corresponds to the central mixing area, where NEs expected to form. (B-C) Adapted from ref ^[123]. (E-G) Adapted from ref ^[213].

To minimize dye leakage, it is also possible to directly graft the dyes to the oil or surfactant component used for the formation of NEs^[214]. Patel *et al.* described an approach to monitor a two oil phase NEs system where each component separately labeled by fluorescent dyes, namely, Cy3 conjugated with perfluoropolyether (PEPE) oil and DiR dissolved in the outer hydrocarbon oil phase. This formulation showed great size stability and resistance to fluorescence signal losing over time. Jarzyna *et al.* described a way to formulate a multifunctional nanoparticle system with Cy5.5 grafted on the lipid surfactant (DSPE-PEG) at its PEG end and iron oxide encapsulated in the oil core^[181]. Another way to prevent leakage of dyes is by using cationic lipid that provide ionic interactions inside oil core, similar to bulky hydrophobic counter-ion TPB, mentioned above. It is reported that cationic lipid stearylamine (SA) can enhance stability of NEs loaded with indocyanine green (ICG), a water-soluble, amphiphilic anionic tricarboyanine dye. The incorporation of this lipid would trigger electrostatic interaction with nearby anionic ICG, thus preventing ICG from aggregation and destabilization of the NEs^[215].

1.2.4- Surface modification of NEs

Surface functionalization of NCs is a key step towards biomedical applications that include targeted imaging and drug delivery. However, so far, surface modification of NEs remains challenging because of their liquid nature. Indeed, in contrast to solid inorganic and organic NPs, the surface of NEs is highly dynamic because surfactant can readily exchange with the environment and thus lose a grafted functionality. Nevertheless, a number of approaches for NEs functionalization were proposed.

The most common method is based on functionalization of PEGylated lipids (e.g. DSPE-PEG), which insert at the NEs interface as a surfactant. On the one hand, it allows grafting fluorescent dyes to the NEs surface^[181]. On the other hand, DSPE-PEG enables grafting tumor targeting

ligands, like RGD. In the study by Texier and co-workers, 9.2% of surfactant was replaced with DSPE-POE5000-maleimide, which bears thiol reactive group used for grafting RGD moiety^[216]. PEGylated surfactant bearing stearate lipophilic chain and reactive groups have also been used for chemical functionalization with RGD ligand^[217]. More recently, Niko and co-workers proposed an original approach, where the commonly used surfactant (Cremophor® ELP) for formulation of NEs was functionalized with azide groups^[218]. Afterward, these obtained azide-bearing NEs successfully functionalized with cell penetrating peptides, which enhanced their internalization into cancer cells *in vitro*. In another recent study, lipophilic amine oleylamine was used to graft targeting ligand RGD and fluorescein to NEs, which showed higher cellular uptake *in vitro* compared to analogues with RGD ligand^[219].

An emerging strategy to modify NEs surface is to use amphiphilic polymers. In a recent study, NEs were formulated with the lipophilic poly(maleic anhydride- alt- 1- octadecene) (PMAO), which can hydrolyze into a amphiphilic polymer containing negatively charged carboxylates localizing at the NEs-water interface^[166]. Followed by this study, our team developed an antibody functionalized NEs based on a similar PEGylated PMAO derivatives. The formed NEs were capable of targeting VCAM-1 for early detection of senescent endothelial cells^[220].

1.2.5- Biological applications of fluorescent NEs

1.2.5.1- Imaging at the cellular level

1.2.5.1.1- Studying the pathway of NEs entering cells

Dye-loaded NEs showed the potential as a tool to understand the interactions of NCs with cells. After internalization, NEs could release their content to the cells. Generally, there exist two main paths for the internalization of NPs: endocytosis^[221] and micropinocytosis^[222]. It was shown that NPs with size above 300 nm preferentially internalize through macropinocytosis, whereas below this size they usually undergo endocytosis^[223]. As the size range of NEs is usually between 20 and 200 nm, endocytosis is their main internalization pathway. Endocytosis is an active energy-consuming process that ensures entry of substances into the cells^[224]. Based on previous reports on NEs, it is clear that their internalization is a complex function of different factors, including size, nature of emulsifiers, carrier oil and interfacial characteristics (surface charges)^[225–227].

Focusing on size effects, Fan *et al.* studied the cellular uptake of NEs with three droplet diameters (170, 265 and 556 nm)^[228]. Through analyzing the cellular uptake efficiency based on the fluorescence intensity of loaded dye inside the cells, authors found strong dependence on the nano-droplet size. The conclusion was that NEs of smaller size could enter into cells by endocytosis faster than larger NEs. Zheng *et al.*^[229] also showed an increased uptake for lower droplet size of NEs loaded with 5-demethyltangeretin (5DT) (Figure 1.18A). In this study, authors measured the internalization of 5DT into a suspension of HCT116 cells from different media. They loaded same amount of the compound into medium chain triglyceride (MCT) and NEs with different sizes (67 nm, 125 nm and 203 nm), after incubation for 0.25, 1, and 4 h. HPLC determination after 5DT extraction from cells suggested that 5DT internalization was highest when delivered in 67 nm NEs. The internalization rate for other conditions was 92.9%, 30.6%, 5.9% and 13.1% (referring to that of in 67 nm) in that of 125 nm NEs, 203 nm NEs, bulk water and MCT, respectively. The low internalization of 5DT when delivered from bulk water and MCT suggested minimal interference of direct leakage from NEs to cells, highlighting the role of endocytosis of NEs containing 5DT. Result of fluorescence microscopy images of Nile Red-loaded NEs internalization, which further confirmed the fact of smaller nano-droplet size favoring better internalization (Figure 1.18B). The effect of nano-droplet size on the internalization was confirmed by fluorescence microscopy of cells. In the study by Yi *et al.*, authors found out that smaller droplet size of lipid-based emulsions improved efficiency of a cargo (drug) delivery, defined by the amount of loaded drug recovered in the aqueous phase after ultracentrifugation^[230]. Two possible mechanisms have been proposed to explain the effect of size^[231,232]. The first one is size-dependent contact curvature: smaller particles have more adhesive contacts with the cellular membrane and less energy is required for deforming membrane around droplets for the formation of the endosome^[232,233]. Second one is size-dependent droplet deformability, where smaller droplets exhibit more defined spherical shape with lower deformability and thus can easier enter the cells^[231,232].

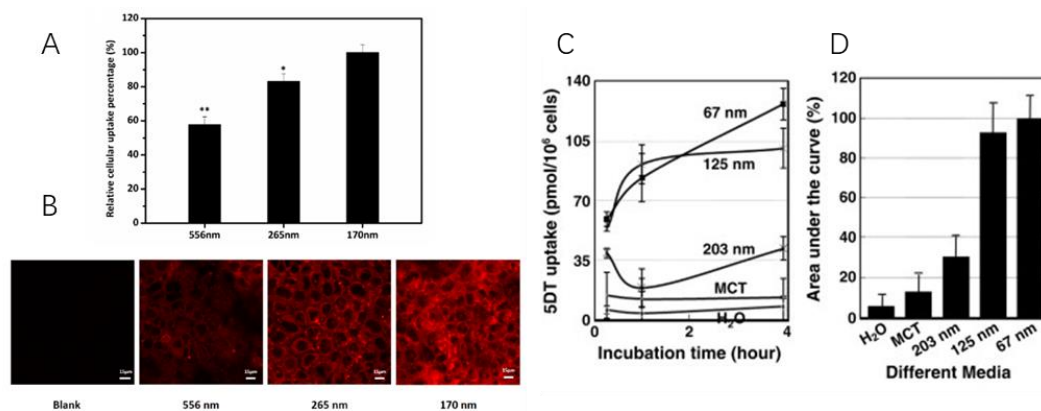


Figure 1.18. The effects of three different droplet sizes on cellular uptake of lipid-based emulsions (A) Relative uptake of emulsions of different diameters by Caco-2 cells. (B) CLSM of Caco-2 cells grown on glass coverslips after exposure to three different droplet size lipid-based emulsions containing Nile red. (C) Intracellular levels of 5DT at different times after incubation with different emulsions. (D) Area under the curve (AUC) of intracellular levels of 5DT after treatment with different emulsions. Adapted from ref ^[228,229].

However, one should also take into account that size of NEs can also influence their stability, especially dye leakage. Indeed, larger NEs with less surface-volume ratio can be more stable in the holding of dyes with lower problem of leakage. Our previous studies showed that the dyes can be released before NEs enter the cells^[123]. Indeed, when NEs loaded with Nile Red incubated with cells, microscopy images showed strong fluorescence emission from cells after 15 min (Figure 1.19B). By contrast, incubation with NR688-loaded NEs showed no detectable fluorescence signal even after 2h of incubation at r.t. (Figure 1.19C). These results suggest that NR668 NEs do not enter the cells in these conditions, whereas Nile Red undergoes fast leakage out of the NEs followed by intracellular accumulation. These data, in line with FRET and FCS results for Nile Red and NR668 (see above), can be explained by insufficient lipophilicity of Nile Red, so that its affinity to the oil core of NEs is not strong enough to be efficiently protected in biological environment. Therefore, great attention should pay in cellular studies using Nile Red or other medium-lipophilic dyes as the loading cargo for NEs. The absence of signal from NR668-loaded NEs with cells suggested remarkably weak interactions with the cell surface. On the one hand, it can be explained by high deformability of these liquid-core NEs, in line with other studied mentioned above ^[231,232]. To modulate NEs surface chemistry, negatively charged carboxylates were inserted to NEs interface using amphiphilic polymer PMAO^[166]. The obtained NEs

containing 1 % of PMAO and loaded with NR668 were able to enter the cells in 2 hours, which was not the case of the parent NEs without polymer. Thus, negatively charged carboxylates on the NE surface favor interactions of NEs with cells and their internalization^[166]. However, surface chemistry of NEs requires further work, in order to control better their interactions with cells.

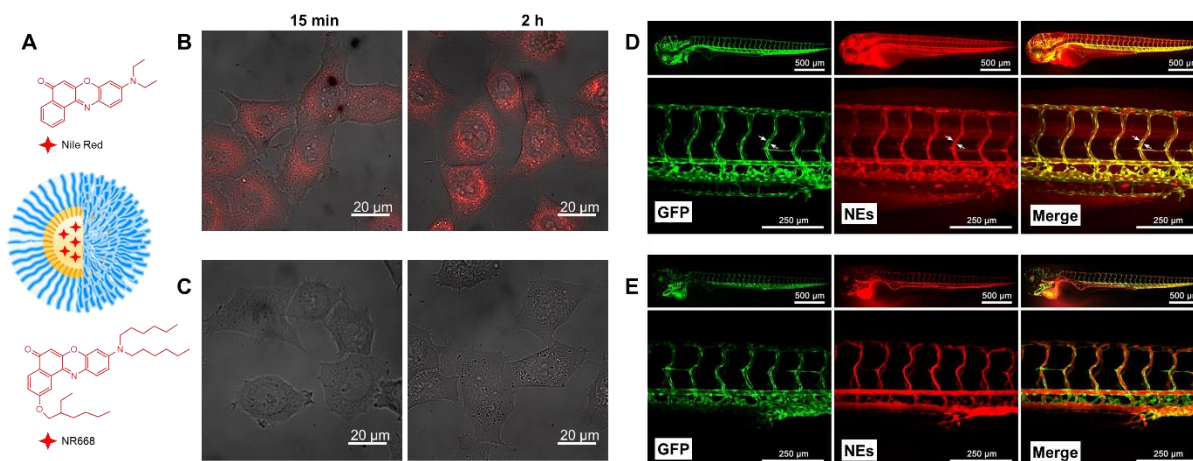


Figure 1.19. Imaging cells incubated with NEs loaded with Nile Red and its lipophilic derivative NR668. (A) Presentation of NEs loaded with Nile Red or NR668. (B,C) Combined fluorescence and transmission images of HeLa cells incubated with nano-droplets containing 0.1 wt.% of Nile Red (B) or 1 wt.% of NR668 (C) for different times: 15 min and 2 h^[123].

1.2.5.1.2- Tracking nano-droplets inside cells

Single particle tracking in cells is a great way to gain insight into the dynamics of intracellular trafficking and other macromolecular behavior^[234]. It is also important for understanding how nano-objects interact with the intracellular environment. The most important aspect of single-particle tracking in cells is usually high signal to noise ratio and tracking time. The first method to improve this is usually by using two-photon excitation (TPE) imaging, since cellular contents are generally transparent under infrared excitation wavelength^[235–237]. However, it is a scanning technique, which is slower than wide-field single-photon excitation, which can easily provide video rate imaging of single molecules and NPs^[144,178,238]. The key approach to improve signal to noise ratio is to use NPs of highest possible brightness. Up to now, most of particle tracking experiments in cells have been done using quantum dots, because they are 10-100 times brighter than single organic dyes and feature high photostability, which allows robust continuous recording of single-particle traces^[239–241]. Nowadays, organic NPs started gaining popularity

because of improved quantum yield, brightness and controlled small size, which enables them to be tracked with high precision and for longer periods^[242–244].

Recently, a novel dioxaborine dye named DBS-C₈ was developed and encapsulated into NEs with vitamin E acetate as liquid core (around 40 nm) at high concentration of 37 mM in oil without obvious aggregation caused quenching issue and a high quantum yield of 0.44^[144]. Moreover, in comparison to NR668, it showed significantly improved photostability and single-particle brightness. These improved optical properties of fluorescent NEs enabled their single-particle tracking as well as determination of their trajectory and velocity in the cytoplasm (Figure 1.20). Remarkably, NEs bearing negative surface charge due to presence of PMAO polymer at the interface significantly decreased the intracellular mobility of NEs, probably due to increased non-specific interactions with the intracellular components (Figure 1.20). This successful example shows a strong potential of dye-loaded NEs as a tool for particle tracking analysis and the importance of dye design for achieving desired optical properties.

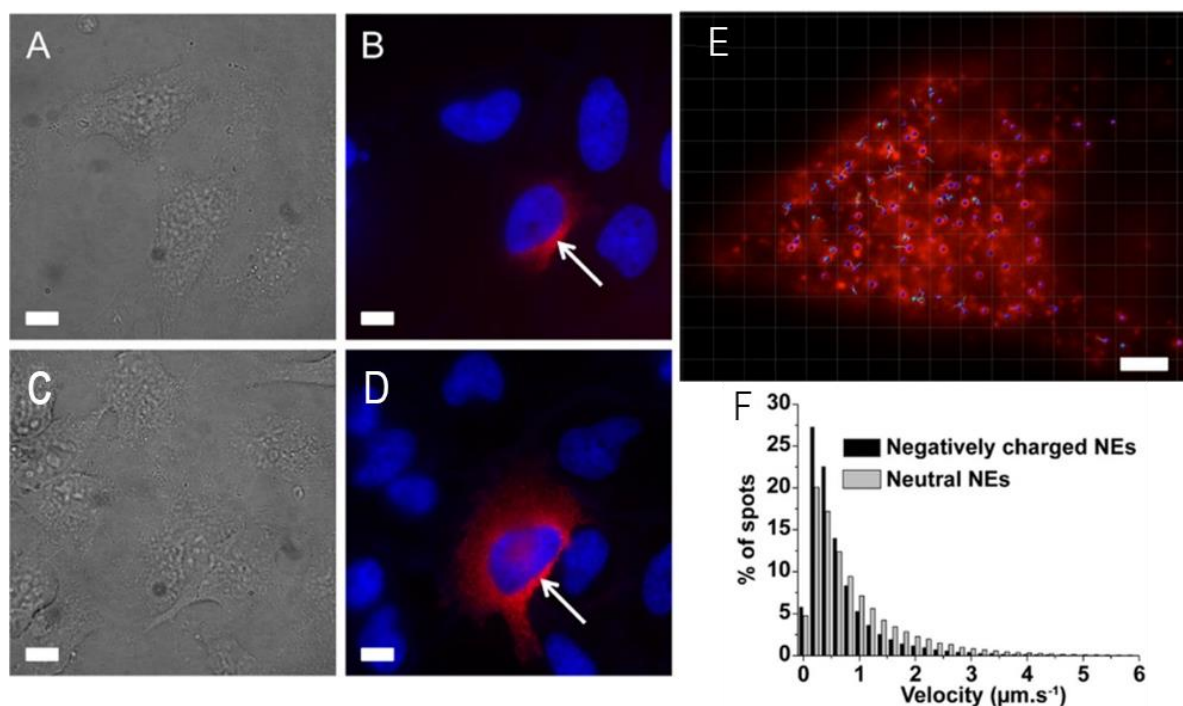


Figure 1.20. Microinjection of DBS-C₈-loaded NEs (41 nm) in HeLa cells and their individual tracking. Images of HeLa cells microinjected with negatively charged NEs (A–B) and neutral NEs (C–D). (A, C) Transmission light microscopy 5 min after injection. (B, D) Epifluorescence imaging 15 s post-injection; the NEs are in red and the nuclei are in blue; white arrows indicate

the injection point. (E) Example of a HeLa cell microinjected with neutral NEs where single NEs have been spotted (blue spots) and their trajectory, scale bar is 3 μm . (F) Histogram of NEs' velocity in the cytosol obtained by individual NEs' tracking from movies right after injection (30 s, 50 ms acquisition time). Adapted from ref ^[144].

1.2.5.1.3- Cytotoxicity

To understand the cytotoxicity of dye-loaded NEs, it is crucial to investigate the cytotoxicity of NEs itself. Among the two components, oil and surfactant, the latter can be a source of toxicity, because surfactants are known to provide multiple toxicity effects on cells and they are the part of NEs directly in contact with cells^[245]. In this case, the earlier studies on drug-loaded NEs shed light on the cytotoxicity of NEs without dyes. Yoon *et al.* focused on the effect of surfactant of NEs cytotoxicity in different cell lines (NIH3T3, H9C2, HepG2, hCPC, and hEPC). They detected no obvious cytotoxicity NEs (2.5 mg/mL of oil) formulated with Tween 80 and lecithin^[246]. Other researches also showed no clear cytotoxicity of NEs under low surfactant concentrations (5 mg/mL)^[246,247]. However, cytotoxicity might vary from one surfactant to another when NEs applied at high concentration. Vater *et al.* compared the cytotoxicity of lecithin-based NEs with NEs based on conventional surfactants on human skin cells (primary human keratinocytes as well as fibroblasts). Result indicated certain toxicity of high concentration of NEs (75 mg/mL of oil), and that toxicity of NEs based on synthetic surfactants (SDS, SLES, APG and Tween 80) showed stronger cytotoxicity (nearly 0% viability) than those based on natural lecithin surfactant. Meanwhile, our previous data showed that in case of NEs formulated with GRAS components (labrafac and Kolliphor[®] ELP), the cytotoxicity observed only at relatively high concentrations (7.5 mg/mL surfactant and 7 mg/mL oil).

Dye loading inside NEs usually does not contribute to increase the cytotoxicity of NEs, because its concentration in the oil rarely exceeds 1 wt.%. In our previous studies, the cytotoxicity of even heavy loaded NEs with cyanine dye (8 wt.%) and its bulky counter-ion (DiI-TPB) remained similar with empty NEs, except the highest concentration (21 μM DiI-TPB dye concentration, 15 mg/mL oil)^[178]. However, this dye concentration was at least 20 times greater than that normally used in imaging experiments, indicating that these dye-loaded NEs are usually non-toxic for bio-imaging at the cellular level.

1.2.5.2- *In vivo* applications

NEs are particularly attractive for *in vivo* imaging and cargo delivery in comparison to small organic dyes because of their prolonged circulation periods, as well as the ability to encapsulate different cargos, both contrast agents and drug molecules^[173]. In the past decades, intensive researches have been conducted about the fate of NEs *in vivo*, their bio-distribution and their disintegration process.

1.2.5.2.1- Dye-loaded NEs in Zebrafish embryo

The zebrafish embryo is becoming a powerful vertebrate model for quantitative optical imaging, owing to its high transparency in the embryonic and larval stages^[248]. Recently, it also appeared as promising *in vivo* model for studying and treating diseases, especially cancer^[249,250]. The application of dye-loaded NEs in zebrafish was initially reported by us using NR668 dye as non-leaking cargo^[123]. Authors injected NEs into the heart of the embryo followed by live imaging of their bio-distribution. Results showed co-localization of fluorescence from NRK with that of eGFP expressed by the zebrafish transgenic line, indicating the evenly distribution of the dye over the whole embryo (Figure 1.21C), whilst, no co-localization for NR668 loaded NEs, which existed exclusively in the blood circulation without leakage (Figure 1.21F) was detected. This study in one aspect, validated NEs as promising tool for imaging blood circulation of zebrafish, in another aspect, showed that it is very important to consider the problem of proper choice of dye cargo, to avoid artifacts during *in vivo* imaging. Later study found that strong illumination of NR668 NEs can trigger release of their content in biological media. This light-controlled cargo release was also tested in zebrafish embryo and it was found that after 5 min illumination (wavelength of 450–490 nm), fluorescence of NR668 was clearly observed outside of the blood vessels, which was not the case of non-illuminated zebrafish^[103]. These experiments, provide a proof-of-concept for the light-controlled release of a dye cargo from NEs *in vivo*.

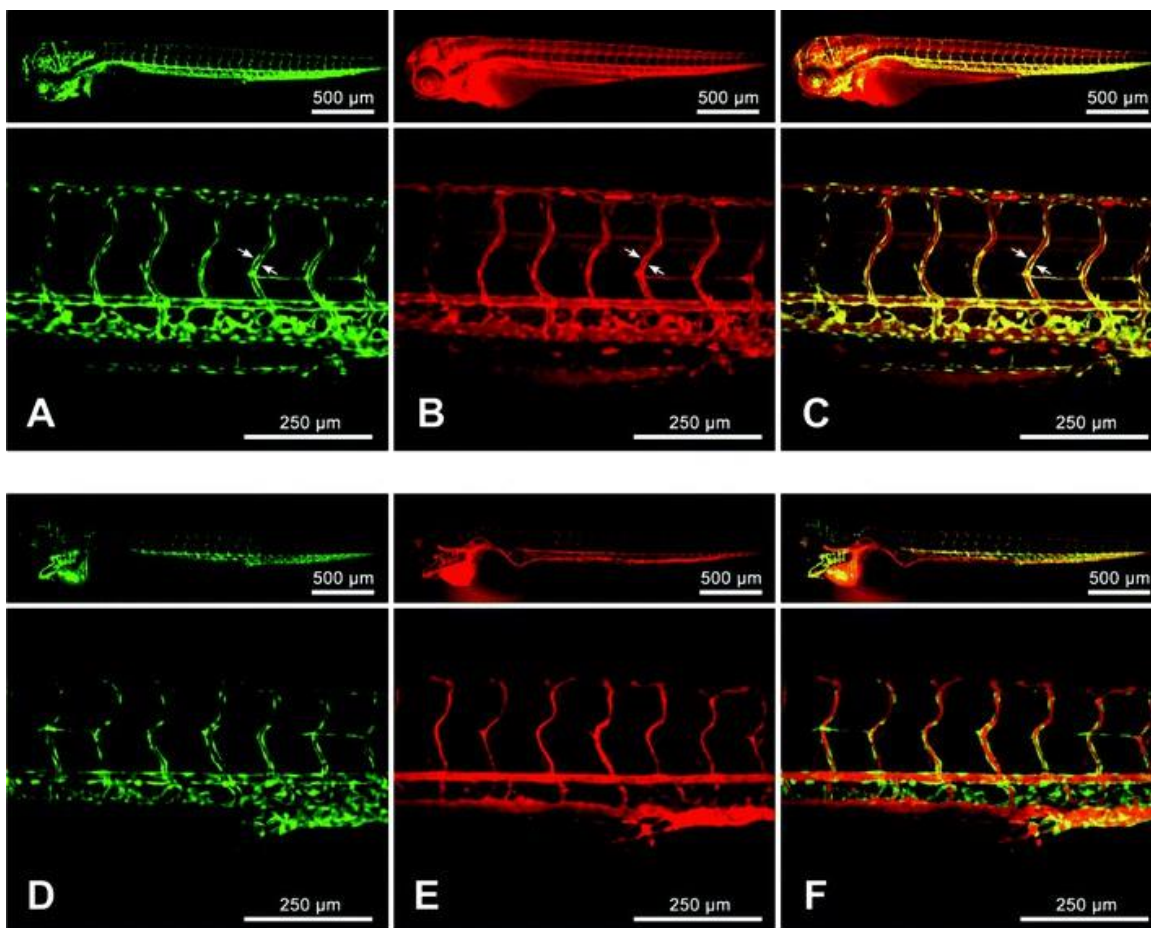


Figure 1.21. Zebrafish microangiography using nano-droplets containing 0.1 wt.% of Nile Red (A, B and C) or 1 wt.% of NR668 (D, E and F); Green channel: endothelial cells expressing eGFP; Red channel: Fluorescence from Nile Red and NR668. Adapted from ref ^[123].

In the further study, we aimed to boost the brightness of nano-droplets in order to track single particles directly in the blood stream of zebrafish. To this end, we loaded 90-nm NEs with DiI with bulky counter-ion TPB (DiI-TPB, Figure 1.22A) at 8 wt%, which corresponded to ~10,000 dyes per particle. At normal dilution before injection (1000-fold) these NEs allowed imaging blood circulation of zebrafish without noticeable dye leakage (Figure 1.22B). At much higher dilution (10^6 -fold), these ultra-bright NEs enabled first single-particle tracking in live zebrafish embryo. (Figures 1.22C,D)^[178]. Other results indicated that the tracking analysis showed strong variation in the single particle velocity produced by a heartbeat of the embryo, which matched well with the velocity of blood cells. Single-particle tracking *in vivo* opens new horizons in

bioimaging and nanomedicine, because it enables monitoring directly individual NCs, and thus understand better bottlenecks in the field of drug delivery^[251].

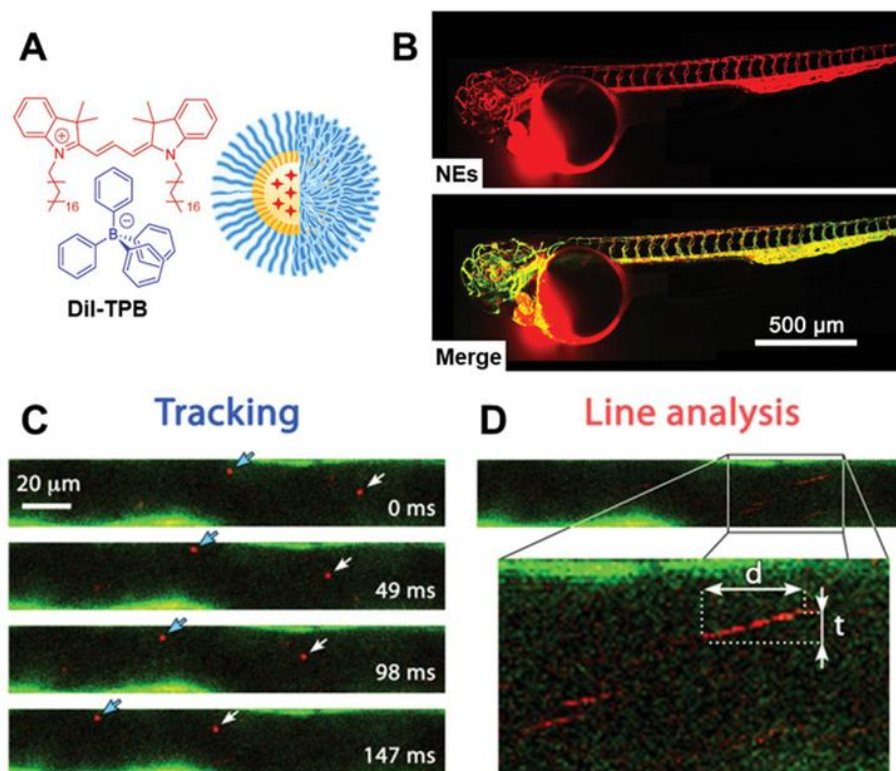


Figure 1.22. Zebrafish microangiography and single-particle tracking using 90-nm nano-droplets containing 8 wt.% of DiI-TPB injected in zebrafish embryos. (A) Scheme of NEs loaded with DiI-TPB. (B) DiI-TPB NEs channel (red) and merged image with GFP channel (green). (C) Single-particle tracking of DiI-TPB NEs in zebrafish vessels followed in consecutive frames. (D) Illustration of calculation of particle velocity by line scanning. Adapted from ^[178] Copyright 2014 Biomaterials.

1.2.5.2.2- Dye-loaded NEs used for mice imaging

Imaging of NEs in mice is very important, because mice is a key model animal used in cancer research and therapy^[252]. However, unlike zebrafish embryo, imaging of mice is strongly altered by auto-fluorescence and light-scattering of tissue and blood^[253,254]. These interferences can be decreased by using NIR dyes (> 700 nm), where those signals from tissue are minimal^[255–257]. A key question related to *in vivo* applications of NEs is whether they are able to keep their cargo

after injection up to reaching target (e.g. tumor). Indeed, the nanomedicine has been established mainly on solid organic and inorganic NPs^[258,259], while NEs, having liquid core, has not been considered as a carrier with sufficient stability. Since more deformable particles tend to be less prone to cellular uptake^[231,232], NEs with a liquid core can present minimal non-specific internalization into cells (see above) and potentially longer blood circulation period. On the other hand, liquid core NEs raise questions about stability of NEs *in vivo*. As mentioned above, the key tool to understand integrity of a NEs and the leakage of cargo is FRET between two encapsulated dyes. This approach has already been used to study integrity of different NPs *in vivo*^[206,260,261]. For instance, Hammond *et al.* reported a micelle polymer chemically modified with two azide-containing near-infrared (NIR) cyanine dyes named Cy 5.5 and Cy 7 by click chemistry^[206]. Through observing the change of FRET efficiency of these two dyes, authors are able to tell the integrity of the polymer particle, and thus, study the *in vivo* fate of the nanoparticle in the blood circulation system of mice.

One of the first attempts to generate FRET NEs for *in vivo* imaging was done by Texier *et al.*, where red DiD was combined in a FRET acceptor NIR dye DiR^[262]. These NEs enabled monitoring bio-distribution of NEs *in vivo*, showing their remarkable stealth character. However, as the FRET signal was relatively weak, it was difficult to quantify the integrity of NEs *in vivo*. Later on, we designed FRET NEs by loading donor (Cy5.5LP) and acceptor (Cy7.5LP), both operating in the NIR region (Figure 1.23A, B). Efficient FRET was achieved by improving dye loading to 1 wt.% with help of bulky hydrophobic counter-ion TPB (Figure 1.23C). Once injected at the tail of mice, donor and acceptor emission was detected by the whole animal imaging setup by exciting the donor dye (Figure 1.23D)^[179]. At the initial injection time, the donor intensity was much lower than the acceptor channel all over the healthy mice. Over time, donor channel intensity increased, while the acceptor intensity dropped, reflecting the loss of FRET over time (the FRET ratio decreased over time with pseudo-color switching from red to cyan), reflecting disintegration of NEs (Figure 1.23E). Using calibration solutions of NEs under the same imaging setup up it was possible to establish a calibration of the FRET ratio and thus directly quantify the integrity of NEs in mice (Figure 1.23D). Remarkably, emission from tail vein revealed that the integrity of these FRET NEs in the blood circulation of healthy mice was preserved at 93% at 6 h of post-administration (Figure 1.23G). On other hand, integrity of NEs dropped faster in liver, i.e. to 66% after 6h (with half-life of 8.2 h). Experiments in tumor bearing mice showed that these

NEs accumulated efficiently in tumors (Figure 1.23F) being nearly intact (77% integrity at 2 h) and then decreased their integrity to 40% at 6 h (with half-life of 4.4 h). This study proposed a robust FRET-based methodology to evaluate quantitatively the NCs integrity in small animals. The results also showed that NEs are remarkably stable, remaining nearly intact in the blood circulation and reaching the target tumor in nearly intact form. The latter validate them as prospective NCs for drug delivery applications.

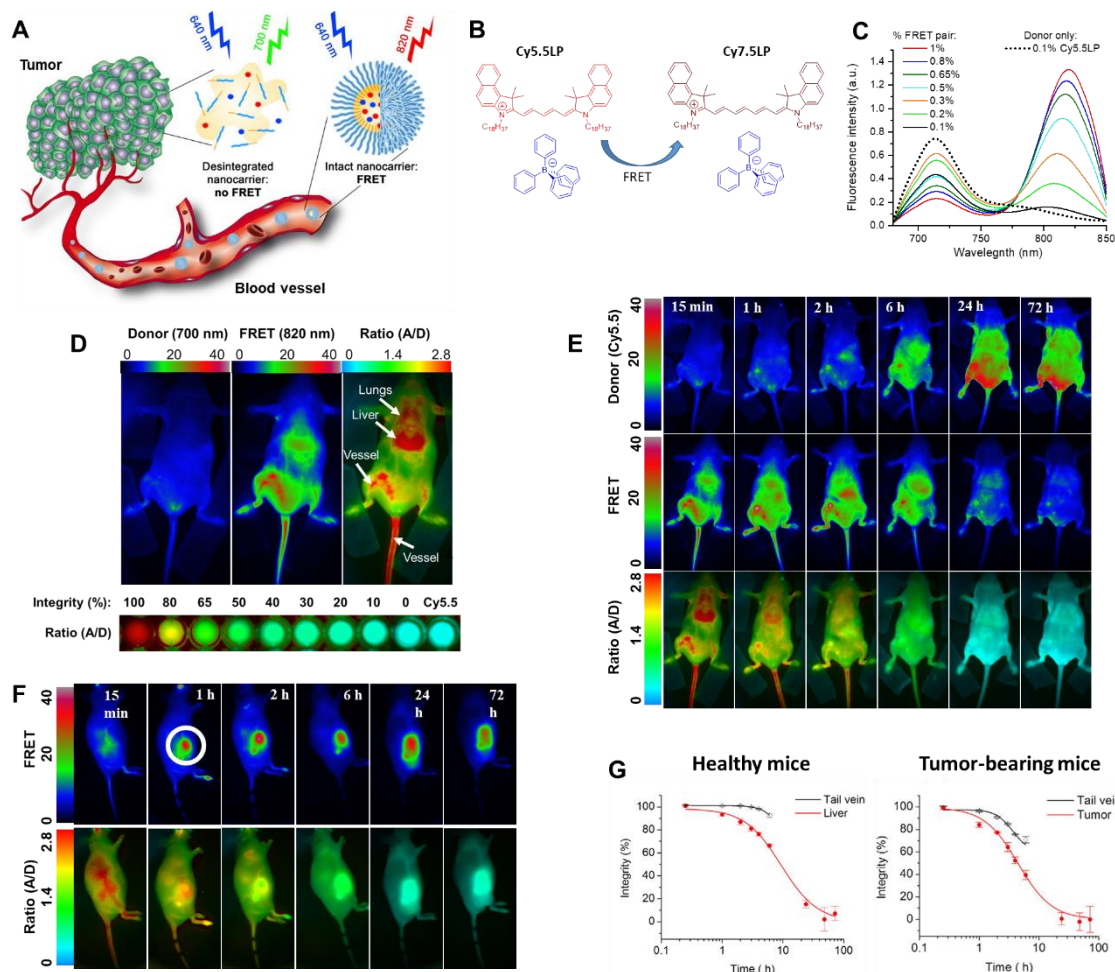


Figure 1.23. Concept of FRET NEs that can report on their integrity by change in their emission color (A) and the NIR dyes with their hydrophobic counter-ion (Cy5.5LP and Cy7.5LP) used for encapsulation (B). (C) Fluorescence spectra of dye-loaded NEs as a function of weight % of FRET pair (corresponds to % of each dye). (D) FRET imaging of healthy nude mice 15 min after injection of NIR-FRET NEs (1% of Cy5.5LP and Cy7.5LP each). (E) FRET imaging of healthy nude mice at different times after injection with NIR-FRET NEs and control NEs containing only Cy5.5LP dye (1%). Upper panels present intensity images of the Cy5.5LP channel (700 nm),

middle panels present images of Cy7.5LP channel (820 nm), while the lower panels present ratiometric images (acceptor/donor). (F) FRET imaging of tumor-bearing nude mice at different times after injected with NIR-FRET NEs. (G) Analysis of NEs integrity in different regions of healthy and tumor-bearing mice as a function of post-administration time. Adapted from ref ^[179].

1.2.6-Targeted imaging with dye-loaded NEs

1.2.6.1- Passive tumor targeting

Dye-loaded NEs with size between 20-100 nm, being large enough to avoid fast renal clearance, but small enough to pass the blood vessels, are attractive agents for the monitoring of the EPR directed accumulation of NEs (drug-loaded or not) in tumors. For instance, Radicchi *et al.*, observed the developing stages of NEs accumulation in tumor areas based on a DiR loaded NEs. Authors observed some increase fluorescence intensity of DiR in tumor areas from its dye-loaded NEs in comparing to DiR administrated alone, indicating that NEs favors accumulation of dye cargo in tumor areas^[263]. Jacquart *et al.* reported two lipophilic dye loaded NEs (around 50 nm) showing passive targeting to tumor areas within hours^[182,264]. However, authors also observed fluorescence from some organs (especially liver) involved in steroid hormone synthesis and storage, since lipid based NEs has a higher affinity for areas rich in the steroid hormones. This could be used as another feature for passive targeting of dye-loaded NEs, since tumor cells in hormone-dependent tumor areas over-express lipoprotein-receptor. Our studies with FRET NEs loaded with NIR dyes (Cy5.5LP and Cy7.5LP) also showed an EPR effect, with strong accumulation in tumor already after 1h post-administration in tumor bearing mice (Figure 1.24). Remarkably, imaging of dissected organs revealed that fluorescence signal from tumor was the largest followed by liver and then lungs, while practically no signal was observed in other organs^[179].

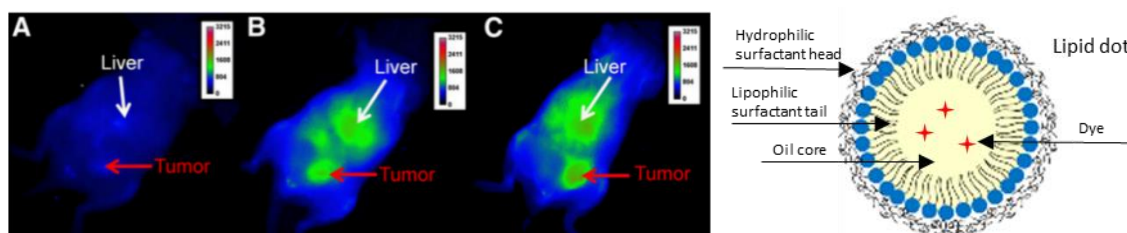


Figure 1.24. Uptake of DiD-loaded lipid dots in PyMT mammary cancer cells. Fluorescence images were obtained before injection (A), 5 h after injection (B), and 24 h after injection (C). Schematic presentation of lipid dot is shown. Adapted from ref [264].

1.2.6.2- Active targeted imaging of tumors

As mentioned in the chapter of drug delivery, for targeted imaging, it is necessary to conjugate a nanoparticle with targeting ligands, which include small molecules (e.g. folate, RGD, etc) and biomolecules (antibodies or aptamers). However, as the chemical functionalization of NEs is rather challenging because of liquid nature of these particles, the examples of NEs bearing targeting ligands are still limited. One approach is to directly insert bio-macromolecules inside of NEs. One example used bovine serum albumin (BSA) conjugated with folic acid to formulate NEs by high pressure homogenization^[10]. This folate-tagged protein NEs showed strong affinity to folate receptor-positive cells.

Another most common used approach for NEs is the functionalization of PEGylated lipids or surfactants. In a previous study, DSPE-POE5000-maleimide was used to formulate NEs (loaded with DiD)^[216], followed by grafting by maleimide-thiol coupling of the targeting cyclic RGD-based ligand (cRGD-SH) as well as control ligands (cRAD-SH, OH-SH) (Figure 1.25A). Authors found significant fluorescence intensity difference between targeting group (LNP-cRGD) with non-targeting groups (LNP-cRAD and LNP-OH) from fluorescence cell imaging results and flow cytometry analysis (Figure 1.25C). Later on, mice experiment showed that this functional NEs showed stronger tendency to accumulate in tumors where there is overexpressing of the target receptor, HEK293(($\beta 3$) (Fig. 1.25D-F)^[216]. These exciting results showed another way that is by grafting of antibodies (Abs) to NEs to enhance the specificity of NEs to accumulate in tumors. Finally, only a rare report shows functionalization of NEs with antibodies, which was realized using PEGylated lipid with a maleimide function (SPE-PEG3400-Maleimide). The obtained NEs

bearing scFv-Fc TEG4-2C antibodies and loaded with iron oxide NPs enabled direct MRI imaging of atherosclerosis in mice models^[7]. Recently our group developed NEs with antibody surface. To do this, our group conjugated PEGylated lipid derivative to a PMAO polymer. Then, an antibody was conjugated to the PEGylated lipid derivative through amine reaction with maleimide^[220]. NEs formulated by using this PEGylated polymer with antibody surface as surfactant showed strong affinity to senescent endothelial cells. The development of dye-loaded NEs bearing antibodies for targeted optical imaging constitutes a promising research direction.

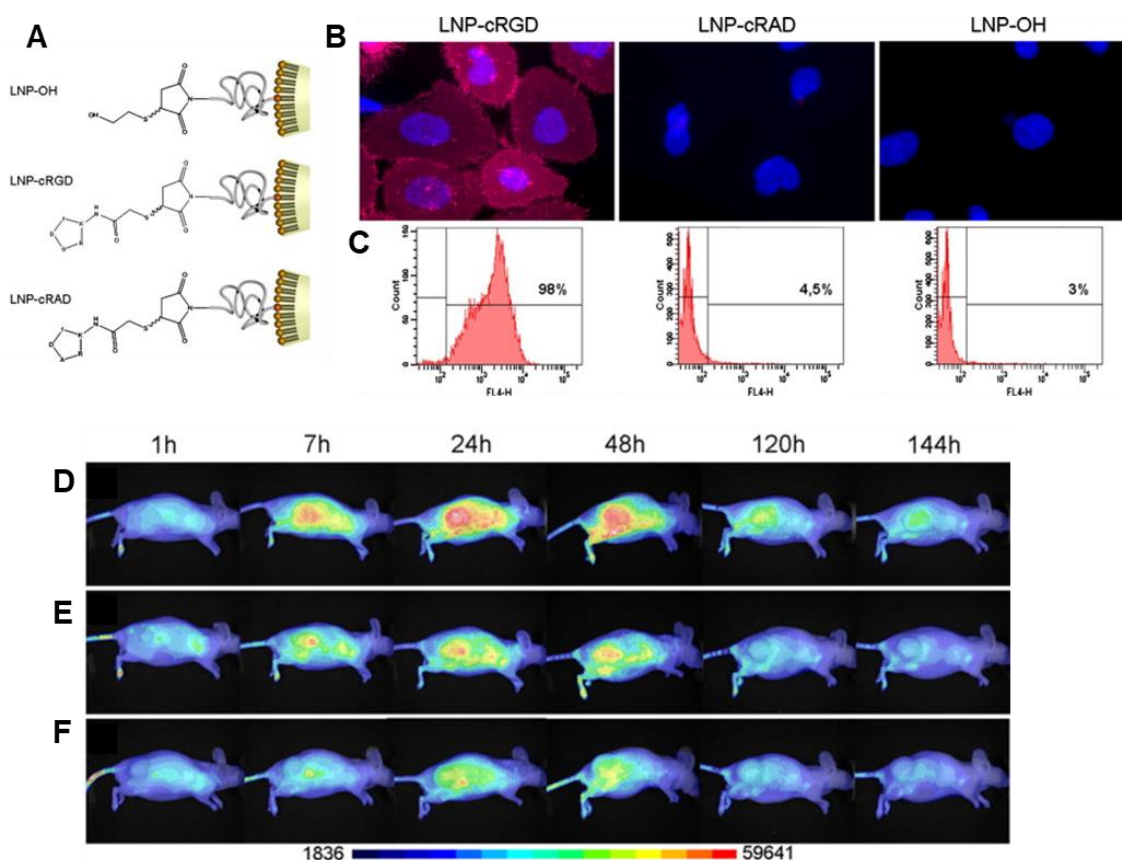


Figure 1.25. (A) Illustration of structure of LNP-OH, LNP-cRGD, or LNP-cRAD lipid nano-droplets. (B) *In vitro* evaluation of LNP-cRGD, LNP-cRAD, LNP-OH targeting specificity to HEK293(β3) cells. (C) and flow cytometry analysis (D-F) *In vivo* injection of LNP-cRGD (D), LNP-cRAD (E), or LNP-OH (F) in HEK293(β3) xenografted Nude mice. Adapted from ref^[216].

One should note that the idea of active tumor targeting by modifying the NEs surface does not always work as expected. The problem can be associated with the Tumor/Skin (T/S) ratio of

specific tumors^[14]. In cases when T/S ratio is low, EPR effect could surpass the effect of active targeting *in vivo*. For instance, Choi and co-workers designed a functional IR780 dye-loaded NEs with surface modified by Arg-Gly-Asp (RGD) peptide, and showed their capacity to target tumor cell overexpressing $\alpha\beta3$ integrin^[217]. Later on, the authors wanted to verify the generality of this targeting NEs for other tumors. Unfortunately, this effect was not universal: although authors found significant accumulation of this NEs on the membrane of HEK293 cells *in vitro*, a negative result of improving accumulation in DU145 tumor in mice was observed comparing with NEs without this targeting agent. This was attributed to the fact that DU145 expressed insufficient amount of $\alpha\beta3$ integrin (T/S ratio of 1.5), compared to HEK293 cells (T/S ratio of 3.0)^[14], so that EPR effect surpassed the specific targeting in the former case. Thus, the targeting effect strongly depends on the cell line, so that systematical test is necessary on multiple cells lines with varied receptor expression.

The ultimate application goal of dye loaded NEs would be the imaging drug-loaded NEs for the treatment of cancer. This requires systematic efforts in these directions, which could further validate NEs as reliable imaging and drug delivery agents.

This chapter is adapted and reproduced with permission with minor adjust from ref ^[265] titled “Dye-Loaded Nanoemulsions: Biomimetic Fluorescent Nanocarriers for Bioimaging and Nanomedicine”. Copyright Willey.

1.3- Dynamic covalent chemistry

Dynamic covalent chemistry (DCC) refers to reversible chemical reactions, which equilibrium could be controlled by both aspects of thermodynamic and kinetics. The thermodynamic influence to the result of dynamic covalent chemistry is well known, however, more and more focuses have been placed on the kinetics contributions. While product distribution under thermodynamic control relies totally on how stable is the final products, in reactions controlled by kinetics, however, transition speed is the key to determining the relative proportion of products. Since reaction speed is generally faster with the decreasing of energy differences. Thus, in the case of the latter, lower energy differences of transition states usually lead to faster reaction. Since dynamic reactions are reversible autonomous reactions sensitive to stimuli, the formation and breaking of dynamic covalent bonds toward either direction of the reaction could be controlled either by thermodynamic or kinetics factors. These bonds are abundantly applied in multiple fields, such as material science and biomedical fields^[266,267].

1.3.1- Requirements for Dynamic Covalent Bonds (DCB)

The most important criteria for dynamic covalent bonds are the covalent nature and the bond strengths. For some systems, a lifetime of each bond in the range $1 \text{ ms} < \tau < 1 \text{ min}$ has been proposed to yield conjugations that are stable and detectable with analysis techniques existing, yet dynamic enough to allow swift adaptation^[268]. This translates into longer equilibrium times in the scale of hours to days for slow dynamic systems. The upper limit of the equilibration time for a DCC is also related to the degradation stability of the components in the system, as equilibrium must retain before the system starts degrading. Due to the reversibility nature of dynamic covalent reactions, eventually, the reaction will reach an equilibrium where there is a certain ratio of reactant and product. This ratio is determined by the so-called equilibrium/association constant (K). This parameter is calculated as ($K = k_1/k_{-1}$), where k_1 indicates the formation rate and k_{-1} signifies the dissociation rate. The k_1 value is positively related to the stability of the resulting covalent bond. It could also be affected by several other conditions, for example heating, increasing of concentration *etc.* Taking the formation of the imine as an example, the reactant is aldehyde /amine, while the product is imine/water. Increasing the stability of the imine product will lead to an

increase in the k_1 value, and thus K value. Then, the equilibrium will shift towards the imine formation. On the other hand, if pH is decreased, the dissociation constant (k_{-1}) will increase, and thus lower down the K value, eventually leading to the degradation of imine bonds, and the equilibrium will shift to the reactant side of aldehyde/amine. Thus, one method of controlling the reaction toward the formation of a certain product is by the modification of the structure of the product to make it more stable. In cases of the product is instable under heating, pH, and so on, these stimuli could be used to control the equilibrium of the reaction. Another way to drive the equilibrium in either direction (towards the products or reactants) is by adding/reducing the concentration of compounds on either end of the equilibrium.

1.3.2- Catalysis for dynamic covalent bonds

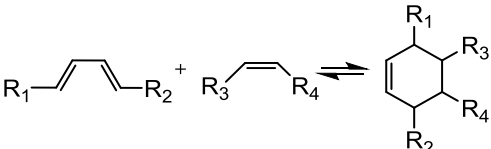
To make the reaction faster, a majority of the dynamic covalent bonds require catalysis to facilitate equilibration. Ideally, a catalyst should only modulate the system exchange rate and not the component distribution, but high catalyst loadings can lead to altered equilibrium due to complexation effects^[269]. Although the energetics of dynamic systems is governed by many response factors, it is preferred to work with lower catalyst concentrations where the catalyst acts fully “innocent”.

1.3.3- Different dynamic covalent reactions types

Depending on whether new bond types are formed during the reaction, dynamic covalent reactions is classified into two general types^[270]. The type of dynamic covalent reaction that created a new bond generally followed the equation: $X+Y \rightleftharpoons A+B$ or $X+Y \rightleftharpoons A$. For Example, reversible addition and condensation^[271], Thiol-Michael addition reaction^[272], and hydrazone (imine) bond formation^[273]. The advantage of this type of reaction is that in some cases, the direction of this type of reaction could be controlled by temperature, pH, *etc.* For instance, DA reaction could occur under low temperature, high temperature would lead to the reverse reaction process. The type of dynamic covalent reaction without the formation of a new bond generally followed the equation: $X_1+Y_1 \rightleftharpoons X_2+Y_2$. This type of reaction usually refers to the dynamic exchange of contents between different starting compounds to create novel products with the same bond types. Various exchange reactions are included in this type of reaction. For instance, S-S exchange reactions^[274,275], S-S,

SH exchange reactions^[276], ester exchange reactions^[277] and alkene exchange reactions^[278,279]. The direction of the reaction is relatively irrelevant to external stimuli, since the bond type of reactant and product are identical, thus reaction to either end happens under the same condition. Various specific dynamic covalent in the Table 1 below.

Table 1. Examples of dynamic covalent reactions^[280]

Reaction type	Condition	Formula	Ref
Schiff base reaction	Acid or base catalyst	$R_1-NH_2 + R_2-C(=O)H \rightleftharpoons R_1-N=CH-R_2 + H_2O$ $R_1-NH-NH_2 + R_2-C(=O)H \rightleftharpoons R_1-NH-N=CH-R_2 + H_2O$ $R_1-O-NH_2 + R_2-C(=O)H \rightleftharpoons R_1-O-NH-C(=O)-N=CH-R_2 + H_2O$	[270, 281]
Double bond exchange reaction	Low polarity organic solvents	$R_1-N=CH-R_2 + R_3-N=CH-R_4 \rightleftharpoons R_1-N=CH-R_4 + R_2-N=CH-R_3$	[278, 279]
	Transition metal catalyst	$R_1-N=CH-R_2 + R_3-CH=CH-R_4 \rightleftharpoons R_1-N=CH-CH=CH-R_4 + R_2-CH=CH-R_3$	[282, 283]
Knoevenagel reaction	Weak base or Lewis acid catalyst	$R_1-C(=O)R_2 + R_3-CH_2-R_4 \rightleftharpoons R_1-C(=CH-R_3)-CH(R_4)-R_2$	[284 – 286]
DA reaction	Temperature control		[287, 288]

Disulfide exchange reaction	Without catalyst	$R_1-S-S-R_1 + R_2-S-S-R_2 \rightleftharpoons R_1-S-S-R_2$	[289 ,290]
Thiol-Michael addition reaction	Base catalyst, neutral pH	$R_1-SH + \text{CH}_2=CH-R_2 \rightleftharpoons R_1-S-S-CH_2-CH_2-R_2$	[272]
Thiol-thioester exchange reaction	Neutral pH, water	$R_1-C(=O)-S-CH_2-CH_2-CH_2OOH + HS-R_2 \rightleftharpoons R_1-C(=O)-S-CH_2-CH_2-R_2 + \begin{matrix} CH_2OOH \\ \\ SH \end{matrix}$	[291 ,292]
Transesterification reaction	Lewis acid catalyst	$R_1-C(=O)-O-R_2 + R_3-OH \rightleftharpoons R_1-C(=O)-O-R_3 + R_2-OH$ $R_1-C(=O)-O-R_2 + R_3-C(=O)-O-R_4 \rightleftharpoons R_1-C(=O)-O-R_3 + R_3-C(=O)-O-R_2$	[293 ,294]
Boronic ester exchange reaction	Room temperature	$R_1-B(OH)(R_2)(R_3) + HO-CH(R_4)-CH(R_5)-OH \rightleftharpoons R_1-B(O-CH(R_4)-CH(R_5)-O)(R_2)(R_3) + HO-CH(R_2)-CH(R_3)-OH$	[295 ,296]
Siloxane equilibration	Acid or base catalyst	$\begin{matrix} R_1 \\ \\ R_2-Si-O-Si-R_4 \\ \\ R_3 \end{matrix} + \begin{matrix} R_7 \\ \\ R_8-Si-O-Si-R_{10} \\ \\ R_9 \end{matrix} \rightleftharpoons \begin{matrix} R_1 \\ \\ R_2-Si-O-Si-R_{10} \\ \\ R_3 \end{matrix} + \begin{matrix} R_7 \\ \\ R_8-Si-O-Si-R_5 \\ \\ R_9 \end{matrix}$	[297 ,298]
Diselenide metathesis reaction	Visible light	$R_1-Se-Se-R_1 + R_2-Se-Se-R_2 \rightleftharpoons R_1-Se-Se-R_2$	[299 - 301]

1.3.3.1- Carbon-Nitrogen C=N dynamic covalent bond

Carbon-Nitrogen C=N bond usually refers to Schiff base^[302]. It is a type of reaction that involves nucleophilic attack of amine or hydrazide groups to carbonyl groups of ketone or aldehyde creating C=N bonds of imine, hydrazone, oxime, *etc.*

One of the most commonly used C=N dynamic covalent bonds is imine bonds, imine bonds are DCBs formed by the conjugation of ammonia or primary amines with aldehydes^[281]. The mechanism of this type of reaction follows the route of first formulation of a hemiaminal intermediate with nucleophilic addition by amine, then followed by an elimination of water to yield the imine bond.

Secondly, hydrazone bonds are resulted from the condensation reaction of hydrazide groups with ketone groups. The reaction follows a similar route to the formation of the imine bonds (switching aldehyde to ketone, and amine to hydrazide). Hydrazone bonds are generally more stable than imine bonds^[303].

Less commonly, the oxime bonds are resulted from condensation reaction of O- hydroxylamine groups (hydroxylamines) to aldehyde groups (ketone groups)^[281,304]. The reaction follows a similar route as imine and hydrazone formation. However, in comparing to the former, it is more stable^[281,305].

1.3.3.2- Carbon-Carbon Dynamic covalent bond

Normally, C-C bonds are considered powerful bonds that cannot easily break. However, by adding bulky groups and/or charged groups the bond could become fragile due to the decrease of dissociation energy^[306]. Here are a few reactions for the formation of dynamic C-C bonds: phenol/aldehyde condensation^[307], aldol reaction^[308], carbene coupling^[309], Friedel-Crafts reaction^[310], Strecker reaction^[311] *etc.* Among them, the aldol reaction is the most frequently mentioned dynamic covalent reaction that creates a new carbonyl compound after the exchange reaction of two carbonyl compounds. However, for now, most reactions of this type in the application of dynamic covalent reaction were mediated by an enzyme with few exceptions, for example, Concellón *et al.* developed an effective catalyst named (TBD/Al₂O₃) for the aldol reaction between aldehydes and ketones^[308].

1.3.3.3- Carbon=Carbon Dynamic double bond

This bond is known for dynamic covalent reversible exchange reactions. It usually referred to Diels-Alder (DA) reaction and Knoevenagel condensation reaction. DA reaction refers to conjugation of dienes and dienophiles (alkenes or alkynes)^[288]. As mentioned before, in the absence of a catalyst, temperature could be used as a switch to control the direction of the reaction^[270]. The DA reaction usually prefers low temperature, while high temperature would reverse the DA reaction process^[288]. Knoevenagel condensation defines nucleophilic addition reactions of an active hydrogen-containing compound to an aldehyde. The reaction could be either catalyzed by weak Lewis bases^[312] or Lewis acid^[286].

1.3.3.4- Dynamic Carbon-Oxygen covalent bond

This type of bond usually refers to the product of the transesterification reaction^[268]. The transesterification reaction refers to exchanging of chemical group on an ester with another one on an alcohol. This reaction usually goes in the presence of a base or acid catalyst^[313]. Under the catalysis of the base, the reaction follows the following mechanism: the hydroxyl group of the alcohol is firstly deprotonated by a base catalyst, follows by the formation of a tetrahedral transition product by nucleophilic attack of the deprotonated hydroxyl group to the carbonyl carbon of the starting ester, which forms a novel ester.

1.3.3.5- S-containing dynamic covalent bond

1.3.3.5.1- Thiol-disulfide exchange reaction

Thiol-X is one of the most commonly adopted DCBs in the aspect of biological applications due to its good biocompatibility and facility^[268,294]. The reaction follows several steps. Firstly, the thiol is negatively charged to form a S^- . Then, the S^- substitutes the original S-S bond through the nucleophilic attack. Then, a novel S^- is released from another sulfur atom. And finally, the side product was protonated to form a thiol^[314].

1.3.3.5.2- Thiol-Michael addition reaction

The reaction starts with a Lewis base that de-protonates a thiol. The formed thiolate anion initiates nucleophilic attack to an alkene (with an electron-withdrawing group) and form an intermediate

carbanion. Then, this carbanion could attract hydrogen from another thiol to generate a new thiolate anion. Allen *et al.* first reported the thiol-Michael addition reaction in the 1960s, and then, this reaction is regarded as a mild reaction with high reactivity and few side products. These advantages made this reaction popular in the field of dynamic covalent chemistry^[315–317].

1.3.3.5.3- Thiol-thioester exchange reaction

Thio-thioester exchange reaction is usually catalyzed by base, which acts as a de-protonation agent for the thiol group, followed by a nucleophilic attack to the carbonyl electrophilic center, and finally the protonation of the $-S^-$. This type of reaction has multiple advantages, for instance general reaction conditions, high reaction speed, and few side products. For example, this reaction is reported for efficient exchange of thiol with multiple functional groups in several organic solvents^[318].

1.3.3.6- Selenium containing dynamic covalent bond

This kind of DCBs is only rarely used because of the difficulty of the direct exchange between two Se-Se bonds, the exchange is usually only possible in the presence of UV light or specific catalyst. Nevertheless, there are still reports about the application of this type of reaction. For example, by using low energy visible light, Ji *et al.* triggered a diselenide exchange reaction^[299].

1.3.4- Applications of dynamic covalent bonds

1.3.4.1- Stimuli sensitive polymeric materials

Most DCB reactions are reversible and responsive to stimuli. This make them interesting methods for developing self-healing and bio-friendly polymer based materials. Such polymer materials were suitable for material sensitive to stimuli, hydrogels for tissue healing, drug delivery, sensors, three-dimensional printing, dyes, coatings, *etc.*

Stimuli-sensitive materials are able to undergo chemical or/and physical changes induced by environmental stimuli. Those stimuli could be heat, chemicals, light, and so on. This unique feature has allowed stimuli-sensitive materials applied in multiple fields.

1.3.4.1.1- Thermal responsive materials

Some products of DA reactions^[287] are sensitive to heat i.e. making them reversible under heating conditions. Fang *et al.*, developed a new kind of thermal-driven self-healing and recyclable waterborne polyurethane film (WPU-DA-x). It was developed based on DA/retro reactions by introducing the DA diol into the polymer's backbone (Figure 1.26). WPU-DA-x films showed temperature responsive self-healing capability^[319].

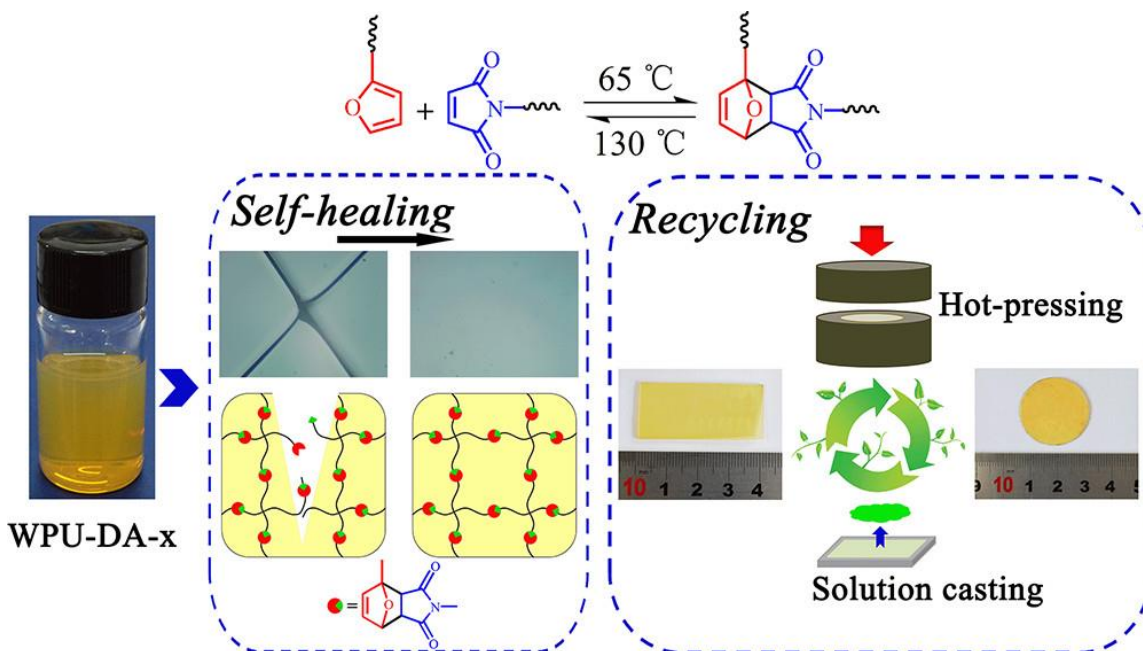


Figure 1.26. Self-healing principle of WPU-DA-x films with DA diol backbone. Adapted from ref^[319].

1.3.4.1.2- Chemically responsive materials

Some dynamic covalent bonds are reversible in the presence of adding a competitive agent or acid. In this way, the polymer structure can be further tuned through DCBs. For instance, Skene *et al.* developed numerous polymers with a framework based on hydrazone bonds. The polymers could easily exchange components with other dynamic covalent polymers under low pH^[320].

1.3.4.1.3- Photosensitive materials

Photosensitive materials exhibit a rapid change of chemical or physical properties in response to external light excitation. Usually, DCBs sensitive to light excitation are used for the formation of light-sensitive polymer materials. As an example, recently, Xu *et al.* developed a polymer

assembly consisting of hydrophilic and lipophilic parts conjugated by Se-S bonds (Figure 1.27). Due to the sensitivity of the bond to 420 nm excitation, authors could control the break of the vesicle by controlling the intensity of light irradiation at this wavelength^[321]. Sometimes, the DCBs could be so sensitive to the wavelength that only reacts to light at a certain wavelength, for instance, 350 nm excitation is beneficial for the dimerization of anthracene, while light below wavelength of 300 nm have the opposite effect and would induce it dissociate to monomeric state. Thus, the response of photosensitive materials could be controlled by both the wavelength and intensity of light.

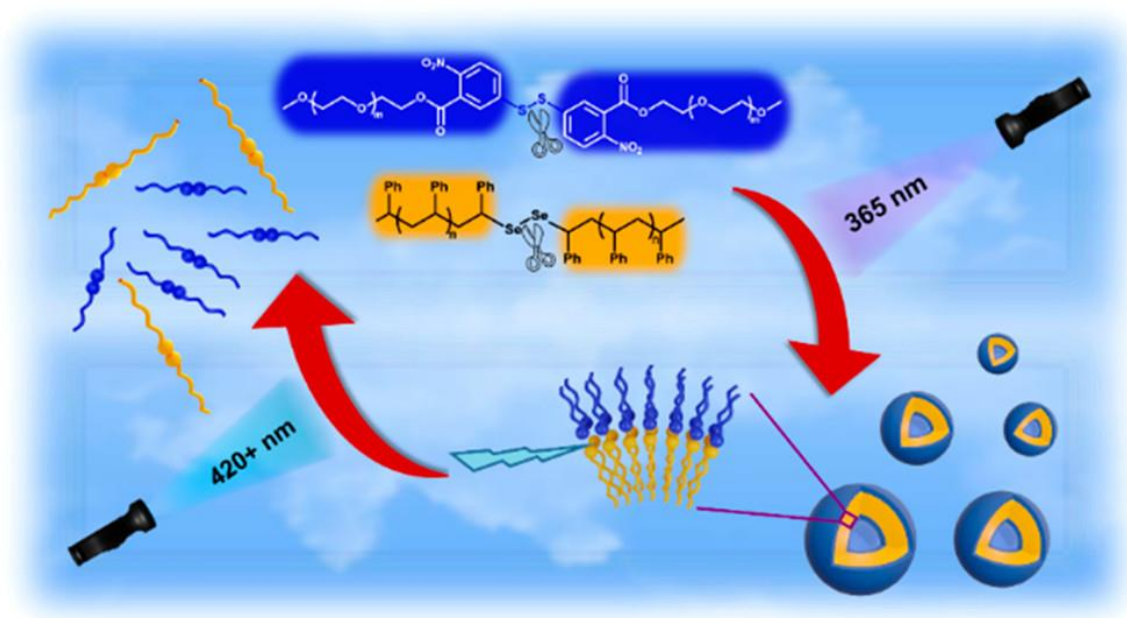


Figure 1.27. Scheme of Wavelength-Controlled Light Response of the Selenide-Sulfide Bond. Adapted from ref^[321].

1.3.4.2- Sensors

Several years ago, DCBs were used to change the mechanical properties of polymer-based materials: DCBs based polymer material process a certain degree of mechanical strength under heating, different from the traditional heat melting polymer materials^[322]. This property could be used for DCBs based polymer materials to sense temperature. Also, some DCBs are responsive to other external stimuli such as pH, light et al. This made them a considerable candidate for sensors for various purposes^[323–325].

1.3.4.3- Biosensors

A biosensor refers to a type of sensor that could interpret the presence of certain compounds or environment conditions, such as pH of the solution, through output optical signals. Usually, some chemically sensitive DCBs based polymer materials are used for this purpose. The principle usually goes with the following steps: chemically sensitive DCBs break/reform after sensing the compound or change of pH, then the mechanical properties of the polymer material will change. Finally, this mechanical change is magnified and converted to an optical signal. As an example, Zhou and coworkers designed a pH and lysine biosensor^[326]. The hydrogel membrane is composed of multiple layers of the partially oxidized dextran-containing amino group *in situ* reacted with the chitosan containing aldehyde group. Based on the fact that the swelling degree of the gel is influenced by the integrity of the DCBs constructing the layer-by-layer film, low pH or the presence of compounds containing acid group would break the DCBs and cause swelling of the film, and thus observed by changes of Fabry-Perot fringes. Similarly, Wang and coworkers developed a glucose detection polymer with layer-by-layer assembly of partially oxidized dextran, chitosan and glucose oxidase. The detecting mechanism follows the converting of glucose to gluconic acid by glucose oxidase, decreasing the pH, thus lead to the degradation of these bonds and the polymer material to swell. Afterward, their reflection spectra would present changes of Fabry-Perot fringes, make it possible to convert chemical signal of glucose concentration to optical signals.

1.3.4.4- 3D printing in biology

3D printing technology is not a novel term, it is now widely used in the production of prototypes for product models. It usually uses 3D printing resins that are light-sensitive and solidify under exposure to light with a certain wavelength. However, in the field of biology, for better biocompatibility, usually DCBs based hydrogels were used as printing material for cell immobilization and modeling^[327]. For example, complex biological 3 D scaffolds were developed by Wang *et al.* in this study, hyaluronic acid was adopted as the framework, then a hydrogel internetwork was formed through DCBs resulted from hydrazide groups reaction with ketone groups^[328]. This hydrogel acted as an elastic shelter for stem cells against the mechanical influence of needle injection and could reversibly dissociate after the process when not no longer required.

1.3.4.5- Fluorescent probes

Fluorescent probes based on DCBs could show fluorescence turning on or off behaviors caused by the breaking or reforming of the DCBs^[329,330]. For example, an imine based hydrogel was developed by Luo *et al.*^[323]. Authors attached an aggregation-induced emission dye to the polymer, and observed fluorescence when the fluorophore-conjugated to the polymer structure, whilst, the conjugate exhibited a fluorescence turning off behavior after the breaking of the bonds under acid conditions. These fluorescent probes are also used for the detection of diseased areas in clinical situations^[331,332]. DCBs are used in this aspect to for detecting certain stimuli or substances in biological specimens^[333]. As an example, Ao *et al.* developed a fluorescent nano-switch for detecting the media pH based on boronic ester. The fluorescence probe only fluorescents when nitrophenol detaches from it. This bond is stable under basic pH while breaks in acidic media. Resulting in a pH-sensitive probe, where the fluorescence turns off under high pH and on under low pH (Figure 1.28)^[334].

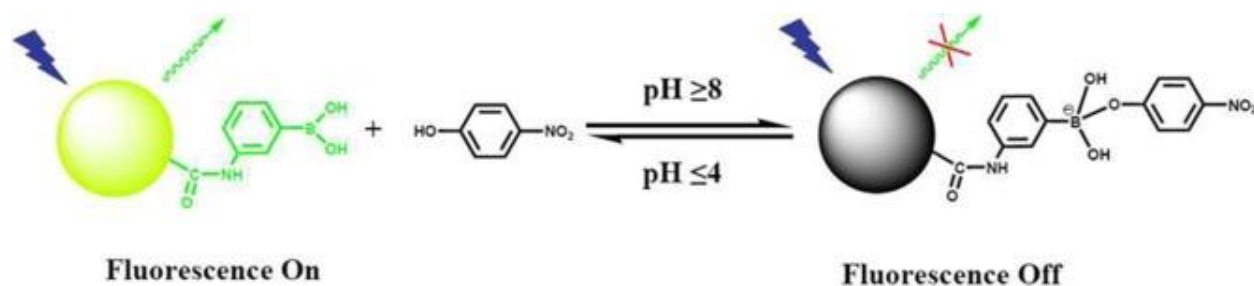


Figure 1.28. A schematic diagram of a fluorescent nano-switch controlled by the dynamic covalent B-O bonds between phenylboronic acid-functionalized carbon quantum dots and p-nitrophenol^[334].

1.3.5- Drug delivery

Dynamic covalent reactions should be compatible with the conditions for intended application. Water and air, as common elements in medical practices, it is of primary importance for the reaction to be moisture and oxygen resistant. For biological applications, a dynamic covalent bond should exchange readily in water or water/organic solvent mixtures. As for drug delivery

applications, in order to avoid interference to organisms, it is important for DCBs to be free from any sort of catalyst. Furthermore, considering the complexity of biological environments, DCBs also need to be stable enough in the conditions they are used. Thus, only some DCBs were commonly used as a bridge to conjugate drug and polymer for drug delivery, as illustrated in Figure 1.29.

The tumor microenvironment would provide unique conditions of slightly lower pH, higher amount of reactive oxygen species (ROS), higher concentration of certain enzymes as well as higher expression of glutathione (GSH), one could use DCBs response according to these stimuli to achieve the purpose of controlled and targeted drug delivery^[335,336]. As a result, the application of DCBs has created a novel way of designing efficient drug carriers which is suitable for specific therapeutic situations^[280,337,338].

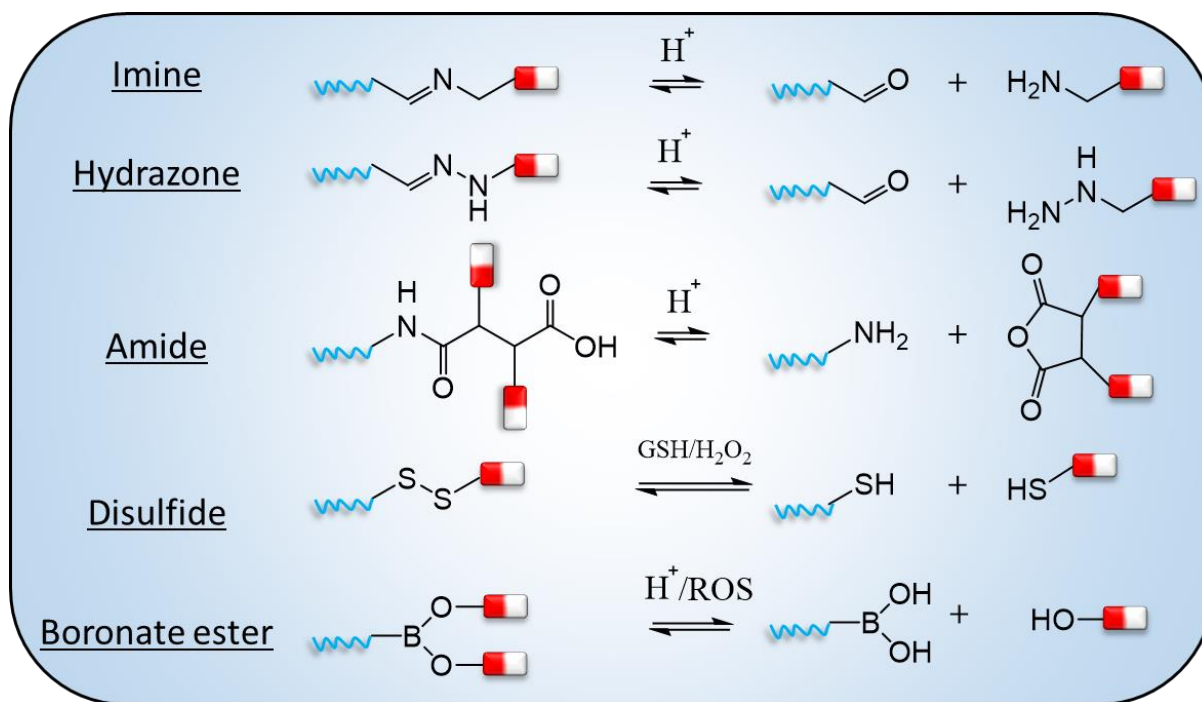


Figure 1.29. Structures of the typical dynamic covalent bonds used in drug delivery applications.

1.3.5.1- Small molecular drugs

Most commonly used drugs are consisted of small molecules. Small molecule drugs, benefiting from their small size and low stereo-hindrance are generally easy to be delivered to target cells on the second or third level of targeting^[339]. To achieve the purpose of controlled drug release, small molecular drugs are usually embedded either covalently or non-covalently inside a polymer matrix linked by DCBs, thus could be responsive to an external stimulus such as heat, pH, light excitation, *etc.*^[291]. The most studied stimuli are pH due to the difference in pH between tumorous areas and bloodstreams as well as the feasibility of several commonly used DCBs such as hydrazone and imine bonds^[340,341]. As an example, Tao *et al.* used imine as the link to conjugate lipophilic Au-containing polymer with hydrophilic PEG chain for the encapsulation of doxorubicin (DOX), the resulting polymer NPs remained stable in normal tissues and bloodstreams where the pH is neutral, while liable to low pH, broke and released DOX into tumorous tissues selectively^[340]. It is also possible to make direct DCBs between drugs with polymer-drug carriers, for instance, Xiong *et al.* developed a way to attach DOX prodrug to cyclodextrin with aldehyde group through imine bonds. The formed DOX prodrug NCs processed the ability to release DOX under acidic conditions^[342]. In similar ways, pH-activatable DOX loaded hydrogels had been developed based on DCBs bridging ketone groups of DOX and the hydrazide groups of PEG-based copolymer^[343]. Sometimes, micelles are also used as carriers for pH-controlled delivery of DOX by DCBs. The technique is consisted by adopting hydrazone bonds to conjugate DOX to a co-polymer, followed by self-assembly to form drug-loaded nanoscale micelles^[344]. Sometimes, two types of dynamic covalent bonds could be applied to one drug carrier system featuring duo stimuli responsive drug release profile. For instance, hydrazone bonds and disulfide bonds were adopted together for the formation of DOX containing micelle, which is capable of releasing DOX under low pH and reduction conditions^[345]. Sugar derivatives were sometimes used in combination with the application of DCBs for enhancing the bioavailability of NCs, for example, a polymer gold NPs was designed by the conjugation of DOX with a D-mannose derivative through hydrazone bonds. The obtained particle showed potential for combined application of fluorescence tracking and pH dependent release^[346]. Similarly, based on another sugar derivative named dextran polysaccharide, a pH-sensitive supramolecular micelle was developed through hydrazone bonds^[347]. DOX was released after internalizing acidic tumor microenvironment (Figure 1.30).

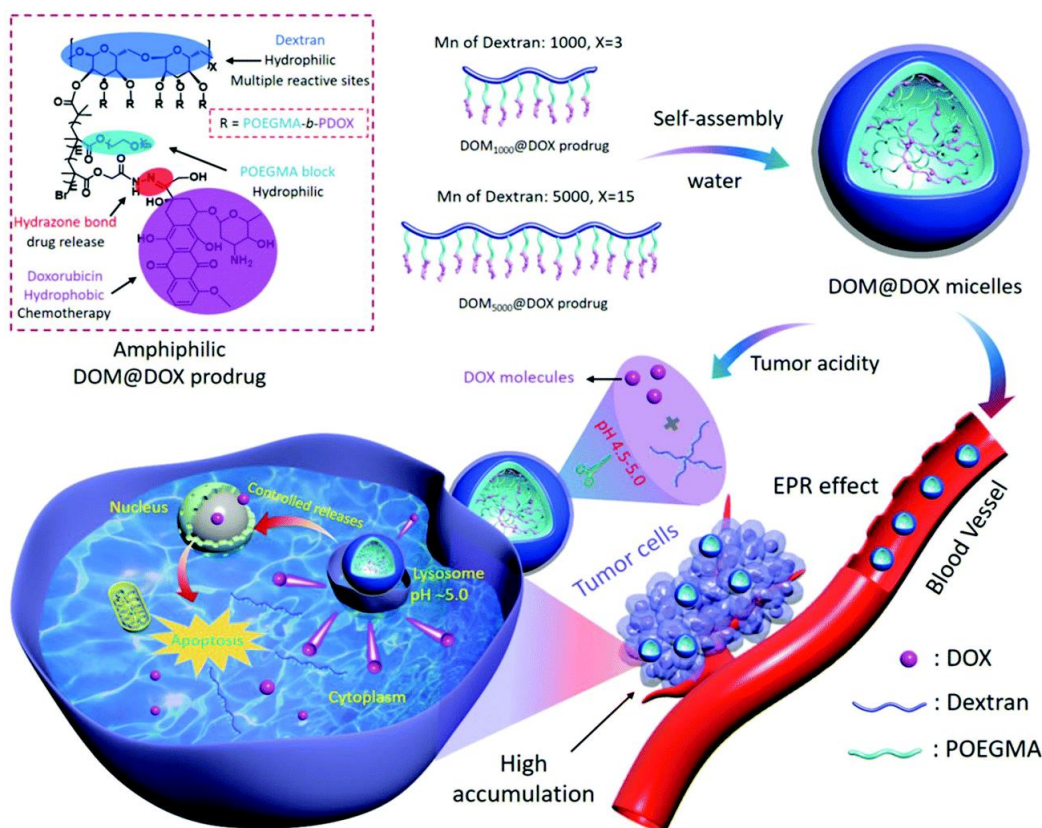


Figure 1.30. Schematic illustration of the synthetic route to DOM@DOX micelles, drug accumulation *via* the EPR effect, cell internalization process, and pH-responsive drug release mechanism. Reproduced from ref. [347].

DCBs were also applied in implantable hydrogels for the purpose of enhancing drug delivery efficiency and prolonged drug delivery. As an example, a hydrogel for injection is developed by Liu *et al.* DCC and Michael addition reaction were adopted to form a PECT polymer embedded with two DOX and a penetrating peptide. Due to the heat sensitivity of PECT polymer, the hydrogel was liquid under low temperature and converted to gel form under high temperature, thus favoring injection application. Besides, DOX is conjugated by hydrazone bonds, thus favoring acid cleavage property. Eventually, the gel could easily penetrate to tumor sites by a targeted peptide group and release DOX under the low pH of the tumor microenvironment^[348].

1.3.5.2- Biomacromolecules

Due to the complex stereo structure of proteins, they are prone to degradation and endocytosis during the delivery process. Thus it remains a huge challenge to develop NCs for the delivery of

these biomacromolecules^[349]. DCBs made the delivery of biomacromolecules possible in mild conditions while favoring advantages of stimuli sensitivity, reversibility, and compatibility with *in vivo* environments. DCBs are also possible to increase the bioavailability of biomacromolecules by processing them with active interaction with bio-membranes, thus improving the delivery efficiency of biomacromolecules. One of the mostly frequently adopted dynamic covalent bonds is S-S, it is commonly used in the formation of cell-penetrating polymers for enhanced drug delivery efficiency^[350]. As an example, Gasparini *et al.* designed a polymer for delivery of streptavidin to the nucleus by conjugation of poly(disulfide)s (CPDs) for cell-penetrating and red-fluorescent biotin-rhodamine conjugate for streptavidin conjugation and tracking by adopting ring-opening S-S exchange polymerization. Authors found that the substrate could target the polymer specifically to the nucleus without interaction with endosomes^[351]. The principle of efficient delivery of proteins by disulfide polymers was reviewed by Laurent *et al.*^[352]. Authors proposed that the improved delivery efficiency is caused by dynamic covalent disulfide exchange reaction with thiols namely glutathione on the cell surface (Figure 1.31). After the discovery of the technique of using disulfide exchange reaction for delivery of large proteins to nucleus membrane, a recent study by Lu *et al.* developed a simple and universal way for the synthesis of reactive cysteine group bearing proteins conjugates with polymers containing disulfide bonds^[353]. Through the disulfide exchange reaction, polymer NCs are able to be covalently conjugated to the nucleus membrane and release encapsulated compounds. One more advantage to mention is that, in all the techniques of using disulfide delivery of proteins, the delivered content remained intact, thus keeping the integrity of the delivered biomacromolecules^[352–354].

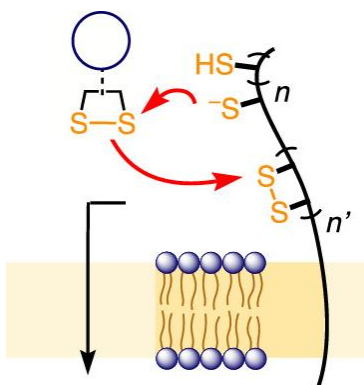


Figure 1.31. Thiol-mediated uptake operates with the dynamic covalent chemistry (DCC) of chalcogenide exchange adapted from ref^[352].

The oligonucleotides are another type of biomacromolecules that faced two major challenges in its delivery to nucleus^[355]. The first challenge with delivery of oligonucleotides is related to their strong negative charge, which prevents them to cross membrane barriers and further targeted to nucleus. Another challenge in its delivery is associated with their chemical fragility, which makes them extremely unstable in biological environment and requires special design of NCs to protect oligonucleotides against bio-degradation. The application of a double type of stimuli-responsive DCBs is regarded as a tool to solve these two challenges in one shot. Some types DCBs allow the conjugation of NCs with oligonucleotide through acid cleavable bonds, thus ensuring their stability in transit. While some other types of DCBs (for instance, the pre-mentioned disulfide bond) have specific interaction with the nucleus membrane. One example of such application was done by adding amino acid with a polymer containing simultaneously pH-sensitive C=N and redox-sensitive S-S bonds^[356]. By adapting the dual type of DCBs, the NCs could be targeted to the nucleus membrane through disulfide exchange reaction, and effectively release silencing RNA (siRNA) after the NCs reach the targeting area with the breaking of C=N bonds under intercellular conditions of low pH.

2- PART 2. Results and Discussions

2.1- Drug-Sponge Lipid Nanocarriers for *in Situ* Cargo Loading and Release Using Dynamic Covalent Chemistry (Article 1)

Nanoparticles (NPs) with the size of around 100 nm have been explored as nanocarriers (NCs) for targeted delivery and controlled release of drug molecules in past decades^[357]. Common approaches to loading drugs in NCs involve direct/physical encapsulation^[358] and chemical encapsulation by using covalent bonds between drugs and NCs or simply the formation of prodrug before encapsulation^[359]. In contrast with prodrug, the advantage of direct encapsulation is that the cargo is not chemically modified after the release. Many of these systems still present ‘burst release’ issues that may hamper their further application. The chemical encapsulation approach is based on the covalent linkage of the drug inside the NCs in form of a prodrug conjugate^[359,360]. This method ensures the high stability of the NCs without burst release of the cargo. However, the drugs are modified chemically through a synthetic protocol, thus raising the question of solvent residues, toxicity, and bio-distribution of the corresponding prodrug.

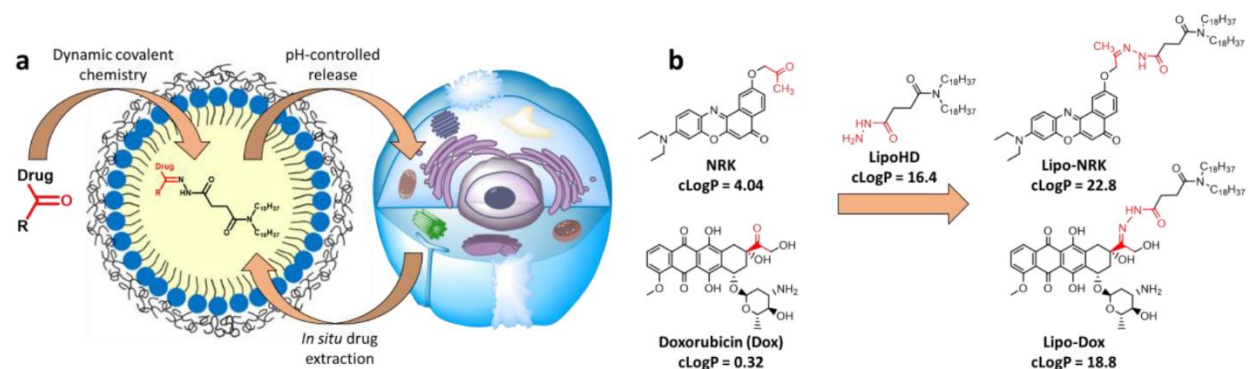


Figure 2.1. Concept of reversible *in situ* reaction and pH-controlled release of drug sponge system

In the present study, we demonstrated a novel approach of drug encapsulation inside NCs. Dynamic covalent chemistry was exploited for the reversible *in situ* cargo loading (Figure 2.1). The system features the advantages of low leakage under neutral pH because of covalent bonds inside the NCs matrix, whilst releasing the drug in the intact form under low pH. These properties would ensure high stability of the NCs in the blood stream (at neutral pH) and high sensitivity to low pH presented in the tumor microenvironment for controlled release. Nanoemulsions (NEs) were chosen to be the NCs in the present study because they are formulated from components (lipids, oils and surfactants), which are generally regarded as safe (GRAS) and biocompatible. For the functionality, a lipophilic reactive capture molecule bearing two long alkyl chains and a hydrazide group (LipoHD) was encapsulated inside. To test the *in situ* reaction process, two ketone-containing compounds were used, one is a Nile Red dye derivative named NRK and another is doxorubicin, an anti-tumor drug. In this work we used the Förster Resonance Energy Transfer (FRET) technique for real-time investigation of the *in situ* reaction process, due to the extreme sensitivity of FRET to donor-acceptor distance^[179]. Consequently, encapsulating blue dye

F888 (as the donor for NRK) or far-red dye Cy5-TPB (as the acceptor for doxorubicin) allowed us to monitor an increase in the FRET signal with the progression of the *in situ* reaction of lipoHD with corresponding ketone. Moreover, by using this technique, the pH-dependent release of NRK and doxorubicin could also be observed with the decrease in FRET signals. Then, fluorescent microscopy was used as a technique to see the pH-controlled release and *in situ* uptake of ketones *in situ* in Hela cells and in chicken skin tissues (Figure 2.2). Finally, NEs loaded with doxorubicin were tested to suppress tumor growth in mice. The controlled release of a cargo at low pH makes them promising for drug delivery into tumor tissues, while its efficient uptake from cells/tissues opens interesting prospective for detoxification using NEs.

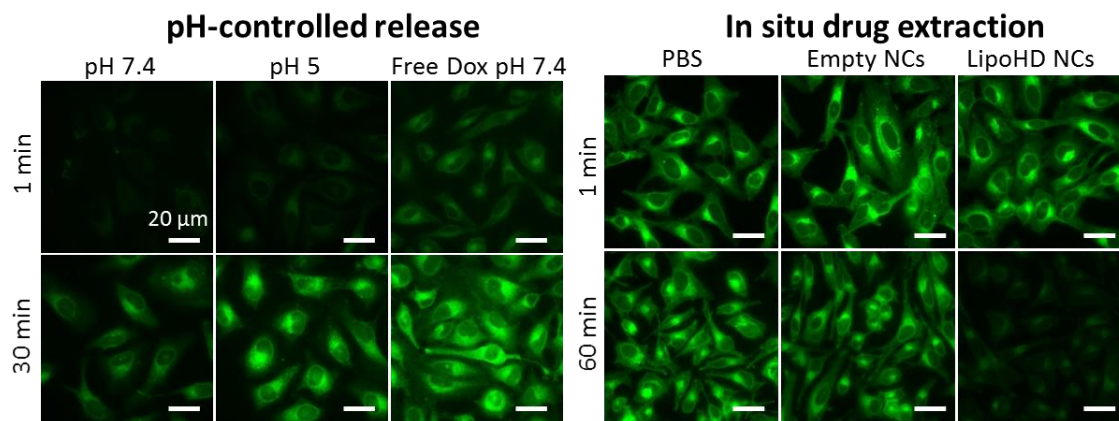


Figure 2.2. Fluorescence microscopy images of in-vitro experiments of pH-controlled release of doxorubicin to Hela cells and *in situ* uptake of NRK from Hela cells using drug-sponge NEs.

Article 1

Drug Delivery

How to cite: *Angew. Chem. Int. Ed.* **2021**, *60*, 6573–6580

International Edition: doi.org/10.1002/anie.202014259

German Edition: doi.org/10.1002/ange.202014259

Drug-Sponge Lipid Nanocarrier for in Situ Cargo Loading and Release Using Dynamic Covalent Chemistry

Fei Liu[†], Yosuke Niko[†], Redouane Bouchaala, Luc Mercier, Olivier Lefebvre, Bohdan Andreiuk, Thierry Vandamme, Jacky G. Goetz, Nicolas Anton, and Andrey Klymchenko*

Abstract: Currently, drug-delivery strategies using nanocarriers (NCs) deal with encapsulation of cargo or its covalently modified prodrug. Herein, we propose a concept of reversible pH-controlled capture and delivery of active cargo based on dynamic covalent chemistry inside lipid nano-droplets (nano-emulsions), coined as “drug sponge”. We designed a highly lipophilic hydrazide (LipoHD) capable of reacting with a free cargo-ketone (fluorescent dye and doxorubicin drug) directly inside lipid NCs, yielding a lipophilic hydrazone prodrug efficiently captured in the oil core. LipoHD-loaded NCs spontaneously accumulated cargo-ketones, yielding formulations stable against cargo leakage at pH 7.4, and further released their dye/drug cargo at low pH range (5.0–6.8) in solution and live cells. Doxorubicin-loaded drug-sponge NCs showed cytotoxicity in four cancer cell lines and capacity to inhibit tumor growth in subcutaneous xenografts of mice. Finally, unprecedented extraction of dye/drug cargos directly from cells and tissues (i.e. detoxification) was realized by the drug-sponge NCs.

Introduction

In the last decades, nanoparticles (NPs) have been explored as nanocarriers (NCs) for the targeted delivery

and controlled release of drug molecules.^[1] Current drug delivery systems based on NCs exploit two common paradigms, based on encapsulation (supramolecular) and covalent chemistry.^[2] In the first approach, the drug is non-covalently encapsulated inside the nanocarrier.^[3] The advantage of this method is that the cargo is not chemically modified before and after the release, however, noncovalent encapsulation is prone to burst release and poorly controlled leakage of the cargo.^[4] The second approach is based on covalent linkage of the drug inside the nanocarrier in form of a prodrug conjugate.^[4a,5] This method ensures high stability of the nanocarrier, while the use of cleavable bonds, such as acetals, orthoesters, hydrazones, disulfide, etc., enables stimuli-responsive cargo release under control of pH, reduction, enzymes, etc.^[6] However, in this case, the drugs are modified chemically through a synthetic protocol, thus raising the question of solvent residues, toxicity and bio-distribution of corresponding prodrug. An ideal solution is to use NCs as a nano-reactor to form prodrug in situ, which after reaching the target cells can be cleaved, thus releasing the drugs under control of environment. In this case, the cargo enters and exits from the nanocarrier in its intact form, which would simplify the preparation and maximize the safety of the drug delivery.

New possibilities appear with dynamic covalent chemistry (DCvC), which deals with dynamic bonds that form and disrupt reversibly under environmental control.^[7] DCvC, which is at the interface of covalent and supramolecular chemistry,^[8] gave rise to new generation of materials with self-healing and adaptive properties.^[9] Reversible and environment-sensitive nature of the dynamic covalent bonds is particularly attractive for the field of drug delivery.^[10] The most popular dynamic covalent bonds include hydrazone,^[11] oxime,^[12] imine,^[13] disulfide,^[14] boronate ester^[15] etc. On one hand, transient formation of these bonds enables crossing of cell membrane barriers for delivery of cargos inside the cells.^[16] On the other hand, these bonds can be used to build nanocarriers^[10,13b,17] and/or conjugate the nanocarrier with drugs^[18] in order to ensure efficient transport and controlled release of the cargo.^[19] Hydrazone bonds, sensitive to pH, are particularly attractive in this respect,^[11,20] because targeted tumor tissues are characterized by low pH.^[19,21] Moreover, after endocytosis of nanomedicines^[22] the lysosomal compartments can further contribute to pH-controlled cleavage of the hydrazones. However, these reports were focused on the covalent approach, where the drug conjugates with the nanocarrier were synthesized before the formulation of the nanocarriers, whereas in situ loading of cargo into nanocarrier

[*] F. Liu,^[†] Dr. Y. Niko,^[†] Dr. R. Bouchaala, Dr. B. Andreiuk, Dr. A. Klymchenko
Université de Strasbourg, Laboratoire de Bioimagerie et Pathologies, UMR 7021 CNRS, 74 route du Rhin, 67401 Illkirch (France)
E-mail: andrey.klymchenko@unistra.fr

F. Liu,^[†] Dr. T. Vandamme, Dr. N. Anton
INSERM UMR 1260, Regenerative Nanomedicine (RNM), FMTS, CNRS 7199, CAMB, Université de Strasbourg
67000 Strasbourg (France)

Dr. Y. Niko^[†]
Research and Education Faculty, Multidisciplinary Science Cluster, Interdisciplinary Science Unit, Kochi University
2-5-1, Akebono-cho, Kochi-shi, Kochi, 780-8520 (Japan)

Dr. L. Mercier, Dr. O. Lefebvre, Dr. J. G. Goetz
Inserm U1109, Tumor Biomechanics, Fédération de Médecine Translationnelle de Strasbourg (FMTS), University of Strasbourg, 67200 Strasbourg (France)

Dr. L. Mercier
Current address: Interdisciplinary Institute for Neuroscience, University of Bordeaux, CNRS UMR 5297, 33077 Bordeaux (France)

[†] These authors contributed equally to this work.

Supporting information and the ORCID identification number(s) for the author(s) of this article can be found under:
https://doi.org/10.1002/anie.202014259.

through dynamic covalent bonds has not been reported to date.

DCvC has been largely used for designing responsive nanocarriers based on polymers.^[10,17,20d] However, the polymer core is solid, and thus cannot serve as a nano-reactor for in situ conjugation of a cargo with a nanocarrier. Lipid-based NCs constitute a promising alternative to polymeric NPs in drug delivery applications. Traditionally, this field is dominated by liposomes, presenting lipid membrane and aqueous core, which has already been approved in clinics as pharmaceutical carriers.^[23] However, lipid membrane of liposomes is a good barrier for hydrophilic cargoes only, while encapsulation of hydrophobic cargoes (such as doxorubicin) requires their precipitation inside the liposome (as for Doxyl). Lipid nanoemulsions (NEs) present an oily core, which can serve as nano-reactor for encapsulation of drugs through DCvC. NEs are highly promising biomimetic nanocarriers for drug delivery because they are (1) inexpensive and easy to produce; (2) composed of excipients generally recognized as safe (GRAS) and (3) biodegradable.^[24] Despite their liquid core, they exhibit rather long circulation time, preserve integrity of their core in the blood circulation and can accumulate in the tumor in nearly intact form.^[25] They were also shown to maintain their integrity after crossing a human intestinal epithelium barrier.^[26] However, a drug having medium lipophilicity has a tendency to leak out rapidly from lipid NCs into biological media, as shown for a model dye Nile Red in serum,^[27] whereas its modification with lipophilic chains can drastically inhibit the leakage.^[27] Moreover, recent studies showed that lipophilic prodrugs of doxorubicin bearing an alkyl chain improved anti-tumor potency of the drug-loaded nanoemulsions.^[28] Therefore, we hypothesized that lipid NCs (NEs) can be used as a nano-reactor to form lipophilic prodrugs in situ through DCvC. In this case, a specially designed lipophilic “capture” molecule could form dynamic covalent bond with a drug, that is, forming prodrugs inside the nano-droplets, which would render the system stable against cargo leakage, and allow the stimuli-responsive drug release. Moreover, this “drug-sponge” system could capture in situ drug molecules from biological media and cells, which is an unexplored field in nanomedicine. Currently, active drug removal (or detoxification from drugs) is known in pharmacology and clinical practice, where excess of drug

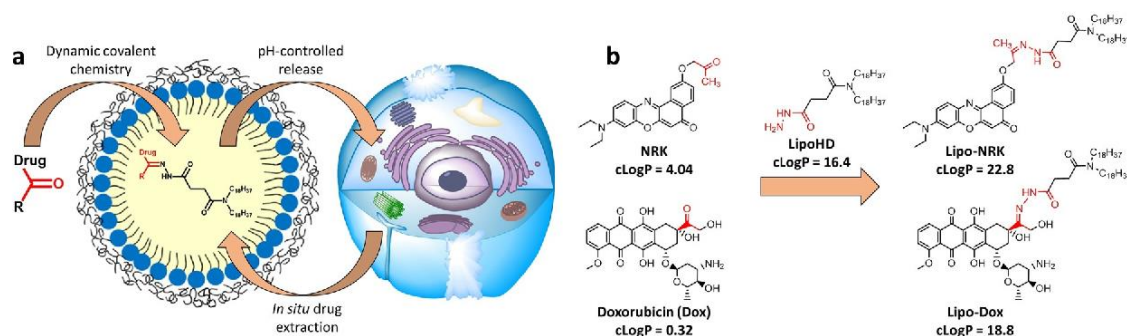
(e.g. an overdose) is removed by hemodialysis, plasma exchange and peritoneal dialysis.^[29] In order to ensure in situ drug capture in form of a prodrug, DCvC with a hydrazone bond can be considered. The latter has been frequently used in prodrugs design because it can be cleaved at weakly acidic pH (≈ 6) and readily applied to a drug bearing ketone/aldehyde groups like doxorubicin.^[17d,20c,30]

In the present study, we developed a concept of “drug-sponge”, wherein a lipid NCs, encapsulating a lipophilic reactive capture molecule (LipoHD, Scheme 1), can spontaneously accumulate cargo by forming dynamic covalent bonds inside the oil core. The drug-sponge concept was validated in solution and live cells and further applied for drug release in tumor bearing mice and drug removal from tissues.

Results and Discussion

To ensure efficient capture of cargo inside oil core of lipid NCs, we designed a highly lipophilic molecule (calculated LogP, cLogP = 16.4) bearing hydrazone group (LipoHD, Scheme 1). It is expected to form dynamic covalent (hydrazone) bond with a cargo bearing aldehyde or ketone group. LipoHD was obtained in three steps starting from diocetylamine (Scheme S1). Two cargo-ketones were selected: Nile Red-ketone (NRK) as a model fluorescent cargo and doxorubicin (Dox) as an anti-cancer drug. NRK was synthesized by reacting Nile Red phenol with chloroacetone (Scheme S2). NRK and Dox, having medium lipophilicity (cLogP is 4.04 and 0.32, respectively), are expected to react with LipoHD inside oil core of NCs to form highly lipophilic “prodrugs” Lipo-NRK and Lipo-Dox (cLogP is 22.8 and 18.8, respectively). This would ensure their retention inside NCs at neutral pH and cargo release at low pH after hydrazone bond hydrolysis. In addition, we also synthesized Lipo-NRK (Scheme S2) and Lipo-DOX (Scheme S3) conjugates in organic solvent and identified by NMR, Mass and FT-IR spectrometry.

We formulated NCs of around 80 nm size using nano-emulsification.^[24b] A solution of pre-synthesized Lipo-NRK (10 mM) or control dye NRK (10 mM) in Labrafac oil was mixed with Kolliphor ELP[®] surfactant and then formulated in milliQ water, yielding desired NCs. To study the NRK cargo



Scheme 1. Concept of drug-sponge nanocarrier (a) and chemical structures of cargoes (NRK and Dox), lipidic capture molecule (LipoHD), and corresponding prodrug conjugates (b). Calculated LogP (cLogP) are presented.

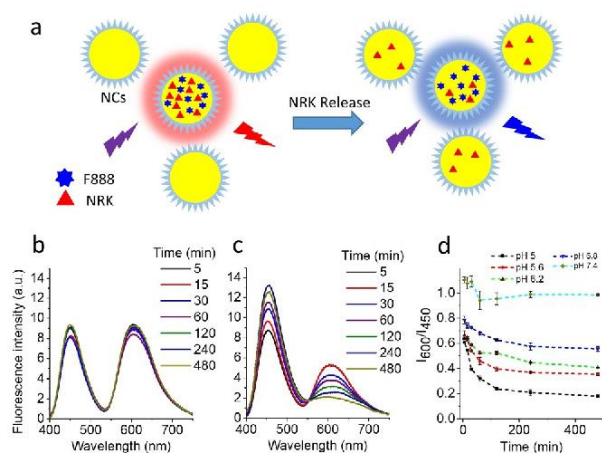


Figure 1. a) Schematic presentation of changes in FRET occurring during the cargo release. b, c) Fluorescence spectra of Lipo-NRK NCs for different incubation time at pH 7.4 (b) and pH 5 (c) after dilution (1000-fold) in the presence of 20-fold excess of blank NCs. d) Fluorescence intensity ratio of acceptor (I_{600}) to donor (I_{450}) over time at different pH values. Excitation wavelength was 405 nm.

release, we co-encapsulated lipophilic blue dye F888^[27] that serves as energy donor for NRK in the Förster Resonance Energy Transfer (FRET)^[25,27,31] assay (Figure 1a). NRK and Lipo-NRK NCs showed similar absorbance values at the maximum ≈ 530 nm (Figure S1a), indicating that encapsulation was successful in both cases. The FRET NCs excited at 405 nm (donor) showed both donor and acceptor emission bands (Figure S1b), confirming FRET inside NCs between F888 donor and acceptor (NRK or Lipo-NRK).

Then, we mixed our FRET NCs with blank NCs, which are expected to work as a recipient medium for the hydrophobic cargo. The presence of blank NCs led to nearly complete loss of FRET for NRK/F888 NCs: the NRK fluorescence intensity dropped while emission of F888 increased (Figure S1c). This result suggested the release of NRK and its transfer to blank NCs (Figure 1a). In sharp contrast, fluorescence spectrum of FRET NCs with Lipo-NRK was only marginally affected, suggesting that Lipo-NRK remains inside the NCs without significant release. It should be also noted that after two weeks, the NRK formulation showed signs of dye precipitation, in line with our earlier data for parent Nile Red,^[27] whereas the corresponding Lipo-NRK NCs were stable.

As the hydrazone bond is cleavable at low pH, we incubated Lipo-NRK/F888 NCs with 10-fold excess of blank NCs at pH varied from pH 7.4 to pH 5 (Figure 1 and S2). For pH 7.4, the emission spectra remained stable over 8 h, suggesting no dye release (Figure 1b). By contrast, at pH 6.8, the donor band gradually increased, while the acceptor band decreased over time (Figure S2). This trend became more

pronounced at lower pH (Figure 1c and S2). The plotted acceptor/donor ratio vs. time (Figure 1d) showed a clear time-dependent release of NRK in pH range 5.0–6.8 and practically no release at neutral pH.

Our next question was whether prodrug model Lipo-NRK can be generated in situ inside NCs without synthesis of the “prodrug” in a flask (Figure 2a). To this end, NCs containing LipoHD were first formulated and then incubated for 6 h (rt) with NRK in pH 4. The reaction mixture then was then extracted by dichloromethane and studied by TLC. Lipo-NRK could be clearly identified as a new spot with higher R_f , which corresponded to pre-synthesized conjugate Lipo-NRK (Figure 2b). Mass spectrometry of the dichloromethane extract confirmed the presence of Lipo-NRK (Figure S3), confirming that the hydrazone conjugate can form in situ. To monitor formation of the conjugate in situ inside NCs, we prepared NCs encapsulating F888 as a FRET donor for NRK. NCs containing LipoHD showed increase in the FRET signal (Figure 2c) as a growth of NRK emission intensity (at 600 nm) and a decrease in F888 intensity (at 450 nm), whereas no change was observed for NCs without LipoHD (Figure 2d). These results suggested that Lipo-NRK conjugate was formed in the NCs containing LipoHD. Monitoring acceptor/donor ratio vs. time revealed relatively fast hydrazone formation within first 30 min (Figure 2e).

Next, we evaluated possibility to form in situ prodrug of doxorubicin (Lipo-Dox) inside NCs using LipoHD. Dox is poorly soluble in oil (≈ 0.001 wt% in Labrafac), making

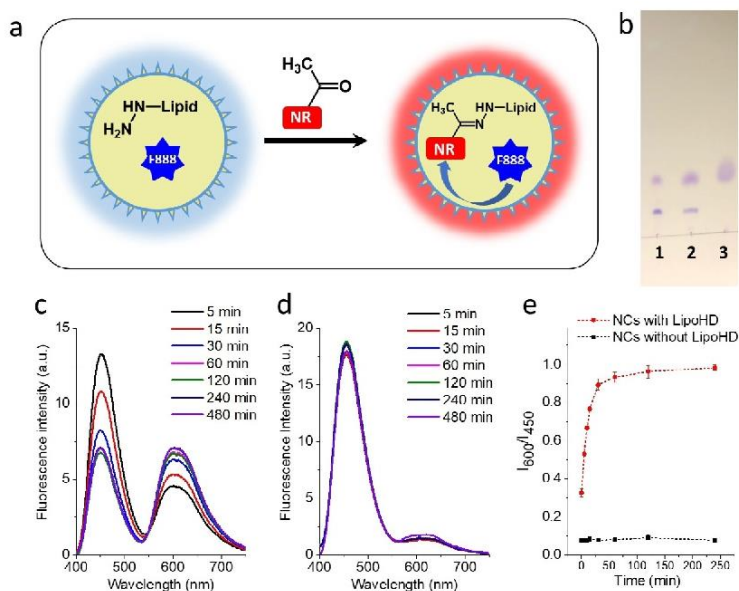


Figure 2. a) Scheme of in situ reaction of NRK and LipoHD monitored by FRET using F888 as energy donor. b) TLC evidence of in situ formation of Lipo-NRK conjugate inside LipoHD NCs: 1) extracted reaction mixture of LipoHD NCs with NRK in DCM phase; 2) the same extracted mixture with pure Lipo-NRK; 3) pure Lipo-NRK. c) Fluorescence spectra of the reaction mixture of LipoHD/F888 NCs with NRK at different reaction times after dilution (1000-fold) with 20-fold excess of blank NCs. Excitation wavelength is 405 nm. d) The same experiments as (c) for NCs without LipoHD. e) Fluorescence intensity ratio at fixed wavelengths (600 to 450 nm) for experiments (c) and (d). The in situ reaction was done at pH 4.

inefficient its encapsulation into lipid NCs. By contrast, lipophilic hydrazone conjugate Lipo-Dox, pre-synthesized in organic solvent, showed high solubility in Labrafac oil (> 1 wt %). Blank and LipoHD-loaded NCs were incubated with Dox for 24 h at pH 4. After the dialysis, no absorbance of Dox was detected in control NCs without LipoHD, whereas the absorbance of Dox was significant for LipoHD NCs (Figure S4). The result was also confirmed by visual observation of aqueous phase after dialysis (Figure S4a). Dox encapsulation with respect to the mass of Labrafac oil was 0.48 % based on extinction coefficient of Dox ($12200 \text{ M}^{-1} \text{ cm}^{-1}$).^[32] Thus, LipoHD makes Dox prone to accumulation inside of NCs. The encapsulation efficiency of Dox into LipoHD-loaded NCs, calculated based on the absorbance of DOX before and after dialysis (Figure S4b) was 25.8 %, whereas for control NCs without LipoHD it was close to zero.

In order to monitor the in situ formation of Dox prodrug within NCs, a FRET system for Dox was designed. As a FRET couple of F888 with Dox gave too weak FRET signal (Figure S5), we selected a far-red lipophilic Cy5 dye (DiD), already used as FRET acceptor for Dox.^[33] NCs loaded with DiD and LipoHD were incubated with Dox. The emission spectra of NCs excited at Dox absorption wavelength (490 nm) revealed the gradual increase in the FRET acceptor emission over time with kinetics (the acceptor/donor intensity ratio vs. time) on the time scale of hours, whereas NCs without LipoHD showed practically no ratio change (Figure S6). According to Dox absorption spectra (Figure S7a), the encapsulation efficiency of Dox into LipoHD NCs was 28.6 %, and resulted loading of Dox was 0.52 % in oil (w/w), consistent with data for LipoHD NCs without DiD (Figure S4b). Thus, our results showed that a drug (or a dye) can be efficiently loaded inside lipid nanocarrier through in situ dynamic covalent bond formation generating encapsulated prodrug. To the best of our knowledge, such “drug-sponge” in situ drug loading has not been reported to date.

We further exploited the dynamic nature of the hydrazone bond to trigger pH-controlled release of Dox from NCs (Figure 3, S8), similarly to experiments with NRK. At pH 7.4, minimal changes of the FRET spectra (Figure 3a) and the acceptor/donor ratio (Figure 3f) were observed over 8 h, suggesting relatively slow release of Dox at pH 7.4. By contrast, at pH 6.8, gradual loss of FRET was observed, and this trend was stronger with gradual decrease of pH (Figure 3b–f). We also found that the Lipo-Dox NCs were stable in physiological buffer PBS (pH 7.4) and in 10 % serum (Figure S8). Thus, with help of LipoHD, Dox release can be triggered by weakly acidic pH (5.0–6.8), which is important for delivery of drugs to acidic microenvironment of cancer tissues.^[19,21]

We compared sizes and polydispersity of different formulations used in this study. The size of LipoHD NCs were close to blank NCs (78 and 85 nm, respectively), which implies that it does not influence directly the NCs formulation (Table S1). NRK formulations without LipoHD showed unexpectedly large size (112 nm). By contrast, NRK conjugate with LipoHD favored small and uniform NCs (71 nm). In case of Dox formulations, the samples after dialysis showed

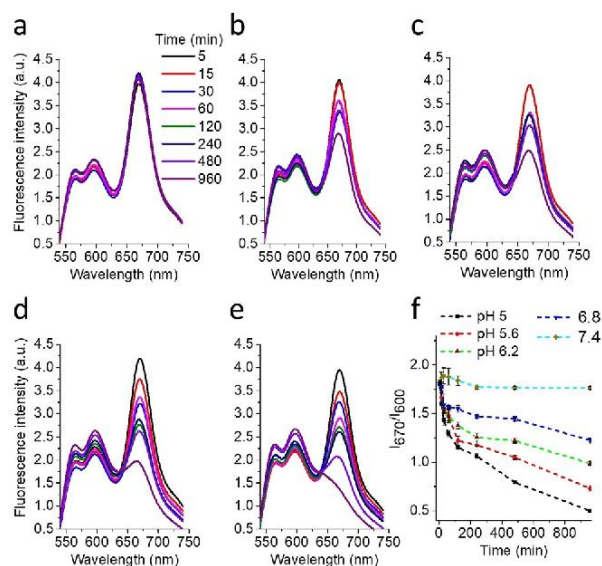


Figure 3. Drug (Dox) release from NCs under pH control, studied by FRET from Dox to Cy5 dye (DiD). a–e) Fluorescence spectra of Lipo-Dox FRET NCs (1000-fold dilution) in the presence of 20-fold excess of blank NCs at pH 7.4 (a), pH 6.8 (b), pH 6.2 (c), pH 5.6 (d), and pH 5 (e) over time. Excitation wavelength was 520 nm. f) Fluorescence intensity ratio of acceptor to donor (670 to 600 nm) at different pH over time.

systematically lower size (70–85 nm) and polydispersity compared to those before dialysis (105–144 nm). Importantly, the Dox-LipoHD NCs size was close to that of blank NCs, which means that drug loading did not affect much the particles.

To study the pH-dependent release of cargo in cells, NCs loaded with dye Lipo-NRK or pro-drug Lipo-Dox were incubated with HeLa cells at pH 7.4 and 5 of PBS followed by washing. At pH 7.4, Lipo-NRK NCs and Lipo-Dox NCs showed poor fluorescence inside the cells for both 1 and 30 min incubation (Figure 4). By contrast, at pH 5 the release of both NRK and Dox was observed after 30 min. Thus, at neutral pH the Lipo-NRK NCs and Lipo-Dox NCs are relatively stable in the presence of cells, but undergo release of NRK and Dox, respectively, at low pH because of hydrazone hydrolysis. However, the release of Dox was somewhat faster compared to NRK, which can be explained by lower lipophilicity of Lipo-Dox compared to Lipo-NRK (cLogP is 18.8 vs. 22.8) that favors higher access to water of encapsulated Lipo-Dox and thus faster hydrazone hydrolysis, in line with our FRET studies. Control experiments with free NRK and Dox at both pH 7.4 and pH 5 showed some signal already after 1 min and strong emission after 30 min incubation (Figure 4), suggesting rapid accumulation of the free cargos in cells independently of pH.

It remained unclear whether NRK and Dox cargos are liberated from NCs inside the cells or in the extracellular medium. The absence of signal for Lipo-NRK NCs in cells after 30 min (Figure 4a) implies that NCs did not rapidly internalize inside the cells. This stealth property, also ob-

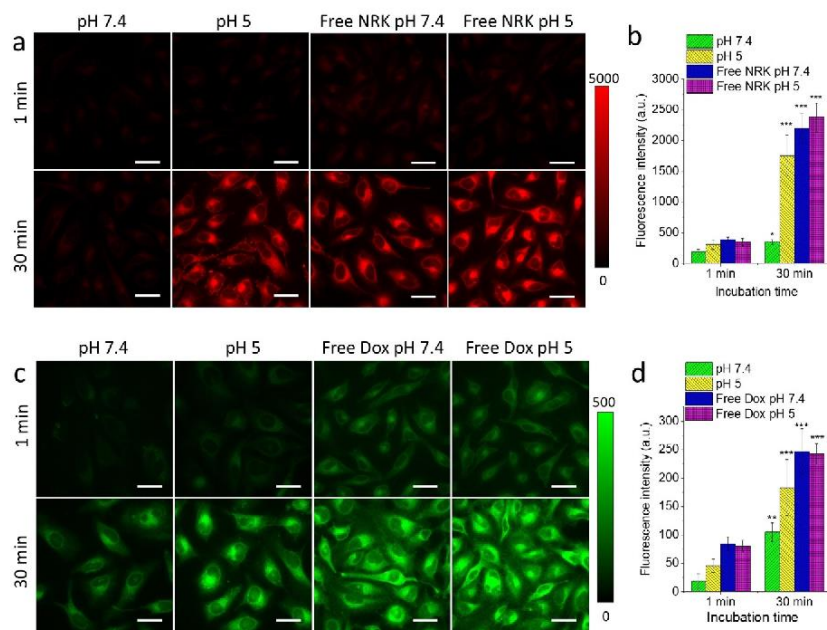


Figure 4. pH-controlled release of cargos from NCs into cells, studied by fluorescence microscopy. a) Fluorescence images of HeLa cells incubated for different lengths of time with Lipo-NRK NCs or free NRK at pH 5 and 7.4 (PBS). Excitation wavelength was 550 nm and the emission filter was 600 nm. b) Mean fluorescence intensity measured in 13 cells from (a) excluding the nucleus area. c) Fluorescence images of HeLa cells incubated for different lengths of time with Lipo-Dox NCs or free Dox at pH 5 and 7.4 (PBS). Excitation wavelength was 470 nm and the emission filter was 530 nm. Scale bars (a,c): 40 μm . d) Mean fluorescence intensity measured in 13 cells from (c) excluding the nucleus area. Statistical analysis (vs. data at pH 7.4, 1 min): $p < 0.5$ (*), $p < 0.1$ (**), $p < 0.01$ (***).

served earlier for lipid NCs loaded with lipophilic dye NR688,^[27,34] is probably linked to their PEG shell. To further verify accumulation of NCs inside the cells, we co-encapsulated our cargos with corresponding lipophilic dye: F888 with NRK and DiD with Dox. After 30 min incubation, neither NRK nor Dox formulations showed signal of corresponding F888 and DiD markers (Figure S9), suggesting absence of NCs inside the cells. By contrast, NRK and Dox channels showed strong signal of the corresponding cargo for LipoHD-based NCs at pH 5 and for control NCs at pH 7.4 (Figure S9), in line with the data above. We can conclude that at low pH Lipo-NRK NCs and Lipo-Dox NCs release their cargo into extracellular medium followed by cargo internalization inside cells.

Since our Lipo-Dox NCs can slowly release Dox in vitro, we studied cytotoxicity of Lipo-Dox NCs with that of free Dox in HeLa cells after 12, 24 and 48 h incubation in culture medium (DMEM). For both formulations, clear cytotoxicity was observed for concentration $\geq 5 \mu\text{g mL}^{-1}$ and it increased with the incubation time (Figure S10). Generally, Lipo-Dox NCs showed a slightly lower cytotoxicity than free Dox, especially for shorter incubation times. This difference in cytotoxicity is probably related to the delayed release of Dox from Lipo-Dox NCs. Nevertheless, after 48 h Lipo-Dox NCs showed high toxicity, similarly to free Dox, suggesting that this incubation is sufficiently long to release free Dox from NCs. Furthermore, we studied cytotoxicity of the two

formulations in three mammary carcinoma cell lines: 4T1, D2A1 from mouse and MDA-MB-231 from human after incubation for 48 hours. Both free Dox and Lipo-Dox NCs were found toxic, with cell viability $< 50\%$ for concentration $\geq 5 \mu\text{g mL}^{-1}$ (Figure S11), although some small differences were observed dependent on a cell line.

Then, the in vivo therapeutic potential of Lipo-Dox NCs was investigated on mice with xenograft tumors (D2A1 and MDA-MB-231, Figure S12). We observed reduced tumor growth profiles in mice that were administered with Lipo-Dox NCs, when compared to control administered with only NCs, which is especially pronounced for D2A1 (Figure S12b). Moreover, in case of D2A1 cells, Lipo-Dox NCs showed more effective suppression of tumor growth, compared to free Dox, which can be explained two factors. First, Dox is poorly soluble in water and thus can aggregate, in contrast to Lipo-Dox formulation. Moreover, we previously showed that lipid NCs of $\approx 100 \text{ nm}$ diameter exhibit strong EPR in D2A1 xenografted tumors,^[25] which can favor accumulation of Lipo-Dox NCs in tumor areas. A

dedicated in vivo study will be needed to explore full therapeutic potential of Lipo-Dox system.

Inspired by a capacity of LipoHD NCs to capture molecules in situ through dynamic covalent bond formation, we wondered whether these NCs can extract ketones, like NRK and Dox, from cells. The cells were treated with NRK or Dox and then incubated in LipoHD NCs, blank NCs and control PBS for 1 and 60 min. In PBS, the changes in the fluorescence were negligible for both NRK and Dox, indicating that they remained inside the cells (Figure 5). In case of blank NCs some decrease in the fluorescence intensity was observed, which could be explained by partial extraction of these apolar molecules into the hydrophobic reservoirs of NCs. In case of Dox, this non-specific extraction was much less efficient, probably because Dox is less lipophilic than NRK (corresponding cLogP is 0.32 vs. 4.04). Strikingly, LipoHD NCs drastically decreased the fluorescence intensity of both NRK and Dox after 60 min incubation, which was much stronger compared to blank NCs (Figure 5). Then, we characterized by fluorescence spectroscopy the extraction media (LipoHD NCs, blank NCs and PBS) incubated with HeLa cells for different time. Fluorescence intensity increased over the studied period of 1 h for all three media, whereas LipoHD NCs showed the strongest intensity increase (Figure S13). Using a calibration curve of the peak fluorescence intensity vs. NRK concentration (Figure S13), we found that the amount of extracted NRK after 1 h was 0.41, 0.29 and

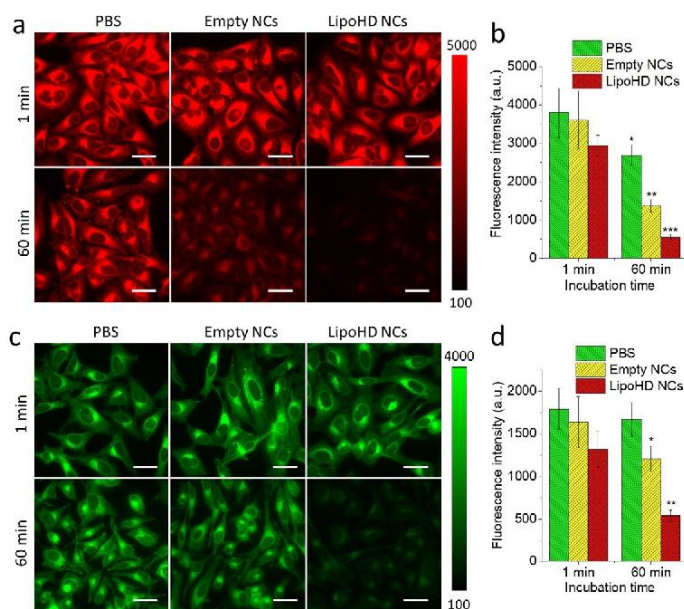


Figure 5. In situ extraction of ketone drugs by LipoHD NCs from HeLa cells. a) In situ extraction of NRK: cells were pre-incubated with 1 μM of NRK for 30 min, washed and then treated for 1 or 60 min with 100-times diluted LipoHD NCs, blank NCs and PBS and then washed with PBS before imaging. Excitation wavelength was 550 nm and the emission filter was 600 nm. b) Mean fluorescence intensity measured in 15 cells from (a) excluding the nucleus area. c) In situ extraction of Dox: cells were pre-incubated with 15 μM of Dox for 30 min, washed, treated or 1 or 60 min with 100-times diluted LipoHD NCs, blank NCs and PBS and then washed with PBS before imaging. Excitation wavelength was 470 nm and the emission filter was 530 nm. Scale bars (a,c): 40 μm . d) Mean fluorescence intensity measured in 15 cells from (c) excluding the nucleus area. Statistical analysis (vs. data in PBS, 1 min): $p < 0.5$ (*), $p < 0.1$ (**), $p < 0.01$ (***)

0.14 pmol for LipoHD NCs, blank NCs and PBS, respectively. Given that the estimated total amount of NRK uptaken by cells (see details in SI) was 0.5 pmol, the three media extracted, respectively 82, 58 and 28% of NRK from cells. This result confirmed our microscopy data showing that LipoHD NCs are significantly more effective extraction agent than the control media. Importantly, TLC and mass spectrometry of the LipoHD NCs extract from cells revealed the presence of LipoHD-NRK conjugate (Figure S14). Thus, we can conclude that this much higher efficiency of extraction with LipoHD NCs is connected with the formation of the dynamic covalent bonds of ketone molecules (NRK and Dox) with the “drug sponge” NCs. As mentioned above, within this short time period NCs cannot enter the cells, so that they extract the internalized ke-

tones being outside the cells. Lipophilic NRK and Dox molecules probably diffuse freely within the lipophilic compartments of the cells, and therefore can reversibly reach the plasma membranes, where they can be transferred to LipoHD NCs. This extraction process is reverse to a classical accumulation of lipophilic molecules in cells by passive diffusion and it is energetically favorable here because of formation of dynamic covalent bonds between the lipophilic ketones and Lipo-HD inside NCs. The obtained result provides the first proof of concept for the use of DCvC for removing drug molecules from cells.

We further explored the capacity of LipoHD NCs to extract ketones from tissues. To this end we selected chicken skin presenting lipid-rich adipose tissue,^[35] which is expected to uptake lipophilic molecules/drugs such as NRK and Dox. Transmission image of the skin showed characteristic morphological features of adipose tissue with individual cells (Figure 6). However, only faint auto-fluorescence was observed in chicken skin (Figure S15). Incubation of the skin with NRK or Dox in PBS resulted in a strong fluorescence signal from the tissue (Figure 6 and S16), suggesting their accumulation in the tissue. Right after addition of blank NCs or LipoHD NCs to the stained chicken skin, the fluorescence signal remained close to that in PBS (Figure 6 and S16) treated samples. However, after incubation for 30 min, the fluorescence intensity for LipoHD NCs dropped significantly for both NRK and Dox ($p < 0.01$), whereas blank NCs showed much smaller ($p < 0.5$) decrease and PBS did not show any change for NRK and Dox (Figure 6 and S16). Thus, LipoHD NCs are able to extract ketones, including Dox drug,

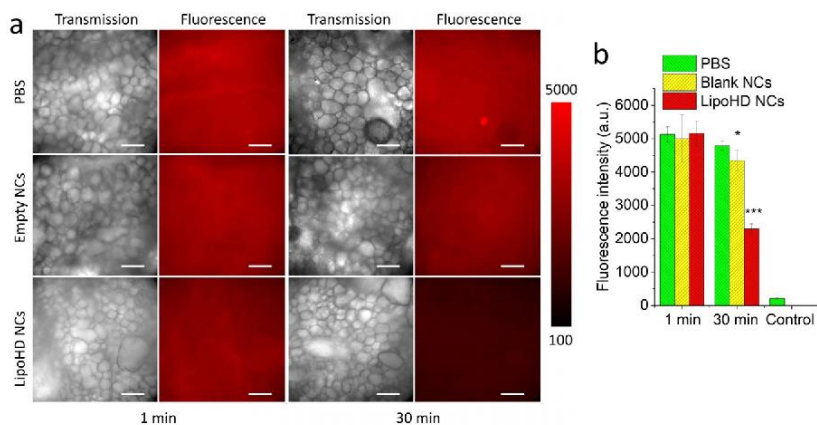


Figure 6. In situ extraction of ketone drug Dox by LipoHD NCs from chicken skin adipose tissue. a) Transmission and fluorescence images of in situ extraction of Dox: the skin tissue was pre-incubated with 45 μM of Dox for 10 min and treated for 1 or 30 min with 100-fold diluted LipoHD NCs, blank NCs or PBS. Excitation wavelength was 550 nm and the emission filter was 600 nm. Scale bar: 120 μm . b) Mean fluorescence intensity measured in the center area (3 images analyzed per condition). Statistical analysis (vs. data in PBS, 1 min): $p < 0.5$ (*), $p < 0.01$ (***)

highlighting the potential of our drug-sponge NCs as a detoxification platform.

Conclusion

In this work, we propose a concept of reversible pH-controlled delivery of active cargo (drug or contrast agent) to the cells based on DCvC inside lipid nano-droplets, so-called “drug sponge”. As most of drugs cannot be kept inside oil core of the lipid nano-droplets because of their moderate lipophilicity, they need to be modified with a highly lipophilic moiety to obtain a lipophilic prodrug conjugate. Here, we changed the prodrug strategy and propose to generate the conjugate directly inside the oil core of a nanocarrier by a dynamic covalent bond between a lipophilic molecule and the cargo. We designed a highly lipophilic hydrazide (LipoHD) capable of forming a hydrazone bond with a cargo (fluorescent dye and doxorubicin drug) bearing ketone group. Lipid nanoemulsions loaded with LipoHD were able to spontaneously accumulate cargo-ketones with a kinetics on the time scale of hours. In contrast to simple formulations of nanocarriers with cargos, nanocarriers loaded using dynamic covalent chemistry were stable at pH 7.4 against cargo leakage. At low pH (5–6.8), relevant to endosomes and cancer tissues, the cargos were successfully released, because of pH-dependent hydrolysis of the hydrazone. This drug-sponge system was validated in a cancer cell line, where it showed efficient pH-controlled release of dye/drug cargos into the cells. LipoHD NCs loaded with doxorubicin showed cytotoxicity in four cell lines after 48 h incubation, similarly to free doxorubicin. The therapeutic potential of drug-sponge NCs loaded with doxorubicin was demonstrated for xenografted tumors (D2A1 and MDA cells) on mice. Remarkably, the capacity of our drug sponge to capture cargo molecules in situ was successfully applied to extract fluorescent ketone and doxorubicin directly from cancer cells as well as from chicken skin adipose tissue. Thus, in addition to conventional pH controlled release, our drug sponge can extract the drug from cells and lipid-rich tissues (e.g. chicken skin), which is an unprecedented result for nanoparticles. The unique features of our drug-sponge NCs rely on liquid nature of the oil core, which allows in situ reactions, and the use of dynamic covalent bonds. In contrast to conventional covalent approach where prodrug is pre-synthesized,^[4a,5] DCvC ensures that chemically stable capture molecule (LipoHD) can react in situ with cargo forming a prodrug directly inside the nanocarrier and, then, at low pH and high dilution, the reaction is reversed towards the cargo release. Remarkably, in this cargo loading-release cycle, prodrug is expected to remain inside the oil core, so that originally loaded cargo is released to biological subject in its intact form. In this way, the approach is different from conventional prodrug approach, where pre-synthesized prodrug is brought directly in contact with cells and tissues. We expect that the developed drug-sponge concept can be applied to any drug/contrast agent bearing ketone or aldehyde group. Moreover, the concept could be extended to other dynamic covalent bonds, which can enlarge the scope of cargos. Finally, the capacity of the drug sponge nanocarriers to

extract drugs from the cells and adipose tissue of chicken skin opens new possibilities in detoxification from toxins and excess of used drugs.

Acknowledgements

This work was supported by the European Research Council ERC Consolidator grant BrightSens 648528, SATT Conectus, institutional funds from INSERM, CNRS and University of Strasbourg. F.L. is supported from China Scholarship council (CSC). Y.N. was supported by a JSPS Fellowship for Research Abroad. B.A. was supported by LabEx Chimie des Systèmes Complexes. L.M. was supported by INSERM and Region Alsace and by SATT Conectus. We thank Valentin Gensbittel for assistance with some drug removal experiments.

Conflict of interest

European patent application n° 19305035.8 has been deposited.

Keywords: controlled release · dynamic covalent bonds · fluorescence · nanotechnology · prodrugs

- [1] T. M. Allen, P. R. Cullis, *Science* **2004**, *303*, 1818.
- [2] a) M. J. Webber, R. Langer, *Chem. Soc. Rev.* **2017**, *46*, 6600; b) H. Cabral, K. Miyata, K. Osada, K. Kataoka, *Chem. Rev.* **2018**, *118*, 6844.
- [3] A. S. Narang, D. Delmarre, D. Gao, *Int. J. Pharm.* **2007**, *345*, 9.
- [4] a) S. Mura, D. T. Bui, P. Couvreur, J. Nicolas, *J. Controlled Release* **2015**, *208*, 25; b) C. Rodrigues de Azevedo, M. von Stosch, M. S. Costa, A. M. Ramos, M. M. Cardoso, F. Danhier, V. Preat, R. Oliveira, *Int. J. Pharm.* **2017**, *532*, 229.
- [5] a) V. Delplace, P. Couvreur, J. Nicolas, *Polym. Chem.* **2014**, *5*, 1529; b) D. Irby, C. Du, F. Li, *Mol. Pharm.* **2017**, *14*, 1325.
- [6] a) W. W. Gao, J. M. Chan, O. C. Farokhzad, *Mol. Pharm.* **2010**, *7*, 1913; b) F. Seidi, R. Jenjob, D. Crespy, *Chem. Rev.* **2018**, *118*, 3965; c) M. Karimi, et al., *Chem. Soc. Rev.* **2016**, *45*, 1457.
- [7] a) A. Herrmann, *Chem. Soc. Rev.* **2014**, *43*, 1899; b) Y. H. Jin, C. Yu, R. J. Denman, W. Zhang, *Chem. Soc. Rev.* **2013**, *42*, 6634; c) S. J. Rowan, S. J. Cantrill, G. R. L. Cousins, J. K. M. Sanders, J. F. Stoddart, *Angew. Chem. Int. Ed.* **2002**, *41*, 898; *Angew. Chem.* **2002**, *114*, 938.
- [8] J. M. Lehn, *Chem. Soc. Rev.* **2007**, *36*, 151.
- [9] a) J. M. Lehn, *Angew. Chem. Int. Ed.* **2015**, *54*, 3276; *Angew. Chem.* **2015**, *127*, 3326; b) Y. Zhang, M. Barboiu, *Chem. Rev.* **2016**, *116*, 809; c) N. Roy, B. Bruchmann, J. M. Lehn, *Chem. Soc. Rev.* **2015**, *44*, 3786.
- [10] S. Ulrich, *Acc. Chem. Res.* **2019**, *52*, 510.
- [11] S. J. Sonawane, R. S. Kalhapure, T. Govender, *Eur. J. Pharm. Sci.* **2017**, *99*, 45.
- [12] D. K. Kölmel, E. T. Kool, *Chem. Rev.* **2017**, *117*, 10358.
- [13] a) A. Dizdarević, N. A. Efiana, T. N. Q. Phan, B. Matuszczak, A. Bernkop-Schnürch, *Eur. J. Pharm. Biopharm.* **2019**, *142*, 92; b) C. A. Zentner, F. Anson, S. Thayumanavan, T. M. Swager, *J. Am. Chem. Soc.* **2019**, *141*, 18048.
- [14] S. P. Black, J. K. M. Sanders, A. R. Stefankiewicz, *Chem. Soc. Rev.* **2014**, *43*, 1861.
- [15] B. Akgun, D. G. Hall, *Angew. Chem. Int. Ed.* **2016**, *55*, 3909; *Angew. Chem.* **2016**, *128*, 3977.

- [16] a) P. R. Westmark, S. J. Gardiner, B. D. Smith, *J. Am. Chem. Soc.* **1996**, *118*, 11093; b) X. Wu, N. Busschaert, N. J. Wells, Y. B. Jiang, P. A. Gale, *J. Am. Chem. Soc.* **2015**, *137*, 1476; c) E. K. Bang, G. Gasparini, G. Molinard, A. Roux, N. Sakai, S. Matile, *J. Am. Chem. Soc.* **2013**, *135*, 2088; d) G. Gasparini, G. Sargsyan, E. K. Bang, N. Sakai, S. Matile, *Angew. Chem. Int. Ed.* **2015**, *54*, 7328; *Angew. Chem.* **2015**, *127*, 7436.
- [17] a) J. M. Priegue, D. N. Crisan, J. Martinez-Costas, J. R. Granja, F. Fernandez-Trillo, J. Montenegro, *Angew. Chem. Int. Ed.* **2016**, *55*, 7492; *Angew. Chem.* **2016**, *128*, 7618; b) J. M. Priegue, I. Lostale-Seijo, D. Crisan, J. R. Granja, F. Fernandez-Trillo, J. Montenegro, *Biomacromolecules* **2018**, *19*, 2638; c) V. S. Vyas, M. Vishwakarma, I. Moudrakovski, F. Haase, G. Savasci, C. Ochsenfeld, J. P. Spatz, B. V. Lotsch, *Adv. Mater.* **2016**, *28*, 8749; d) M. Prabakaran, J. J. Grailer, S. Pilla, D. A. Steeber, S. Q. Gong, *Biomaterials* **2009**, *30*, 5757.
- [18] C. Z. Ding, Z. B. Li, *Mater. Sci. Eng. C* **2017**, *76*, 1440.
- [19] M. Kanamala, W. R. Wilson, M. M. Yang, B. D. Palmer, Z. M. Wu, *Biomaterials* **2016**, *85*, 152.
- [20] a) T. Etrych, L. Kovar, J. Strohalm, P. Chytil, B. Rihova, K. Ulbrich, *J. Controlled Release* **2011**, *154*, 241; b) S. Aryal, C. M. J. Hu, L. F. Zhang, *ACS Nano* **2010**, *4*, 251; c) Y. Bae, S. Fukushima, A. Harada, K. Kataoka, *Angew. Chem. Int. Ed.* **2003**, *42*, 4640; *Angew. Chem.* **2003**, *115*, 4788; d) Y. M. Zhao, et al., *Nat. Commun.* **2016**, *7*, 11221.
- [21] a) F. Danhier, O. Feron, V. Preat, *J. Controlled Release* **2010**, *148*, 135; b) M. M. Chen, et al., *Oncotarget* **2017**, *8*, 45759.
- [22] a) G. Sahay, D. Y. Alakhova, A. V. Kabanov, *J. Controlled Release* **2010**, *145*, 182; b) S. Mukherjee, R. N. Ghosh, F. R. Maxfield, *Physiol. Rev.* **1997**, *77*, 759.
- [23] a) J. O. Eloy, M. C. de Souza, R. Petrilli, J. P. A. Barcellos, R. J. Lee, J. M. Marchetti, *Colloids Surf. B* **2014**, *123*, 345; b) V. P. Torchilin, *Nat. Rev. Drug Discovery* **2005**, *4*, 145.
- [24] a) D. J. McClements, *Soft Matter* **2012**, *8*, 1719; b) N. Anton, T. F. Vandamme, *Pharm. Res.* **2011**, *28*, 978; c) L. Salvia-Trujillo, R. Soliva-Fortuny, M. A. Rojas-Grau, D. J. McClements, O. Martin-Belloso, *Annual Review of Food Science and Technology*, Vol. 8 (Eds.: M. P. Doyle, T. R. Klaenhammer), Annual Reviews, Palo Alto, **2017**, pp. 439; d) N. Anton, J. P. Benoit, P. Saulnier, *J. Controlled Release* **2008**, *128*, 185; e) A. S. Klymchenko, F. Liu, M. Collot, N. Anton, *Adv. Healthcare Mater.* **2021**, *10*, 2001289.
- [25] R. Bouchaala, L. Mercier, B. Andreiuk, Y. Mely, T. Vandamme, N. Anton, J. G. Goetz, A. S. Klymchenko, *J. Controlled Release* **2016**, *236*, 57.
- [26] E. Roger, J. C. Gimel, C. Bensley, A. S. Klymchenko, J. P. Benoit, *J. Controlled Release* **2017**, *253*, 11.
- [27] A. S. Klymchenko, E. Roger, N. Anton, H. Anton, I. Shulov, J. Vermot, Y. Mely, T. F. Vandamme, *RSC Adv.* **2012**, *2*, 11876.
- [28] A. L. dos Santos Câmara, G. Nagel, H. R. Tschiche, C. M. Cardador, L. A. Muehlmann, D. M. de Oliveira, P. Q. Alvim, R. B. Azevedo, M. Calderón, J. P. F. Longo, *Nanomedicine* **2017**, *12*, 1751.
- [29] a) R. B. Ibrahim, C. Liu, S. M. Cronin, B. C. Murphy, R. Cha, P. Swerdlow, D. J. Edwards, *Pharmacotherapy* **2007**, *27*, 1529; b) C. W. Cheng, J. E. Hendrickson, C. A. Tormey, D. Sidhu, *Am. J. Clin. Pathol.* **2017**, *148*, 190; c) J. T. Kielstein, A. Schwarz, A. Arnava, O. Sehlberg, H. M. Emrich, D. Fliser, *Clin. Nephrol.* **2002**, *57*, 484.
- [30] a) C. C. Lee, E. R. Gillies, M. E. Fox, S. J. Guillaudeu, J. M. J. Frechet, E. E. Dy, F. C. Szoka, *Proc. Natl. Acad. Sci. USA* **2006**, *103*, 16649; b) X. P. Duan, J. S. Xiao, Q. Yin, Z. W. Zhang, H. J. Yu, S. R. Mao, Y. P. Li, *ACS Nano* **2013**, *7*, 5858; c) X. Q. Yang, J. J. Grailer, I. J. Rowland, A. Javadi, S. A. Hurley, V. Z. Matson, D. A. Steeber, S. Q. Gong, *ACS Nano* **2010**, *4*, 6805.
- [31] a) K. E. Sapsford, L. Berti, I. L. Medintz, *Angew. Chem. Int. Ed.* **2006**, *45*, 4562; *Angew. Chem.* **2006**, *118*, 4676; b) B. L. Sanchez-Gaytan, F. Fay, S. Hak, A. Alaarg, Z. A. Fayad, C. Perez-Medina, W. J. M. Mulder, Y. Zhao, *Angew. Chem. Int. Ed.* **2017**, *56*, 2923; *Angew. Chem.* **2017**, *129*, 2969.
- [32] L. Bromberg, M. Temchenko, T. A. Hatton, *Langmuir* **2002**, *18*, 4944.
- [33] G. Nagel, H. R. Tschiche, S. Wedepohl, M. Calderon, *J. Controlled Release* **2018**, *285*, 200.
- [34] a) C. Simonsson, G. Bastiat, M. Pitorre, A. S. Klymchenko, J. Bejaud, Y. Mely, J. P. Benoit, *Eur. J. Pharm. Biopharm.* **2016**, *98*, 47; b) A. Saito, S. Yamamoto, R. Ochi, K. Inoue, S. Hadano, S. Watanabe, T. Nakayama, Y. Niko, *Bull. Chem. Soc. Jpn.* **2020**, *93*, 568.
- [35] R. Crespo, M. Pizarro, *Avian Dis.* **2006**, *50*, 309.

Manuscript received: October 24, 2020

Revised manuscript received: November 26, 2020

Accepted manuscript online: December 7, 2020

Version of record online: February 4, 2021



Supporting Information

Drug-Sponge Lipid Nanocarrier for in Situ Cargo Loading and Release Using Dynamic Covalent Chemistry

*Fei Liu⁺, Yosuke Niko⁺, Redouane Bouchaala, Luc Mercier, Olivier Lefebvre, Bohdan Andreiuk, Thierry Vandamme, Jacky G. Goetz, Nicolas Anton, and Andrey Klymchenko**

anie_202014259_sm_miscellaneous_information.pdf

Experimental Section

All starting materials for synthesis were purchased from Alfa Aesar, Sigma-Aldrich unless specifically mentioned. To be specific, Acetic acid (>99.0%, Sigma-Aldrich), Sodium phosphate monobasic (>99.0%, Sigma-Aldrich) and sodium phosphate dibasic dihydrate (>99.0%, Sigma-Aldrich) were used to prepare 20 mM phosphate buffers at pH 7.4 and pH 4. DiD oil (1,1'-dioctadecyl-3,3,3',3'-tetramethylindodicarbocyanine perchlorate) (Cy5) were purchased from ThermoFisher Scientific. 4'-dioctylamino-3-octyloxyflavone (F888) were synthesized as described before.^[1] Labrafac WL1349[®] was purchased from Gattefossé (Saint-Priest, France) Milli-Q water (Millipore) was used in all experiments. Chicken skin were obtained from chicken legs (Tyson industry) purchased in supermarket Lidl. Synthesis and characterization of all new compounds, including LipoHD, Nile Red Ketone (NRK), Nile Red Ketone-LipoHD conjugate (Lipo-NRK) and doxorubicine-LipoHD conjugate (Lipo-Dox) are described in the Supporting Information. Calculated LogP (cLogP) values for reported molecules were obtained using ChemDraw 16.0. All error bars correspond to standard deviation of the mean. Statistical analysis was done based on the one-tailed T-test, using Microsoft Excel. NMR spectra were recorded on a Bruker Avance III 400 MHz spectrometer. Mass spectra were obtained using an Agilent Q-TOF 6520 mass spectrometer.

Optical spectroscopy

The water used for spectroscopy was Milli-Q water (Millipore), and all the solvents were spectral grade. Labrafac (Labrafac WL 1349[®]) is composed of medium-chain triglycerides and caprylic/capric triglyceride and was obtained from Gattefossé (Saint Priest, France). Absorption and emission spectra were recorded on a Cary 4000 Scan ultraviolet–visible spectrophotometer (Varian) and a FluoroMax-4 spectrofluorometer (Horiba Jobin Yvon) equipped with a thermostated cell compartment, respectively. For standard recording of fluorescence spectra, the emission was collected 10 nm after the excitation wavelength. All the spectra were corrected for the wavelength-dependent response of the detector. Size distribution was determined by DLS using a Zetasizer Nano ZSP (Malvern Instruments SA). In DLS, measurement statistics by volume was used.

Formulation of cargo-loaded NCs

NCs were produced by spontaneous nanoemulsification: the cargo (dyes, LipoHD and/or Pro-NRK) were dissolved in Labrafac (50 mg and placed in sonication bath at 40 °C for 10 min. Then, the surfactant Kolliphor ELP[®] was added (50 mg), and the mixture was homogenized under magnetic stirring at 40 °C for 10 min up to complete homogenization. Finally, NCs were generated with the addition of ultrapure (Milli-Q) water (230 mg).

pH-dependent release of Lipo-NRK

In order to prove that LipoHD modified NRK (Lipo-NRK) is more lipophilic and resistant to leakage than NRK, the conjugate was first synthesized chemically and used for the release model study. For NRK and Lipo-NRK release model study, five formulations were prepared:

NRK with and without F888, Lipo-NRK with and without F888 and F888 alone. The concentration of each dye in labrafac was 10 mM. The condition for testing the dye stability in the presence of empty NCs was created by mixing 100 μ L 100 times diluted dye-loaded NCs (by mixing 10 μ L NCs with 990 μ L distilled water) with 10-fold excess of blank NCs (10 μ L), which acted as the acceptor medium for the released dyes. The pH dependent release of Lipo-NRK was conducted by using buffers of ranging pH from pH 5 to pH 7.4 prepared by mixing different portion of acetate buffer (pH 4) with phosphate buffer (pH 7.4) during mixing with 10-fold excess of blank particles. Fluorescence of the sample was tested at several time points (5, 10, 15, 30, 60, 120, 240 and 480 min). Fluorescence intensity ratio of F888 and NRK (taken at 453 and 603 nm, respectively) under the excitation wavelength of 405 nm was measured. All the spectra were corrected by subtracting the blank corresponding to the empty NCs.

***In situ* formation of Lipo-NRK detected by FRET**

To evaluate the *in situ* reaction inside NCs, NRK was used as a model drug. 300 mL of NCs prepared from Labrafac containing LipoHD (90 mM) and Kolliphor ELP® (see above) was mixed with 12.6 μ L of 47 mM NRK and 300 μ L of pH 4 acetate buffer and reacted for 6 h (rt). Then, the emulsion was extracted by 600 μ L dichloromethane. TLC was used to examine the content in the organic phase compared with pure Lipo-NRK. Dichloromethane:MeOH=95:5 was used as the mobile phase for TLC. With the help of F888 as energy donor, the reaction was monitored by the FRET efficiency between F888, the FRET donor, and NRK, the acceptor. NCs prepared from Labrafac containing F888 (10 mM) and LipoHD (90 mM) were used for the reaction. NCs prepared from Labrafac containing only F888 (10 mM) were used as a control. The reaction was initiated by adding 300 μ L of pH 4 acetate buffer along with 12.6 μ L of 47 mM NRK. The reaction was diluted at different time points by mixing 10 μ L of the reacted solution with 990 μ L of pH 7.4 phosphate buffer. Then 100 μ L of this diluted solution was mixed with 10 μ L empty NCs and 880 μ L milliQ water, and the emission spectrum was measured under the excitation wavelength of 405 nm. The fluorescence intensity ratio of peak at 450 and 600 nm was calculated from the spectrum. All the spectra were corrected from the blank by subtracting the corresponding spectrum of empty NCs.

***In situ* formation of Lipo-Dox conjugate detected by FRET**

Doxorubicine (Dox), an anti-tumor drug, was also tested by this *in situ* pro-drug formation system. Similarly, 300 mL of NCs prepared from Labrafac containing LipoHD (90 mM) were mixed with 300 μ L acetate buffer (pH 4) along with 10 μ L of Dox-HCl (150 mM). In the control experiment NCs without LipoHD were used. The mixtures were vortexed for 24 h at 37 °C. The resulting solutions were dialyzed in 500 mL of 0.1 M NaHCO₃ for 24 h. After the dialysis, encapsulation efficiencies were tested based on the absorbance at 500 nm of the NCs solution before and after dialysis using 100 fold diluted reaction solution. Afterwards, NCs containing 90 mM LipoHD and 0.95 mM of DiD (Cy5) in Labrafac were prepared to monitor the reaction by FRET. To start the reaction, 10 μ L of 150 mM Dox-HCl solution in DMSO were added to 330 μ L of NCs along with 300 μ L pH 4 buffer, control was conducted with NCs containing only 0.95 mM of Cy5 in Labrafac. To study the *in situ* reaction kinetics, the reaction

at different time points was quenched with 100 fold of phosphate buffer (pH 7.4). Then, 100 μ L of this diluted solution were mixed with 10 μ L of empty NCs and 980 μ L milliQ water. The reaction was examined by measuring the fluorescence intensity ratio of Cy5 and Dox at 670 and 600 nm, respectively, under the excitation wavelength of 520 nm. After the reaction, the mixture underwent dialysis for 24 hours. UV absorption was used to determine the encapsulation ratio of Dox in the form of Lipo-Dox. NCs with the same concentration of Cy5 but without LipoHD were used as a control in the same protocol above.

Lipo-Dox NCs pH dependent release study

To monitor the pH-controlled release of Dox, we used FRET technique similar to that used for Nile Red derivative NRK. Cy5/Lipo-Dox NCs were prepared by in situ reaction of NCs containing 90 mM LipoHD and 0.95 mM of DiD (Cy5) in Labrafac for 6 h and for dialysis to remove unreacted Dox. The obtained Cy5/Lipo-Dox NCs were mixed with 10-fold excess of blank nano-droplets and the emission spectra were recorded as a function of time at a range of pHs from pH 5 to pH 7.4 prepared by pH 7.4 (phosphate buffer) and pH 4 (acetate buffer). Finally, in order to test the compatibility with cell experiments media, PBS with pH 7.4 and pH 5 adjusted with acetic acid as well as 10% serum were also tested in similar manner. Fluorescence intensity ratio of Cy5 and Dox (peaks at 670 and 600 nm, respectively) under the excitation at 520 nm was measured.

Cell experiments

HeLa cells (ATCC® CCL-2) were grown in Dulbecco's modified Eagle's medium (DMEM, Gibco-Invitrogen), supplemented with 10% fetal bovine serum (FBS, Lonza) and 1% antibiotic solution (penicillin–streptomycin, Gibco-Invitrogen) at 37 °C in a humidified atmosphere containing 5% CO₂. HeLa cells (ATCC) were seeded on 12 mm coverslips at 30,000 cell per well in DMEM medium with penicillin (100 U/mL), 1% glycan (100 U/mL) and 10 % FBS overnight. The pH of PBS was adjusted with 1 M acetic acid and 1 M disodium phosphate to 5 and 7.4, respectively. Solution of F888/Lipo-NRK NCs (10 mM each in labrafac) or Cy5/Lipo-Dox NCs (sample from in situ reaction) pre-diluted 100-times in milliQ water (100 μ L) was added to PBS of a given pH to a final volume of 1 mL, corresponding to 1000-times total dilution of NCs. The cells were washed 3 times with PBS and then the medium was replaced with a diluted solution of NCs at corresponding pH. Control NCs, containing F888/NRK or DiD/Dox, were also used in PBS medium at pH 7.4 and pH 5 to check the release of free NRK and Dox in cells. Cell imaging were conducted at two different time points: 1 min and 30 min. For both time points, the samples were imaged after washing with PBS.

All cellular imaging studies were done using epi-fluorescence mode with a Nikon Ti-E inverted microscope, equipped with CFI Plan Apo \times 60 oil (numerical aperture = 1.4) objective, and a Hamamatsu Orca Flash 4 sCMOS camera. For Lipo-NRK and NRK imaging, the excitation wavelength was 550 nm, and emission was detected through 600/50 nm filter. For Lipo-Dox and Dox imaging, the excitation wavelength was 470 nm, and emission was detected through 531/40 nm filter. In the colocalization studies, F888 was detected using 390 nm excitation and 470 nm detection filter, whereas DiD was detected using 640 nm excitation and 705/80 nm detection filter.

The *in situ* extraction of molecules from cells was done as follows. Briefly, cells were first incubated with 15 μ M of Dox or 1 μ M of NRK (concentration determined by the absorption spectrum) for 30 minutes in the cell culture medium. Afterwards, cells were washed with PBS once, the fluorescence images were checked to ensure all the groups of cells were stained with similar amount of Dox and NRK (data not shown). Then, the medium was changed to 100-times diluted LipoHD NCs (above mentioned) in PBS medium. Control group was treated with empty NCs (the same dilution) in PBS, and the PBS buffer without NCs was used as blank control. Images were acquired immediately after the changing of medium defined as time point 1 min (<1 min) and after 1 hour for Dox and NRK *in situ* uptake study. After imaging, mean intensity from each cell for NRK and Dox channels was analyzed excluding nucleus (the center black part of each cells). The obtained values are the mean fluorescence intensity from ~15 cells.

To study the extraction media, HeLa cells were first stained with 1 μ M of NRK for 30 min, washed with PBS and then treated with different extraction media (1 mL): 100-fold diluted LipoHD NCs, blank NCs or PBS. The extraction media were collected after 1, 5, 15, 30 and 60 min of incubation with HeLa cells to examine the emission spectrum (each condition was done in triplicate). For PBS group, 100-times diluted LipoHD NCs were added to the extraction solution to ensure the comparable measuring condition for NRK. To quantify NRK concentration in the extraction media, the calibration curve of peak fluorescence intensity vs NRK concentration was built after measuring fluorescence spectra of LipoHD NCs (100-fold dilution) with increasing concentration of NRK. For estimating the total amount of NRK accumulated in HeLa cells, the emission spectra of the 1 μ M of NRK (1 mL), used for cell staining, was measured before and after cell staining in the presence of 100-times diluted LipoHD NCs.

To provide chemical identification of Lipo-NRK conjugates in the extract, NRK-stained HeLa cells were treated with the LipoHD NCs for 60 min. Then, the medium was collected and the extraction by dichloromethane was performed. The presence of Lipo-NRK in the extract studied by TLC (Dichloromethane:MeOH = 95:5) using as references pure Lipo-NRK and a the *in-situ* reaction mixture of NRK with LipoHD NCs extracted by dichloromethane (see above the protocol for the *in-situ* reaction). Finally, the Lipo-NRK from the same dichloromethane extract (cell medium with LipoHD NCs) was also identified by mass spectrometry.

Cytotoxicity study

Four cancer cell lines were used: D2A1, 4T1 (mouse origin) and HeLa, MDA-MB-231 (human origin). The MTS cytotoxicity assay was used, which is based on the reduction of the MTS tetrazolium compound by viable mammalian cells to generate a colored formazan dye. The formazan dye is quantified by measuring the absorbance at 490-500 nm. Briefly, tumor cells (D2A1, 4T1, MDA-MB-231 or HeLa cells) were seeded at 5000 cell per well in a 96 wells plate. After 24h, the medium was removed and replaced by drug-containing (Lipo-DOX NPCs or DOX alone) medium (DMEM). To study time-dependent effect, HeLa cells were incubated for 12, 24 and 48 hours. For other three cell lines, incubation was done for 48 hours. After incubation, the medium was removed and replaced with MTS containing medium (0.5 mg/mL).

After 4h of incubation, absorbance was read at 490-500 nm. The values of absorbance corresponding to cell viability was normalized to 100% of the non-treated control cells.

In vivo experiments on mice

All mice were housed and handled according to the guidelines of INSERM and the ethical committee of Alsace, France (CREMEAS), under the APAFIS agreement number 12780-2017122016498879. For all experiments, 8 weeks-old female Rj:NMRI Foxn1 nu/nu mice were purchased from Janvier Labs.

2 millions of D2A1 or MDA-MB-231 stably expressing Luciferase cells were diluted in 50 μ l of PBS and injected subcutaneously in the back of 8-week-old female Rj:NMRI Foxn1 nu/nu mice. When tumors reached a tumor volume of $\pm 0.5 \text{ cm}^3$ (measured with a caliper using the following formula $(\text{width}^2 \times \text{length})/2 \text{ (mm}^3)$), mice were randomized in 4 groups of 8 mice and subjected to the 4 different treatments: PBS, Doxorubicin, LipoHD NCs or Lipo-Dox NCs. Lipo-Dox NCs were prepared in situ as described above by incubating LipoHD NCs with Dox at pH 4, followed by dialysis of the reaction mixture to remove excess of Dox. Final Dox loading in this formulation was 0.7 % with respect to oil. Before the injection, the nanoemulsion was diluted twice in PBS. Mice received the treatments by i.v. injection through the retro-orbital sinus, 2 times per weeks (alternating eyes at each round) of 100 μ l corresponding solution. For free Dox and Lipo-Dox formulations, the single injection dose of Dox was the same (51 μ g corresponding to $\sim 2.5 \text{ mg/kg}$). Tumor growth was tracked two times/week either by caliper measurement (D2A1) or by in vivo bioluminescence imaging (MDA-MB-231). For bioluminescence imaging, mice were anesthetized with isoflurane and subjected to i.p. injection of 166 μ g/g of a luciferin solution (Perkin Elmer). Imaging was done 5 min upon injection on a IVIS Illumina LT (Perkin Elmer). Photon counts (photon/second/ cm^2/sr) were analyzed using Living Image software 4.5 (Perkin Elmer).

Experiment with adipose tissue from chicken skin

A serial of specially cut chicken skin circles (5 mm diameter) was washed with ethanol for 3 times to remove oil on the surface, followed by washing 3 times with water to remove ethanol. Then, chicken skin was immersed into aqueous solutions of 5 μ M NRK or 45 μ M Dox for 10 min. Then, the chicken skin tissue was washed with PBS once. The wet skin then was evenly spread in wells of a Lab-Tek® chamber, and the fluorescence images were acquired. Then, the medium was changed to 100-times diluted LipoHD NCs in PBS medium (300 μ L). Control group was treated with blank NCs (300 μ L, the same dilution) in PBS, and the PBS buffer (300 μ L) without NCs was used as a control. Fluorescence images were acquired immediately after changing the medium, defined as time point 1 min ($<1 \text{ min}$). Then the skins with the buffers were removed into a 1.5 mL Eppendorf® tube and shaken for 30 min at speed of 600 r/min on a ThermoMixer at rt. Later on, skins were again flatly spread on the Lab-Tek® wells for the fluorescence microscopy measurements. Fluorescence imaging was done by the Nikon microscope (see above) using Nikon 20x air objective (Nikon CFI Plan Apo, NA = 0.75). For Dox and NRK imaging, the excitation wavelength was 550 nm, and emission was detected

through 600/50 nm filter. After the imaging, mean intensity for NRK and Dox channels was analyzed by selecting the center area (same size) of each images (3 images for each condition).

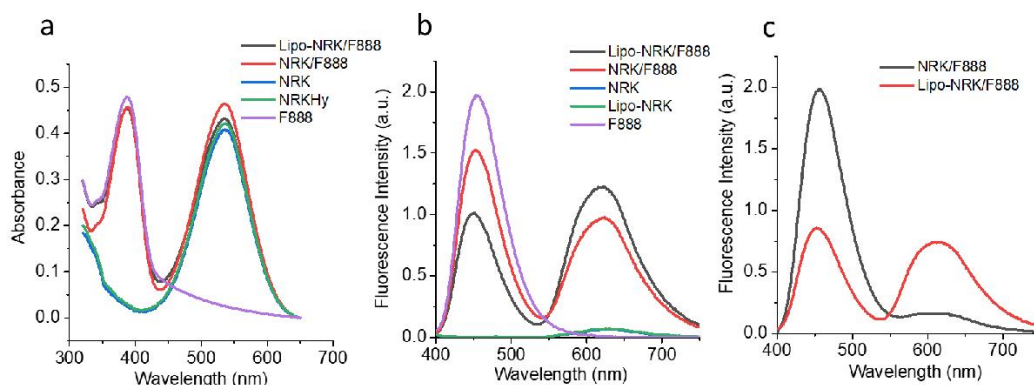


Fig. S1. (a) Absorption spectra of NCs loaded with NRK, Lipo-NRK, NRK/F888, Lipo-NRK/F888, F888. (b) Fluorescence spectra of NCs loaded with NRK, Lipo-NRK, NRK/F888, Lipo-NRK/F888 or F888. (c) Fluorescence spectra of Lipo-NRK/F888/ and NRK/F888 NCs after dilution and addition 20 fold-excess of black NCs.

The FRET NCs showed additional absorption band of F888 centered at ~390 nm (Fig. S1a). Control NCs containing F888 only showed strong donor emission, while the NCs loaded with only acceptor (NRK or Lipo-NRK), excited at 405 nm showed poor emission, suggesting inefficient direct excitation of the acceptor (Fig. S1b). These results confirmed FRET inside NCs between co-encapsulated donor (F888) and acceptor (NRK or Lipo-NRK).

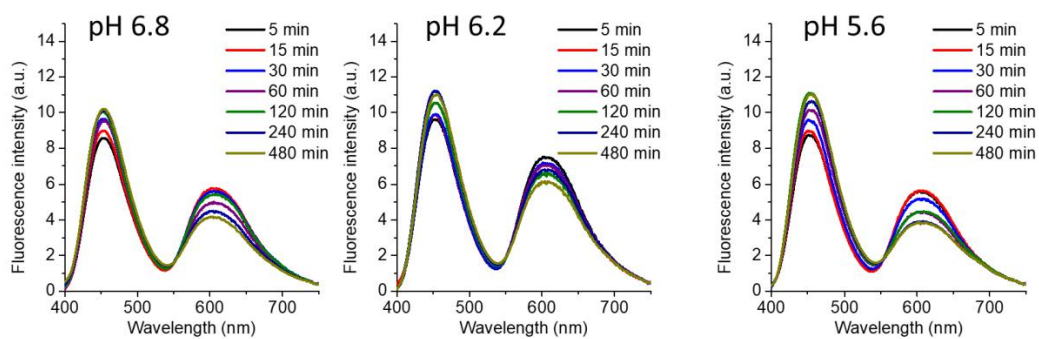


Fig. S2. Fluorescence spectra of Lipo-NRK conjugate NCs for different incubation time pH 6.8, pH 6.2 and pH 5.6 after dilution (1000-fold) in the presence of 20-fold excess of blank NCs. (j) Fluorescence intensity ratio of acceptor (I_{600}) to donor (I_{450}) over time at different pH. Excitation wavelength was 405 nm throughout.

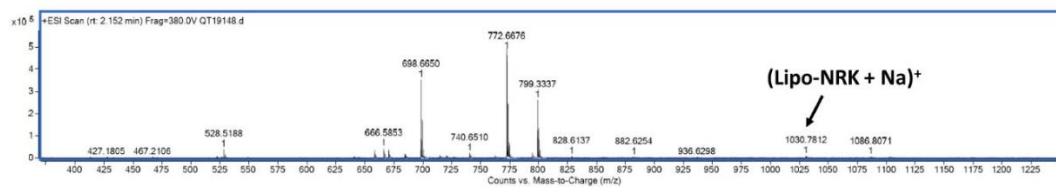


Fig. S3. Mass spectrometry of the in situ reaction mixture of LipoHD NCs with NRK after 4 h (40 °C), extracted with dichloromethane. Characteristic pick of (Lipo-NR + Na)⁺ can be seen.

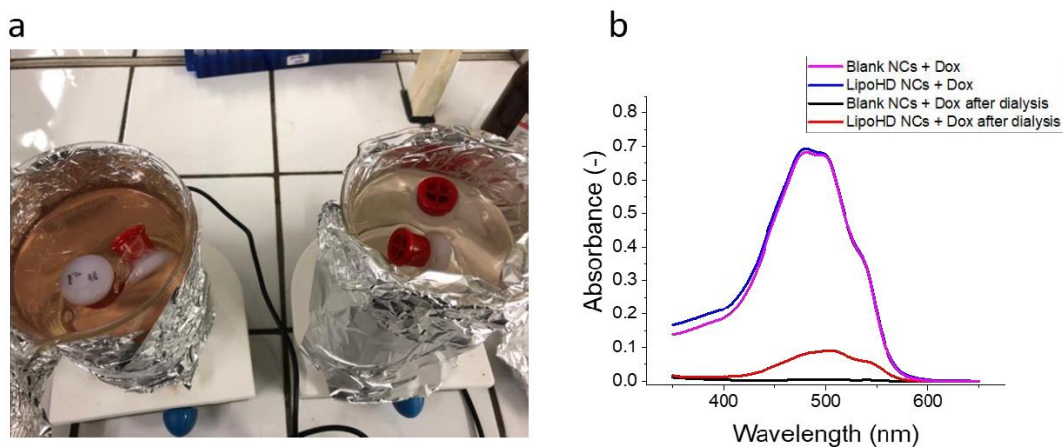


Fig. S4. (a) Photo of dialysis for the reaction mixture of Dox with control NCs without LipoHD (left) and with LipoHD NCs (right) after 24 h of dialysis. Deeper color of released Dox for control NCs compared to LipoHD-loaded NCs, suggest that Dox was captured inside LipoHD NCs. (b) Absorption spectra before and after dialysis of reaction mixture Dox with control (blank) NCs and LipoHD NCs incubated for 24h at rt.

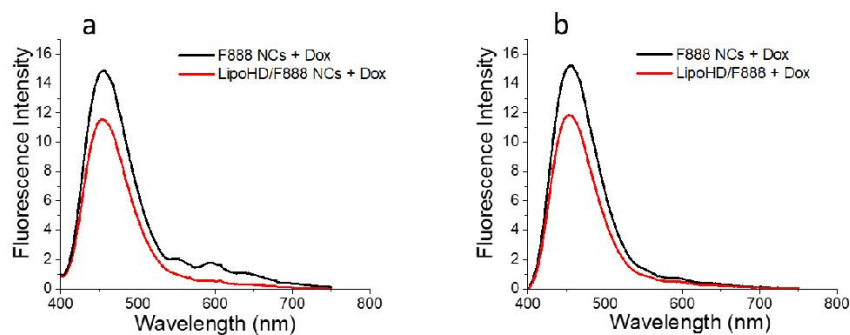


Fig. S5. Fluorescence spectrum of a reaction mixture of LipoHD/F888 NCs and Dox before (a) and after (b) dialysis, monitored by exciting FRET donor F888 (at 380 nm).

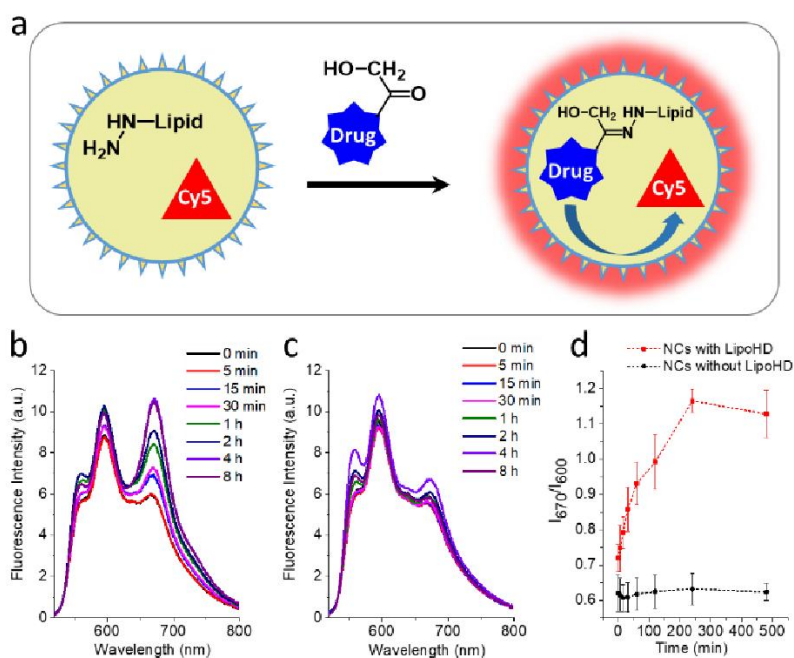


Fig. S6. *In situ* reaction of Dox with LipoHD monitored by Cy5. (a) Scheme of *in situ* formation of Lipo-NRK changing FRET of NCs. (b) Emission spectra of reaction mixture of LipoHD/Cy5 NCs with Dox at different reaction times after dilution (1000-fold) with 20-fold excess of blank NCs. Excitation wavelength is 520 nm. (c) The same experiment as (b) for NCs without LipoHD. (d) Fluorescence intensity ratio at fixed wavelengths (674 to 600 nm) for experiments (b) and (c). The *in situ* reaction was done at pH 4.

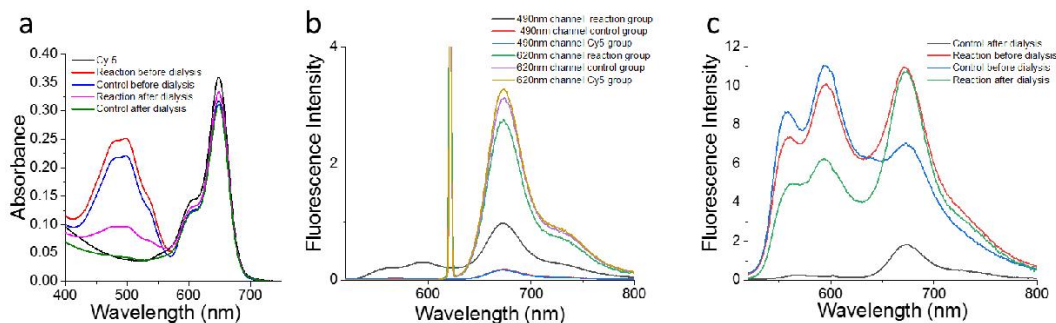


Fig. S7. (a) UV absorption of Dox-Cy5 mixture in situ reaction before and after dialysis along with control groups; (b) Fluorescence spectra of NCs exciting at absorption wavelength of DOX and Cy5 after dialysis. All the three NCs types showed similar fluorescence emission from Cy5 excited at 620 nm, confirming that all three samples contained similar amount of FRET acceptor. (c) Comparison of fluorescence spectra exciting at absorption wavelength of DOX of NCs with and without reaction with LipoHD before and after dialysis.

After the dialysis, the acceptor/donor ratio increased (Fig. S7c) because only unreacted Dox was removed, whereas without LipoHD this ratio was very low, corresponding to Cy5 NCs without Dox.

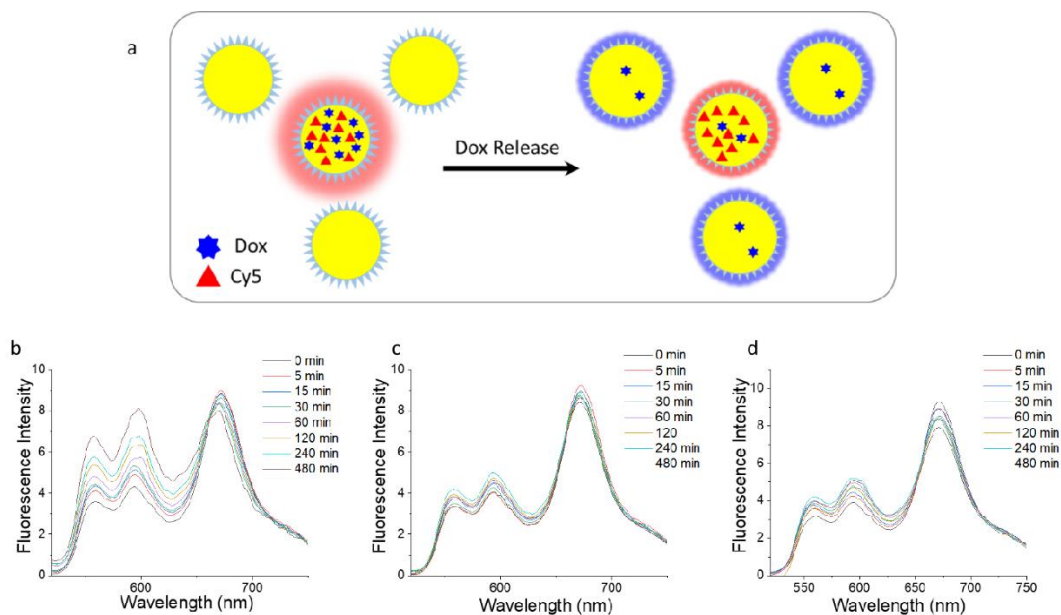


Fig. S8. (a) Schematic representation DOX release in Lipo-DOX/Cy5 NCs and DOX/Cy5 NCs in the presence of blank NCs, which is expected to decrease FRET from DOX to Cy5 at given condition. DOX-LipoHD loaded NCs stability test monitored by FRET in physiological conditions: (a) pH 5 PBS; (b) pH 7.4 PBS; (c) 10% Serum. Fluorescence spectra of Lipo-DOX FRET NCs (1000-fold dilution) in the presence of 20-fold excess of blank NCs. Excitation wavelength was 520 nm.

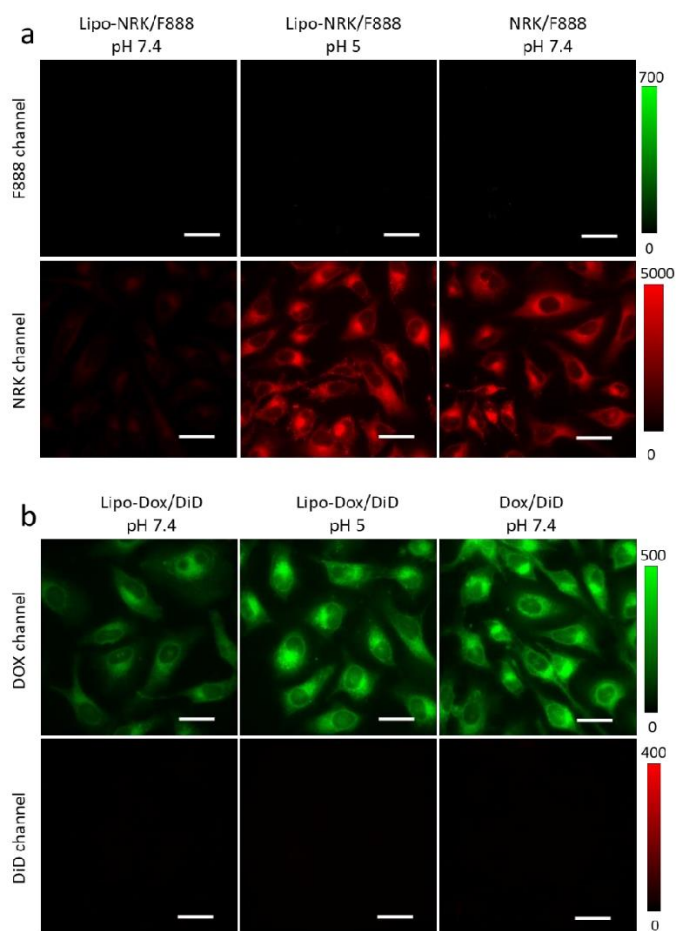


Fig. S9. Fluorescence imaging cells incubated for 30 min with (a) LipoNRK/F888 NCs (pH 5 and 7.4) and NRK/F888 (pH 7.4) and (b) Lipo-Dox/Cy5 NCs (pH 5 and 7.4) and Dox/Cy5 NCs (pH 7.4). F888 channel: 390 nm excitation and 470 nm detection filter. NRK channel: 550 nm excitation and 600/50 nm emission filter. DiD channel: 640 nm excitation and 705/80 nm detection filter.

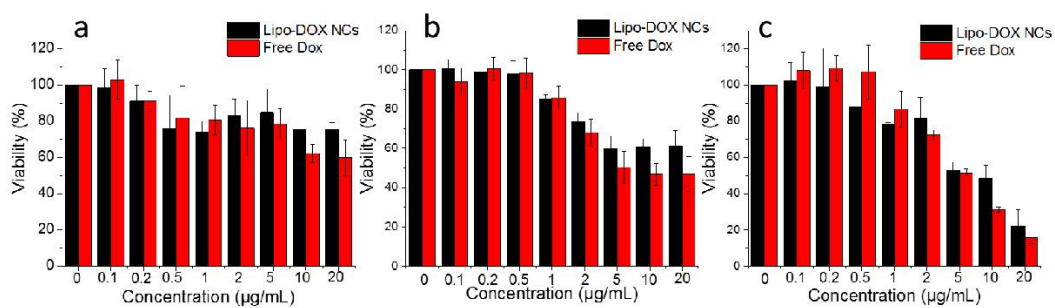


Fig. S10. Cytotoxicity of Lipo-Dox loaded NCs compared with free Dox in Hela cell line. Incubation was done for 12 (a), 24 (b) and 48h (c) with Lipo-HD-Dox loaded NCs or free Dox at different drug concentrations. Errors are standard deviation of the mean (n = 6).

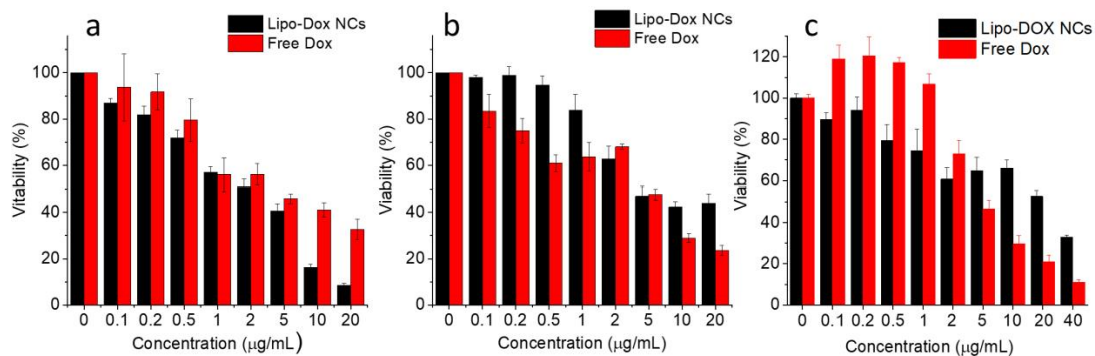


Fig. S11. Cytotoxicity of Lipo-Dox loaded NCs compared with free Dox in three cell lines: 4T1 (a), MDA-MB-231 (b) and D2A1 (c). Incubation was done for 48h with Lipo-HD-DOX loaded nanoemulsion or free DOX drug at different concentrations of the drug. Errors are standard deviation of the mean (n = 6).

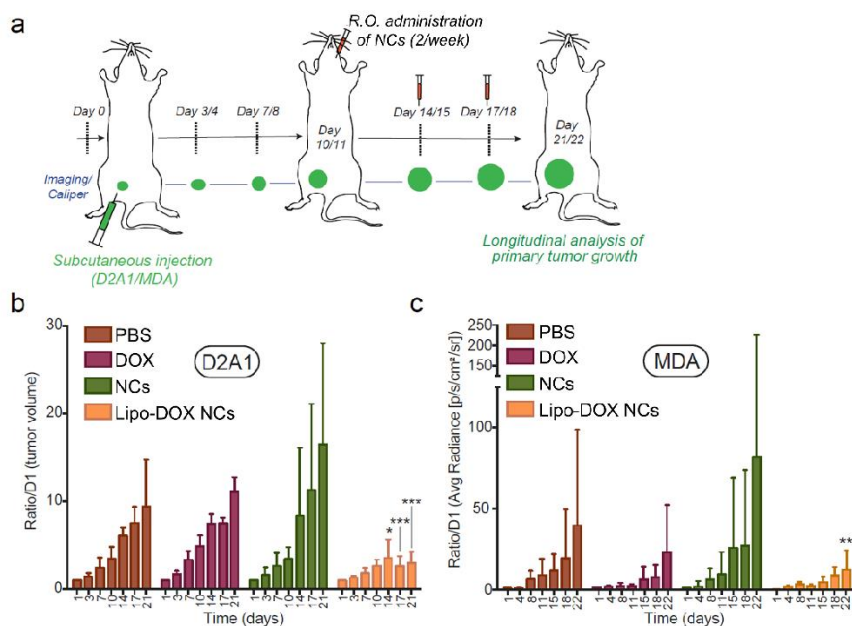


Fig. S12. In vivo studies on nude mice bearing D2A1 or MDA-231 tumor xenografts, treated with Lipo-DOX NCs. (a) Tumor implanting and drug administration protocol. (b) Tumor volume (mm³) assessment for using D2A1 as tumor implanting cell line over 21 days. (c) Tumor bioluminescence assessment for using MDA-231 as tumor implanting cell line over 21 days. Errors are standard deviation of the mean (n = 8).

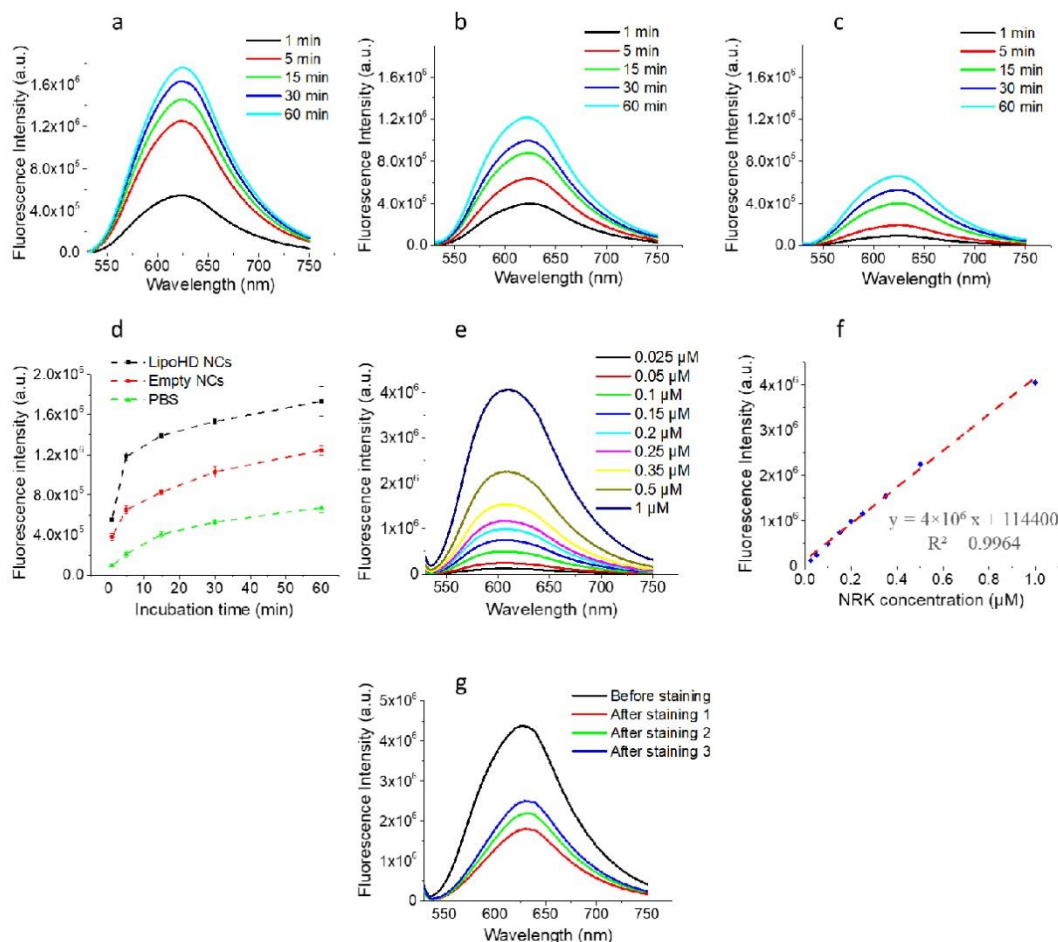


Fig. S13. Fluorescence analysis of the extraction medium incubated with HeLa cells stained with NRK (1 μM). (a-c) Fluorescence spectra of the cell culture (extraction) media, LipoHD NCs (a), blank NCs (b) and PBS (c), after incubation with NRK-stained HeLa cells for different time. 100-times diluted LipoHD NCs and blank NCs or PBS were used. (d) Time-dependent peak fluorescence intensity for three cell culture (extraction) media based on emission spectra presented in (a-c). Errors are standard deviation of the mean ($n = 3$). Quantification of NRK extraction from LipoHD NCs, empty NCs and PBS: fluorescence spectra (e) and a calibration curve of NRK pick fluorescence intensity (f) for different concentrations of NRK in the presence of LipoHD NCs (100-fold dilution). (g) Fluorescence spectra of NRK staining solution before and after staining of HeLa cells for 1h. NRK concentration in the staining medium was 1 μM .

Using pick fluorescence intensity from the cell culture (extraction) media (Fig. S13a-c) and the calibration curve (Fig. S13f), we estimated the amount of extracted NRK from cells. Then, using the loss of the fluorescence intensity during staining (Fig. S13g, corresponding to the internalized NRK) and the calibration curve (Fig. S13f), we could estimate the total amount of the internalized NRK. These data allowed us to further calculate the fraction (%) of the extracted NRK from HeLa cells.

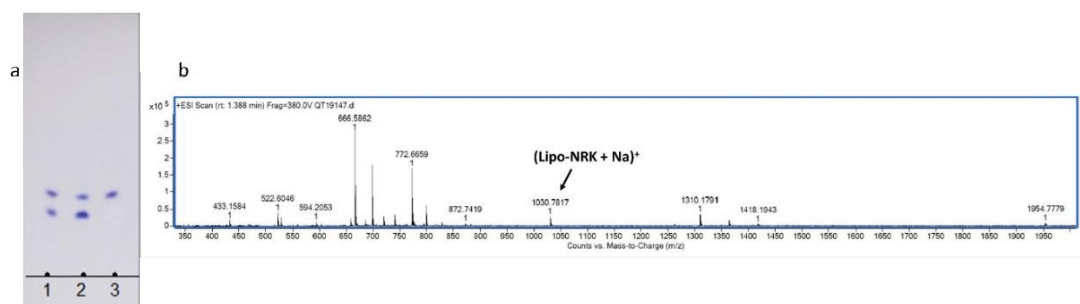


Fig. S14. TLC and mass spectrometry data that evidence in-situ formation of Lipo-NRK during the extraction of NRK from HeLa cells. (a) TLC of three samples (eluent dichloromethane:MeOH = 95:5): (1) dichloromethane extract from LipoHD NCs incubated with NRK-stained cells (1h); (2) dichloromethane extract from the in-situ reaction of NRK with LipoHD NCs after 1 h (40 °C); (3) pure Lipo-NRK. (b) Mass spectrum of the dichloromethane extract from LipoHD NCs incubated with NRK-stained cells (1h), presenting a characteristic pick of (Lipo-NR + Na)⁺.

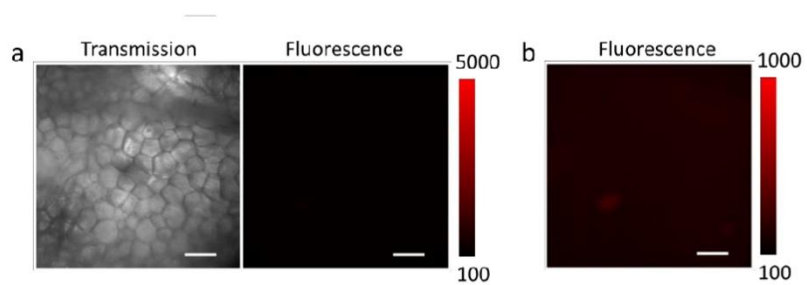


Fig. S15. Auto-fluorescence from chicken skin adipose tissue. (a) Transmission and fluorescence images. (b) The same fluorescence image as in (a) but with a different intensity scale. Excitation wavelength was 550 nm and the emission filter was 600 nm.

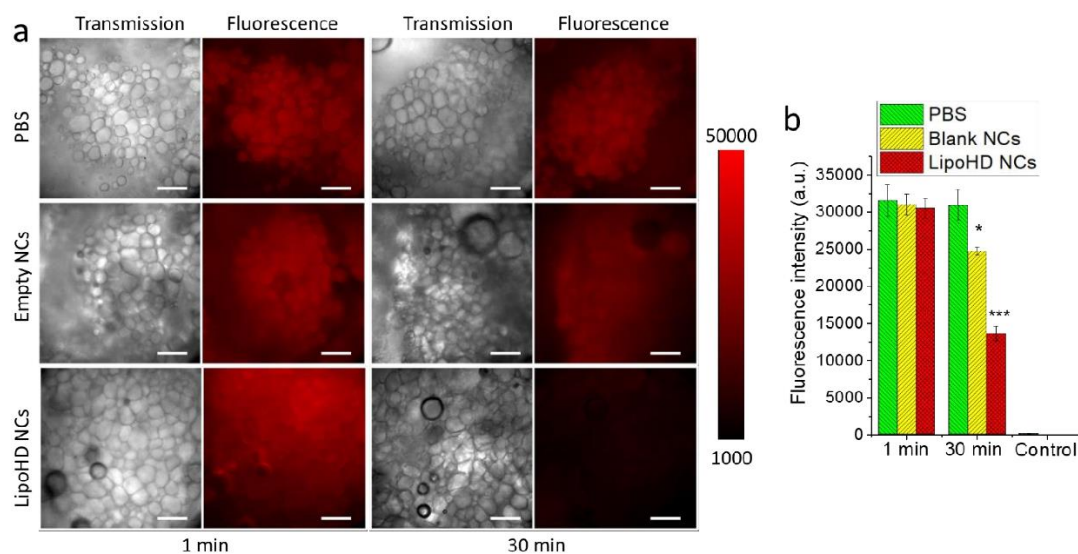


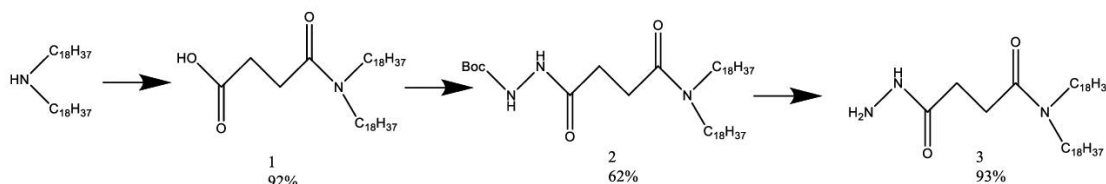
Fig. S16. *In situ* extraction of ketone dye NRK by LipoHD NCs from chicken skin adipose tissue. (a) Transmission and fluorescence images of *in situ* extraction of NRK: tissue was pre-incubated with 5 μ M of NRK for 30 min, washed, treated or 1 or 30 min with 100-fold diluted LipoHD NCs, empty NCs and PBS and then washed with PBS before imaging. Excitation wavelength was 550 nm and the emission filter was 600 nm. (b) Mean fluorescence intensity measured in the center area (3 images analyzed per condition). Statistical analysis (vs. data in PBS, 1 min): $p < 0.5$ (*), $p < 0.01$ (***).

Table 1. Size measurements of formulated nano-droplets.

Sample	Size (nm)	PDI
Blank NCs	85	0.22
LipoHD	78	0.15
F888	79	0.11
NRK	112	0.36
Lipo-NRK	71	0.10
NRK-LipoHD/F888	77	0.15
NRK/F888	114	0.24
NRK-LipoHD/F888, <i>in situ</i>	79	0.15
NRK-F888, <i>in situ</i>	113	0.23
Dox NCs, before dialysis	134	0.23
Dox-LipoHD NCs, before dialysis	144	0.22
Dox NCs after dialysis	71	0.13
Dox-LipoHD, after dialysis	85	0.06
Dox/Cy5 before dialysis	105	0.22
Dox/Cy5 after dialysis	70	0.10
Dox-LipoHD/Cy5 before dialysis	116	0.19
Dox-LipoHD/Cy5 after dialysis	71	0.10

^a Dye concentration in labrafac: F888 (10 mM); Lipo-NRK (10 mM); NRK (10 mM); Cy 5 (0.95 mM). Concentration for *in situ* reactions is not shown.

Synthesis and chemical characterization



Scheme S1. Synthesis of LipoHD.

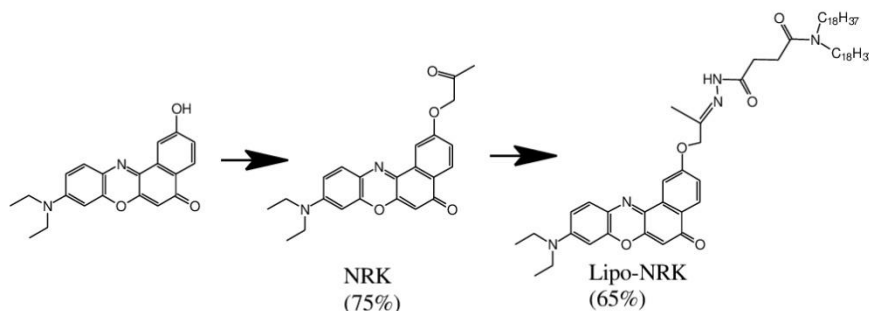
Synthesis of LipoHD

To the solution of succinic anhydride (192 mg, 1.92 mmol) in THF (20 mL) was added dioctadecylamine (500 mg, 0.96 mmol), then mixture was refluxed overnight under argon atmosphere. The solvent was evaporated in vacuo, then resulting residue was purified by recrystallization from dioxane to give desired product as a colorless solid (550 mg, 92%).

Compound 1. To the solution of succinic anhydride (192 mg, 1.92 mmol) in THF (20 mL) was added dioctadecylamine (500 mg, 0.96 mmol), then mixture was refluxed overnight under argon atmosphere. The solvent was evaporated in vacuo, then resulting residue was purified by recrystallization from dioxane to give desired product as a colorless solid (550 mg, 92%). ¹H NMR (400 MHz, CDCl₃) δ ppm 11.72 (1H, bs), 3.34 (4H, t), 3.19 (4H, t), 1.56 (4H, bs), 1.24 (60H, bs), 0.86 (6H, t). MS for [C₄₀H₇₉NO₃ – H⁺]⁻ m/z (M-1) calc. 620.61, found 620.60.

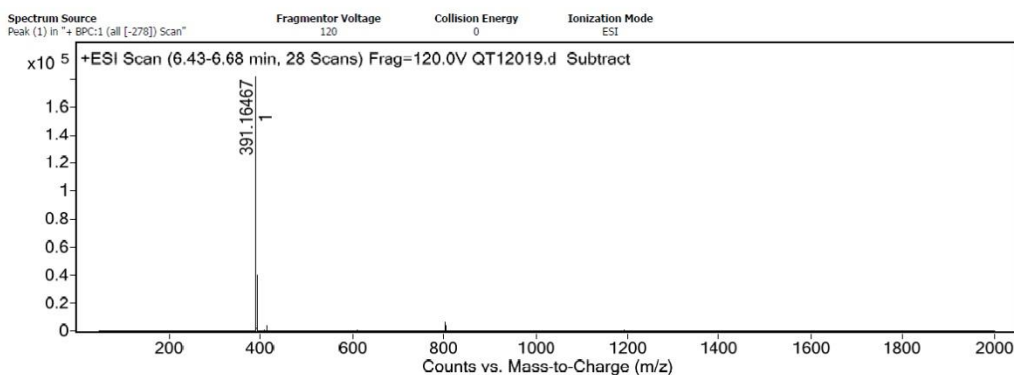
Compound 2. To the solution of **1** (500 mg, 0.080 mmol) in DMF (10 mL), tert-butylcarbazate (159 mg 1.21 mmol), PyBOP (630 mg, 1.21 mmol), and DIPEA (1.11 mL, 6.4 mmol (8 eq)) were added and stirred at room temperature overnight under argon atmosphere. The solvent was evaporated in vacuo, then resulting residue was purified by flash column chromatography on silica gel (eluent EtOAc/Hepane 50:50) to give desired product as a colorless solid (365 mg, yield 62%). ¹H NMR (400 MHz, CDCl₃) δ ppm 8.14 (1H, bs), 6.36 (1H, bs), 3.29 (2H, t), 3.21 (2H, t), 2.68 (2H, t), 2.58 (2H, t), 1.53 (13H, bs), 1.20 (60H, bs), 0.88 (6H, t). MS for [C₄₅H₈₉N₃O₄+H⁺]⁺ m/z (M+1) calc. 736.69, found 736.69.

Compound 3 (LipoHD). To the solution of **2** (350 mg, 0.48 mmol) in DCM (10 mL), TFA (10 mL) and 2 drops of MiliQ water were added and stirred at room temperature for 2 h. After confirming the reaction completely proceeded with TLC, the solvents were evaporated under reduced pressure, and then the residue was dissolved in MeOH and evaporated 3 times to remove TFA and give desired product **3** as a colorless solid (362 mg). ¹H NMR (400 MHz, CDCl₃) δ ppm 7.77 (1H, bs), 3.27 (2H, t), 3.16 (2H, t), 2.65 (2H, t), 2.49 (2H, t), 1.50 (4H, bd), 1.24 (60H, bs), 0.84 (6H, t). MS for Chemical Formula: [C₄₀H₈₁N₃O₂+H] m/z (M+1) calc. 636.63, found 636.63.

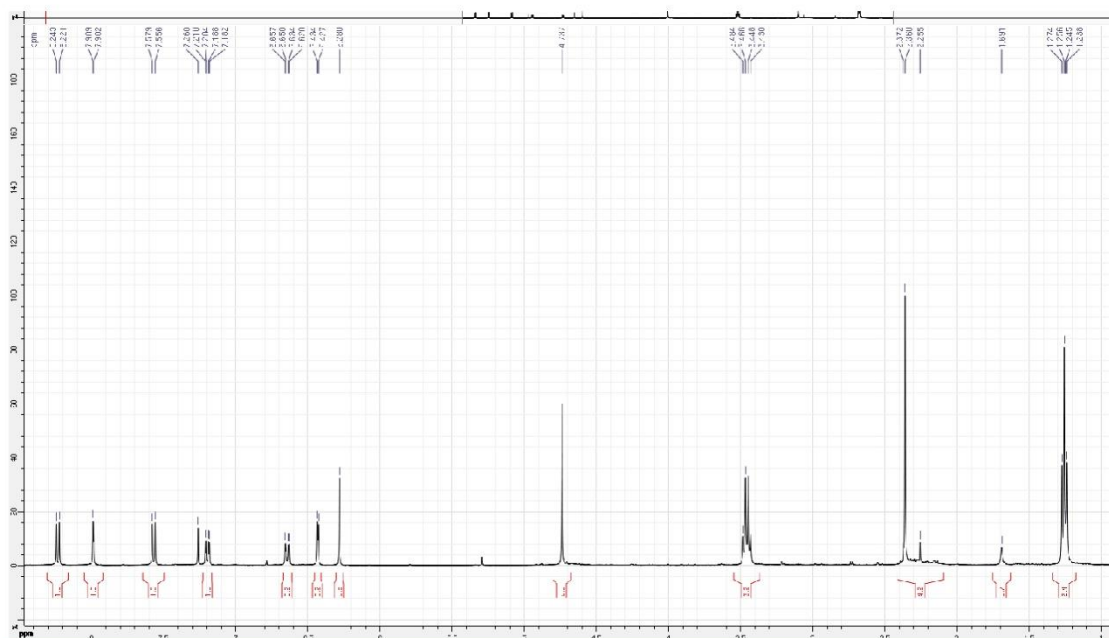


Scheme S2. Synthesis of Lipo-NRK

Compound 4 (NRK). To the solution of 2-hydroxy-Nile Red (150 mg, 0.45 mmol), potassium carbonate (310 mg, 2.24), catalytic amount of potassium iodide in DMF (10 mL), (159 mg 1.21 mmol), chloroacetone (160 μ L, 2.24 mmol) was added and stirred at 100 °C for 3 h under argon atmosphere. The solvent was evaporated in vacuo, then resulting residue was washed by brine. The organic layer was dried over MgSO_4 , filtered and evaporated in vacuo. The residue was purified by flash column chromatography on silica gel (eluent DCM/MeOH = 98:2) to give desired product as a violet solid (132 g, yield 75%). ^1H NMR (500 MHz, CDCl_3) 8.24-8.22 (d, $J=10.4$ Hz, 1H), 7.99-7.96 (d, $J = 3.6$ Hz, 1H), 7.21-7.18 (q, $J=11.6$ Hz, 1H), 6.66-6.63 (q, $J=10.8$ Hz, 1H), 6.43-6.42 (d, $J=2.8$ Hz, 1H), 6.28 (s, 1H), 4.74 (s, 1H), 3.46-3.43 (q, $J=24.3$ Hz, 4 H), 2.36 (s, 3 H), 1.27-1.24 (t, $J=13.9$ Hz, 6H). MS(ESI+) calcd for $\text{C}_{23}\text{H}_{22}\text{N}_2\text{O}_4\text{H}$ (M+H) $^+$; 391.164 observed.

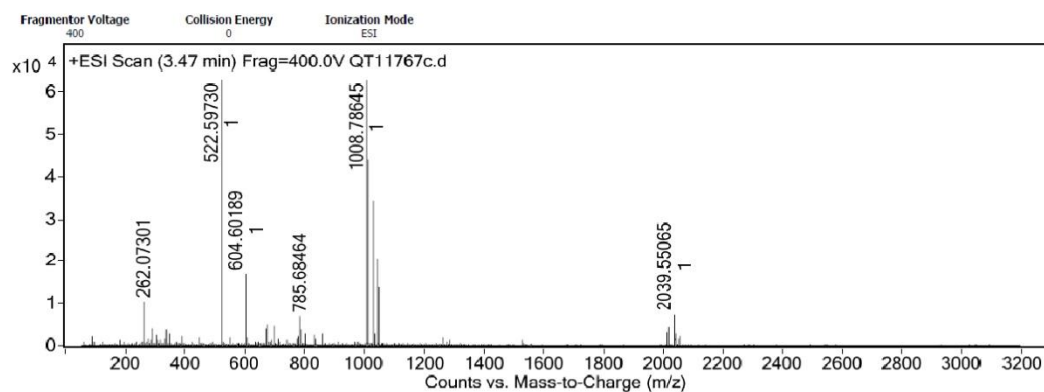


Mass spectrum of NRK.

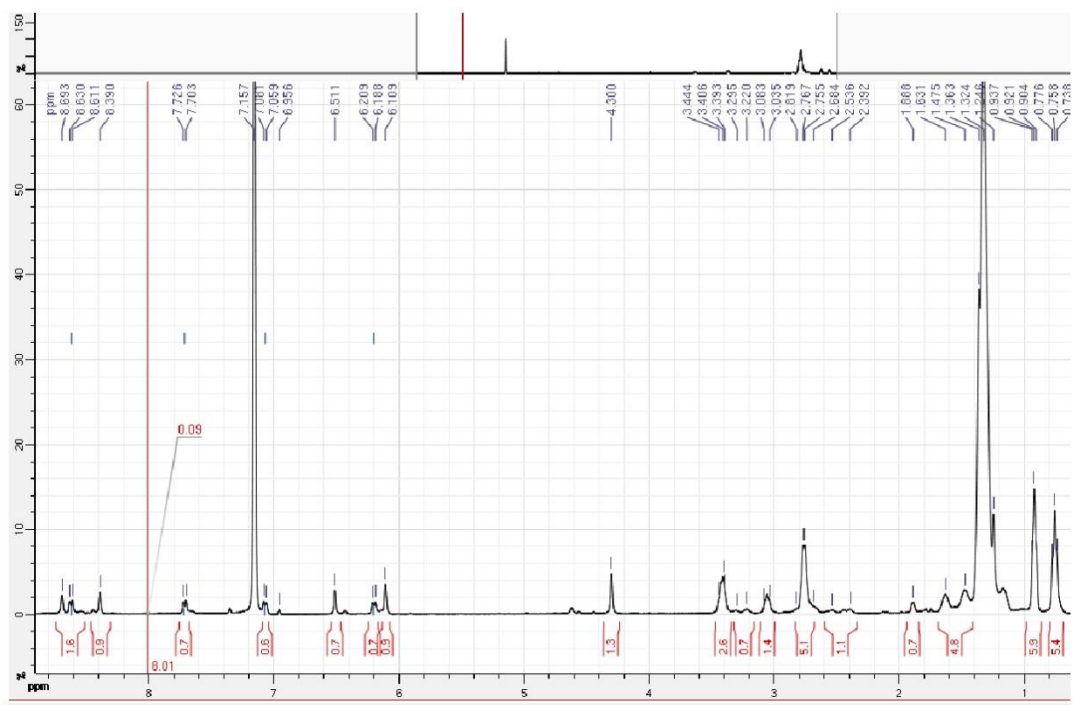


^1H -NMR spectrum of **NRK**.

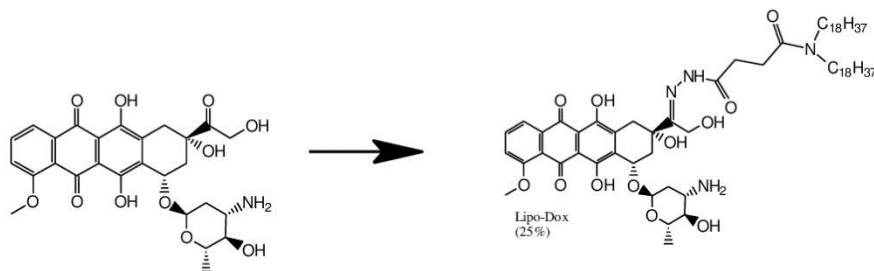
Lipo-NRK. To the solution of **LipoHD** (30 mg, 0.077 mmol), in EtOH (2 mL), **NRK** (115 mg 0.15 mmol), triethylamine (22 μL , 0.15 mmol) was added and refluxed for 3 h under argon atmosphere. The solvent was evaporated in vacuo, then resulting residue was purified by puri-flash HPLC (eluent DCM/MeOH = 98:2 to 96:4) to give desired product as a violet solid (50 mg, yield 65%). ^1H NMR (500 MHz, CDCl_3) 8.69 (s, 1H), 8.63 (d, $J = 7.0$ Hz, 1H), 8.39 (s, 1H), 7.73-7.70 (d, $J = 8.1$ Hz, 1H), 7.08-7.06 (d, $J = 9.3$ Hz, 1H), 6.51 (s, 1 H), 6.20-6.19 (d, $J = 8.1$ Hz, 1H), 6.10 (s, 1H), 4.3 (s, 1H), 3.44 – 3.39 (m, $J = 29.1$ Hz, 3H), 3.30-3.22 (m, $J = 33.7$ Hz, 1H), 3.08-3.04 (m, $J = 19.8$ Hz, 2H), 2.82 – 2.68 (q, $J = 47.7$ Hz, 5H), 2.54-2.39 (m, $J = 57.0$ Hz, 1H), 1.89 (s, 1H), 1.63-1.48 (m, $J = 67.5$ Hz, 4 H), 0.94-0.90 (t, $J = 12.8$ Hz, 6H), 0.78-0.74 (t, $J = 12.4$ Hz, 6H), 1.36-1.25 (m, $J = 47.7$ Hz, 63 H). MS(ESI+) calcd for 1009 $\text{C}_{63}\text{H}_{101}\text{N}_5\text{O}_5\text{H}$ (M+H) $^+$; 1008.79 observed, 1008.78 cal.



Mass spectrum of **Lipo-NRK**.



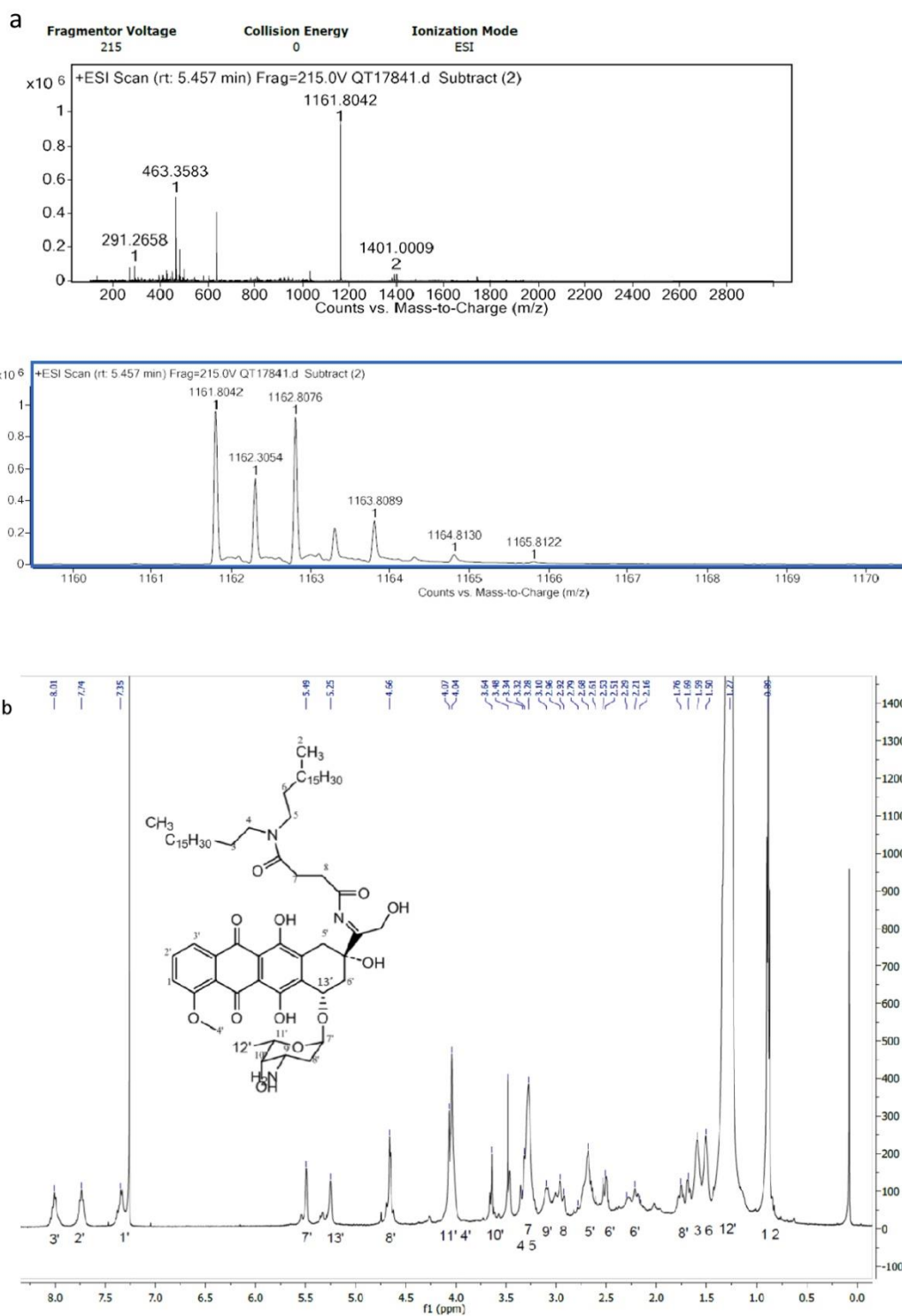
H-NMR spectrum of **Lipo-NRK**.

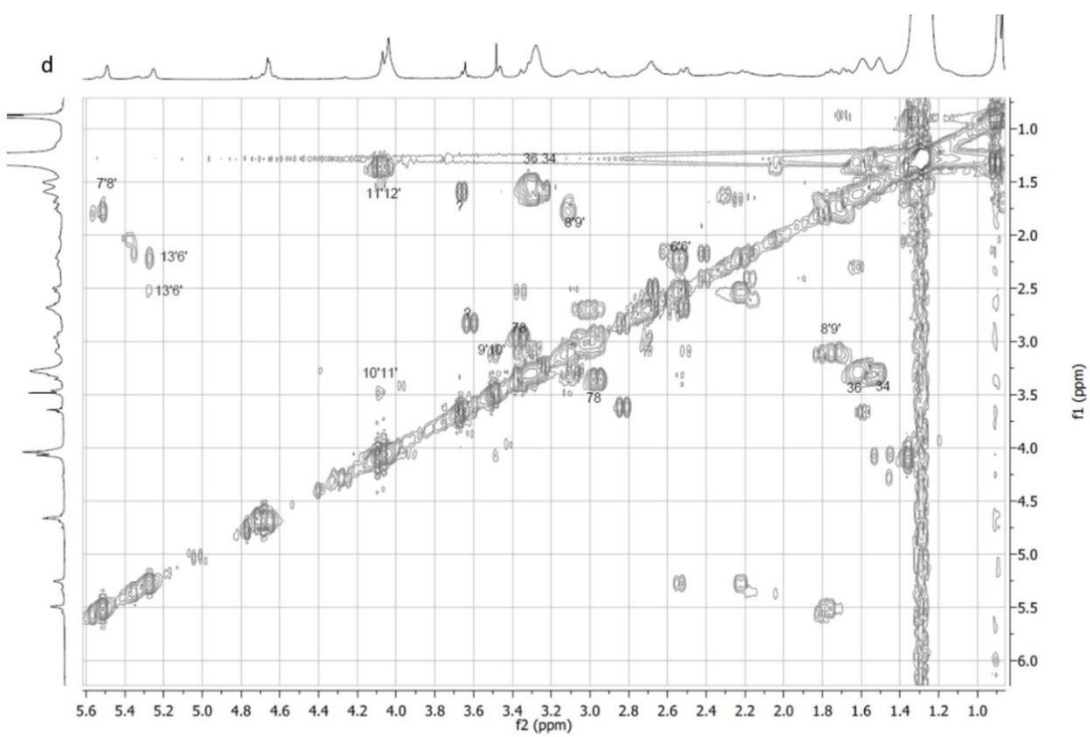
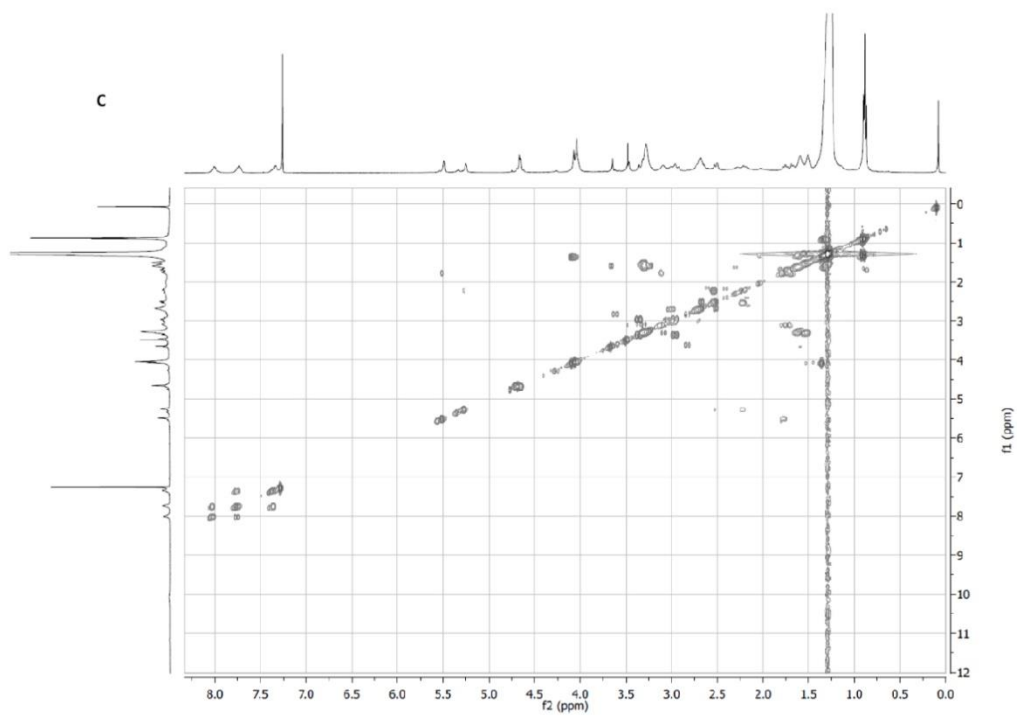


Scheme S3. Synthesis of **Lipo-Dox**.

Lipo-Dox. To the solution of doxorubicin/hydrochloride (Dox, 40 mg, 0.069 mmol), in MeOH (45 mL) and DCM (5 mL), **LipoHD** (57 mg 0.09 mmol), TFA (50 μ L) was added and stirred overnight under argon atmosphere. The solvent was evaporated in vacuo, then resulting residue was purified by flash column chromatography on silica gel (eluent DCM/MeOH/triethylamine = 85:14: 1) to give desired product as a red solid (45 mg, yield 25%). ^1H NMR (500 MHz, CDCl_3) 8.01 (m, $J = 8.0$ Hz, 1H), 7.74 (m, $J = 7.7$ Hz, 1H), 7.35 (m, $J = 7.4$ Hz, 1H), 5.49 (s, 1H), 5.26 (s, 1H), 4.75 - 4.57 (m, $J = 4.7$ Hz, 2H), 4.05 (d, $J = 4.1$ Hz, 4H), 3.48 (s, 1H), 3.38 - 3.18 (m, $J = 3.3$ Hz, 6H), 3.18 - 2.89 (m, $J = 3.0$ Hz, 3H), 2.79 - 2.61 (m, $J = 2.7$ Hz, 2H), 2.52 (d, $J = 2.52$ Hz, 1H), 2.37 - 2.12 (m, $J = 2.2$ Hz, 1H), 1.81 - 1.64 (m, $J = 1.7$ Hz, 2H), 1.55 (d, $J = 1.6$ Hz, 4H), 1.27 (s, 63 H), 0.89 (t, $J = 0.9$ Hz, 6H). MS (ESI+) calcd for $\text{C}_{87}\text{H}_{110}\text{N}_4\text{O}_{13}\text{H}$ ($\text{M}+\text{H}^+$): 1162; observed: 1161.8.

The compound was characterized by ^1H -NMR and COSY spectrum. The carbon spectrum was difficult to obtain for the reason of compound aggregation at higher concentrations. As shown in the FT-IR spectrum, the peak at 1730 cm^{-1} which represented the presence of ketone disappeared in the spectrum of Lipo-Dox. The intensity of peaks at 2896 cm^{-1} increased in comparing to that of Dox. This resulted from the long alkyl chains of Lipo-Dox. Peaks observed in Dox around 3312 cm^{-1} came from the moisture within the commercially available Dox. This peak disappeared in the synthesized Lipo-Dox, this showed the dryness of Lipo-Dox obtained, which is for stability of Lipo-Dox, sensitive to hydrolysis.





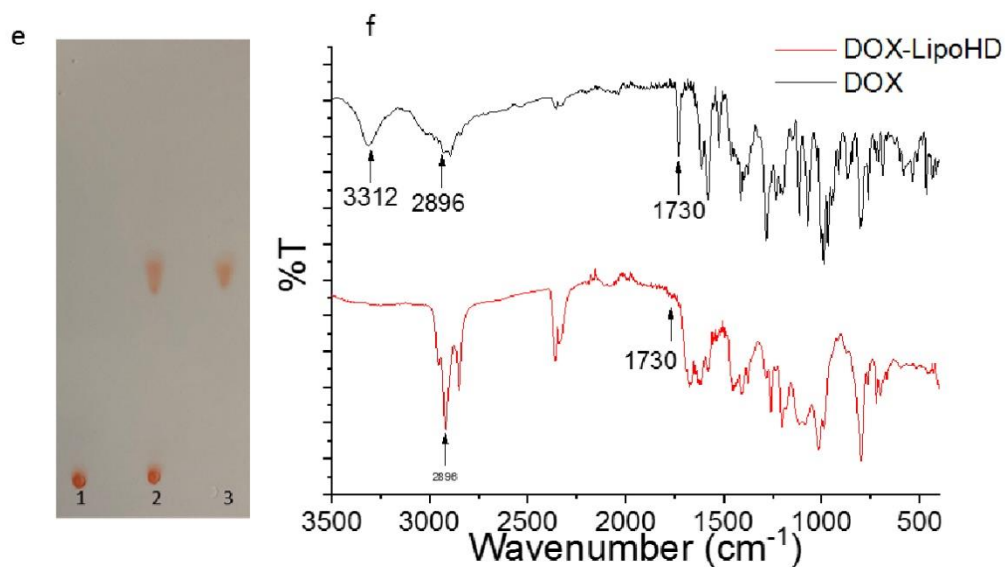


Figure S17. Identification of Lipo-Dox (a) Mass spectrum; (b) ^1H -NMR spectrum; (c) Full spectrum of COSY; (d) COSY spectrum characterization in zoomed areas of interest; (e) TLC after Lipo-Dox purification. 1. Free Dox; 2. Mixture of free Dox and purified Lipo-Dox; 3. Purified Lipo-Dox; (f) FT-IR of Dox and Lipo-Dox.

References

- [1] A. S. Klymchenko, E. Roger, N. Anton, H. Anton, I. Shulov, J. Vermot, Y. Mely, T. F. Vandamme, *RSC Adv.* **2012**, 2, 11876.

2.2- Functional nanoemulsion based on reversible imine bonds for controlled cargo delivery and capture (Article 2 – manuscript)

Based on the success of the previous drug sponge system using LipoHD-loaded nanoemulsion, we started to look for possibilities to extend this technology to more biocompatible dynamic covalent bonds. The imine is also a reversible covalent bond that is liable in an acidic environment. However, its chemical formation is difficult because it is highly sensitive to moisture and the product is expected to degrade during purification. This inspired us to use the above-mentioned nanoemulsion nano-reactor to provide a hydrophobic oil core environment for the imine formation. In the previous study, FRET was used as a powerful tool to study the reversible *in situ* reaction process. Here, we looked for an alternative method where imine bond formation switches the emission color of a model fluorescent dye.

The objective of this study was to develop a dual-functional nano-carrier system based on dynamic imine bonds with pH sensitivity for drug release and with the ability to uptake hydrophilic toxic aldehyde. Similar to the first project, a lipophilic reactive capture molecule bearing two long alkyl chains and an amine group (LipoAmine) was synthesized and encapsulated inside for the functionalization of nanoemulsion (Figure 2.3).

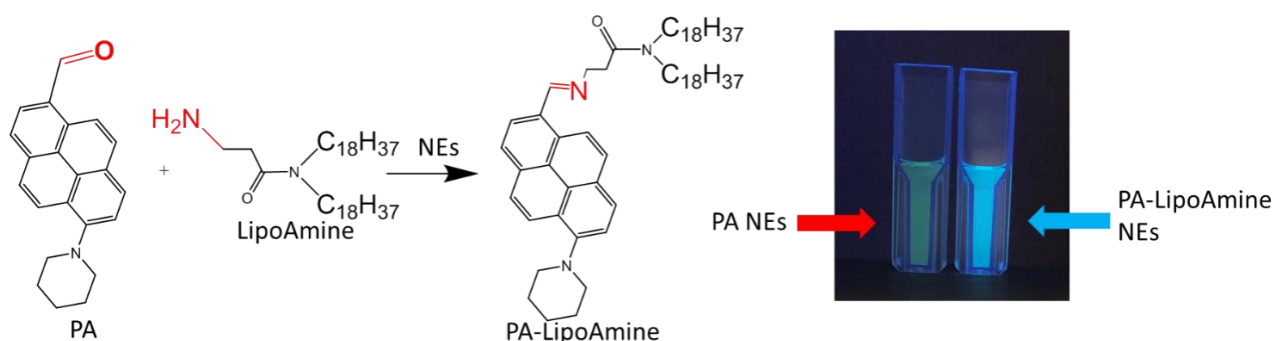


Figure 2.3. Formation of PA-LipoAmine and change of emission wavelength of NEs with (LipoAmine NEs) and without (Empty NEs) mixed with PA reacted after 2 hours, observed under UV lamp (excitation wavelength 365 nm).

For the model study, we started by using fluorescent dye bearing aromatic aldehyde group (PA) as a model compound for the examination of the imine bond formation, since there is a blue shift resulting from the change in the push-pull dye system after the formation of imine bond ^[361]. We found that this system worked for the formation of the imine bond as indicated by the emission spectra (Figure 2.4).

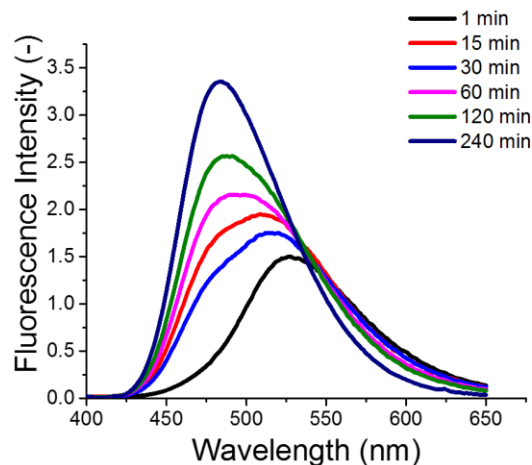


Figure 2.4. Emission scan under excitation wavelength of 380 nm for the monitoring of *in situ* formation of LipoAmine-PA conjugate at different time points.

Afterward, to prove the formation of this bond, we reduced imine to a stable amine and extracted the produced PA conjugate into the organic phase. After the extraction, we successfully identified the reduced compound by TLC mass spectrometry. The pH-controlled release in cells experiments showed that the imine bond containing nanoemulsion was stable at neutral pH, while released PA cargo under an acidic environment. The functional NEs also showed the capability to extract PA from pre-stained cells and chicken skin surfaces (Figure 2.5). Next, we successfully applied the functional NEs to extract toxic aldehydes (4-hydroxynonenal) from the cells, showing the first proof of concept for cell detoxification.

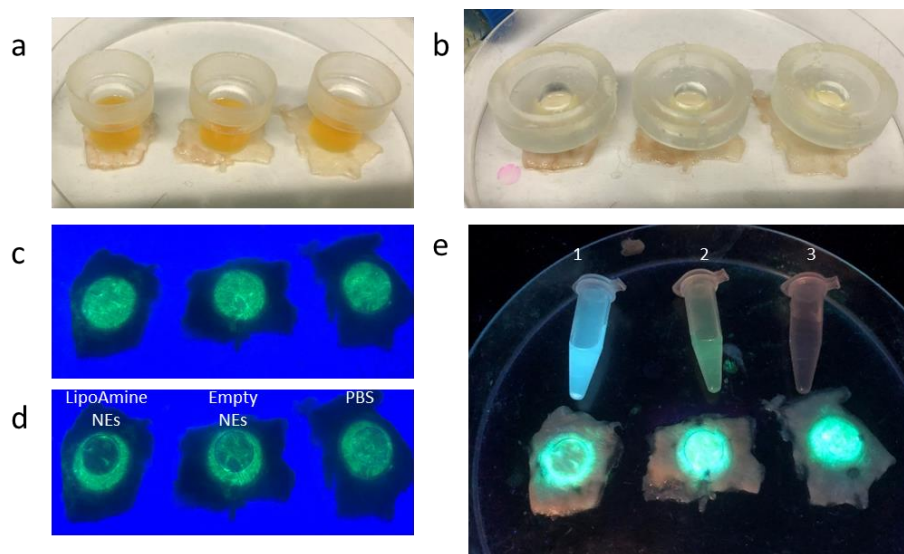


Figure 2.5. Illustration of PA loading to (a) and *in situ* extraction from (b) skin surface. The skin fluorescence images after PA loading (c) and extraction (d) under UV lamp excitation wavelength of 254 nm. (e) Fluorescence from different extraction media under excitation of 365 nm (with extraction medium from 1. LipoAmine NEs; 2. NEs; 3. PBS).

Article 2 – Manuscript

Capture and release of aldehydes in cells and tissues by dynamic covalent chemistry in nanoemulsions

Fei Liu,^{1,2} Nicolas Anton,² Yosuke Niko,³ and Andrey Klymchenko^{1,*}

¹Université de Strasbourg, Laboratoire de Bioimagerie et Pathologies, UMR 7021 CNRS, 74 route du Rhin, 67401 Illkirch (France)

²INSERM UMR 1260, Regenerative Nanomedicine (RNM), FMTS, CNRS 7199, CAMB, Université de Strasbourg, 67000 Strasbourg (France)

³Research and Education Faculty, Multidisciplinary Science Cluster, Interdisciplinary Science Unit, Kochi University, 2-5-1, Akebono-cho, Kochi-shi, Kochi, 780-8520 (Japan)

* Corresponding author: E-mail: andrey.klymchenko@unistra.fr

Abstract

Currently, biomedical applications of nanocarriers are focused on drug delivery, where encapsulated cargo is released in the target tissues under control of external stimuli. Here, we propose a very different approach, where the active toxic molecules are removed from biological tissues by the nanocarrier. It is based on the drug-sponge concept, where specific molecules are captured by the lipid nanoemulsion droplets due to dynamic covalent chemistry inside their oil core. To this end, we designed a highly lipophilic amine (LipoAmine) capable to react with a free cargo-aldehyde (fluorescent dye and 4-hydroxynonenal toxin) directly inside lipid NEs, yielding lipophilic imine conjugate well encapsulated in the oil core. The formation of imine bond was first validated using a push-pull pyrene aldehyde dye, which changes its emission color during the reaction. The conjugate formation was independently confirmed by mass spectrometry. As a result, LipoAmine-loaded nanoemulsions (NEs) spontaneously loaded cargo-aldehydes, yielding formulations stable against leakage at pH 7.4, which can further release the cargo at low pH range (4-6) in solutions and living cells. Using fluorescence microscopy, we showed that LipoAmine NEs can extract pyrene aldehyde dye from cells as well as from an epithelial tissue (chicken skin). Moreover, successful extraction from cells was also achieved for a highly toxic aliphatic aldehyde 4-hydroxynonenal, which allowed to obtain the proof of concept for detoxication of living cells. Taken together, these results show that the dynamic imine chemistry inside NEs can be used to develop detoxication platforms.

1. Introduction

Traditional biological application of nanoparticles is drug delivery, with the concept of “magic bullet” that ensures specific targeting and local release of drug at a diseased site in the body with a simultaneous reduction of toxic effects towards non-targeted normal tissues.^{1, 2} Ideally, to meet this standard, smartly designed drug delivery system should release the drug in response to the physiological stimuli in the body.³ One of the most popular stimuli in the field of controlled drug

delivery is pH, since tumor microenvironment, inflammatory sites⁴ and bacterial infections tissues⁵ have slightly more acidic pH values than physiological media and healthy tissue. To this end, various pH-responsive drug delivery vehicles have been prepared from different pH-responsive chemical functionalities, including hydrazone^{6, 7} acetal,^{1, 8} ortho ester,^{9, 10} imine^{11, 12} and vinyl ether.^{13, 14}

On the other hand, a largely underexplored direction in bio-nanotechnology is to design of nanomaterials capable to uptake toxic molecules and drugs from biological tissues. Indeed, high surface to volume ratio and presence and/or presence of reaction nano-reservoir inside NPs core could enable extraction of toxic species from biological specimen or medium and their further accumulation in the NPs. Among rare examples in literature, one should mention cross-linked cationic surfactant NPs (micelle_ENREF_4) in combination with dialysis membrane, capable of removing anionic species found in natural water for de-pollution.¹⁵ The silica-containing redox NPs were designed for scavenging reactive oxygen species with help of peritoneal dialysis.¹⁶ The lack of examples in literature can be probably explained by difficulty to capture specific molecules within the multitude of other species present in biological fluids. In this respect, capturing aldehydes is of particular interest, because they are naturally present in small concentrations. An example is 4-hydroxynonenal (4HN), which has a significant importance since it is associated with numerous diseases, such as chronic inflammation, neurodegenerative diseases, adult respiratory distress syndrome, atherogenesis, diabetes and different types of cancer.¹⁷

An original approach to capture toxic molecules including aldehydes is to use lipid nano-emulsion droplets composed of oil core stabilized by a surfactant. Their oil core can serve as reservoir, to encapsulate hydrophobic species. NEs are highly promising for biomedical applications because they are (1) inexpensive and easy to produce; (2) composed of excipients generally recognized as safe (GRAS) and/or FDA approved and (3) biodegradable.¹⁸⁻²² In addition, NEs are highly stable in biological media like serum and *in vivo* in blood circulation.^{23, 24} However, encapsulation in NEs is efficient only for lipophilic molecules with low water solubility, whereas partially water soluble compounds undergo a fast leakage from droplets in presence of acceptor media.²⁵ Accordingly, a strategy to enhance stability of encapsulated NEs is their functionalization with lipophilic groups.^{25, 26} Therefore, we hypothesized that efficient uptake in NEs, of the toxic molecules like aldehydes, could be done through *in situ* reaction of the aldehyde with a highly lipophilic molecule, with the objective to generate *in situ*, a stable highly lipophilic conjugate. For this purpose, one could exploit dynamic covalent chemistry, which deals with dynamic bonds that form and disrupt reversibly under environmental control.²⁷⁻²⁹ Dynamic covalent chemistry was successfully applied for designing intelligent materials with self-healing and adaptive properties.³⁰⁻³² Dynamic covalent bonds are particularly attractive for the field of drug delivery, because these bonds can be broken under environment stimuli providing controlled drug release.³³ The most popular dynamic covalent bonds include hydrazone,³⁴ oxime,³⁵ imine,^{36, 37} disulfide,³⁸ boronate ester³⁹ etc. Recently, we have shown that lipophilic hydrazide LipoHD encapsulated inside NEs can form *in situ* dynamic hydrazone bonds with ketones, which ensure efficient capture of model cargo dye NRK and ketone drug doxorubicin.⁴⁰ This approach showed a unique possibility to remove molecules bearing ketone group from cells and tissues. However, hydrazine derivatives are limited by their toxicity, which makes this system incompatible with detoxication applications

in living systems. In this respect, dynamic imine bonds⁴¹ appear as attractive alternative to hydrazones, because it would exploit amines, which are much less toxic than hydrazine derivatives.

In the present work, we explored a possibility to capture aldehyde molecules by *in situ* formation of dynamic imine bonds with lipophilic amine inside oil core of NEs, using amine-based molecule with low toxicity. To this end, we synthesized lipophilic amine LipoAmine and studied its reactivity with different aldehydes inside NEs. A push-pull pyrene dye (PA) reported by us⁴² was selected as a model aldehyde, because of its high fluorescence brightness suitable for cell imaging and presence of the aldehyde group in the fluorophore. In this push-pull dye, the modification of the aldehyde group with an imine should alter electronic configuration of the dye and thus its fluorescence properties, making the reaction observable.⁴³ We found that the dynamic imine bond between PA and LipoAmine inside NEs can be formed *in situ* inside NEs, which leads to significant change in the emission color of the dye. The stability of this bond can be altered by low pH, leading to control release of the dye into medium and cells. Even more importantly, we showed that LipoAmine-loaded NEs can effectively capture PA aldehyde from cells and tissues. Moreover, LipoAmine NEs were able to extract a highly toxic aldehyde 4HN, increasing cell survival, which provided a proof of concept of the detoxication by NEs.

2. Results and discussion

2.1. Principle and task in the present work

In our design, lipophilic amine encapsulated inside oil core of NEs is expected to form dynamic imine bonds with an aldehyde, which would produce lipophilic conjugate and thus effective aldehyde capture. To this end, we designed a lipophilic amine LipoAmine, bearing a primary amino group and two octadecyl alkyl chains. As model aldehyde, we selected reported push-pull pyrene dye PA.⁴² Its electron acceptor aldehyde group is expected to drastically change optical properties of the dye on formation of dynamic imine bond with amines (Fig. 1). The latter would allow us to monitor formation of the dynamic covalent bond. On the other hand, due to the pH sensitivity of the imine bond, the formed conjugate is supposed to be cleaved under low pH, thus releasing the native cargo.

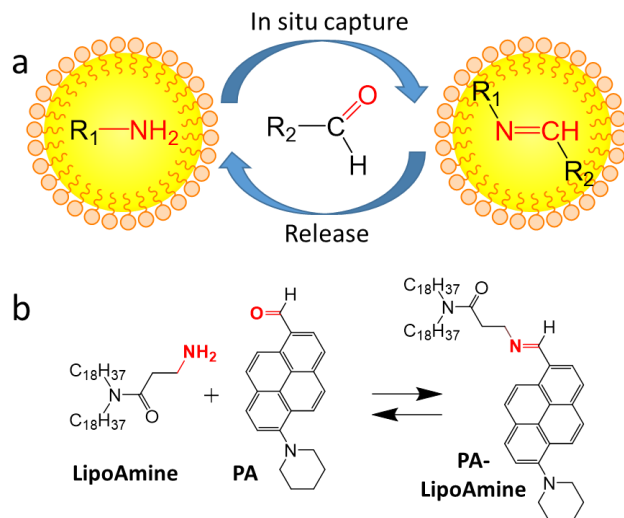


Fig. 1. (a) Scheme of *in situ* dynamic imine bond formation inside NEs for in situ capture and release of aldehydes. (b) Chemical reaction between LipoAmine and PA aldehyde.

2.2. *In situ* formation of PA-LipoAmine conjugate

We explored NEs as a nano-reactor for the *in situ* imine formation. As it could be observed in the excitation (Fig. 2a) and emission spectra (Fig. 2b, c), PA dye in the presence of NEs loaded with LipoAmine showed a blue shift of ~25 nm in the absorption and 50 nm in the emission spectrum. Thus, the *in situ* reaction can be monitored by emission spectra. As it could be observed in Fig. S1, the emission spectrum blue shifted gradually over time and stabilized after 4 h of reaction at 40 °C, indicating the completion of the reaction. The blue shift was accompanied by the increase in the fluorescence intensity. However, when excited at 420 nm, the blue shifted band was less intense, because at 420 nm, the excitation of the newly formed conjugate is less efficient than at 380 nm, in line with the corresponding excitation spectra (Fig. 2a).

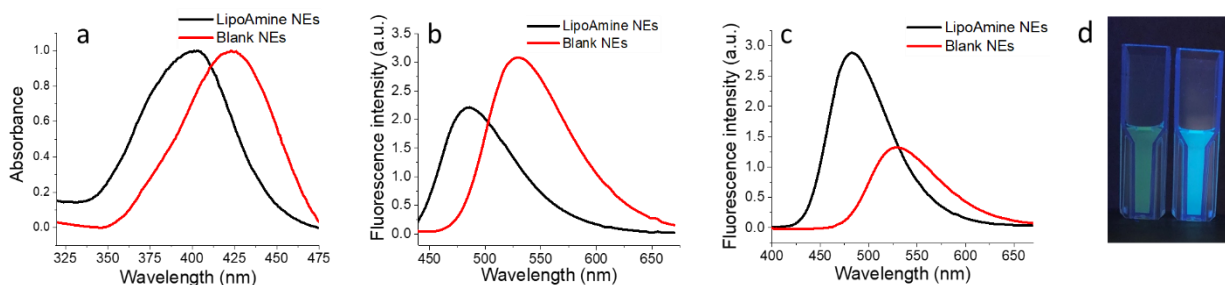


Fig. 2. Spectroscopic study of LipoAmine NEs mixed with PA versus blank NEs (without LipoAmine) mixed with PA, after 4 h incubation at rt. Normalized absorption spectra (a) and emission spectra at excitation wavelength of 420 nm (b) and 380 nm (c). (d) Change in the emission color of NEs without LipoAmine (left) and with (right) mixed with PA reacted after 4 h at rt and photographed under UV lamp (excitation wavelength 365 nm).

In order to verify the formation of PA-LipoAmine conjugate, the extraction by dichloromethane of the reaction mixture was performed (with or without reduction by NaBH_4) and followed by a thin layer chromatography (TLC) (Fig. 3a). According to TLC, compound isolated from the reaction mixture (yellow spot, sample 1) without NaBH_4 showed the same R_f value as its control without LipoAmine (yellow spot, sample 2). However, in the presence of NaBH_4 , which is expected to reduce imine bond to a stable amine, a novel blue spot (sample 3) was observed, characterized by higher R_f compared to its control without LipoAmine (sample 4, Fig. 3b). One should note that change in the color of PA in the control samples with NaBH_4 is probably linked to a reduction of the PA aldehyde into an alcohol. The observed much higher R_f in the presence of LipoAmine supports the formation of highly lipophilic conjugate. This blue spot (circled in red) was then isolated from TLC and studied by mass spectrometry. We found that this new spot corresponded to the molecular weight of reduced PA-LipoAmine conjugate (calculated molecular weight: 889.78 g/mol; observed 889.73 g/mol). These experiments suggested that PA-LipoAmine conjugate was formed *in situ* inside the oil core, but it was hydrolyzed during the extraction process due to the instability of imine bond yielding starting material PA dye. After reduction of this imine by NaBH_4 into more stable amine, it was possible to identify the conjugate.

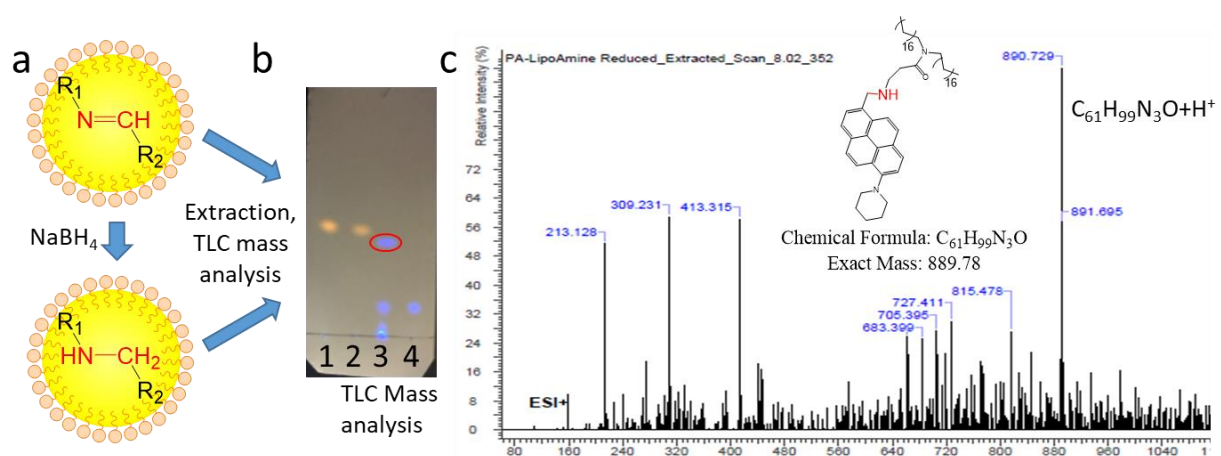


Fig. 3. (a) Scheme of PA-LipoAmine NEs reduction by NaBH_4 and extraction process (by dichloromethane) for TLC mass analysis. (b) Photographed TLC plate (under excitation of UV lamp at 360 nm) of the extraction from (1) PA + LipoAmine NEs, (2) PA + blank NEs, (3) PA + LipoAmine NEs after the reduction and (4) PA + NEs after the reduction. (c) Chemical structure and theoretical molecular weight of reduced PA-LipoAmine and TLC mass examination of the new TLC spot (red mark) from the reduced reaction mixture of PA + LipoAmine NEs.

2.3. Size characterization of NEs

We compared sizes and polydispersity of different formulations used in this study. As shown in Table S1, the presence of PA-LipoAmine or LipoAmine inside NEs did not have a significant impact on the size of NEs, with the sizes 69.0 and 70.3 nm, respectively, close to blank NEs (73 nm). Some increase in the size was observed for control sample with PA added to blank NEs (without LipoAmine). Overall, the absence of the effect of LipoAmine on NEs size and

polydispersity suggests that the formulation process is not affected and LipoAmine do not interfere with interfacial properties. This highly lipophilic molecule is probably well encapsulated inside NEs oil core without affecting the NEs formulation process and its colloidal stability.

2.4. pH controlled release of PA-LipoAmine

A fundamental aspect of using dynamic imine bonds is the reversibility of the loading process in order to allow a controlled release of the native cargo. Based on the pH-sensitivity of imine bond, PA-LipoAmine loaded NEs could enable controlled release PA. As the formation of PA-LipoAmine conjugate changed the emission color of PA, pH-controlled release of PA due to imine bond disruption was also monitored with fluorescence spectroscopy. A 10-fold excess of blank NEs were added, as an acceptor medium in the PA-LipoAmine NEs suspension. The results were reported in Fig. 4, in which decreasing the pH to values equal to 6 and 4 (for Fig. 4.b and Fig. 4.c, respectively) led to a red shift of PA emission spectra, suggesting cleavage of the imine bond. Control studied under neutral pH did not show any spectra shift of the emission band, confirming the stability of the PA-LipoAmine inside NEs (Fig 4. a). Importantly, the release of model dye already occurred after slight pH decrease from 7.4 to 6, (Fig 4.c), characteristic for some tumor microenvironment.⁴⁴ Then, the release accelerated at lower pH, equal to 4 (Fig 4.c), so that PA release was nearly completed after 15 min.

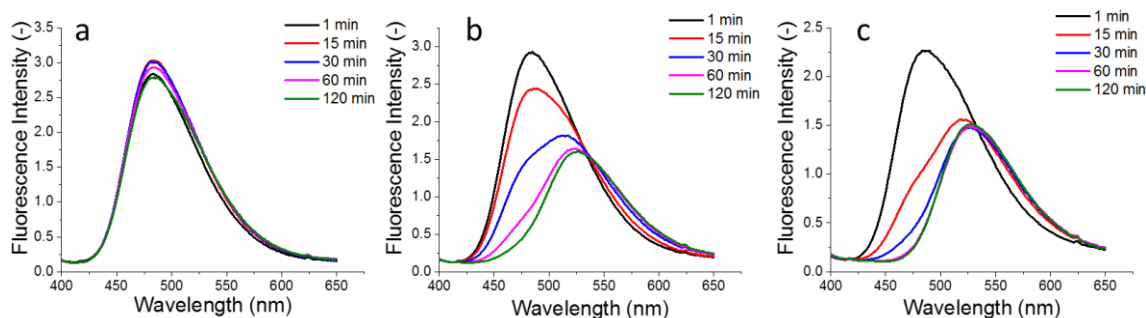


Fig. 4. pH-controlled release of PA from PA-LipoAmine NEs in the presence of 10-fold excess of blank NEs. Emission spectra under excitation wavelength of 380 nm at different pH: (a) pH 7.4, (b) pH 6 and (c) pH 4. The spectra were corrected from the blank NEs to remove of the effects of the light scattering.

In order to explore the potential of this functional NEs for controlled delivery in contact with living cells, experiments were conducted with PA-LipoAmine loaded NEs, incubated with HeLa cells, at neutral and low pH. The cellular PA fluorescence intensity could be used to detect PA released into cells. As shown in Fig. 5, intracellular fluorescence was readily detected after 5 min incubation with free PA under both neutral and acidic pH, suggesting that PA can easily penetrate the cells. The incubation of cells the PA-LipoAmine NEs in neutral conditions showed relatively low fluorescence even after 30 min. Trace of signal could be related to NEs internalization, in line with previous data.⁴² Importantly, at pH 6, after 30 min incubation, a dramatic increase of the PA emission was observed inside the cells. This observation is confirmed

by a quantitative analysis of the images (Fig. 5b). These results suggest that lipophilic NEs loaded with PA-LipoAmine conjugate inside oil core are stable at neutral pH, and release PA cargo at slightly lower pH.

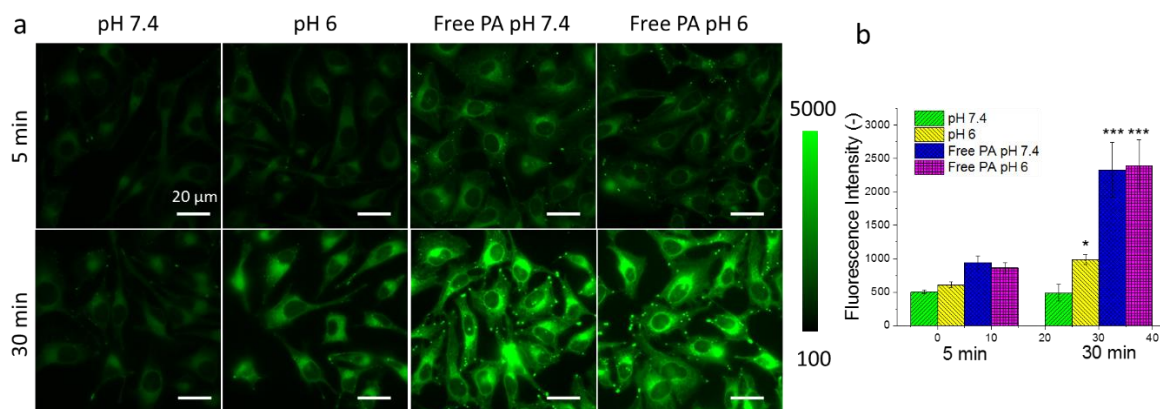


Fig. 5. pH-dependent release of PA from NEs in HeLa cells. (a) Fluorescence images of cells incubated for 5 and 30 min with PA-LipoAmine NEs at pH 7.4 and 6 and with the same concentration of free PA (at pH 6 and 7.4), under excitation at 470 nm. (b) Mean fluorescence intensity of 10 cells. Statistical analysis (vs. data same condition, 5 min): $p < 0.1$ (*), $p < 0.001$ (***).

2.5. *In situ* cellular uptake of PA by LipoAmine-loaded NEs

The capacity of LipoAmine NEs to spontaneously accumulate PA opens a possibility to develop a system for capturing toxic aldehydes in biological environments. To explore this application, PA was used as a model of the aldehyde for administrated into HeLa cells. Then, they are incubated with LipoAmine NEs (blank NEs or PBS as controls) with an objective perform PA extraction from the cells. As reported in Fig. 6, after 30 min of incubation with LipoAmine NEs, drastic decrease in the fluorescence intensity of PA, by ~7-fold, was observed. In contrast, only 1.4-fold drop in the fluorescence intensity was induced after incubation with blank NEs, and nearly no changes were observed for the control with PBS. This tendency could also be observed in the videos (enclosed as Supplementary material) that showed a rapid fluorescence decrease after the application of LipoAmine NEs, compared to the control blank NEs and PBS. In addition, the presence of PA inside cells induced a phototoxicity, which was higher for blank NEs and PBS compared to LipoAmine NEs, as identified by the shrinking of the cells, followed by formation of bubbles at the cell membrane in the first two cases (Fig. S2). This was the consequence of the prolonged excitation of PA in cells that generated highly toxic singlet oxygen, which was known to produce similar morphological changes in the stressed cells.⁴⁵ On the other hand, this phenomenon did not happen with LipoAmine NEs, likely due to the fast and efficient extraction of PA from the cells, thus providing first demonstration of the detoxication effect by these NEs.

Then, quantification of the PA extraction was done by fluorescence spectroscopy of the extraction media (LipoAmine NEs, blank NEs and PBS) beforehand incubated with HeLa cells (Fig. S3). Standard calibration curves of fluorescence intensity were established for PA alone in

NEs. Due to different spectroscopic properties of PA-LipoAmine conjugate, calibration curves were also done for PA-LipoAmine in NEs. We found that the amounts of extracted PA from cells after 30 min were 220, 20 and 2 pMol, for LipoAmine NEs, blank NEs and PBS, respectively. The estimated total amount of PA uptaken by cells was 270 pmol, which was obtained from comparison of the fluorescence intensity in the extracellular medium before and after cell staining (see details in Fig. S3). Therefore, LipoAmine NEs, NEs and PBS media extracted 81%, 7% and 0.7 % of total PA from the cells, respectively. These results confirmed the microscopy data and the quantitative image analysis.

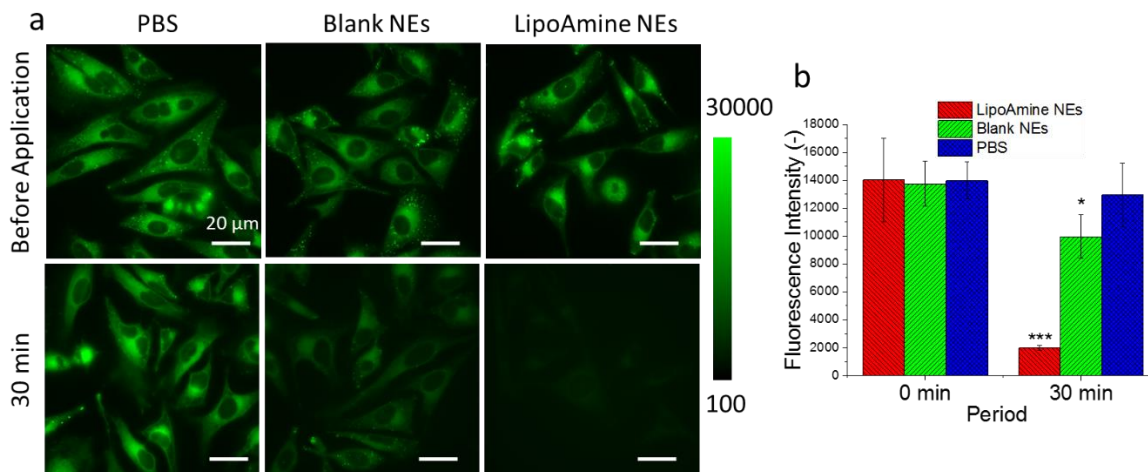


Fig. 6. Extraction of PA from HeLa cells with LipoAmine NEs. (a) Fluorescence images of cells stained with PA, before and after incubation with LipoAmine NEs, blank NEs or PBS for 30 min. Excitation wavelength was 470 nm. NEs were 200-fold diluted from the original formulation. (b) Mean fluorescence intensity of 10 cells selected avoiding border. Statistical analysis (vs. data before application): $p < 0.1$ (*), $p < 0.001$ (***).

2.6. PA *in situ* extraction by LipoAmine NEs from model avian epithelial tissue

Further investigation of the capability of LipoAmine NEs to extract model aldehyde dye, was conducted on model epithelial tissue from avian origin (chicken skin). Transmission microscopy image of the skin showed characteristic morphological features of epidermis tissue, of stratum corneum with specific textures (Fig. 7a). Only faint (negligible) auto-fluorescence was observed in these imaging conditions (Fig. S4). After incubation with PA solution, all tissues gave good fluorescence signal under UV lamp (excitation wavelength of 365 nm) (Fig. S5c) and especially from the texture parts of the tissue (Fig. 6), suggesting PA accumulation. After 3 h incubation with LipoAmine NEs, the PA fluorescence intensity in the skin tissue dropped significantly in the area contacted with the NEs in comparison to that before incubation ($p < 0.001$). In contrast, the fluorescence intensity drop of PA in tissues brought in contact with blank NEs was less significant ($p < 0.01$), whereas almost negligible changes were observed for PBS (Fig. 7 and Fig. S5d). In addition, strong blue shifted fluorescence was observed in the extraction medium from LipoAmine NEs in comparison to that of NEs under UV lamp excitation (Fig. S5e), indicating imine formation and *in situ* formation of PA-LipoAmine conjugate. Thus,

LipoAmine NEs were able to extract aldehyde compound from the skin surface, highlighting the potential of our drug-sponge NEs as a skin detoxication tool.

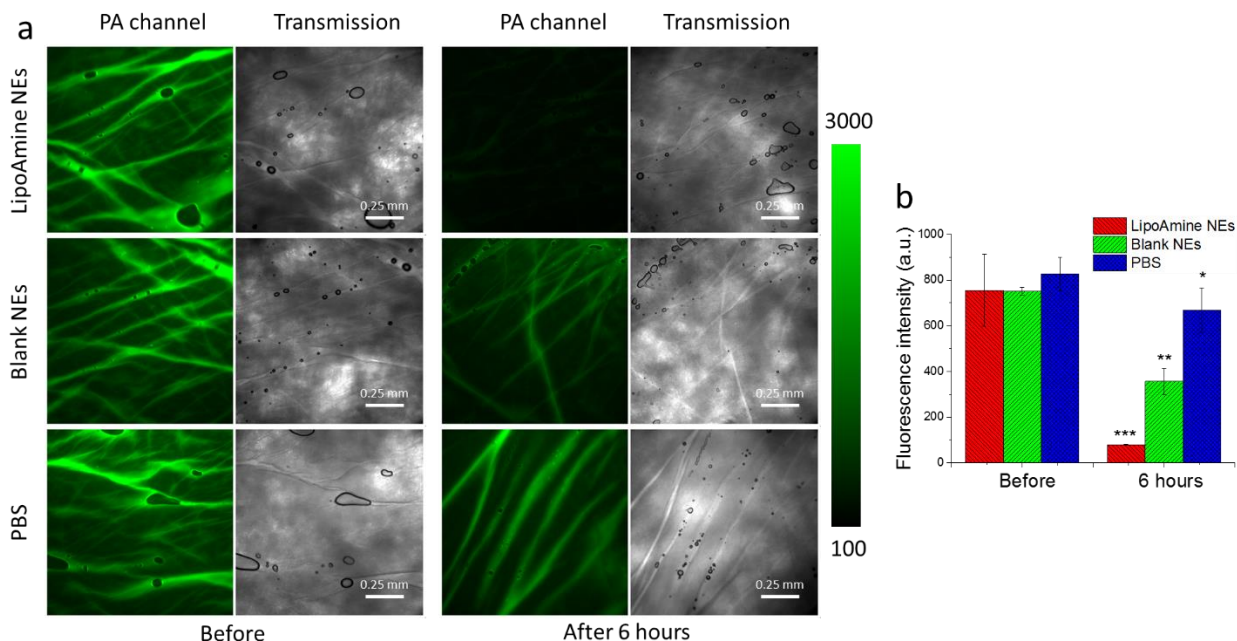


Fig. 7. *In situ* extraction of PA by LipoAmine NEs from epithelial tissue (chicken skin). (a) Transmission (grey) and fluorescence (green) images of *in situ* extraction of model aldehyde compound PA: the skin tissue was pre-incubated with 3 μ M of PA for 30 min and treated for 6 h with LipoAmine NEs, blank NEs or PBS. NEs were 100-fold diluted from the original formulation. Excitation wavelength was 470 nm and the emission filter was 531/40 nm. Scale bar: 250 μ m. (b) Mean fluorescence intensity measured in the center area (3 images analyzed per condition). Statistical analysis (vs. data before application): $p < 0.1$ (*), $p < 0.01$ (**), $p < 0.001$ (***)

2.7. Detoxication of cells from 4-hydroxynonenal by LipoAmine NEs

In order to test the potential of LipoAmine loaded NEs to capture toxic biological aldehydes, 4-hydroxynonenal (4HN) was studied as a drug model. This compound is of significant biological importance, because it is associated with numerous diseases, such as chronic inflammation, neurodegenerative diseases, adult respiratory distress syndrome, atherogenesis, diabetes and different types of cancer.¹⁷ Reports showed that this compound could induce apoptosis, causing around 60% cell death at 20 μ M concentration in human osteosarcoma cell line MG63.⁴⁶ Firstly, *in situ* reaction was conducted between 4HN and LipoAmine inside NEs. The conjugate of 4HN with LipoAmine was successfully identified by mass from the DCM extraction phase of the reaction mixture (Fig. S6), suggesting the potential of using LipoAmine NEs as extraction agent to detoxify cells from 4HN.

Treatment of Hela cells with growing concentrations of 4HN revealed that the latter was cytotoxic, with 55% cell death for 20 μ M of 4HN, consistent with the earlier data on a different cell line (MG63 cell line).⁴⁶ This concentration was then applied to investigate the detoxication potential of LipoAmine NEs at different NEs concentrations. In the absence of 4HN, the viability

of the cells incubated with NEs containing or not LipoAmine (Fig. 8b) was similar, showing that LipoAmine did not have significant impact on the cytotoxicity of NEs. However, both blank NEs and LipoAmine NEs displayed non-negligible cytotoxicity at high concentrations (10% from the original formulation), in line with the earlier studies.⁴⁷ This could be due to the surfactant of NEs, which might cause at high concentrations harmful effect on the cell membranes.

In the presence 4HN, significantly higher cell viability (around 62%) was observed for LipoAmine NEs compared to the blank NEs (around 42 %) at optimal NEs concentration (4% from the formulation). One should note that the detoxification effect of LipoAmine NEs was observed only at concentrations over 4 % of the NEs dilution. We can speculate that at lower concentrations the extraction of 4HN was too weak, while at higher concentrations the detoxication effect was compensated by some cytotoxicity of NEs. Meanwhile, at the highest used concentration of the NEs, cells with and without 4HN showed similar level of cell viability, except for cells incubated with 4HN and blank NEs. The statistical analysis between the individual groups confirmed the detoxification effect of LipoAmine NEs against 4HN (Fig. S8).

Several conditions were selected to demonstrate the detoxication effect by naked eye in a 6-well plate. According to Fig. S7, well number 4 without 4HN showed much darker yellow color compared to the well number 1 with 4HN in PBS, indicating strong cytotoxicity effect of the latter. For blank NEs, the toxicity effect of 4HN was also clearly observed (wells 3 and 6). However, in the presence of 10 % LipoAmine NEs (i.e. 10-fold diluted NEs), the wells showed similar strong yellow color with or without 4HN (wells 2 and 5, respectively). These results are consistent with the quantitate analysis shown above. Our results provide evidence that LipoAmine NEs are able to remove 4HN toxin from cells, which is linked to their capacity to form imine bonds with 4HN inside the oil NEs core.

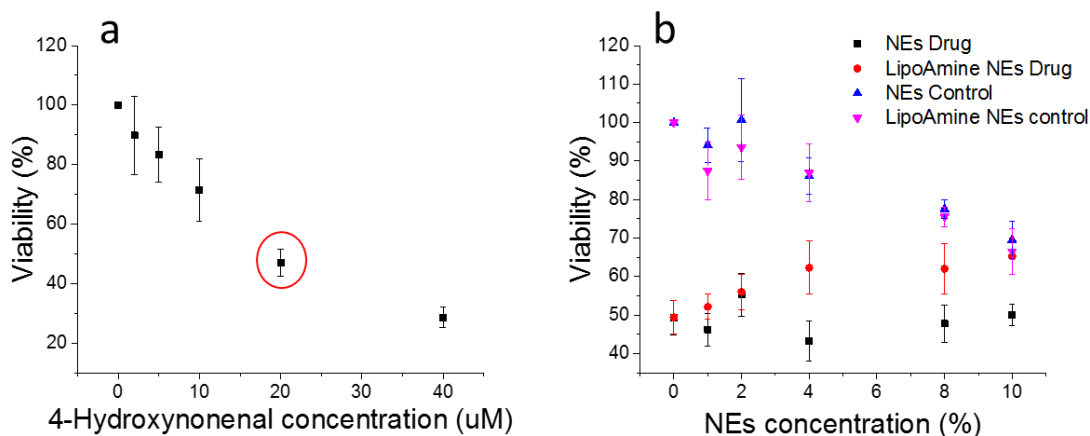


Fig. 8. (a) Viability of HeLa cell incubated for 4 h with different concentrations of 4-hydroxynonenal (4HN). (b) Detoxication study with LipoAmine NEs based on four different conditions: cells with 4HN (20 μM) treated with blank NEs (NEs 4HN); cells with 4HN (20 μM) treated with LipoAmine NEs (LipoAmine NEs 4HN); cells without 4HN treated with NEs (NEs Control); cells without 4HN treated with LipoAmine NEs (LipoAmine NEs Control).

3. Conclusion

In the present study, we developed a “drug sponge” platform for reversible uptake and delivery of aldehyde-bearing molecules, exploiting dynamic imine bond formation inside oil core of NEs. In this system a highly lipophilic amine (LipoAmine) was designed and its capacity to form reversible imine bonds inside NEs was investigated using a model fluorescent aldehyde, push-pull pyrene PA. We found that PA aldehyde undergoes a blue shift in its emission on incubation with LipoAmine NEs, suggesting in situ formation of the imine bond. The obtained PA-LipoAmine conjugate in form of reduced amine derivative was successfully identified by the mass spectrometry. PA-LipoAmine conjugate inside NEs was found stable at neutral pH of 7.4, while at acidic pH (pH 6 and 4), a characteristic red shifted emission indicated the cleavage of the imine bond and the release of free PA. Cell imaging experiments showed that acidic conditions (pH 6) trigger the release of PA into the cells, while at neutral pH, the release of PA was minimal. Thus, drug sponge NEs based on dynamic imine chemistry could become a platform for loading and further pH-controlled release of active molecules bearing aldehyde function. Furthermore, LipoAmine NEs showed great potential for the uptake of aldehyde compounds from cells. Using fluorescence microscopy, we showed that LipoAmine NEs can extract PA aldehyde from cells on the time scale of 30 min and thus protect the cells from phototoxic effects. LipoAmine NEs could also effectively remove PA from epithelial tissue (chicken skin), showing the first demonstration that dynamic imine chemistry can be used for detoxication of skin. Moreover, successful extraction was also achieved for a highly toxic aliphatic aldehyde 4HN, which allowed to obtain a proof of concept for detoxication of the cells from aldehydes. Taken together, these results show that the dynamic covalent chemistry of imine bonds inside NEs could be exploited to develop detoxication platforms, for example by simple application of NEs to the skin surface. This concept of drug-sponge NEs could be extended to other green chemistry reactions, which allow specific capture and release of other biologically active molecules.

4. References

1. F. Liu, Y. Niko, R. Bouchaala, L. Mercier, O. Lefebvre, B. Andreiuk, T. Vandamme, J. G. Goetz, N. Anton and A. Klymchenko, *Angewandte Chemie International Edition*, 2021, DOI: 10.1002/anie.202014259, anie.202014259-anie.202014259.
2. T. Yoshida, T. C. Lai, G. S. Kwon and K. Sako, *Journal*, 2013, **10**, 1497-1513.
3. P. Gupta, K. Vermani and S. Garg, *Journal*, 2002, **7**, 569-579.
4. E. R. Gillies, A. P. Goodwin, J. M. J. F. B. chemistry and undefined, *ACS Publications*.
5. A. F. Radovic-Moreno, T. K. Lu, V. A. Puscasu, C. J. Yoon, R. Langer and O. C. Farokhzad, *ACS Nano*, 2012, **6**, 4279-4287.
6. Y. Bae, S. Fukushima, A. Harada and K. Kataoka, *Angewandte Chemie - International Edition*, 2003, **42**, 4640-4643.
7. T. Etrych, M. Šírovaé, L. Starovoytova, B. Říehovaé and K. Ulbrich, *Molecular Pharmaceutics*, 2010, **7**, 1015-1026.
8. J. K. Kim, V. K. Garripelli, U. H. Jeong, J. S. Park, M. A. Repka and S. Jo, *International Journal of Pharmaceutics*, 2010, **401**, 79-86.
9. R. Tang, W. Ji, D. Panus, R. N. Palumbo and C. Wang, *Journal of Controlled Release*, 2011, **151**, 18-27.
10. R. Tang, W. Ji and C. Wang, *Macromolecular Bioscience*, 2010, **10**, 192-201.
11. J. Wang, X. Chen, W. Cui and S. Yi, *Physicochem. Eng. Aspects*, 2015, **484**, 28-36.

12. L. Akyuz, *Microporous and Mesoporous Materials*, 2020, **294**, 109850-109850.
13. J. Shin, P. Shum, D. H. T. J. o. C. Release and undefined, *Elsevier*.
14. Z. Xu, W. Gu, L. Chen, Y. Gao, Z. Zhang and Y. Li, *Biomacromolecules*, 2008, **9**, 3119-3126.
15. M. Chen and C. T. Jafvert, *Environmental Science: Nano*, 2018, **5**, 1350-1360.
16. Y. Nagasaki, T. Yaguchi, T. Matsumura, T. Yoshitomi, Y. Ikeda, A. Ueda and A. Hirayama, *Biomaterials Science*, 2014, **2**, 522-529.
17. N. Zarkovic.
18. D. J. McClements, *Soft Matter*, 2012, **8**, 1719-1729.
19. N. Anton and T. F. Vandamme, *Pharm. Res.*, 2011, **28**, 978-985.
20. L. Salvia-Trujillo, R. Soliva-Fortuny, M. A. Rojas-Grau, D. J. McClements and O. Martin-Belloso, in *Annu. Rev. Food. Sci. Technol.*, eds. M. P. Doyle and T. R. Klaenhammer, Annual Reviews, Palo Alto, 2017, vol. 8, pp. 439-466.
21. N. Anton, J. P. Benoit and P. Saulnier, *J. Control. Release*, 2008, **128**, 185-199.
22. A. S. Klymchenko, F. Liu, M. Collot and N. Anton, *Advanced Healthcare Materials*, 2021, **10**.
23. R. Bouchaala, L. Mercier, B. Andreiuk, Y. Mely, T. Vandamme, N. Anton, J. G. Goetz and A. S. Klymchenko, *Journal of Controlled Release*, 2016, **236**, 57-67.
24. I. Khalin, N. Adarsh, M. Schifferer, A. Wehn, B. Groschup, T. Misgeld, A. Klymchenko and N. Plesnila, *Small*, 2022, **18**.
25. A. S. Klymchenko, E. Roger, N. Anton, H. Anton, I. Shulov, J. Vermot, Y. Mely and T. F. Vandamme, *Rsc Advances*, 2012, **2**, 11876-11886.
26. S. Bou, X. Y. Wang, N. Anton, A. S. Klymchenko and M. Collot, *Journal of Materials Chemistry B*, 2020, **8**, 5938-5944.
27. A. Herrmann, *Chem. Soc. Rev.*, 2014, **43**, 1899-1933.
28. Y. H. Jin, C. Yu, R. J. Denman and W. Zhang, *Chem. Soc. Rev.*, 2013, **42**, 6634-6654.
29. S. J. Rowan, S. J. Cantrill, G. R. L. Cousins, J. K. M. Sanders and J. F. Stoddart, *Angew. Chem.-Int. Edit.*, 2002, **41**, 898-952.
30. J. M. Lehn, *Angew. Chem.-Int. Edit.*, 2015, **54**, 3276-3289.
31. Y. Zhang and M. Barboiu, *Chem. Rev.*, 2016, **116**, 809-834.
32. N. Roy, B. Bruchmann and J. M. Lehn, *Chem. Soc. Rev.*, 2015, **44**, 3786-3807.
33. S. Ulrich, *Acc. Chem. Res.*, 2019, **52**, 510-519.
34. S. J. Sonawane, R. S. Kalhapure and T. Govender, *Eur. J. Pharm. Sci.*, 2017, **99**, 45-65.
35. D. K. Kolmel and E. T. Kool, *Chem. Rev.*, 2017, **117**, 10358-10376.
36. A. Dizdarevic, N. A. Efiana, T. N. Q. Phan, B. Matuszczak and A. Bernkop-Schnurch, *Eur. J. Pharm. Biopharm.*, 2019, **142**, 92-100.
37. C. A. Zentner, F. Anson, S. Thayumanavan and T. M. Swager, *J. Am. Chem. Soc.*, 2019, **141**, 18048-18055.
38. S. P. Black, J. K. M. Sanders and A. R. Stefankiewicz, *Chem. Soc. Rev.*, 2014, **43**, 1861-1872.
39. B. Akgun and D. G. Hall, *Angew. Chem.-Int. Edit.*, 2016, **55**, 3909-3913.
40. F. Liu, Y. Niko, R. Bouchaala, L. Mercier, O. Lefebvre, B. Andreiuk, T. Vandamme, J. G. Goetz, N. Anton and A. Klymchenko, *Angew. Chem.-Int. Edit.*, 2021, **60**, 6573-6580.
41. W. Qin, S. Long, M. Panunzio and S. Biondi, *Molecules*, 2013, **18**, 12264-12289.
42. Y. Niko, P. Didier, Y. Mely, G. I. Konishi and A. S. Klymchenko, *Scientific Reports*, 2016, **6**, 18870.
43. J. Valanciunaite, E. Kempf, H. Seki, D. I. Danylchuk, N. Peyri  ras, Y. Niko and A. S. Klymchenko, *Analytical Chemistry*, 2020, **92**, 6512-6520.
44. A. Anemone, L. Consolino, F. Arena, M. Capozza and D. L. Longo, *CANCER AND METASTASIS REVIEWS*, 2019, **38**, 25-49.
45. N. S. Chang, *Journal*, 2016, **241**, 1306-1315.
46. G. R. Ji, N. C. Yu, X. Xue and Z. G. Li, *The Scientific World Journal*, 2014, **2014**.

47. N. Feizi Langaroudi and N. Motakef Kazemi, *Nanomed Res J*, 2019, **4**, 48-55.

Supplementary information

Capture and release of aldehydes in cells and tissues by dynamic covalent chemistry in nanoemulsions

Fei Liu,^{1,2} Nicolas Anton,² Yosuke Niko,³ and Andrey Klymchenko^{1,*}

¹Université de Strasbourg, Laboratoire de Bioimagerie et Pathologies, UMR 7021 CNRS, 74 route du Rhin, 67401 Illkirch (France)

²INSERM UMR 1260, Regenerative Nanomedicine (RNM), FMTS, CNRS 7199, CAMB, Université de Strasbourg, 67000 Strasbourg (France)

³Research and Education Faculty, Multidisciplinary Science Cluster, Interdisciplinary Science Unit, Kochi University, 2-5-1, Akebono-cho, Kochi-shi, Kochi, 780-8520 (Japan)

* Corresponding author: E-mail: andrey.klymchenko@unistra.fr

Materials and Methods

All starting materials for synthesis were purchased from Alfa Aesar, Merck-Sigma-Aldrich unless specifically mentioned. Acetic acid (>99.0%, Sigma-Aldrich), sodium phosphate monobasic (>99.0%, Sigma-Aldrich) and sodium phosphate dibasic dihydrate (>99.0%, Sigma-Aldrich) were used to prepare 20 mM phosphate buffers at pH 7.4, pH 6 and pH 4. Milli-Q water (Millipore) was used in all experiments. Labrafac (Labrafac Lipophile WL 1349) is composed of medium-chain triglycerides and caprylic/capric triglyceride was obtained from Gattefossé (Saint Priest, France). Synthesis and characterization of all new compounds, including LipoAmine, are described in the Supporting Information. PA dye was synthesized as previously described.¹

Spectroscopy

Absorption and emission spectra were recorded on a Cary 4000 Scan ultraviolet–visible spectrophotometer (Varian) and a FS5 spectrofluorometer (Edinburgh instrument). All the emission spectra were corrected from the lamp fluctuations and wavelength-dependent response of the detector. Size distribution was determined by DLS using a Zetasizer Nano ZSP (Malvern Instruments SA). In DLS, measurement statistics by volume was used. All error bars correspond to standard deviation of the mean. Statistical analysis was based on the one-tailed T-test, using Microsoft Excel. NMR spectra were recorded on a Bruker Avance III 400 MHz spectrometer. Mass spectra were obtained using an Agilent Q-TOF 6520 mass spectrometer.

LipoAmine NEs, PA-LipoAmine formulation

LipoAmine containing NEs were prepared in the following sequence. Firstly, 3 mg LipoAmine were dissolved in 50 µL of dichloromethane (DCM), then, 50 mg of both

LabrafacWL and surfactant Cremophor ELP® (also called Kolliphor ELP®) were added. The mixture was homogenized by ultrasound under 40 °C for 10 min, followed by DCM evaporation under vacuum. Finally, NEs were generated with the addition of ultrapure (Milli-Q) water (230 µL) mixed by a thermo-shaker at the speed of 1400 r/min under 40 °C. For *in situ* reaction, 30 µL of this LipoAmine NEs were used to react with 5 µL of PA (3 mM in DMSO) in 1 mL of ultrapure (Milli-Q) water under 40 °C. The molar ratio of LipoAmine to PA was calculated to be 30 to 1. Control NEs was obtained by mixing 30 µL of blank NEs with 5 µL of PA (3 mM in DMSO) in 1 mL Milli-Q water. The reaction was monitored by fluorescence spectrum under the excitation wavelength of 380 nm and 420 nm.

Identification of formed PA-LipoAmine

The reacted NEs (30 µL LipoAmine NEs reacted with 5 µL 3 mM PA in 1 mL Milli-Q water) were mixed with excess of NaBH₄ (1.2 mg) for 2 hours to reduce the formed proton sensitive imine into stable amine. Control NEs (30 µL blank NEs added by 5 µL 3 mM PA in 1 mL Milli-Q water) were treated using the same reduction protocol. After this process, samples before and after the reduction were extracted by DCM and Milli-Q water. The organic phase was collected for TLC analysis (DCM:MeOH=9:1). The novel blue spot on TLC for the reduced PA-LipoAmine was extracted by MeOH and analyzed by mass spectrometry.

pH-dependent release of PA-LipoAmine

The stability of pre-formed PA-LipoAmine containing NEs was tested under different pH conditions. Briefly, 100 µL of PA-LipoAmine NEs (formed after 4 hours of *in situ* reaction under 40 °C) was mixed with 10 µL of concentrated blank NEs (corresponding to 10-fold mass excess of blank NEs) as PA acceptor in 1 mL of phosphate buffer with pH of 4, 6, 7.4. Emission spectra at the excitation wavelength of 380 nm were recorded to monitor the degradation process for the time points of 1, 15, 30, 60 and 120 min.

pH-dependent release of PA from PA-LipoAmine NPs to cells

Hela cells (ATCC® CCL-2) were seeded on 35 mm ibidi dish (40000/dish) with glass bottom and coverslips in DMEM medium with penicillin (100 U/mL), 1% glycan (100 U/mL) and 10 % FBS at 37 °C in a humidified atmosphere containing 5% CO₂ overnight. The cells were washed 3 times with PBS and then the medium was changed to 50 times diluted solution of PA-LipoAmine NEs (containing 300 nM PA-LipoAmine) at pH 6 and 7.4. Control sample containing 300 nM PA at pH 7.4 and pH 6 PBS medium was also prepared to test the release of free PA in cells. Cell imaging were acquired after washing at 1 and 30 min time points.

In situ uptake of PA from cells by LipoAmine NPs

The *in-situ* extraction of PA from cells was done as follows. Cells were first incubated with 600 nM of PA for 30 min in Opti-Mem. After cells were washed with PBS, fluorescence images were checked to ensure the cells were stained with similar amount of PA (before application of NEs). Then, the medium was changed to 200-times diluted LipoAmine NEs in PBS medium. Control cells were treated with 200-times diluted blank NEs in PBS. Finally, PBS buffer without NEs was used as blank control. Video was acquired immediately after changing the medium by taking 30 frames over 30 min for PA *in situ* uptake study. The individual images were also taken to compare PA fluorescence intensity from cells. After imaging, mean intensity

from each cell for PA channel was analyzed excluding nucleus (the center black part of each cell). The obtained values were the mean fluorescence intensity from 15 cells.

All cellular imaging studies were done using epi-fluorescence mode with a Nikon Ti-E inverted microscope, equipped with CFI Plan Apo $\times 60$ oil (numerical aperture = 1.4) objective, and a Hamamatsu Orca Flash 4 sCMOS camera. For PA imaging, the excitation wavelength was 470 nm of Lumencor Spectra X LED, and emission was detected through 531/40 nm filter.

In order to calculate the amount of PA extracted from cells, the emission spectra of the extracellular PA dye (10 x dilution) were measured before and after cell staining. To study the extraction media, the extraction media were collected to examine the emission spectrum (in triplicates). For the control PBS group, 200-times diluted blank NEs were added to the extraction solution to ensure the comparable measurement condition for PA. To quantify PA or PA-LipoAmine concentration in the extraction media, the calibration curve based on peak fluorescence intensity of PA or PA-LipoAmine in solutions of a gradient dilution of PA or PA-LipoAmine (15 μ M) NEs. For estimating the total amount of PA accumulated in HeLa cells, the emission spectra of PA staining solution was measured before and after cell staining in the presence of 200-times diluted NEs. Excitation wavelength were set at 420 nm and 380 nm for efficient PA or PA-LipoAmine excitation, respectively.

Experiment with adipose tissue (chicken skin)

A series of specially cut chicken skin circles (around 3 cm diameter) was washed with ethanol for 3 times to remove oil on the surface, followed by washing 3 times with water. The wet skin was then evenly spread on a 150 mm plastic plate with epidermis side on the top. Then our 3D printed funnel with diameter of 25 mm was pressed on the skin tissue and filled with 2 mL PA solution in PBS (3 μ M) for 30 min (Fig. S5a), then medium was removed and the tissue washed with PBS. The image was taken under UV lamp (excitation 254 nm), followed by taking fluorescence images of the epidermis side. Then, a funnel with diameter of 15 mm (Fig. S5b) was pressed on the central PA-stained area on epidermis side, and the device was loaded with 100-times diluted LipoAmine NEs in PBS medium (2 mL). Control samples were treated with blank NEs (2 mL, the same dilution) in PBS, and only PBS buffer (2 mL) as blank control. After 6 h incubation, the solutions were removed, images were taken under UV lamp (excitation 254 nm), fluorescence images (epidermis side) were acquired immediately. Extracted media were also imaged under UV lamp (excitation 365 nm). Fluorescence imaging was done by the Nikon microscope (see above) using Nikon 10x air objective (Nikon CFI Plan Apo, NA = 0.75). For PA imaging, the excitation wavelength was 470 nm, and emission was detected through 531/40 nm filter. After the imaging, mean intensity for PA channel was analyzed for each image (3 images for each condition).

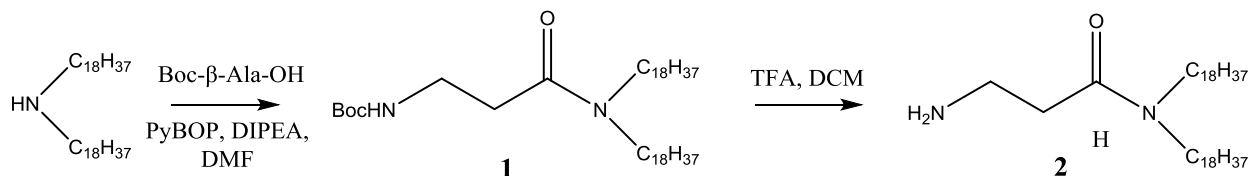
3D printing

Form 3, 3D printer (Formlabs) was used for 3D printing of incubation chambers. The chambers were designed with FreeCAD parametric 3D modeler software (STL file is available upon request). Clear V4 resin (Formlabs) was used for 3D printing. After the 3D printing, polymer stents were rinsed with isopropyl alcohol to remove the excess of resin and exposed under UV light for 30 minutes.

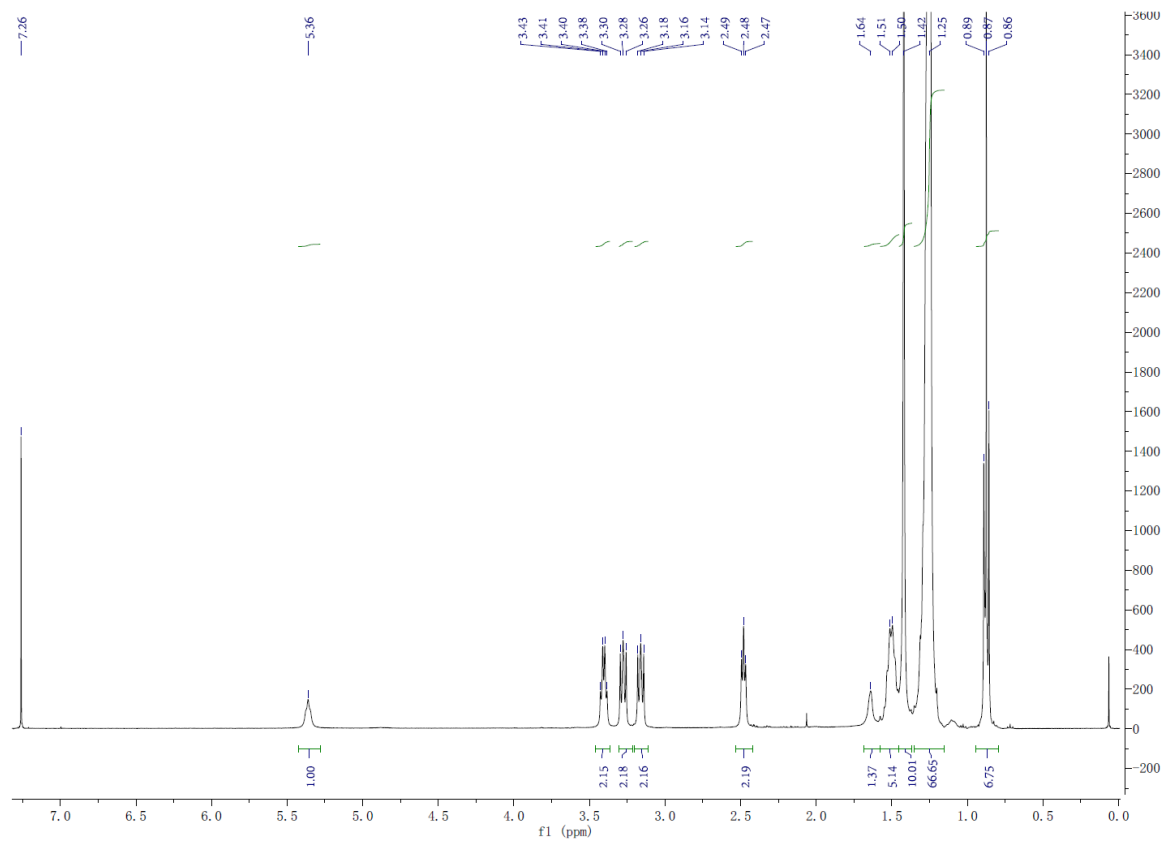
Cytotoxicity assay

In order to test the capability of LipoAmine NEs to uptake toxic compounds from cells, toxic natural aldehyde 4-hydroxynonenal (Merck-Sigma-Aldrich) was chosen. Cytotoxicity was evaluated by a WST-1 assay. Briefly, 96-well plate and 6-well plate was seeded with Hela cells (5000 cells/well and 30000 cells/well, respectively) overnight, washed by PBS twice before changing to PBS containing testing samples. The cytotoxicity of 4-hydroxynonenal was tested under different concentration of 4-hydroxynonenal (0, 2, 5, 10, 20, 40 μ M) in PBS. Afterward, 20 μ M solution of 4-hydroxynonenal was used for the testing the detoxification potential of LipoAmine NEs or blank NEs (as control) at different concentrations (0-10% dilution). The cytotoxicity of NEs (blank or with LipoAmine) were also tested in PBS. After adding PBS containing NEs, cells were incubated for 4 h, washed with PBS twice and then the medium was changed to WST-1 containing cell culture medium (5 μ L/200 μ L for 96-well plate and 25 μ L/1000 μ L for 6-well plate). Then, cells were incubated for 30 min. For 96 well plates, the absorbance at 440 nm were tested under a microplate reader, with 6 replicates for each condition. Cell viability was calculated in according to UV absorbance data. Statistical analysis including the calculating of derivation and significance between two set of data was conducted using Origin.

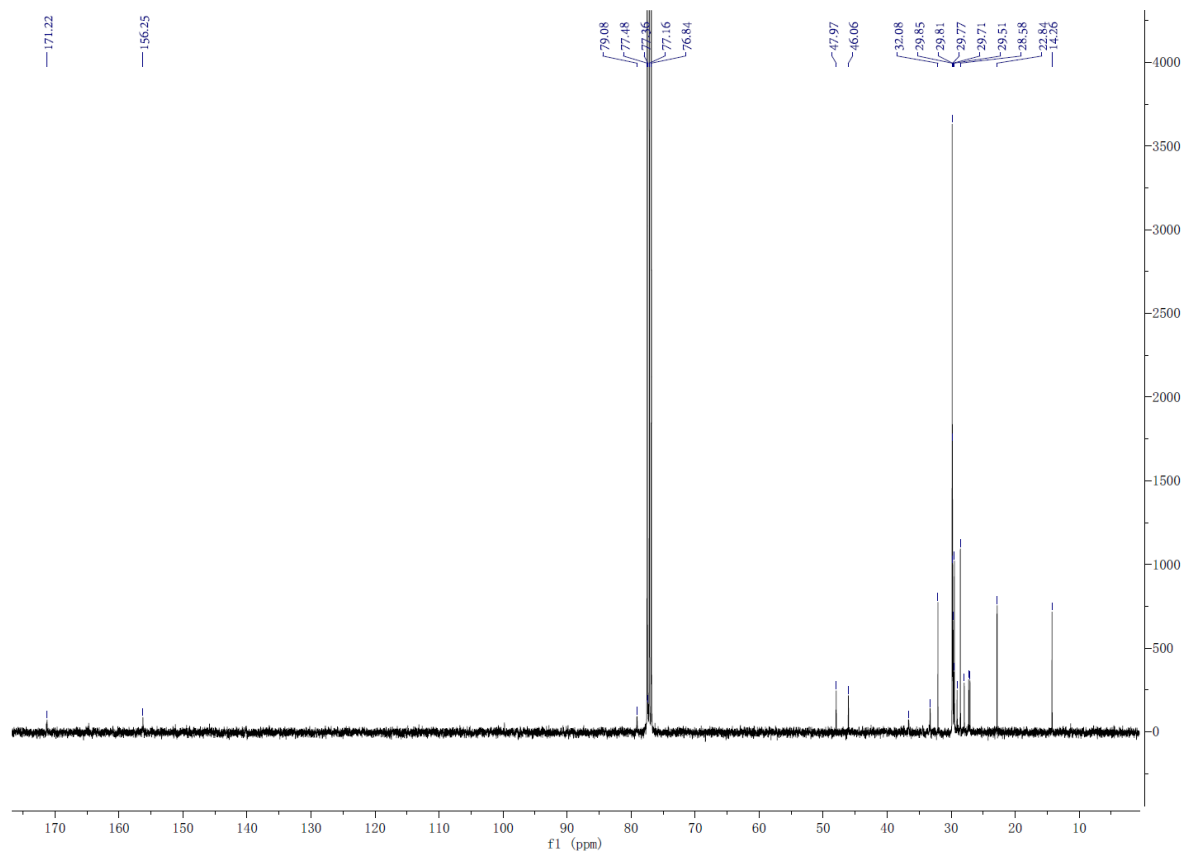
Synthesis and chemical characterization



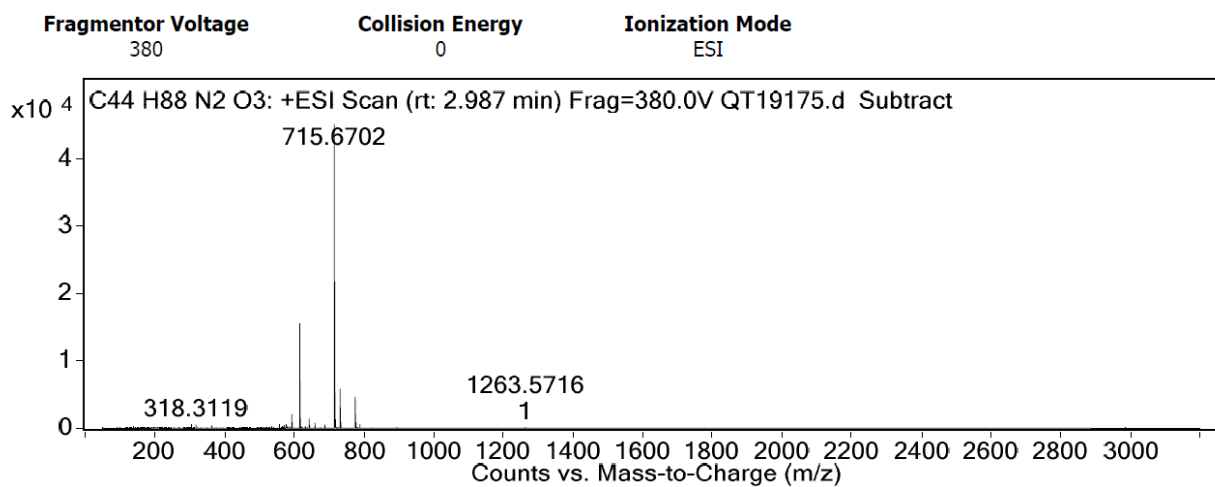
Tert-butyl (3-(di-octadecylamino)-3-oxopropyl)carbamate (1). To the solution of Boc-β-Ala-OH 190 mg (1.0 mmol) in DMF (10 mL) was added dioctadecylamine (388 mg, 0.7 mmol), PyBOP (500 mg, 1.0 mmol), and DIPEA (1.1 mL, 6.4 mmol) were added and stirred at room temperature overnight under argon atmosphere. The solvent was evaporated in vacuo, the resulting residue was purified by flash column chromatography on silica gel (eluent EtOAc/Hepane 50:50) to give desired product as a colorless solid (268 mg, yield 75%). ¹H NMR (400 MHz, CDCl₃) 5.36 (s, 1H), 3.41 (p, J=11.3, 6.0, 2H), 3.30 - 3.21 (t, 2H), 3.20 - 3.11 (t, 2H), 2.48 (t, J=5.5, 2H), 1.50 (m, J=6.7, 6H), 1.42 (s, 9H), 1.25 (s, 64H), 0.87 (t, J=6.9, 6H). ¹³C NMR (101 MHz, CDCl₃) δ 170.42, 77.32, 77.21, 77.01, 76.69, 48.03, 46.24, 36.63, 31.93, 29.71, 29.66, 29.63, 29.59, 29.56, 29.52, 29.36, 29.27, 28.63, 27.56, 27.06, 26.89, 22.69, 14.10. HRMS(ESI⁺) calcd for C₄₄H₈₈N₂O₃ 692.6795 and 715.6693 (M+Na)⁺; observed 715.6702.



^1H -NMR spectrum of **1** in CDCl_3 .



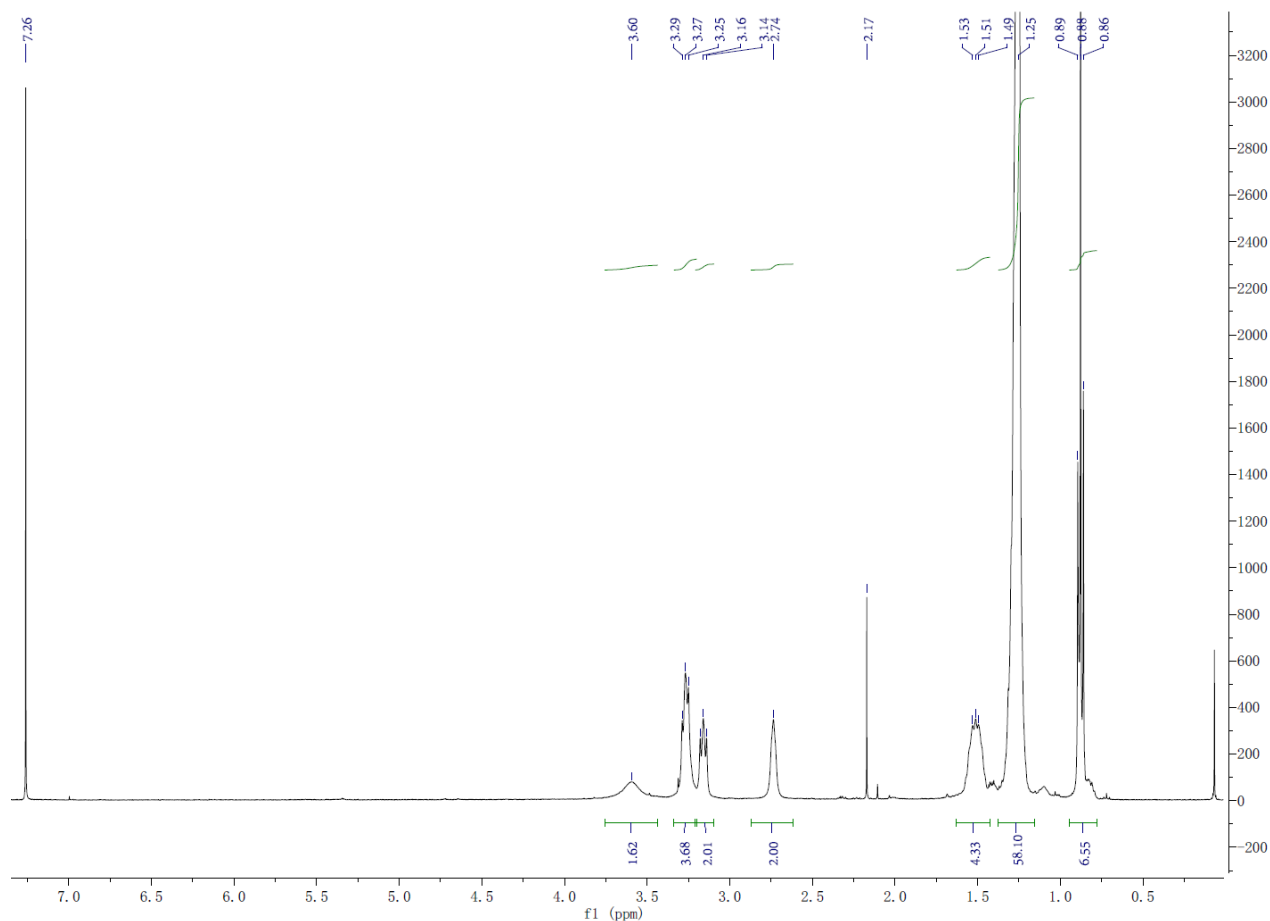
^{13}C -NMR spectrum of **1** in CDCl_3 .



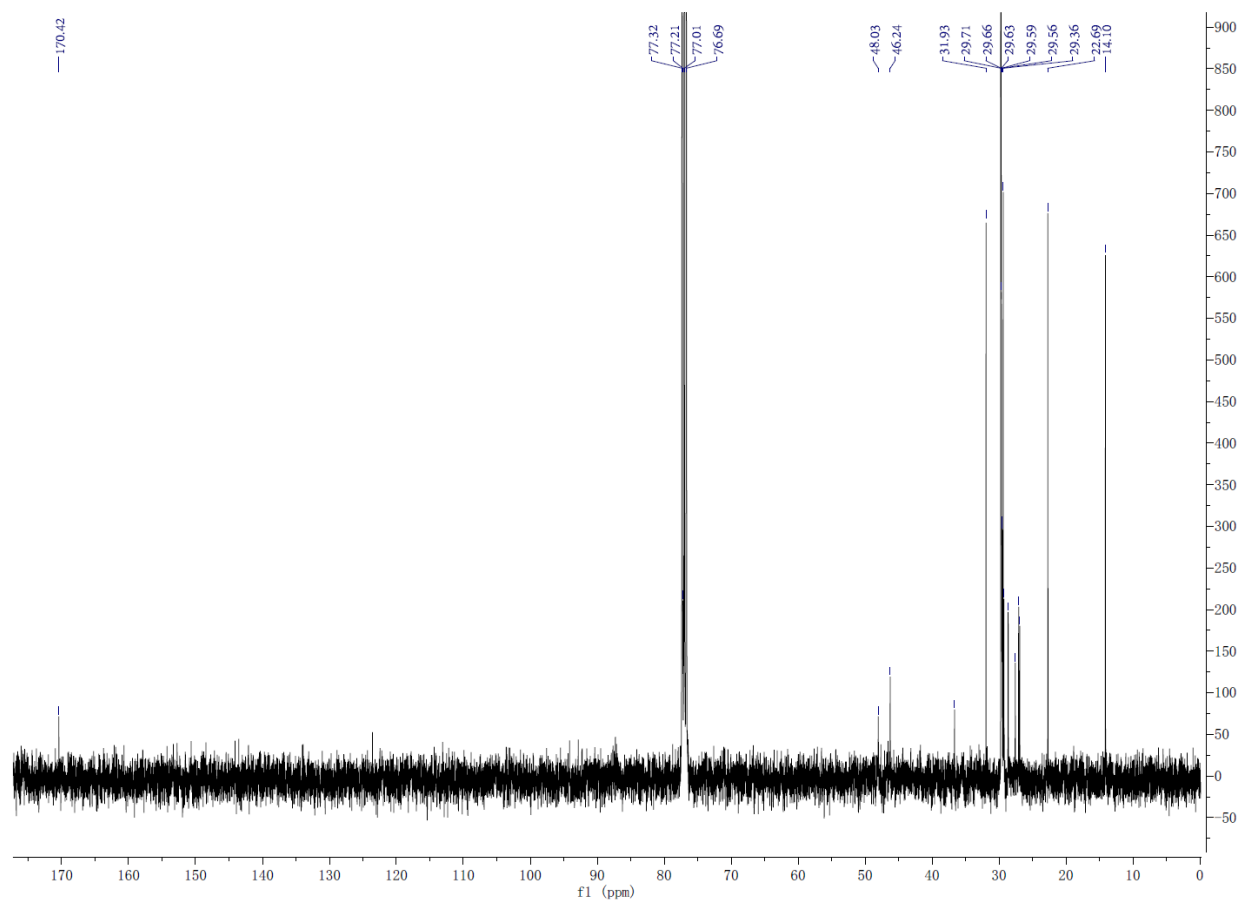
Mass spectrum of **1**.

3-Amino-N,N-diocetadecylpropanamide (2). The solution of compound **1** (268 mg, 0.39 mmol) in DCM (5 mL), TFA (5 mL) and 2 drops of MiliQ water was stirred at rt for 2 h. After

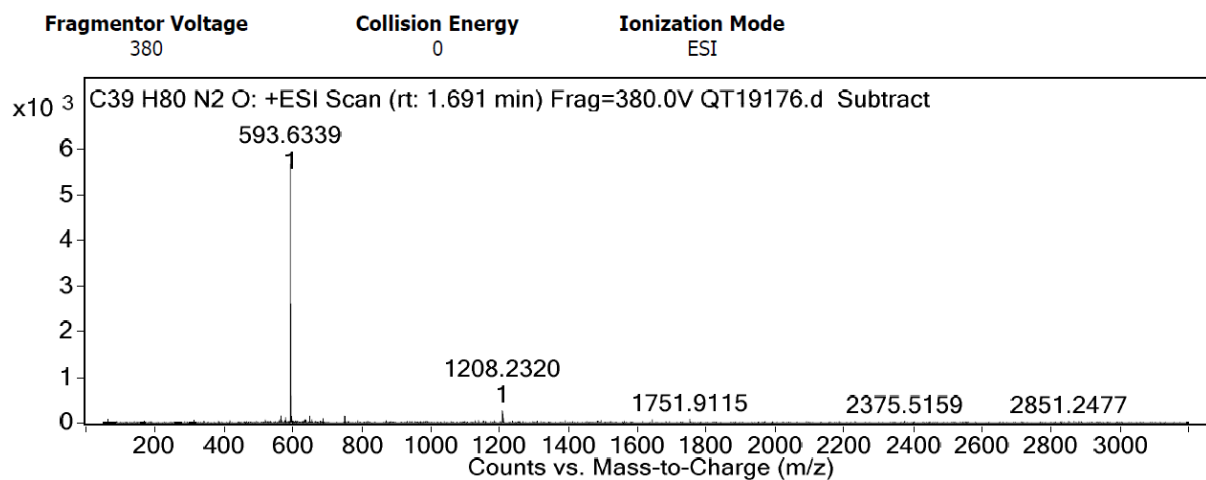
confirming the reaction completely proceeded with TLC, the solvents were evaporated under reduced pressure, and then the residue was dissolved in MeOH and evaporated 3 times to remove TFA and give desired product **3** as a colorless solid (214 mg). ^1H NMR (400 MHz, CDCl_3) 3.60 (s, 1H), 3.34-3.20 (m, 4H), 3.21-3.10 (t, 2H), 2.74 (s, 2H), 1.63-1.42 (m, 4H), 1.25 (s, 64H), 0.88 (t, $J=6.9$, 6H). ^{13}C NMR (101 MHz, CDCl_3) δ 170.58, 77.48, 77.36, 77.16, 76.84, 48.18, 46.39, 36.79, 32.08, 29.87, 29.82, 29.78, 29.74, 29.71, 29.68, 29.52, 29.42, 28.78, 27.72, 27.21, 27.05, 22.84, 14.26. HRMS (ESI+) 592.6271 calcd for $\text{C}_{39}\text{H}_{80}\text{N}_2\text{O}$ and 593.6349 ($\text{M}+\text{H}$) $^+$; observed 593.6339.



^1H -NMR spectrum of **2** in CDCl_3 .



^{13}C -NMR spectrum of **2** in CDCl_3 .



Mass spectrum of **2**.

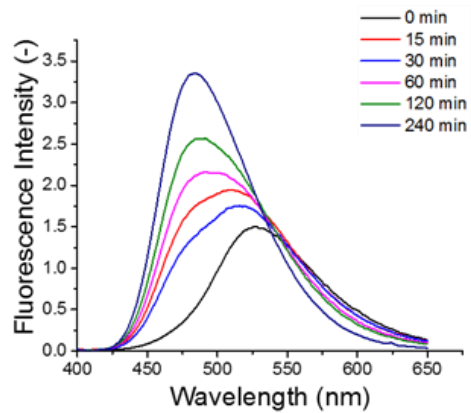


Fig. S1. Emission spectra of PA during reaction with PA-LipoAmine NEs at different time points. Excitation wavelength: 380 nm.

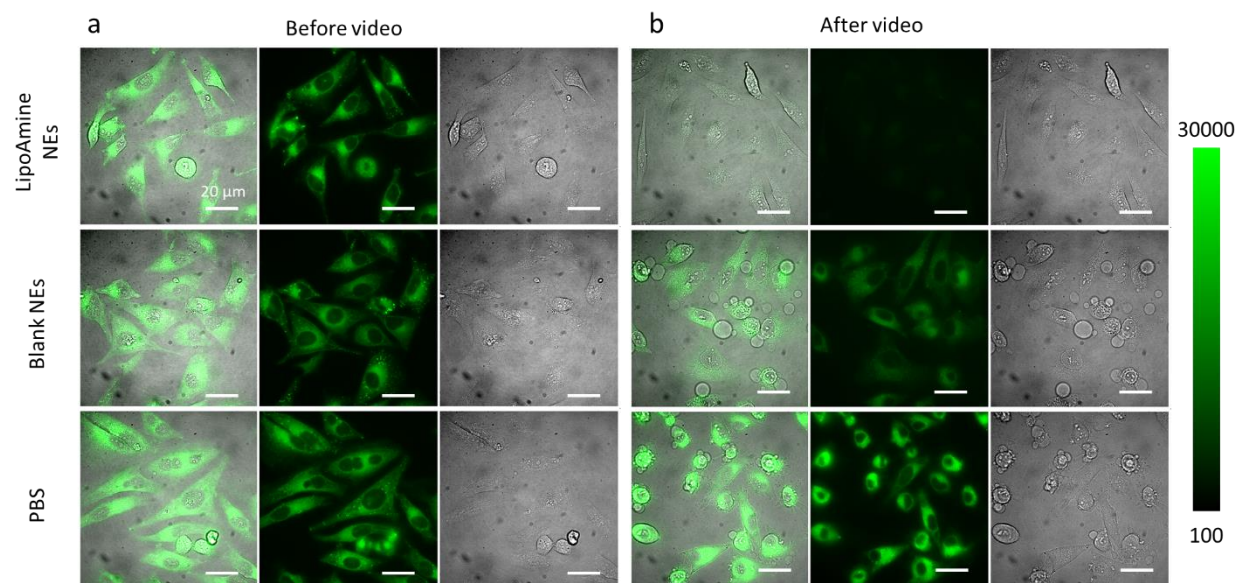


Fig. S2. Cellular images before and after 30 min video recording at PA excitation channel (excitation 420 nm). (a) Before application of NEs and video recording; (b) after 30 mins video recording. Three images each condition from left to right: merge of DIC and PA channel, PA channel and DIC channel.

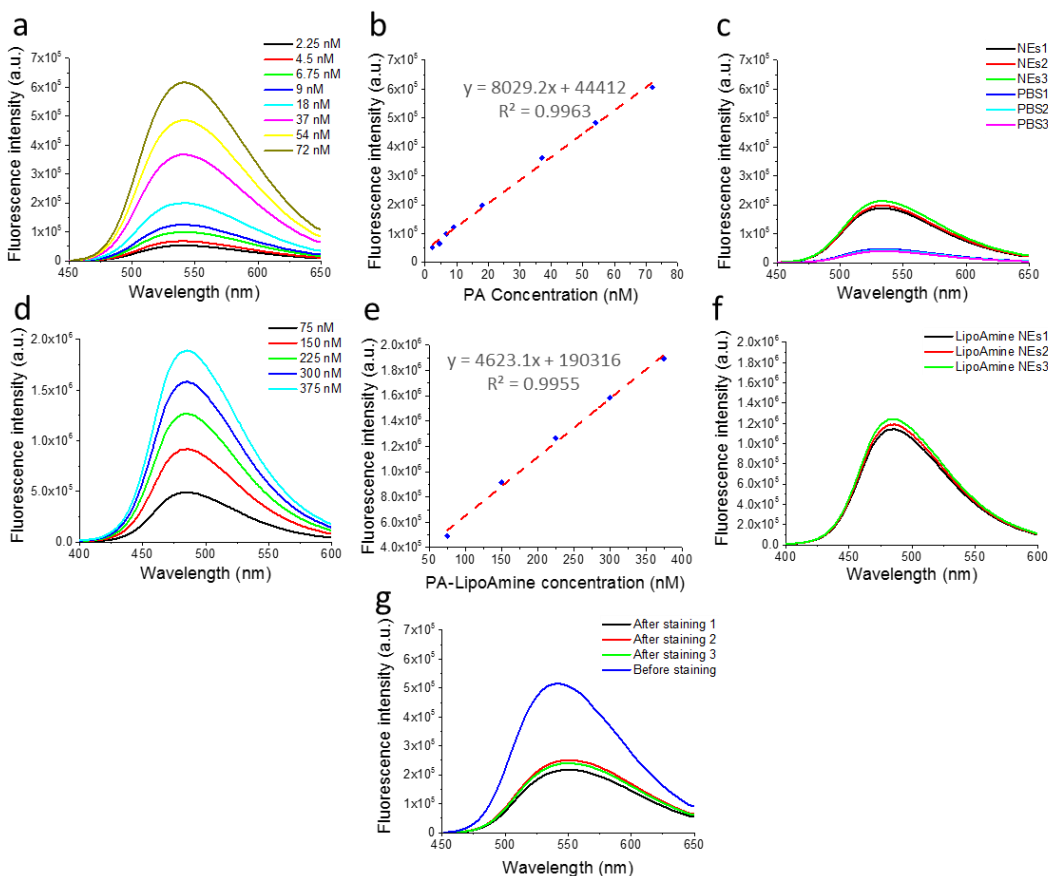


Fig. S3. Calibration of PA and PA-LipoAmine emission signal for their quantification in the cell extraction medium. (a) PA emission spectra at different concentrations in the presence of NEs (excitation wavelength: 420 nm). (b) Calibration curve of PA fluorescence intensity vs PA concentration. (c) Emission spectra of PA extraction medium from cells by blank NEs and PBS (excitation wavelength of 420 nm). (d) PA-LipoAmine NEs emission spectra at different PA concentrations (excitation wavelength: 380 nm); (e) Calibration curve of PA-LipoAmine NEs fluorescence intensity vs PA-LipoAmine concentration. (f) Emission spectra of PA extraction medium from cells by LipoAmine NEs and PBS (excitation wavelength of 380 nm). (g) Fluorescence spectra of PA staining solution (10 x dilution) before and after staining of HeLa cells for 30 mins. PA concentration in the staining medium was $0.6 \mu\text{M}$.

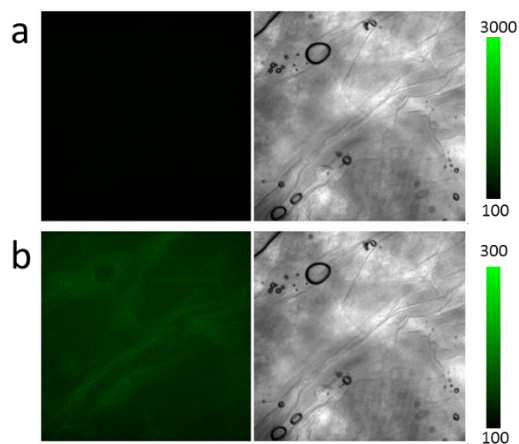


Fig. S4. Auto-fluorescence microscopy images of chicken skin surface. (a) Transmission (grey) and fluorescence (green) images of chicken skin surface. (b) The same fluorescence image as in (a) but with a different intensity scale. Excitation wavelength was 550 nm and the emission filter was 600 nm.

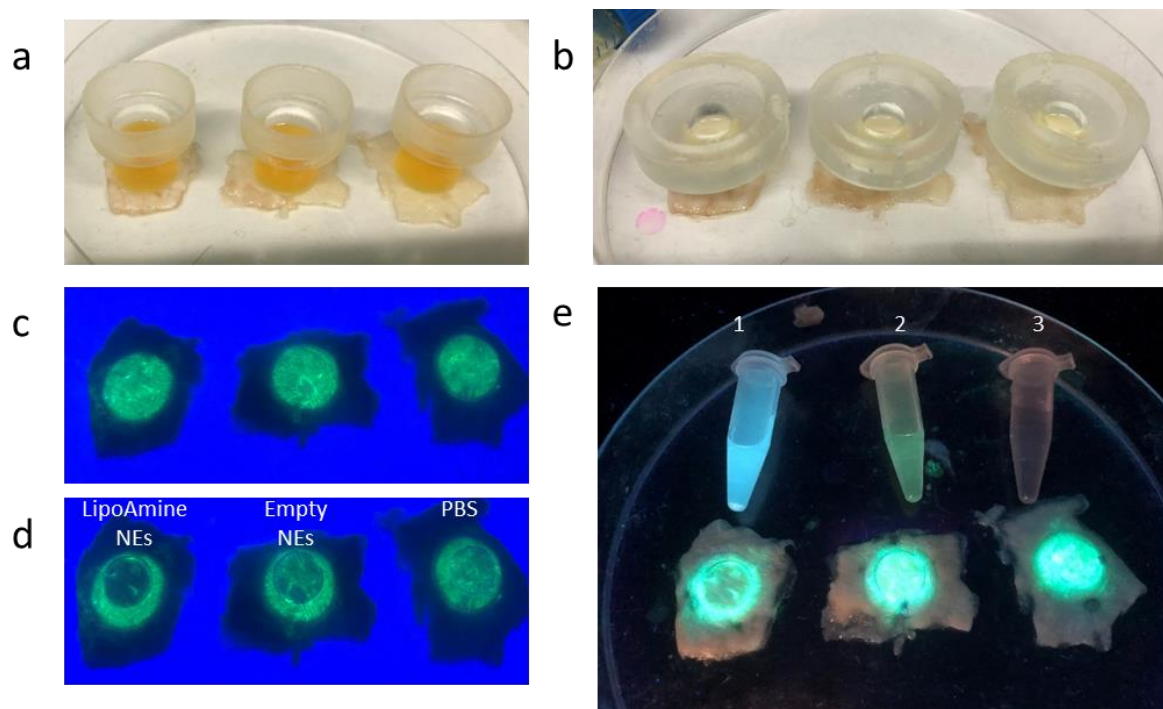


Fig. S5. Experimental setup for (a) PA staining and (b) *in situ* extraction of PA from chicken skin. The incubation chambers were 3D printed. Chicken skin fluorescence after PA staining (c) and extraction (d) under UV lamp (excitation wavelength: 254 nm). (e) Fluorescence from different extraction media: (1) LipoAmine NEs; (2) blank NEs and (3) PBS (excitation wavelength: 365 nm).

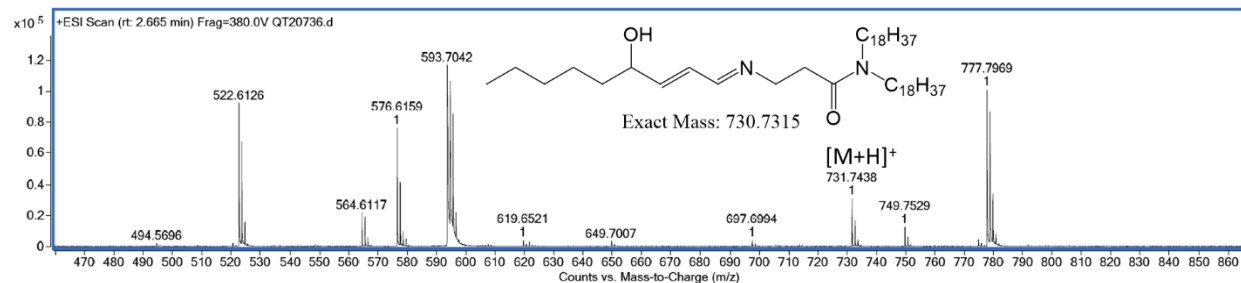


Fig. S6. Mass spectrum of DCM extraction phase from the *in-situ* reaction of 4-hydroxynonanal with LipoAmine NEs. The formula of the identified imine of 4-hydroxynonanal with LipoAmine is shown.

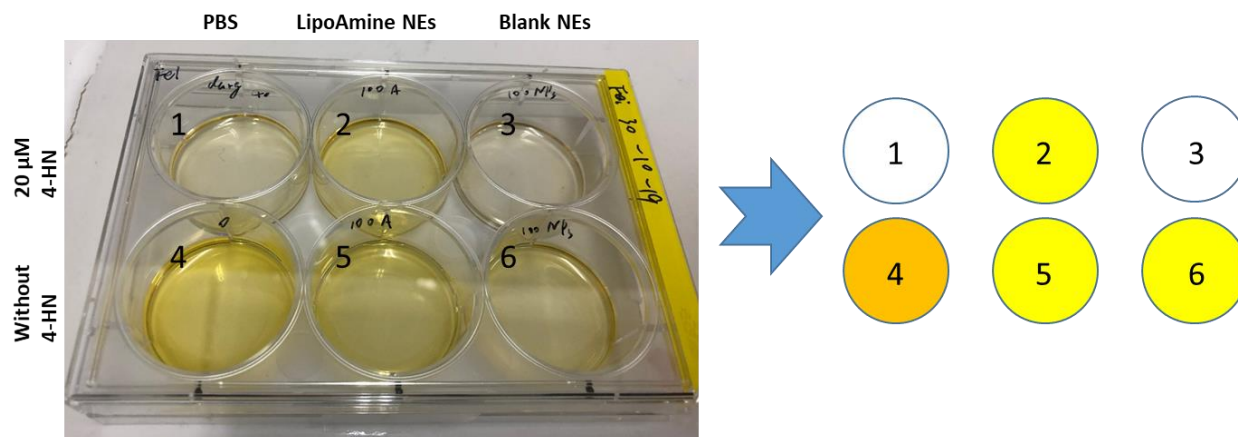


Fig. S7. Photo of WST-1 cytotoxicity assay in 6 well plate for demonstrating detoxification of cells from 4-hydroxynonenal (4-HN) by LipoAmine NEs compared with blank NEs. Darker yellow color corresponds to higher cell viability.

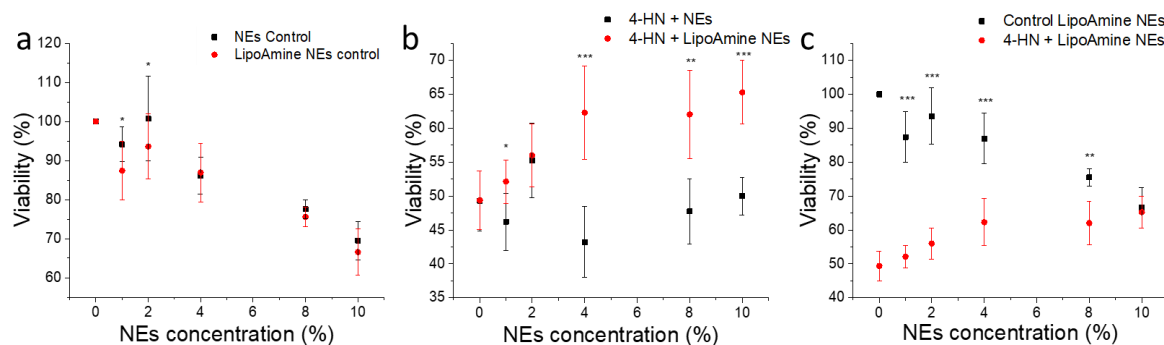


Fig. S8. Significance study by comparing cytotoxicity data of two independent tests: (a) blank NEs and LipoAmine NEs; (b) blank NEs and LipoAmine NEs in the presence of 20 μ M 4-HN; (c) LipoAmine NEs with 4-HN and a control without 4-HN. The values $p < 0.1$ (*), $p < 0.01$ (**), and $p < 0.001$ (***) were assumed as the level of significance for the statistical analysis.

Table S1. Size measurements of formulated nano-droplets

Sample	Size (nm)	PDI
LipoAmine NEs	69.0	0.131
PA-LipoAmine NEs	70.3	0.148
Blank NEs	73.0	0.119
PA NEs	84.5	0.234

References

1. Y. Niko, P. Didier, Y. Mely, G. I. Konishi and A. S. Klymchenko, *Scientific Reports*, 2016, **6**, 18870.

2.3- Preparation of functionalized nanoemulsion by *in situ* covalent chemistry and exploring the potential for tumor targeting applications (Article 3 – manuscript)

The ultimate goal of NCs is specific targeting tumor areas. In this way, the loaded drug could be efficiently carried to the targeted tissue. Thus, minimizing the effect to normal tissues and reducing the side effects of the loaded drug as well as reducing the administrating drug dosage (the drug concentration to the treating area would be the same as the high dosage using conventional non-targeting carriers) benefited from this active targeting ability.

In this project, the possibility of preparing targeting NEs was explored based on the above-mentioned successful *in situ* reactions. Cholesterol, a natural lipid generally considered as a harmless, was selected as the lipophilic counterpart. Cholesterol was reacted with 4-nitrophenyl carbonochloridate to form a carbonate, which can react with amines. We encapsulated this functional cholesterol (NPC-Chol) in NEs, assuming that this functional NEs could *in situ* react with amines. To explore the capability of NPC-Chol of reacting *in situ* with molecules containing primary amine, we first tested the reaction with ethanolamine. Then, we designed a Biotin-PEG3000-lysine linker, which is expected to expose biotin at NEs surface after reaction with NPC-Chol. In this design, lysine end bearing with two amines would be grafted with cholesterol, thus fixed inside the core of NEs, while long PEG3000 would ensure exposure of the biotin outside of the NEs. These biotinylated NEs loaded with DiI-TPB dye were capable to specifically bind to the Neutravidin (streptavidin analogue) on glass surface, observed by fluorescence microscopy.

Electrophoresis was used for the validation of successful inserting of biotin on NEs surface from *in situ* reaction of Biotin-Peg-lysine with NPC-Chol loaded NEs. We expected that biotinylated NEs would have strong affinity to streptavidin, thus making the streptavidin-biotinylated NEs migrate together on gel during electrophoresis. Co-localization of fluorescence from Cy5 labelled streptavidin and DiI-TPB loaded NEs confirmed successful grafting of biotin on NEs surface. Then, using biotin-Neutravidin-biotinylated antibody (cetuximab) sandwich structure, we tested capacity of NEs to target cells (SKBr3) overexpressing EGFR. A good cell membrane targeting by NEs (loaded with DiI-TPB dye) was observed if the sandwich structure was constructed in separate steps on cell membrane, by sequential addition of biotinylated antibody, then Neutravidin and finally, biotinylated NEs, with washing after each step. We also aimed to obtain separately NEs-antibody conjugate by removing the excess of free antibody and Neutravidin, which can compete in the experiments on cell targeting. Size exclusion chromatography with a special resin was explored as a possible way to purify NEs-antibody conjugate. Firstly, as a prove of concept of this purification technique, we attempted purification of DiI-TBP loaded biotinylated NEs conjugated with Cy5-Streptavidin with size exclusion chromatography. Result showed a fraction combining fluorescence from both DiI-TPB and Cy5 could be obtained, which could be separated from the fraction of free Cy5-Streptavidin, indicating the efficacy of using this method for the purification of functional NEs. Then we purified DiD-TBP loaded NEs grafted with antibody using size exclusion chromatography. The latter showed good membrane targeting ability on SKBr3 cells

based on the confocal microscopy (Figure 2.6). The *in vivo* experiments on mice are planned in the near future, in cooperation with Dr. Jacky GOETZ team.

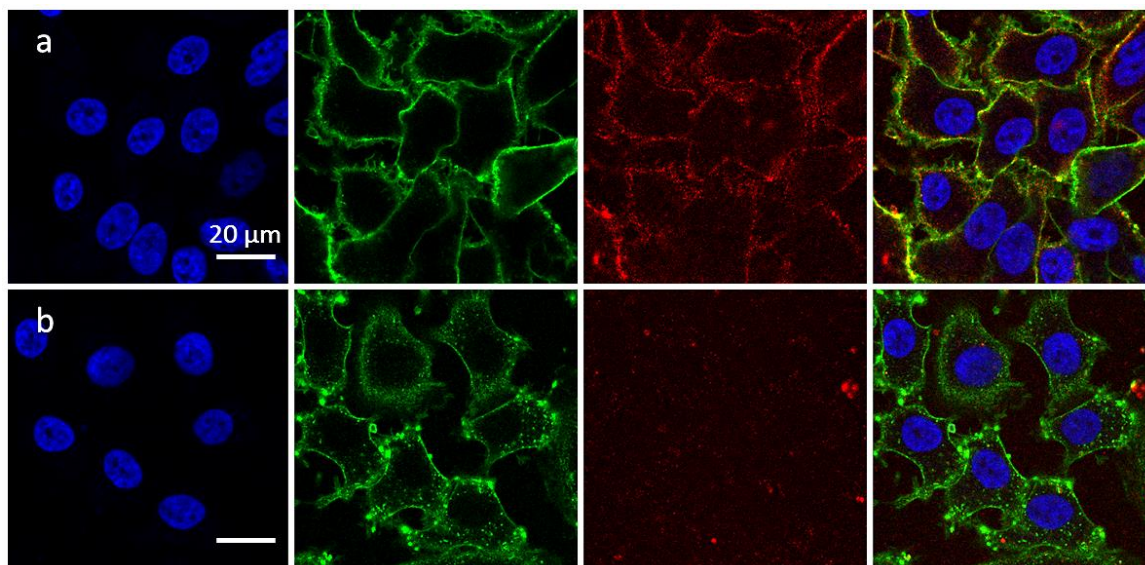


Figure 2.6. Confocal microscopy of purified antibody NEs targeting SKBr3 cells. (a) Antibody NEs group; (b) Biotinylated NEs group.

Article 3 – manuscript

Functionalization of lipid nanoemulsions with antibodies by green chemistry

Fei Liu,^{1,2} Bohdan Andreiuk,¹ Tesla Yudhistira,¹ Nicolas Anton,² Andrey S. Klymchenko²

¹Université de Strasbourg, Laboratoire de Bioimagerie et Pathologies, UMR 7021 CNRS, 74 route du Rhin, 67401 Illkirch (France)

²INSERM UMR 1260, Regenerative Nanomedicine (RNM), FMTS, CNRS 7199, CAMB, Université de Strasbourg, 67000 Strasbourg (France)

Introduction

Nanoemulsions (NEs) composed of biocompatible lipids and PEGs generally considered as green nanocarriers (NCs) for lipophilic drugs as well as dyes.^[1] With size ranging from 50 to 200 nm, and relatively long blood circulation period due to its structure similarity with lipid droplet and liquid nature. Some research formulated NEs with enhanced permeability and retention (EPR) effect, *i.e.* accumulating long-circulating particles in tumors. Those characteristics made NEs good candidate for image guided surgery and tumor targeting NCs. This encouraged researches to challenge further to formulate NEs bearing targeting moieties to make the targeting effect even more specific. Different targeting moieties were attempted to give NEs active targeting property, for example, (i) conjugating folic acid to the NEs surface make the droplets selectively internalized into folate receptor-positive cells;^[2] or (ii) conjugating Arginylglycylaspartic acid (RGD) on the surface, the NEs are capable to target $\alpha v \beta 3$ integrin rich cells.^[3] However, only a rare report shows functionalization of NEs with a low molecular weight antibody, scFv-Fc TEG4-2C (37 KDa) enabled direct MRI imaging of atherosclerosis in mice models.^[4] The development of dye-loaded NEs bearing a variety of antibodies for targeted optical imaging constitutes a promising research direction. Since the antibody and antigen binding is more specific and precise for different tumor types. In the present study, an universal way of modifying NEs surface with antibody by using green chemistry method was developed. The idea is to create the *in situ* reaction of a targeting ligand with a highly lipophilic molecule present in the oil core of the NEs. Nitrophenol-formate of Cholesterol was chosen as a reactive lipophilic entity for *in situ* reactions in NEs with amino-containing compounds (*e.g.*, Biotin-PEG₆₄-lysine derivative, ligand with linker). Cholesterol is a natural lipid compound, which make it attractive for formulating non-toxic NCs. In this design, we expect that PEG₆₄ inserted into the surfactant layer, while lysine, bearing two amines would react *in situ* with modified cholesterol. This design is expected to ensure that lysine coupled to two cholesterol units would remain anchored into oil core of the NEs droplet, while the biotin, connected through PEG₆₄ is trapped at the interface towards aqueous bulk phase. Then, this biotinylated-NEs will allow building biotinylated-NEs-streptavidin-biotinylated antibody sandwich, through a step by step addition streptavidin and biotinylated antibody to the NEs. As a result, NEs decorated with antibody will be obtained. *In situ* reaction was verified by chemical and spectra method, biotinylated-NEs was proved by glass surface staining and gel electrophoresis, and cell imaging to prove that the obtained NEs functionalized with antibodies and able to target cells overexpressing corresponding antigens. To summarize this study provides a green, spontaneous and universal way of conjugating antibody to NEs surface.

Results and discussion

Methodology of functionalization.

We aimed at developing NEs with decorated with antibodies to enable targeting tumor cell membrane with the corresponding antigen. Given liquid nature of the oil core, we considered that

efficient anchoring of large biomolecule at the surface, can only be achieved by a linking with a highly hydrophobic anchor counterpart. In our original design, we prepared reactive cholesterol derivative, (4-nitrophenyl) carbonate of cholesterol (NPC-Chol) and dissolved it in the oil core of NEs. We also synthesized a PEG linker bearing lysine moiety on one end and biotin on the other. The two amino groups of lysine would react *in situ* with NPC-Chol thus generating anchoring of PEG linker in the oil droplet's core, by two highly hydrophobic Chol moieties. Due to sufficiently long PEG₆₄ linker, we expect that the biotin moiety would be exposed well outside of NEs surface. Then, biotinylated antibody would be coupled to biotinylated-NEs through a Neutravidin (avidin analogue) bridge. The selected antibodies were cetuximab since they were commonly used for targeting EGFR on the surface of cancer cells.

NPC-Chol was synthesized in one step from cholesterol and p-nitrophenol-chloroformate in basic conditions.^[5] The biotin-PEG-Lys linker was synthesized in several steps, starting from mono-Boc protected PEG₆₄ diamine, followed by its coupling with biotin. Then, Boc group was removed in TFA and the obtained amine (1), which was reacted with Boc-protected lysine to yield conjugate 2. The latter was deprotected affording final linker biotin-PEG-Lys. The identity of the final compound was confirmed by NMR and mass spectrometry. To formulate NEs loaded with NPC-Chol, the latter was dissolved in vitamin E diacetate oil (6 wt.%), mixed with Kolliphor ELP[®] surfactant.

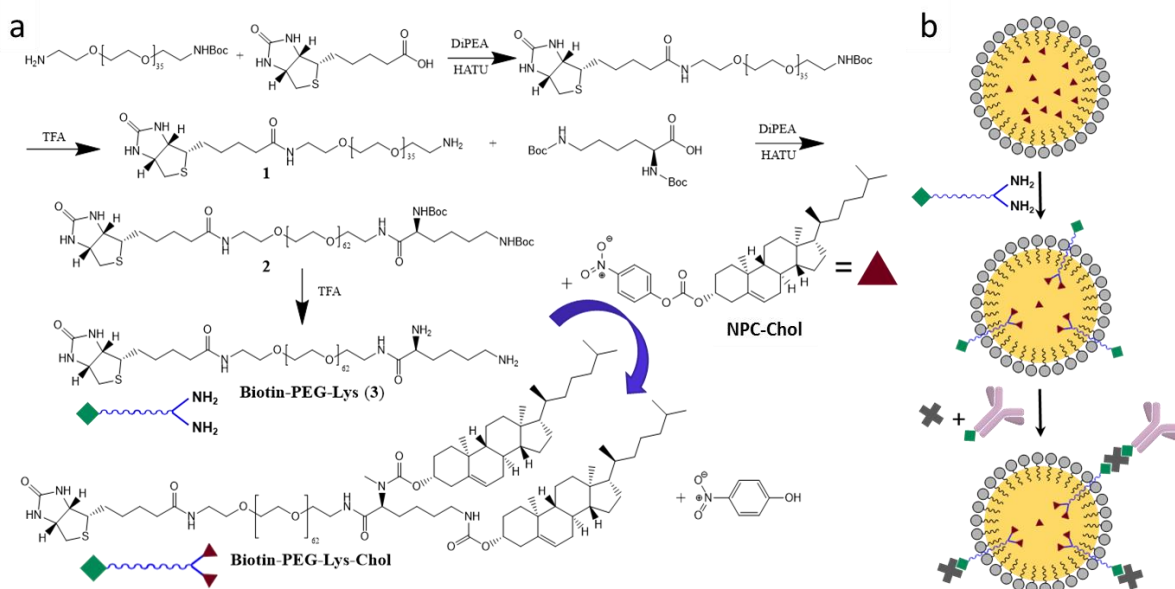


Fig. 1. Synthesis of the biotin-PEG-lysine linker (a) and its further application for functionalization of NEs with an antibody (b).

Model study of *in situ* reaction of NPC-Chol loaded NEs with ethanolamine

The possibility of the *in situ* reaction of NPC-Chol with an amine inside NEs was firstly tested by a reaction with model compound ethanolamine. Thanks to a side product nitrophenol in basic with a characteristic absorption band in an aqueous solution, we are able to monitor the reaction by photometry. In the presence of ethanolamine (Fig. S1), a strong increase in the absorbance was observed in comparison to the control group. The non-negligible absorbance of nitrophenol in the control could be caused by the slow degradation of NPC-Chol in pH 8.5 phosphate aqueous solution. Mass spectrometry of the organic phase extraction of the reaction mixture revealed the presence of the conjugate Chol-ethanolamine (Fig. S2), which provided a direct proof for the *in*

situ reaction of NPC-Chol with ethanolamine inside NEs.

***In situ* reaction of NPC-Chol loaded NEs with Biotin-PEG64-lysine**

Similarly to ethanolamine, biotin-PEG-Lys reaction with NPC-Chol is expected to form Chol conjugate and thus liberate the p-nitrophenol (Fig. 1). The reaction was again monitored by the yellow side product p-nitrophenol (Fig. S3). After reaction of NPC-Chol loaded NEs, with the linker biotin-PEG-Lys for 24 h, we observed a significant increase in the absorbance at 400 nm compared to the control (without linker). Then, to quench the non-reacted NPC-Chol, we incubated the mixture with an excess of ethanolamine, which led to further increase in the absorbance of p-nitrophenol. Assuming that after incubation with ethanolamine, 100% of NPC-Chol reacted with the amines, all of p-nitrophenol, we could estimate the reaction ratio for the reaction of NPC-Chol with biotin-PEG-Lys around 40 %. Based on the total NPC-Chol amount of 3 mg (6 wt.% in oil), the total concentration (in 1 mL) of reacted NPC-Chol was expected to be 2 mM. Since each biotin-PEG-lysine could react with 2 molecules of NPC-Chol, the total biotin concentration calculated to be ~1 mM.

Biotin NEs immobilization on glass surface with Neutravidin

Biotin is a water-soluble vitamin that forms a stable complex with avidin. Although the bond between the biotin and the avidin is not covalent, its dissociation constant is among the lowest in nature (K_d 10^{-14} mol L⁻¹). Thus, the biotin-avidin complex is commonly used in molecular biology and bio-nanotechnology for its rapid, efficient and robust bio-conjugation.^[6] Neutravidin is an analogue of avidin, which also shows high affinity to biotin, is frequently used for immobilization of biotinylated biomolecules on the surface.^[7,8] Therefore, we use it to verify whether the surface of NEs is decorated with biotin groups. For this purpose, as illustrated in the scheme (Fig. 2), the glass surface was first coated with BSA-biotin, followed by a layer of Neutravidin. With this surface at hand, we compared targeting specificity of biotinylated-NEs with control NEs without biotin. As showed in Fig. 2a, biotinylated-NEs were clearly visible on the glass surface by fluorescence microscopy in form of dots. The density of dots and the overall intensity on the images decreased with dilution of these NEs (Fig. 2a). The concentration dependence was confirmed by the analysis of the mean fluorescence intensity (Fig. 2d). In case of control non-modified NEs, fluorescence intensity was minimal for all tested dilutions, suggesting non-specific interaction for these NEs is negligible (Fig. 2b). Similar low binding of NEs was found for the Neutravidin surface initially pre-treated (blocked) with excess biotin, and then incubated with biotinylated-NEs (Fig. 2c). These results clearly show that the biotinylated-NEs were targeted to the glass surface through biotin-Neutravidin specific interaction, suggesting that NEs were successfully functionalized with biotin.

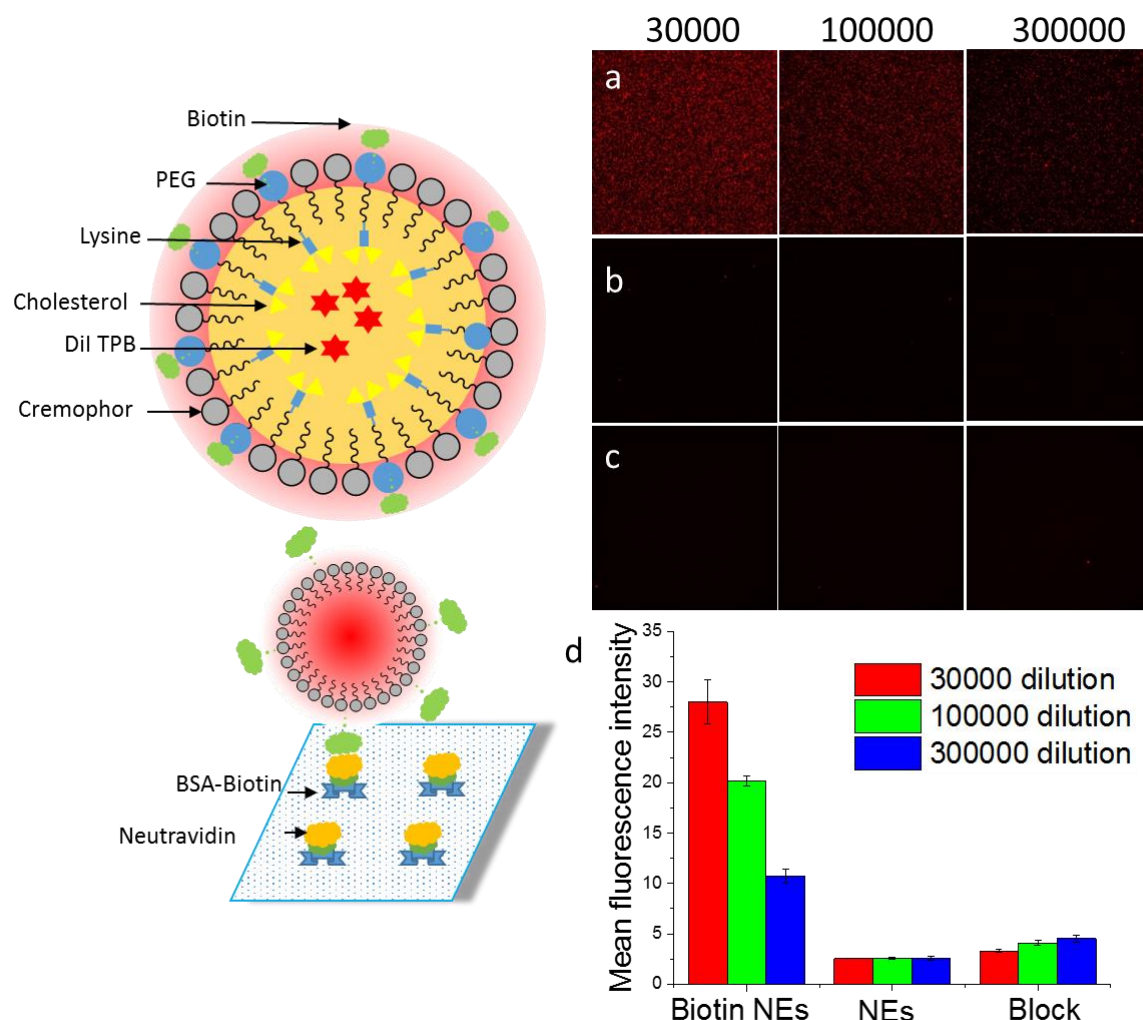


Fig. 2. Fluorescence microscopy of glass surface coated with BSA-biotin and Neutravidin and then incubated with NEs at three dilutions from the original formulation: 30000, 100000 and 300000-fold. Three conditions were tested: (a) Biotinylated-NEs; (b) Non-functionalized NEs; (c) Biotinylated-NEs with surface pre-treated with biotin competitor.

In order to assess the efficiency of the bio-conjugation of biotinylated-NEs with Cy5-streptavidin (analogue of Neutravidin), we chose to use electrophoresis gels revealed by fluorescence. To this endeavor, we used a fluorescently labeled streptavidin (Cy5-streptavidin), whereas the prepared biotinylated-NEs were loaded, at 750 times dilution, with a highly hydrophobic green emitting fluorophore, namely DiI-TPB (Fig. 2). The two complementary fluorophores using distinct green and red fluorescence channels allowed us to monitor both NEs and Cy5-streptavidin independently. The dye-loaded biotinylated-NEs were formulated as mentioned before, briefly, by *in situ* reaction of NPC-Chol inside dye-loaded NEs with biotin-PEG-Lys, and further purification by dialysis. With the pure dye-loaded biotinylated-NEs at hands, several experiments with appropriate controls were performed and analyzed by electrophoresis revealed by fluorescence (Fig. 3). First, we observed that streptavidin alone appeared as a red smearing spot (well 1). When non-biotinylated-NEs were mixed with Cy5-streptavidin (well 3), the red moving band was still observed, while the

green spot of NEs remains immobilize at the starting point, probably because these NEs are not charged. In the case of Cy5-streptavidin was mixed with the biotinylated-NEs (well 2), the green spot representing NEs disappeared, showing new moving band of yellow color, probably corresponding to NEs coated with Cy5-streptavidin. The excess of Cy5-streptavidin was also observed as for Cy5-streptavidin alone. The effect of the presence of free biotin (competitor) on the migration of the biotinylated-NEs was also investigated (well 4). The result showed that when the binding sites of streptavidin are occupied by free biotin, the biotinylated-NEs did not migrate, thus proving that the interaction of NEs with Cy5-streptavidin observed in well 2 is biotin-specific. Controls were also conducted to study the migration of biotinylated or non-biotinylated-NEs (well 5 and 6) without streptavidin, or biotinylated-NEs in the presence of excess biotin (well 7). As expected, NEs did not show migration on the gel in all these three cases.

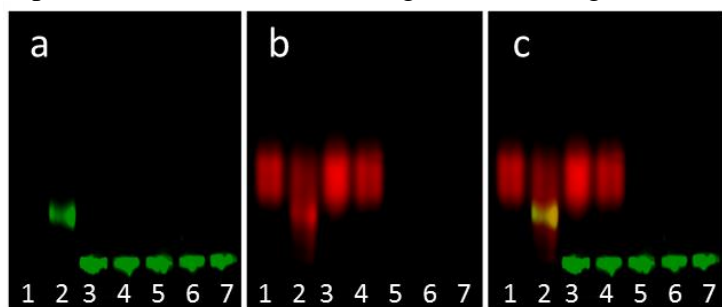


Fig. 3. Electrophoresis profile of biotinylated-NEs mixed with Cy5-streptavidin and its controls. (a) Cyanine 3 channel for imaging DiI-TPB loaded NEs; (b) Cyanine 5 channel for imaging Cy5-streptavidin; (c) Merged channel of (a) and (b). Content of the wells is: (1) Cy5-streptavidin, (2) Cy5-streptavidin + biotinylated-NEs, (3) Cy5-streptavidin + control NEs, (4) Cy5-streptavidin + biotin + biotinylated-NEs, (5) biotinylated-NEs (6) Control NEs, (7) biotinylated-NEs + biotin.

Size exclusion chromatography for purification of functionalized NEs

Our ultimate goal is to modify NEs with antibodies. However, this would require a method a purification of NEs functionalized with Abs from non-conjugated Abs. For this purpose, we tested size exclusion chromatography using Sephacryl S300 HR gel, which is specially adapted for separating relative large macromolecules or globular proteins in the range 10 to 150 KDa. We started with model experiments to separate non-conjugated Cy5-streptavidin from functionalized NEs. DiI-TPB loaded NEs with (or without for control) biotin ligand was mixed with Cy5-streptavidin and further subjected to size exclusion chromatography. Different fractions were collected and checked by fluorescence spectroscopy and electrophoresis.

According to the emission spectra of initial colored fractions of elution, the relative fluorescence intensity of DiI and Cy5 firstly followed similar decline tendency in the first three tubes (Fig. S4c). This confirms that a DiI loaded NEs functionalized with Cy5-streptavidin was first eluted. Then, the fluorescence intensity of DiI from NEs continued to decline, while the fluorescence intensity of Cy5 from streptavidin-Cy5 increased. This second part resulted from free Cy5-streptavidin having a longer retention time. Excess of Cy5-streptavidin, eventually, came out as the final fractions. Gel electrophoresis confirmed these observations conclusions (Fig. 4a) with a good co-localization of functional NEs and Cy5-streptavidin (yellow in merged image) that was observed in the first tubes, with progressive decline of both signals. In contract, Cy5-streptavidin showed significant increase reaching maximal values in the fraction 5, where no sign of NEs was observed. In case of control NEs (Fig. 4b), no co-localization band was observed, with green fluorescence from NEs observed at the early fractions and red fluorescence of Cy5-streptavidin in the final

fractions. The electrophoresis data confirmed successful separation of NEs grafted with Cy5-streptavidin using size-exclusion chromatography.

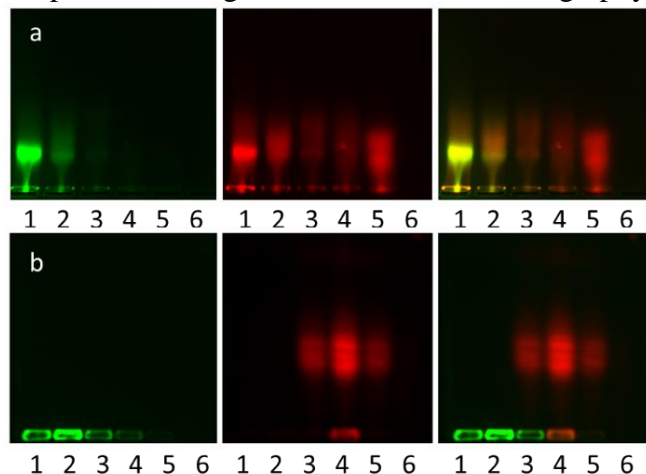


Fig. 4. Electrophoresis profile of elution fractions collected from size exclusion chromatography of biotinylated-NEs (a) and control NEs (b). Green is DiI channel; red is Cy5 channel.

Determination of biotin to antibody ratio

To eventually bind antibody through the biotin NEs-Neutravidin-biotinylated antibody sandwich structure to the NEs surface, biotinylated antibody was first prepared. For this purpose, biotin was conjugated with cetuximab using EDC-chemistry. The conjugate was further purified by ultrafiltration using 50 kDa filter in order to remove low-molecular weight reagents. Then, excess of Cy5-streptavidin was coupled with the biotinylated Abs, assuming that each Cy5-streptavidin molecule could conjugate with one biotin. Then, the ratio of biotin to antibody could be calculated through absorbance from Cy5 and proteins (Fig. S5). To perform these measurements, excess of non-reacted Cy5-streptavidin was removed by ultrafiltration using 100 kDa filter. According to our estimation (calculation in supporting information), the obtained the ratio of Cy5-streptavidin to cetuximab of 2.8, which should also correspond to biotin to antibody ratio.

Confocal microscopy imaging of NEs-Abs conjugate for targeting SKBr3 cells

To evaluate specific targeting capacity of NEs conjugated with cetuximab, we performed fluorescence microscopy experiments on SKBr3 cell line, which is known to overexpress EGFR. For this purpose, we first performed a sequential labelling method, where the cell were step by step treated with biotinylated cetuximab, Neutravidin, and finally biotinylated-NEs, with washing after each step. To colocalize NEs with the membrane surface, plasma membrane marker WGA-Alexa488 was used. According to Fig. S6a, strong red fluorescence from cetuximab-NEs was observed, which colocalized well with green membrane marker WGA-Alexa488. The 3D image reconstruction of the confocal image stacks confirmed the presence of NEs on the cell surface (Vedio S1). Importantly, in case of non-functionalized NEs and biotinylated-NEs in the presence of excess of biotin competitor, the red signal at the cell surface was negligible, indicating relatively low non-specific interactions of NEs with cells. These results indicate that cetuximab-NEs were successfully targeted to the membrane of SKBr3 cells through cetuximab using a biotin-Neutravidin coupling strategy.

We also explored a possibility to prepare NEs with grafted antibody by purification with size exclusion chromatography, validated before with Cy5-streptavidin. Cell experiments was

conducted to test the efficacy of purified NEs with antibody surface (loaded with 1 wt.% of DiD-TPB). In this case, the nucleus of cells was stained with Hoechst 33342 (20 μ M in Opti-Mem). Then, cells were directly incubated with purified cetuximab-NEs conjugate (loaded with 1% DiD-TPB) or biotinylated-NEs (1% DiD) as a control. The incubation was conducted on ice for 3 hours to prevent internalization and then, before imaging, cell membrane was stained with WGA (5 μ g/mL) over 5 min.

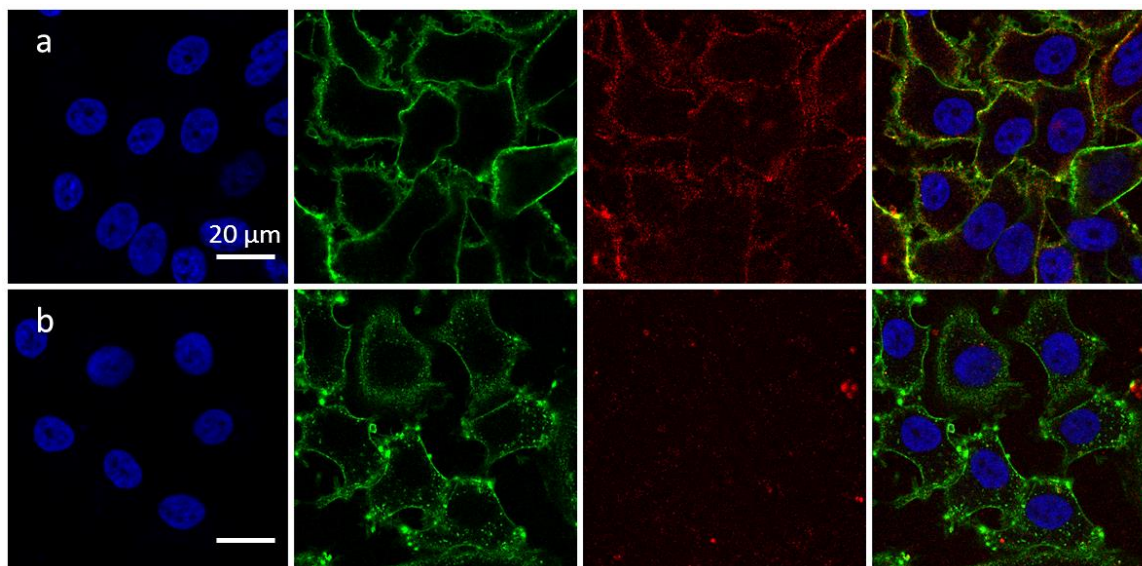


Fig. 5. Confocal microscopy of purified NEs functionalized with (or without for control) cetuximab targeting SKBr3 cells. (a) Purified cetuximab-NEs group (100 times diluted); (b) Purified biotinylated-NEs group (100 times diluted).

According to the confocal microscopy, cetuximab-NEs gave red fluorescence at the cell surface, which was co-localized well with green fluorescence from membrane marker by WGA-Alexa488 (Fig. 6a). The control biotinylated-NEs without Abs showed negligible signal, indicated low non-specific off-target binding of NE to the cell surface (Fig. 6b). These results suggested that the purified cetuximab-NEs targets SKBr3 cell membrane through antigen-antibody specific interaction.

Conclusions

Functionalization of lipid NEs with biomolecules for specific targeting remains a challenge. Here, we developed an original strategy to graft antibodies on the surface of NEs, using *in situ* green chemistry approach and biodegradable linkers. For this purpose, we synthesized a reactive derivative of cholesterol, cholesteryl (4-nitrophenol) carbonate (NPC-Chol), can be readily encapsulated in the oil core of NEs and react *in situ* with amines. We also designed biotin-PEG-Lys linker with two amino groups of lysine at one end for *in situ* reaction with NPC-Chol to be covalently grafted to two highly lipophilic cholesterol units, ensuring its strong anchorage in the nanodroplet. On the other end of the linker, long hydrophilic PEG₆₄ is expected to expose biotin moiety at NEs surface for further grafting antibody using biotin-streptavidin coupling. In this work we formulated lipid NEs size ranging from 100 nm to 130 nm. In a first time, the *in situ* reaction between amine and NPC-Chol was proved with ethanolamine, with identifying the conjugate formed Chol-ethanolamine. Then NEs were modified with biotin using biotin-PEG-Lys, which

according to the production of the nitrophenol, reacted with 40 % of encapsulated NPC-Chol. Fluorescence microscopy showed that the biotinylated-NEs could be targeted to the Neutravidin modified glass surface in contrast to non-modified NEs, a result confirmed by gel electrophoresis analysis. Then, the obtained biotinylated-NEs loaded with fluorescent dyes were used to target EGFR on the surface of SKBr3 cells according to a sequential protocol using biotinylated antibody cetuximab, streptavidin and biotinylated-NEs. These *in vitro* results achieved to confirm the efficiency of approach worked out in this study, showing the specificity of the active targeting of NEs droplets into cells. This approach turned to give highly efficient labelling of cell surface in a receptor specific manner. We also explored a possibility to purify NEs conjugates with grafted antibody using size exclusion chromatography. In model experiments, we found efficient separation of Cy5-streptavidin-biotinylated-NEs conjugate from excess of Cy5-streptavidin. We used the same method to purify cetuximab-NEs from excess cetuximab and Neutravidin. Confocal microscopy indicated that purified NEs are still capable to target on SKBr3 cell membrane, in contrast to control NEs without antibody. In the next steps, we plan application of these NEs for *in vivo* targeting of cancer cells. Functionalization of NEs allowed combining the high encapsulation properties with the surface modification necessary for designing targeted drug delivery systems. These tunable functionalized NEs systems provide a platform for conjugation of different targeting ligands and encapsulation of a large variety of contrast agents and drugs and thus can be used for imaging, therapeutic and targeted drug delivery applications.

- [1] A. S. Klymchenko, F. Liu, M. Collot, N. Anton, *Adv. Healthc. Mater.* **2021**, *10*, 2001289.
- [2] A. Loureiro, E. Nogueira, N. G. Azoia, M. P. Sárria, A. S. Abreu, U. Shimanovich, A. Rollett, J. Härmak, H. Hebert, G. Guebitz, et al., *Colloids Surfaces B Biointerfaces* **2015**, *135*, 90.
- [3] A. Karageorgis, S. Dufort, L. Sancey, M. Henry, S. Hirsjarvi, C. Passirani, J. P. Benoit, J. Gravier, I. Texier, O. Montigon, et al., *Sci. Rep.* **2016**, *6*, 1.
- [4] G. Prévot, M. Duonor-Cérutti, M. Larivière, J. Laroche-Traineau, M. J. Jacobin-Valat, P. Barthélémy, G. Clofent-Sanchez, S. Crauste-Manciet, *Data Br.* **2017**, *15*, 824.
- [5] M. Vangala, G. P. Shinde, *BEILSTEIN J. Org. Chem.* **2016**, *12*, 2086.
- [6] F. Nau, C. Guérin-Dubiard, T. Croguennec, *Bioact. Egg Compd.* **2007**, 75.
- [7] N. Melnychuk, A. S. Klymchenko, *J. Am. Chem. Soc.* **2018**, *140*, 10856.
- [8] J. R. Wayment, J. M. Harris, *Anal. Chem.* **2009**, *81*, 336.

Supporting information

Functionalization of lipid nanoemulsions with antibodies by green chemistry

Fei Liu,^{1,2} Bohdan Andreiuk,¹ Tesla Yudhistira,¹ Nicolas Anton,² Andrey Klymchenko²

¹Universit8 de Strasbourg, Laboratoire de Bioimagerie et Pathologies, UMR 7021 CNRS, 74 route du Rhin, 67401 Illkirch (France)

²INSERM UMR 1260, Regenerative Nanomedicine (RNM), FMTS, CNRS 7199, CAMB, Universit8 de Strasbourg, 67000 Strasbourg (France)

Conjugation of Abs with biotin Experiment General Remarks

Conjugation experiments were carried out in the Eppendorf, DNA low-binding tube 1.5 mL at atmospheric pressure at room temperature unless otherwise stated. All buffer solutions were prepared with deionised water and filter-sterilised prior to use. Borate buffer was prepared from 25 mM sodium tetraborate, 25 mM NaCl, and 1 mM EDTA at pH 8.1 or 8.4. Phosphate-buffer saline (PBS) was 140 mM NaCl and 12 mM sodium phosphate at pH 7.4. Sodium azide 0.5% (w/v) was prepared by dissolving 5 mg of sodium azide in 1 mL of water. Ultrapure DMF (analytical reagent grade) was purchased from Fischer Chemical. Solutions of tris(2-carboxyethyl) phosphine hydrochloride (TCEP) 10 mM (2.87 g/mL) were prepared in borate buffer. pH 8.5 phosphate buffer was prepared by dissolving 3.5 g of dipotassium hydrogen phosphate and 4.5 g of sodium chloride in 500 mL of water. pH was adjusted with diluted phosphoric acid. Ultrafiltration was carried out in vivaspin 500 polyethersulfone (PES) membrane concentrator with a molecular weight cut-off (MWCO) of 50 kDa. Centrifugation was carried out on an Eppendorf mini spin operating at 12.000 rpm at room temperature.

cetuximab is a chimeric IgG1 full length antibody directed against EGFR overexpresses in SKBr3 cells. The antibody was obtained from ERBITUX as 5 mg/mL solution (ERBITUX). The buffer exchange of antibody was carried for borate buffer pH 8.1 via ultrafiltration (MWCO 50 kDa, vivaspin). Concentration of antibody was determined by UV-vis absorbance ($\epsilon_{280} = 210.000 \text{ M}^{-1} \text{ cm}^{-1}$ for cetuximab mAb), adjusted to 33 μM (5.0 mg/mL) and stored as aliquots at 4 °C.

Conjugation of cetuximab with biotin-NHS ester

The antibody-biotin conjugate was prepared through a modification of a reported protocol^[360]. cetuximab (32 μM , 500 μL) was prepared in the sodium carbonate buffer pH 8.4. Next, biotin-NHS ester was prepared in DMSO (100 mM, 5 μL) and added to the cetuximab. The reaction was incubated at 24°C overnight, rotating at 240 rpm. Afterwards, excess reagent was removed by ultrafiltration (50 kDa MWCO) with PBS to afford the modified antibody-biotin in PBS.

Afterward, sodium azide 0.5% (w/v) was added to make the final concentration of 0.05% (w/v) for conservation; this agent was removed by ultrafiltration (50 KDa) before each use.

Conjugation of cetuximab-biotin with streptavidin-Cy5

Firstly, absorbance of Cy5-streptavidin (17 μ M, 35 μ L, 0.60 nmol) in PBS buffer (1 mL) was tested. Then, the cetuximab-biotin (33 μ M, 40 μ L, 0.132 nmol) in PBS buffer (20 mM, pH 7.4) was added. Cy5-streptavidin (17 μ M, 35 μ L, 0.60 nmol) in PBS buffer (1 mL). The reaction was incubated at 24 °C in a shaker at 450 rpm for 2 h. Afterwards, excess reagent was removed by ultrafiltration (100 kDa MWCO) with PBS. Absorbance was measured before and after the process of ultrafiltration.

Determination of fluorophore to antibody ratio (FAR)

UV-vis spectra measurements were recorded on a Cary 4000 Scan UV-visible spectrophotometer (Varian) operating at room temperature. Sample buffer was used as blank for baseline correction. Calculation of Cy5, antibody ratio (FAR) follows the formula presented below with $\epsilon_{\text{cetuximab}} = 210,000 \text{ M}^{-1} \text{ cm}^{-1}$ for cetuximab, $\epsilon_{657} = 250,000 \text{ M}^{-1} \text{ cm}^{-1}$ for Cyanine-5 and 0.03 as a correction factor (cf_{280}) of the dye absorption at 280 nm. According to the absorbance spectra of Cy5-streptavidin, $Abs_{657}=0.57$, $Abs_{280}=0.34$. Based on the equation $Ab_{s657}=n \cdot c_{\text{strep}} \cdot \epsilon_{\text{Cy5}}$ number of Cy5 per streptavidin was calculated as 3.9. The absorbance of streptavidin at 280 nm was corrected to 0.32 using the equation $Ab_{s280\text{strep}}=Ab_{s280}-Ab_{s657} \cdot cf_{280}$. According to the equation $Ab_{s280\text{strep}} = c_{\text{strep}} \cdot \epsilon_{\text{strep}}$, the extinction coefficient of streptavidin (ϵ_{strep}) was calculated as $550,000 \text{ M}^{-1} \text{ cm}^{-1}$. After filtration, according to the equation $Ab_{s657}=3.9 \cdot c_{\text{strep}} \cdot \epsilon_{\text{Cy5}}$, the concentration of streptavidin was calculated to be 238 nM. Then, according to the equation of $Ab_{s280\text{strep}}+Ab_{s280\text{cetuximab}}=Ab_{s280}-Ab_{s657} \cdot cf_{280}$, $Ab_{s280\text{strep}} = c_{\text{strep}} \cdot \epsilon_{\text{strep}}$ and $Ab_{s280\text{cetuximab}} = c_{\text{strep}} \cdot \epsilon_{\text{cetuximab}}$. The concentration of cetuximab was calculated as 92.1 nM, slightly decreased from the original 100 nM, this is probably due to slight precipitation during the ultrafiltration process. $FAR=c_{\text{strep}}/c_{\text{cetuximab}}=2.8$.

General protocol for nanoemulsions (NEs) formation

NEs were produced by spontaneous nanoemulsification: the cargo (3 mg NPC-NPC-Chol, 1 eq and certain percentage of dyes, 1 wt.% of Cy5.5-TPB, 1 wt.% of DiD-TPB or 1 wt.% of DiI-TPB with respect to oil in cases of dye loaded NEs) were dissolved in Vitamin E acetate (50 mg) and placed in sonication bath at 40 °C for 10 min. Then, the surfactant Kolliphor ELP® was added (50 mg), and the mixture was homogenized under magnetic stirring (400 rpm) under 40 °C for 10 min to complete homogenization. Finally, NEs were generated by addition of 40 °C ultrapure (Milli-Q) water (230 μ L) on a heat-shaker (1400 rpm, 40 °C).

In situ reaction of NPC-CholNPC-Chol loaded NEs with an amine

To 100 μ L of NPC-Chol loaded (6 wt.%) NEs, 5 μ L ethanolamine was added (or not for control), followed by addition of pH 8.5 phosphate buffer (0.2 M) to final volume of 500 μ L. Reaction was conducted in a heat-shaker vortexed at speed of 500 rpm over 6 h under 40 °C. Absorption spectra of 100 times diluted NEs solution was checked for the sample and the control. After the reaction, the resulting mixture was dialyzed (membrane cut off size of 14 KDa) in Milli-Q water for 24

hours with changing of medium every 8 hours. After this process, the solution was extracted by 500 μ L DCM by centrifugation. Organic phase was examined by mass spectrometry.

Preparation of NEs functionalized with biotin (Biotin-NEs)

In situ reaction of 330 mg of NEs (containing NPC-Chol at 6 wt.%) with (or without for control) 50 mg biotin-Peg-lysine was conducted by mixing them to final volume of 1 mL by pH 8.5 buffer and vortexing at speed of 500 rpm over 24 hours under 40 °C. After reaction, 10 μ L ethanolamine was added. The mixture was incubated further for 4 hours to consume the excess NPC-Chol. Absorption spectras were checked after reaction and after adding ethanolamine in order to calculate the reaction ratio. Control NEs were prepared by mixing NPC-Chol (6 %) loaded NEs with excess of ethanolamine (40 mM) to final volume of 1 mL of pH 8.5 buffer and further measured the absorbance. Dialysis using membrane (Mw 14 KDa) in Milli-Q water was conducted in the end, to remove the reagents and the side product nitrophenol.

Biotin-NEs immobilization protocol

8 well LabTek® chambers were washed 3 times with PBS and incubated with 200 μ L BSA-Biotin (0.5 mg/mL) for 5 min. Then, BSA-Biotin was removed, the chambers were washed 3 times with PBS and replaced by 200 μ L of 30000, 100000 and 300000 times diluted Biotin-NEs and control of the original NEs (particle concentration of 300 nM). Then, the NEs were incubated in darkness at room temperature for 30 min. For biotin competition experiment, 200 μ L of biotin (0.5 mg/mL) were added and incubated for 30 min and washed with PBS 3 times before adding 200 μ L of Biotin-NEs and further incubated for 30 min. All samples were washed with Mili-Q water 2 times with PBS before final measurement.

Electrophoresis

The electrophoresis was performed on 0.5% agarose gel in trisacetate EDTA (TAE). 12 μ L of each solution was added into the wells and subjected to electrophoresis for 30-60 min at 125 V in darkness. The gels were analyzed with a gel imager (LAS 4000) using two different channels. Cy5-Streptavidin was monitored by excitation at 630 nm and with an emission filter at 670 nm, FWHM 10 nm. DiI-TPB loaded NEs were monitored by excitation at 540 nm and using a bandpass emission filter at 570 nm. The exposure time for each picture was set at 10 sec. The images were processed and analyzed by using ImageJ software. To perform gel electrophoresis, the following solutions were prepared: (1) Cy5-streptavidin (9 μ M); (2) Biotinylated-NEs + Cy5-streptavidin (9 μ M); (3) Control NEs (750 times diluted) + Cy5-streptavidin (9 μ M); (4) biotinylated-NEs + free biotin (200 mM)+Cy5-Streptavidin (9 μ M); (5) Biotinylated-NEs (750 times diluted, max biotin concentration of 8 μ M); (6) Control NEs (NPC-Chol containing NEs neutralized by ethanolamine, 750 times diluted); and (7) biotinylated-NEs (maximum biotin concentration of 8 mM) + free biotin (200 mM) .

Preparation of NEs functionalized with antibody

DiD-TPB (1% in oil) loaded biotinylated-NEs were mixed with Neutravidin (67 μ M, 2 eq by volume) and incubated in room temperature for 3 h. Then, biotinylated cetuximab (33 μ M, 2 eq by volume) was added to the mixture and incubated in room temperature for 5 h. Then, the sample

was subjected to size exclusion chromatography. Sephacryl S-300 High Resolution resin (in ethanol) was used for the size exclusion purification of NEs functionalized with an antibody. Column loading was performed as listed in the instruction of the provider. Briefly, the resin was filled in 1.5 cm diameter (30 cm) column, then, ethanol as preserving agent of the gel was removed by pH 7.4 PBS buffer at speed of 150 cm/h for 3 column volumes. Then, the tap of the column was closed and placed still overnight. Finally, 100 μ L of sample was loaded to the column and eluted at speed of 150 cm/h, fractions were collected by Fraction Collector Frac-920 (2 mL/fraction).

Evaluation of size exclusion for the purification of functional NEs

Conjugation of biotinylated-NEs loaded by DiI-TPB (1%) with Cy5-streptavidin (5 eq by volume, 17 μ M) was conducted in room temperature for 5 h. In the control NEs, biotinylated-NEs were substituted by the same volume of neutralized and dialyzed NEs (loaded with 1 wt.% DiI-TPB and 6 wt.% NPC-Chol (with respect to oil), neutralized by excess of ethanolamine and dialyzed with membrane cut off size of 14 KDa). The two samples were subjected to size exclusion chromatography (see above), then, several fractions were checked by fluorescence spectroscopy (at Cy3 channel and Cy5 channel, respectively) and gel electrophoresis. For Cy3 channel, excitation was conducted under wavelength of 520 nm, emission was collected in the wavelength range of 550-750 nm, while for Cy5 channel, excitation was conducted under wavelength of 620 nm, emission was collected in the wavelength range of 650-750 nm.

Dynamic light scattering

The hydrodynamic diameters and polydispersity index (PDI) of the NEs were measured, in triplicate, by dynamic light scattering (DLS) along with zeta potential measurement using a Malvern Nano ZS instrument (Malvern Instruments, Orsay, France), equipped with a helium–neon laser (4 mW) operating at 633 nm, with a scatter angle of 173° and the temperature maintained at 25 °C.

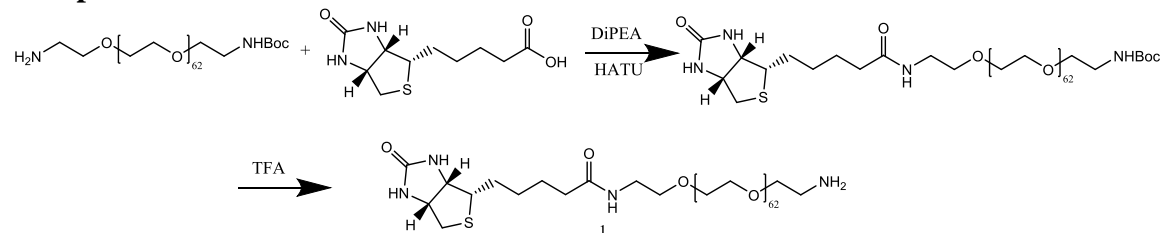
Cell experiments

SKBr3 cells were grown in Dulbecco's modified Eagle's medium (DMEM, Gibco-Invitrogen), supplemented with penicillin (100 U/mL), 1% glycan (100 U/mL) and 10 % FBS at 37 °C in a humidified atmosphere containing 5% CO₂. 4000 cells per well of cells was later split on 8 well LabTec with coverlid and incubated over 2 days for imaging experiments. The first experiment was conducted in the following order to observe the capability of Biotinylated-NEs to attach on cell surface with Neutravidin surface. Before the experiment, cell nucleus was stained with Hoechst 33342 (20 μ M in Opti-Mem). For the sequential protocol, firstly, cells were incubated with (or without for controls) biotinylated antibody (60 pM in Opti-Mem) for 30 min, then washed with PBS to remove excess of biotinylated antibody. After this, the medium was changed (or not for biotin NEs control) to Neutravidin (80 pM in Opti-Mem) and further incubated for 30 min and washed with PBS to remove excess Neutravidin. Finally, cells were incubated with 100 times diluted biotinylated NEs (with 1 wt.% of DiI-TPB) and incubated on ice for 1 hour. For purified NEs functionalized with antibody, cells were incubated with 100 times diluted NEs functionalized

with (or without for control) antibody. Before imaging, cell membrane was stained with WGA (5 $\mu\text{g/mL}$) over 5 min.

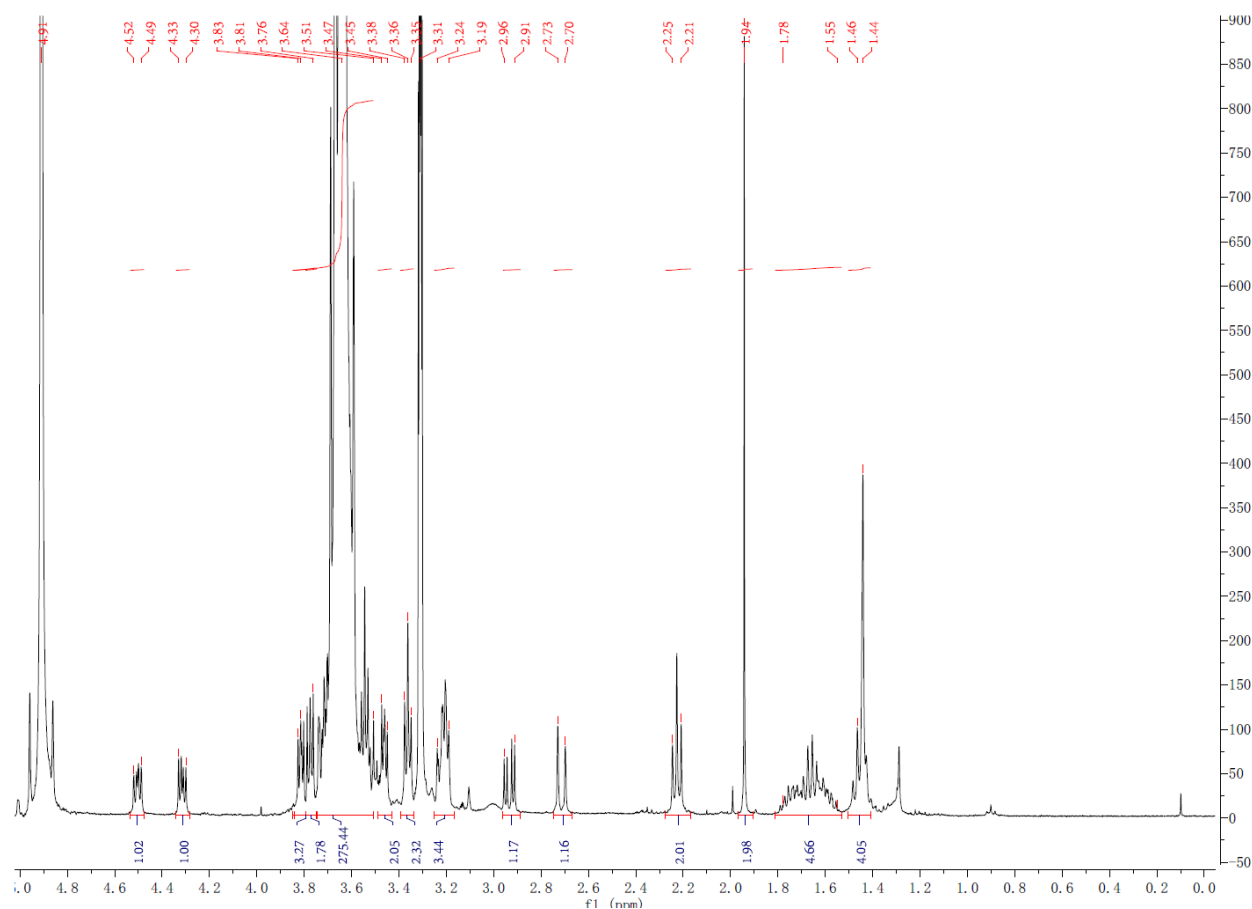
Synthesis

Compound 1

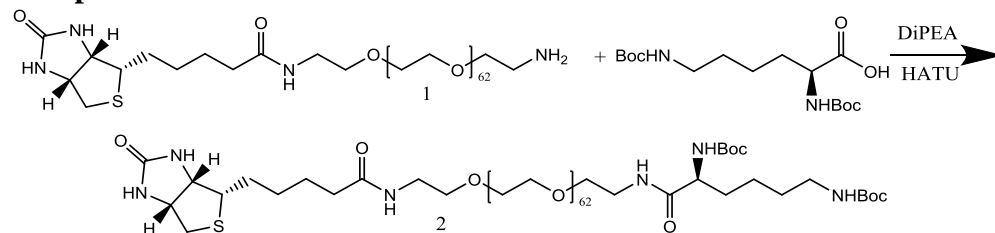


To a solution of PEG3000 amine (100 mg, 0.033 mmol) and biotin (24 mg, 0.1 mmol) in DMF, HATU (30 mg, 0.079 mmol) and TEA (60 μL) were added. The reaction mixture was stirred under 40 $^{\circ}\text{C}$ overnight. The resulting solution was then concentrated in vacuum and purified by dialysis in water (dialysis membrane molecular cut off weight: 2000 Da). After dialysis, 110 mg product in the form of light yellow liquid was obtained after evaporation. The resulting compound was vigorously stirred in 20% TFA/DCM solution for 3 h. The reaction solution was then concentrated and dried in vacuum to afford compound 2 (93 mg) as light-yellow lipid.

^1H NMR (400 MHz, MeOD) δ 4.52-4.49 (q, 1H), 4.33-4.30 (q, 1H), 3.83-3.35 (m, ~286H), 3.24-3.19 (m, 3H), 2.96-2.91 (q, 1H), 2.73-2.70 (d, 1H), 2.24-2.20 (t, 2H), 1.79-1.56 (m, 4H), 1.55-1.44 (t, 2H).

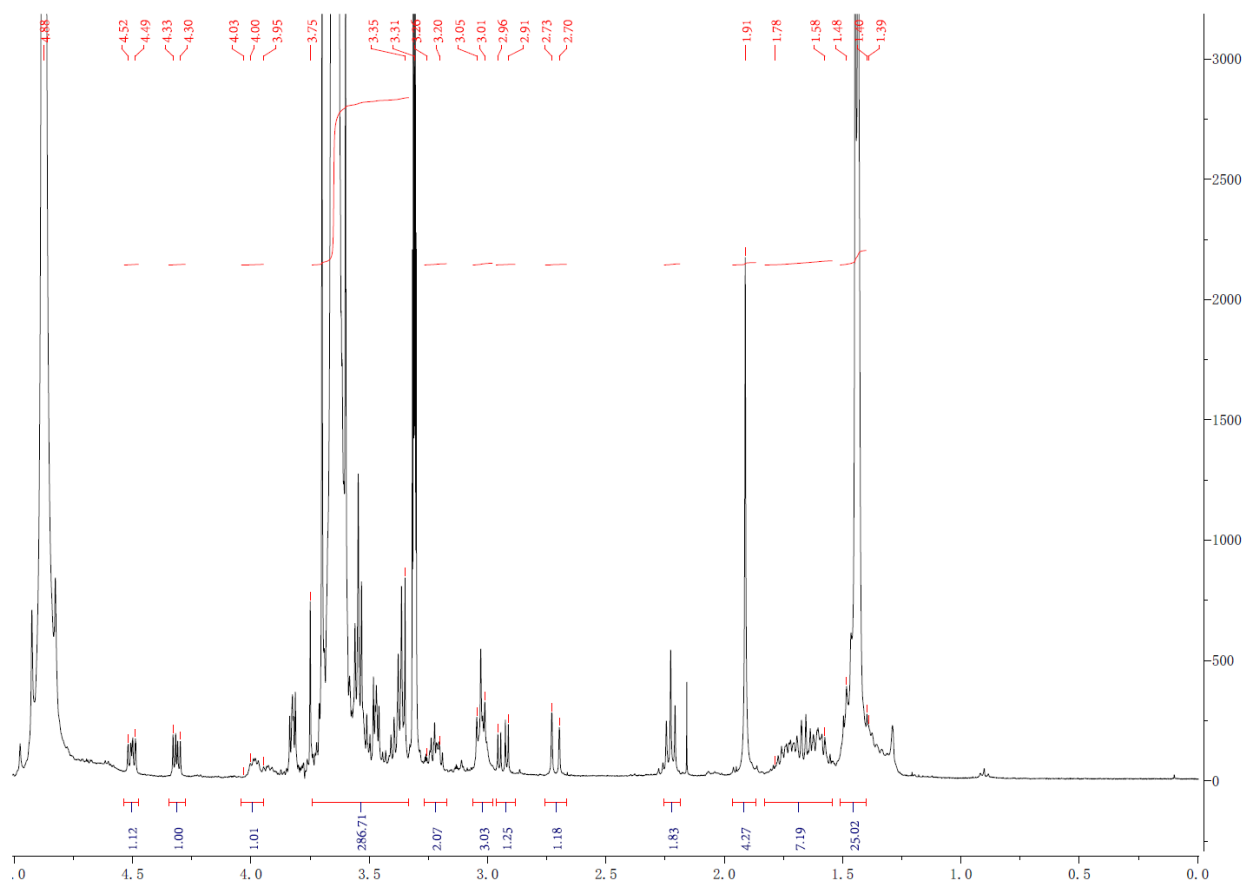


Compound 2

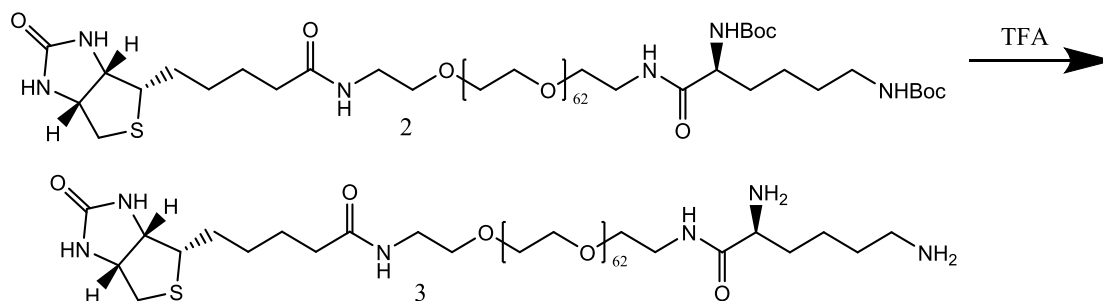


To a solution of compound **1** (50 mg, 0.016 mmol) and Boc-lysine-OH (12 mg, 0.05 mmol) in DMF, HATU (15 mg, 0.04 mmol) and triethylamine (30 μ L) were added. The reaction mixture was stirred under 40 $^{\circ}$ C overnight. The resulting solution was then concentrated in vacuum and purified by dialysis in water (dialysis membrane molecular cut off weight: 2000 Da). After dialysis, 53 mg product in the form of colorless lipid was obtained after evaporation.

^1H NMR (400 MHz, MeOD) δ 4.51-4.47 (q, 1H), 4.33-4.30 (q, 1H), 4.01-3.95 (m, 1H), 3.83-3.34 (m, ~286 H), 3.26-3.21 (d, 2H), 3.04-3.01 (t, 3H), 2.96-2.91 (q, 1H), 2.73-2.70 (d, 1H), 2.24-2.20 (t, 2H), 1.79-1.55 (m, 8H), 1.49-1.39 (m, 22H).

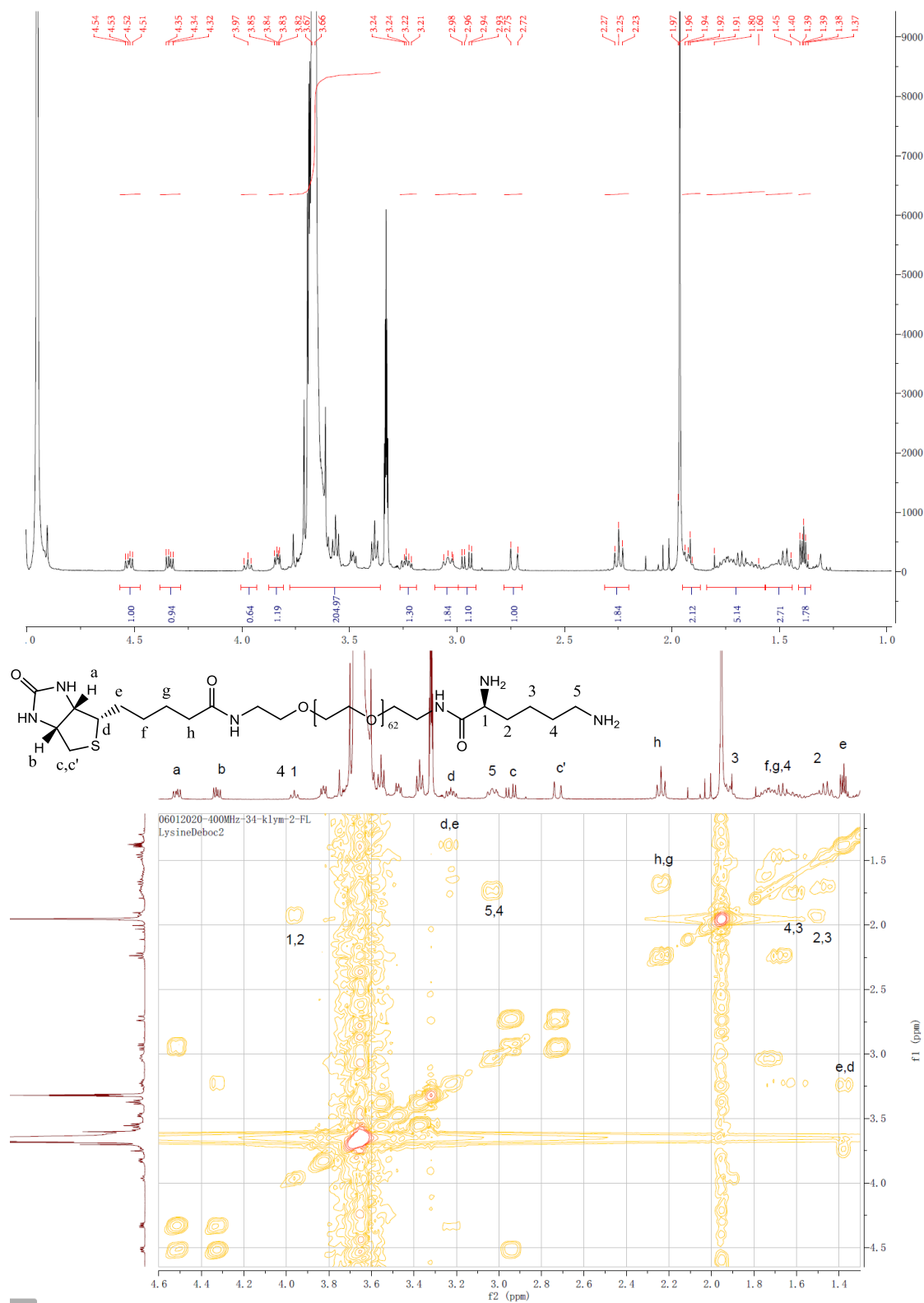


Compound 3



Compound **2** (53 mg) was vigorously stirred in 1 mL 20% TFA/DCM solution for 3 h. The reaction solution was then concentrated and dried in vacuum to afford compound **4** (46 mg) as light yellow lipid.

^1H NMR (400 MHz, MeOD) δ 4.54-4.94 (d, 1H), 4.35-4.32 (d, 1H), 4.50-3.97 (t, 1H), 3.75 – 3.41 (m, ~200 H), 3.24-3.21 (m, 1H), 3.15-3.05 (t, 2H), 2.97-2.93 (dd, 1H), 2.75-2.72 (d, 1H), 2.27-2.23 (t, 2H), 1.94-1.92 (q, 2H), 1.91-1.60 (m, 6H), 1.59-1.45 (q, 2H), 1.39-1.37 (m, 2H). $\text{C}_{144}\text{H}_{286}\text{N}_6\text{O}_{66}$ (3187.92) Mass detected: 1617.70 and 1086.09 (calc.: $(\text{M}+2\text{Na}+)/2=1616.96$ and $(\text{M}+3\text{Na}+)/3=1085.64$).



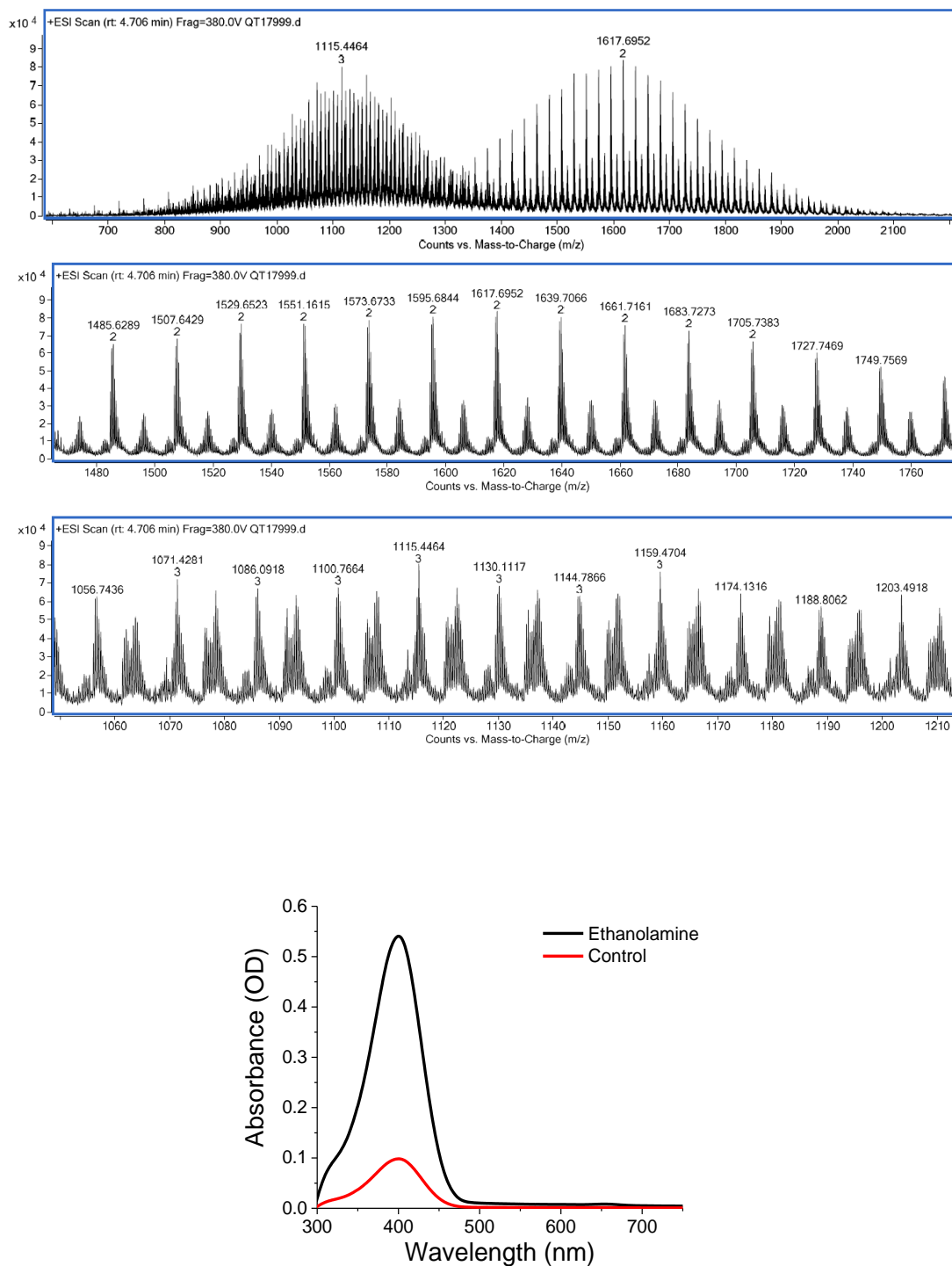
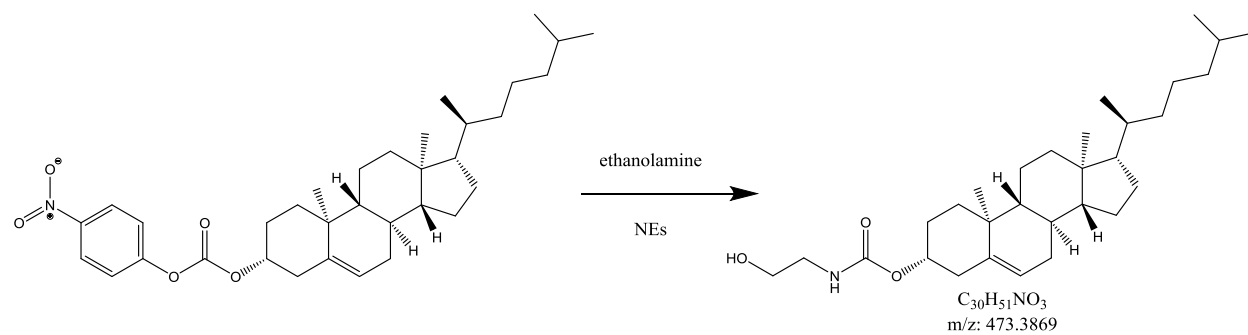


Fig. S1. Absorbance spectra after NPC-Chol containing NEs reacted with (or without for control) ethanolamine for 6 h. NEs were loaded with NPF-Chol to 6 wt.% concentration (to oil) and diluted 5-fold. Concentration of ethanolamine 160 mM. pH 8.5 phosphate buffer (0.2 M) buffer was used for the reaction.

a



b

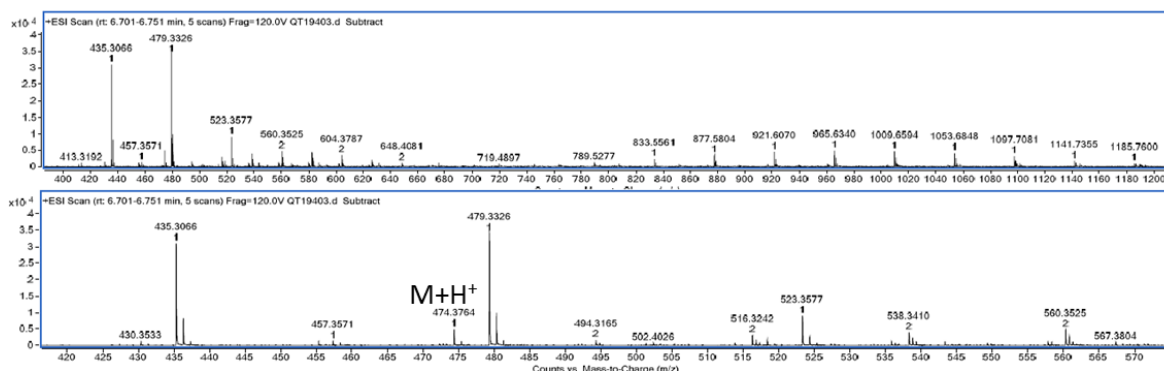


Fig. S2. (a) Scheme of *in situ* reaction of NPF-Chol with ethanolamine in NEs. (b) Mass spectra of organic phase of extraction mixture from the *in situ* reaction.

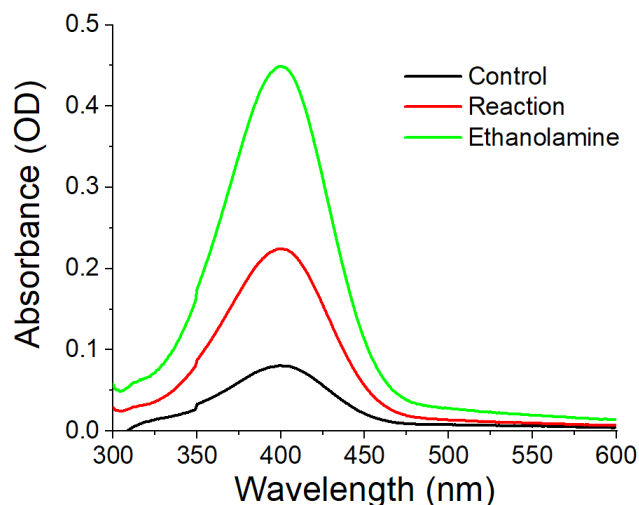


Fig. S3. Absorbance spectra of NPC-CholNEs loaded with NPF-Chol incubated (or without for control) with biotin-PEG-Lysine (15 mM) for 24 h at 40 °C and NPC-Chol quenched by excess ethanolamine (160 mM), over 4 h.

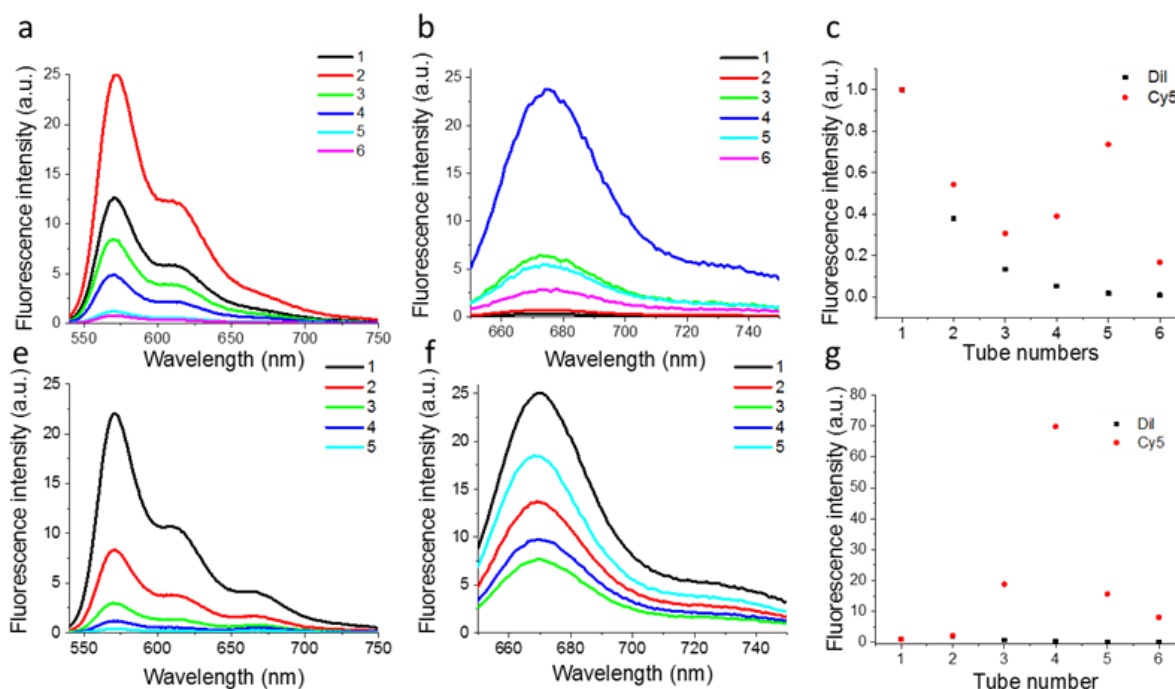


Fig. S4. Emission spectra of elution collected from size exclusion chromatography. Cy3 channel of functional NEs group (a) and control group (e); Cy5 channel of functional NEs group (b) and control group (f); Relative fluorescence intensity in ratio to the tube number 1 functional NEs group (c) and control group (g); (d) and control group (h). Retention volume for 1,2 and 3 were 2 mL and for 3, 4, 5, 6 were 10 mL.

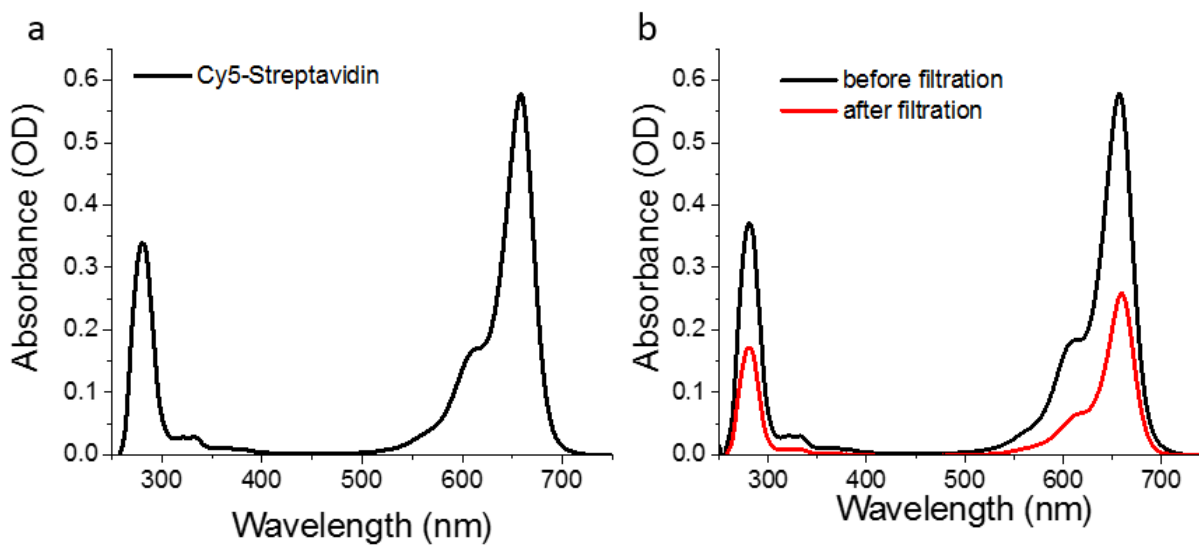


Fig. S5. Absorption spectra of (a) Cy5-streptavidin; (b) Cy5-streptavidin (600 nM) conjugated with biotinylated cetuximab (132 nM) before and after ultrafiltration for calculation biotinylation degree for cetuximab.

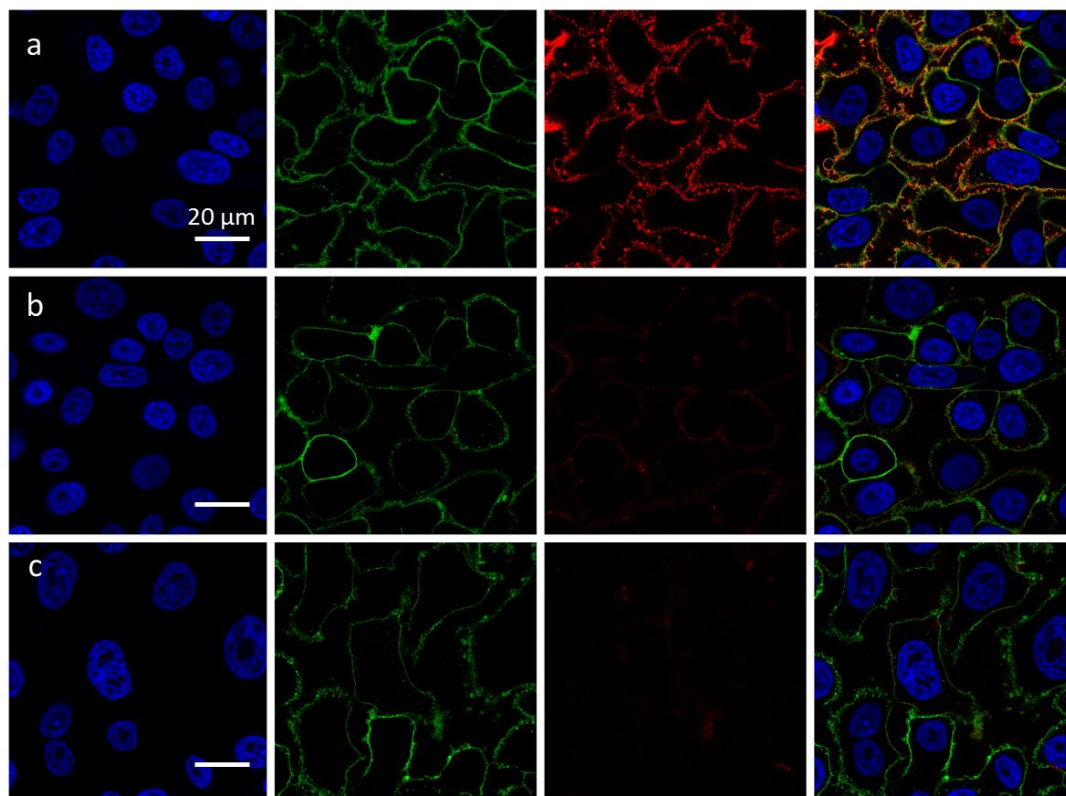


Fig. S6. Testing of feasibility of targeting NEs to cell membrane by biotin-Neutravidin-biotinylated antibody sandwich structure by separating steps adding and washing. (a) Conjugation group, SKBr3 cells were separately added with 60 pM biotinylated antibody over 30 min, 80 pM Neutravidin over 30 min and biotinylated NEs (100 times dilution) over 1 h on ice, each step was washed after incubation; (b) Control without antibody, cells were firstly incubated with 80 pM Neutravidin over 30 min, washed and further incubated with biotinylated NEs (100 times dilution) over 1h on ice and washed; (c) Control without antibody or Neutravidin, SKBr3 cells incubated directly with biotinylated NEs (100 times dilution), incubated over 1 h on ice and washed.

Table S1. Size of NEs measured by DLS.

NEs types	Z-average size (nm)	Polydispersity (PDI)
DiO-TPB and NPC-Chol NEs	106	0.121
DiO-TPB NEs	99	0.170
NPC-Chol NEs	100	0.129
Biotinylated NEs	99	0.185
Empty NEs	109	0.161
Biotinylated DiI-TPB NEs	92	0.214
Antibody DiD-TPB NEs	100	0.213
Biotinylated Cy5.5-TPB NEs	125	0.057
Cy5.5-TPB NEs	112	0.207

References

- [1] S.-Y. Mao, *Methods Mol. Biol.* **2010**, 588, 49.

2.4- Dynamic covalent chemistry in live cells for organelle targeting and enhanced photodynamic action (Article 4)

Based on the results described in the previous chapters, we concluded that dynamic covalent chemistry could enable formation of molecular conjugates *in situ* within lipid NEs. Therefore, we considered that similar reactions could be done in the biological lipid structures of cell organelles. Organelle-specific targeting in live cells is an emerging field of bioimaging and drug delivery [30,31]. Targeting photosensitizers (PS) to cell organelles, especially mitochondria and plasma membranes could improve the efficacy and precision of photodynamic therapy (PDT) [362,363]. In this study, the aim is to design, using dynamic covalent chemistry, a method to target a biologically active molecule (photodynamic agent or drug) to different subcellular organisms *in situ* and then to check the biological effect (for example, photodynamic action) caused by this specific intracellular localization.

Inspired by the *in situ* reaction of ketones and a hydrazide LipoHD described in the first project, we supposed that this dynamic covalent bonding is not limited to NEs, but it is also possible in cells. The concept of this project was to design hydrazide-containing targeting moieties, which could target different subcellular organelles. Then, ketone molecules, such as NRK or doxorubicin, are expected to form dynamic hydrazone bonds with the hydrazide-ligands *in situ* within the targeted organelles (plasma membranes, lipid droplets or mitochondria) (Figure 2.7).

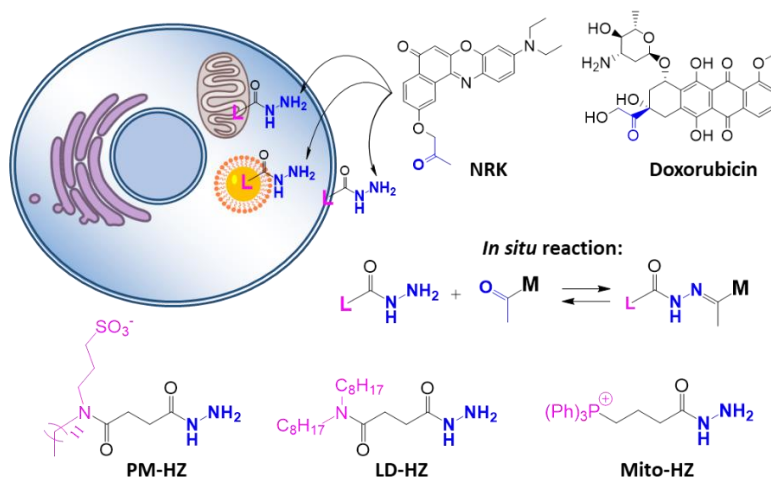


Figure 2.7. The concept of dynamic covalent targeting and chemical structures of the targeting moieties and targeted dye and drug.

We designed three hydrazide bearing ligands, namely, PM-HZ, LD-HZ and Mito-HZ, for the targeting of plasma membrane, lipid droplet and mitochondria, respectively (Figure 2.7).

Firstly, in order to study the feasibility of the *in situ* reaction, inspired by previous projects, we designed a model *in situ* reaction system by using several NPs to mimic organelles: large

unilamellar vesicles (LUVs) to mimic plasma membrane and mitochondria membrane and NEs to mimic lipid droplets. After the *in situ* reaction, we identified the mass of formed conjugates from the EtOAc extraction. With the help of thin layer chromatography and absorption spectroscopy, we examined the yields of these *in situ* reactions by measuring the absorbance of isolated NRK and the NRK conjugates with different targeting moieties. Then, in order to test the organelle targeting capability of our approach, we performed cellular imaging experiments. We found that NRK together with the targeting ligands was colocalized with corresponding organelle markers: F2N12SM, SMCy5.5, and MitoTracker Deep Red for the plasma membranes, lipid droplets, and mitochondria, respectively. Afterward, the stability of the hydrazone bond was tested in conditions of low pH and long incubation in the plasma membrane targeting group. We found that, with the application of washing, low pH, or long incubation, the equilibrium of the dynamic covalent reaction shifted towards the degradation of the hydrazone bond, thus leading to lower targeting specificity. This result showed dynamic nature of this targeting approach. Finally, we found that targeting NRK to plasma membrane and mitochondria resulted in stronger phototoxicity, as evidenced by CellTox™ Green assay (Figure 2.8). Thus, we established a new method of specific targeting of organelles based on dynamic covalent chemistry and showed that targeting the same molecule to different subcellular structures can tune its biological activity. These results will help to design new generation of targeting systems for precision medicine, where the drug effect could be improved because of its more precise localization in the cells.

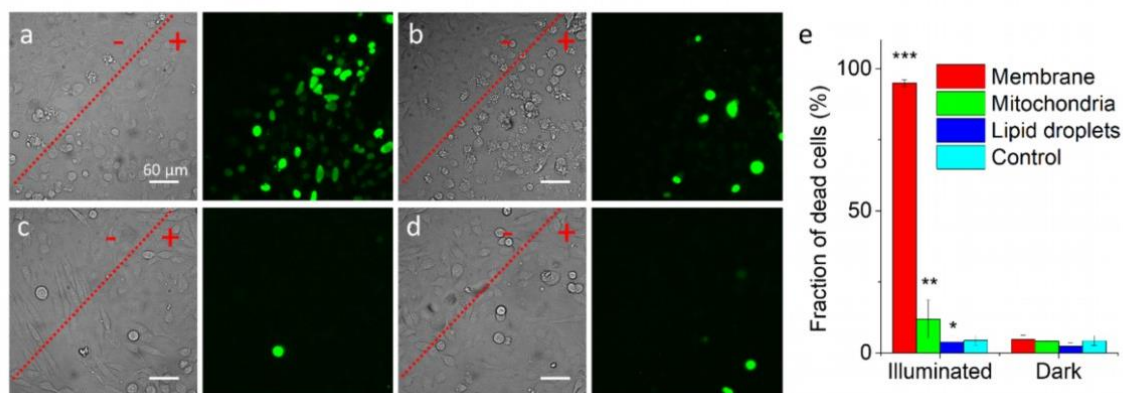


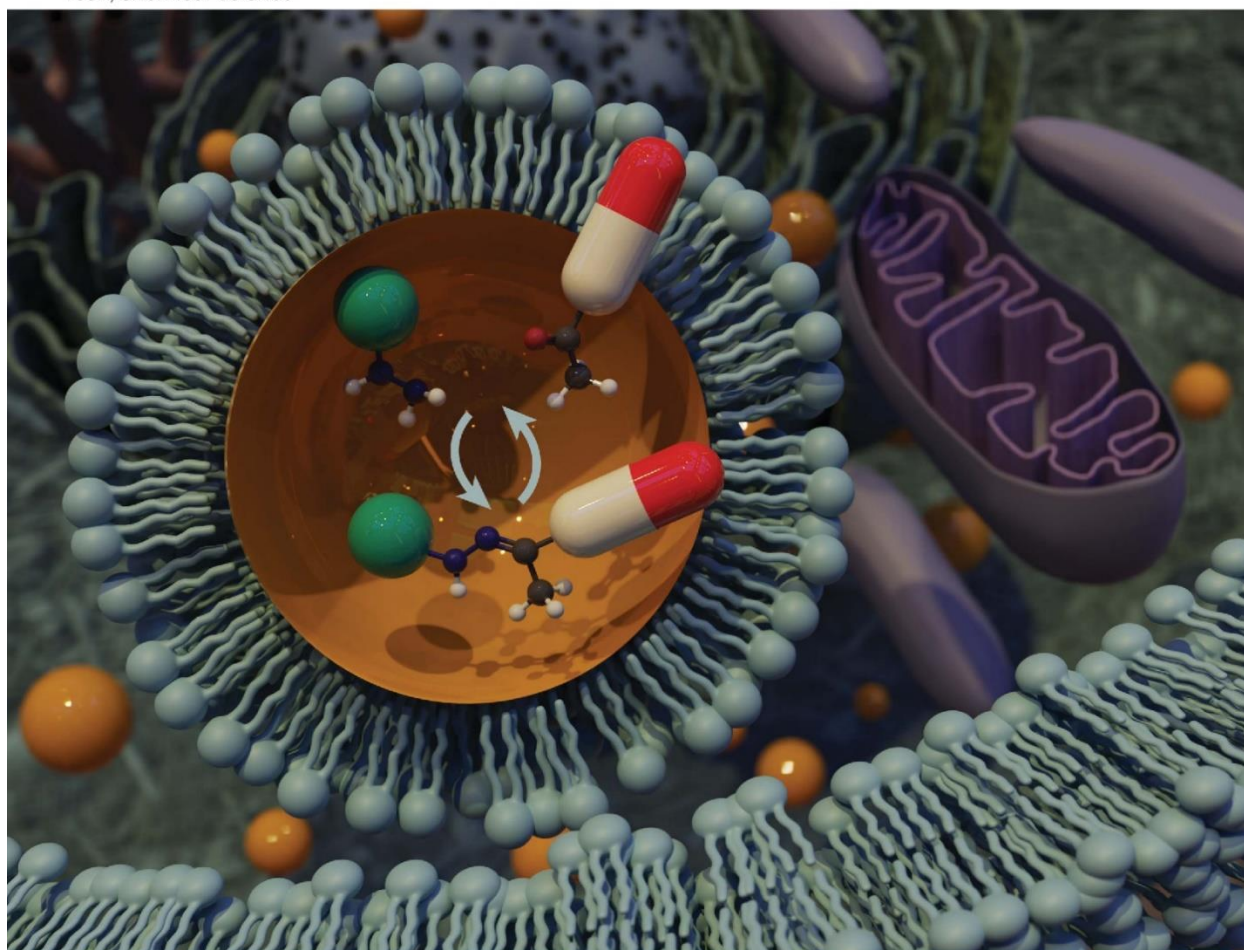
Figure 2.8. Phototoxicity of targeted NRK dye evaluated by CellTox™ Green assay. Transmission (left panels) and CellTox™ Green fluorescence (right panels) of cells pretreated with (a) PM-HZ, (b) Mito-HZ, and (c) LD-HZ at and (d) control. Areas labeled as “+” were illuminated under a microscope for 1 min at 550 nm, while “-” areas were not illuminated. Images were taken after incubation for 30 min with CellTox™ Green assay. (e) Phototoxicity analysis by using Hoechst-CellTox™ Green assay-staining.

Article 4

Chemical Science

rsc.li/chemical-science

Volume 13
Number 13
7 April 2022
Pages 3613–3904



ISSN 2041-6539




EDGE ARTICLE

Andrey S. Klymchenko *et al.*
Dynamic covalent chemistry in live cells for organelle
targeting and enhanced photodynamic action



Cite this: DOI: 10.1039/d1sc04770a

 All publication charges for this article have been paid for by the Royal Society of Chemistry

Dynamic covalent chemistry in live cells for organelle targeting and enhanced photodynamic action†

Fei Liu, Dmytro I. Danylchuk, Bohdan Andreiuk and Andrey S. Klymchenko *

Organelle-specific targeting enables increasing the therapeutic index of drugs and localizing probes for better visualization of cellular processes. Current targeting strategies require conjugation of a molecule of interest with organelle-targeting ligands. Here, we propose a concept of dynamic covalent targeting of organelles where the molecule is conjugated with its ligand directly inside live cells through a dynamic covalent bond. For this purpose, we prepared a series of organelle-targeting ligands with a hydrazide residue for reacting with dyes and drugs bearing a ketone group. We show that dynamic hydrazone bond can be formed between these hydrazide ligands and a ketone-functionalized Nile Red dye (NRK) *in situ* in model lipid membranes or nanoemulsion droplets. Fluorescence imaging in live cells reveals that the targeting hydrazide ligands can induce preferential localization of NRK dye and an anti-cancer drug doxorubicin in plasma membranes, mitochondria and lipid droplets. Thus, with help of the dynamic covalent targeting, it becomes possible to direct a given bioactive molecule to any desired organelle inside the cell without its initial functionalization by the targeting ligand. Localizing the same NRK dye in different organelles by the hydrazide ligands is found to affect drastically its photodynamic activity, with the most pronounced phototoxic effects in mitochondria and plasma membranes. The capacity of this approach to tune biological activity of molecules can improve efficacy of drugs and help to understand better their intracellular mechanisms.

Received 30th August 2021
Accepted 3rd February 2022

DOI: 10.1039/d1sc04770a

rsc.li/chemical-science

Introduction

Organelle-specific targeting in live cells is an emerging field of bioimaging and drug delivery.^{1–7} Targeting therapeutic molecules to desired intracellular areas can improve their efficacy and help to understand mechanisms of their action.^{8–11} On the other hand, targeting fluorescent probes to specific organelles is useful for monitoring and tracking of behavior and functions of different organelles in normal and stress conditions.^{2,5,12–14} Previous studies showed that photosensitizers (PS) targeted to cell organelles, especially mitochondria and plasma membranes could improve the efficacy and precision of photodynamic therapy (PDT).^{15–22} This remarkable effect originates from the short half-life of singlet oxygen (¹O₂) (~40 ns), generated locally by PS after light excitation, which could only diffuse within the limited distance from PS (~20 nm).^{23–25}

To address a specific organelle, the molecules of interest are usually conjugated with targeting units,^{2,11} well established for plasma membrane,²⁶ lysosomes,²⁷ mitochondria,^{28,29} and endoplasmic reticulum (ER).³⁰ However, chemical modification may alter the properties of the molecule, which presents an important limitation of the method. Alternatively, specific targeting of cell compartments could be achieved using bioorthogonal chemistry,^{31–33} where a molecule of interest can react in cells with a target molecule (*e.g.* sugars or lipids), usually using highly efficient “click” reactions.^{34,35} Moreover, target proteins fused with protein tags, such as the SNAP-tag,³⁶ CLIP-tag³⁷ and HaloTag³⁸ can react with corresponding chemical ligands, which allows targeting of small (dye) molecules to specific organelles and imaging their local properties.^{39,40} However, these approaches exploit essentially irreversible reactions, so that the molecule localized within a target organelle is chemically modified. Is it possible to target the same molecule to different specific cell compartments while preserving its native chemical structure before and after this targeting processes? One could consider dynamic covalent chemistry to localize a molecule by an *in situ* reaction with targeting ligand localized in a given cell compartment. In this case, even after targeting to the site (organelle) of interest, reversible processes will ensure presence of unmodified species. Dynamic covalent chemistry is a powerful approach to generate and break covalent bonds

Laboratoire de Bioimagerie et Pathologies, UMR 7021 CNRS, ITI Chimie des Systèmes Complexes, Université de Strasbourg, 74 Route du Rhin, 67401, Illkirch, France.
E-mail: andrey.klymchenko@unistra.fr

† Electronic supplementary information (ESI) available: Materials and methods. Synthesis and characterization of the targeting hydrazides. Spectroscopy data in LUVs. Colocalization microscopy for plasma membrane, mitochondria and LDs targeting and phototoxicity studies. See DOI: 10.1039/d1sc04770a



(including imine, hydrazone, disulfide, *etc.*) under control of environment.^{41–44} Nature uses dynamic covalent bonds (disulfide) to maintain the tertiary structure of proteins, while chemists use them for bioconjugation⁴⁵ and to generate responsive, self-healing and adaptive materials.^{46–48} Dynamic covalent chemistry has been also applied for a controlled drug release⁴⁹ and intracellular delivery.^{50,51} In the previous works dynamic imine bonds enabled targeting amino-lipid at the cell surface, which was used for detection of bacteria⁵² or targeting specific proteins with aldehyde derivatives of dyes.⁵³ However, dynamic covalent chemistry has not been explored to date for localizing molecules in cellular organelles. For this purpose, hydrazone bonds are particularly attractive because of their relatively high stability and applicability for bioconjugation,⁴⁵ drug and gene delivery.^{54–57} Our recent study showed that hydrazone bond could help nanoemulsions to uptake and release free ketones in the environment, like a “drug sponge”.⁵⁸ We hypothesized that *in situ* formation of hydrazone dynamic bonds could be a driving force for localizing molecules in cell compartments, which could enable tuning their biological activity.

In the present study, we introduce a concept of “dynamic covalent targeting” of organelles based on reversible hydrazone bond formation between a molecule of interest (a dye or a drug bearing a ketone moiety) and a ligand localized in specific subcellular compartments, such as plasma membranes, lipid droplets and mitochondria. We show that dynamic covalent targeting of the same dye molecule to different organelles can tune its photodynamic action in cells.

Results and discussion

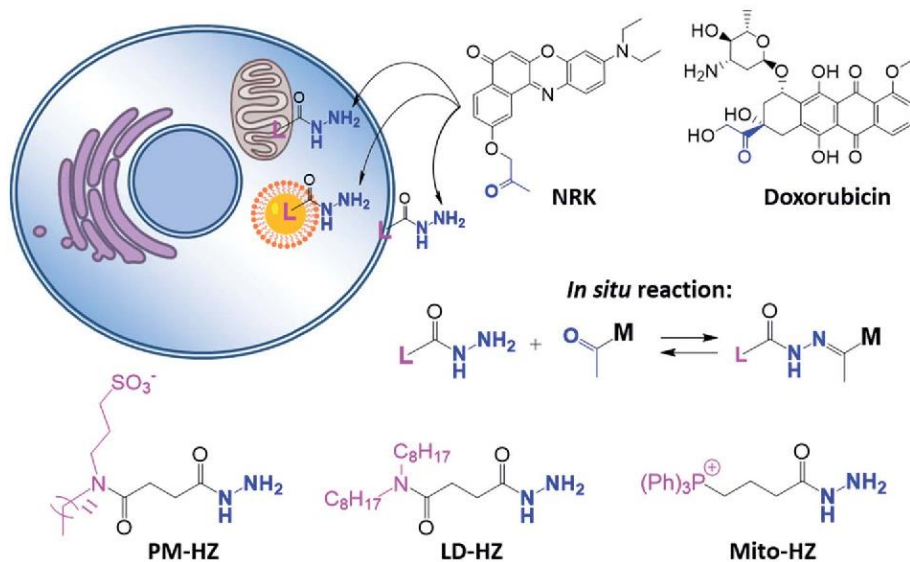
In our concept of dynamic covalent targeting, a specially designed targeting ligand, bearing hydrazide reactive group will be localized in the cell organelle of interest and then form *in situ* a dynamic covalent bond with a given molecule bearing a ketone group. In this case, a ketone molecule, which does not have any organelle specificity, may redistribute due to the *in situ* reaction and thus localize in the targeted organelle (Scheme 1). In this case, the ketone molecule does not require any pre-functionalization with the targeting ligand. Then, after *in situ* reaction with the target site, dynamic nature of the hydrazone bond will ensure reversibility of the process, allowing presence of free ketone molecules (Scheme 1). In order to direct ketone containing Nile Red dye NRK (Scheme 1) into different cell organelles, we designed three hydrazide bearing ligands. Tri-phenylphosphonium was used to achieve mitochondria targeting due to its ability to accumulate in mitochondria driven by their transmembrane potential.^{2,7,29} To target lipid droplets (LDs), a hydrazide moiety was functionalized with two octyl chains in order to favor partitioning of molecules into hydrophobic oily core of LDs.^{59,60} For plasma membrane targeting, we used an anchor group, composed of dodecyl chain and sulfonate, which was recently proposed for designing membrane probes.²⁶ The targeting groups were conjugated to the hydrazide using short linkers, based on either succinic acid or butyric acid (Scheme 1). As ketone molecules, we selected a fluorescent dye

NRK, composed of Nile Red dye and ketone moiety,⁵⁸ and an anti-cancer drug doxorubicin.^{61,62} The Nile Red fluorophore, owing to the solvatochromic and fluorogenic properties,⁶³ is expected to light up and blue shift its emission after binding to lipid rich compartments.^{12,26,63} Moreover, previous study showed that NRK stained indiscriminately different lipid compartments of the cells,⁵⁸ which is suitable to test our dynamic targeting concept. On the other hand, doxorubicin was selected because this common anti-cancer drug is fluorescent and it originally bears the ketone moiety.

Firstly, the *in situ* reaction of NRK with plasma membrane targeting hydrazide (PM-HZ) was verified in model lipid membranes, large unilamellar vesicles (LUVs) composed of dioleoylphosphatidylcholine (DOPC, Fig. 1a). In a buffer, NRK showed expected weak red-shifted fluorescence, whereas in the presence of LUVs containing PM-HZ, a strong increase in the fluorescence intensity was observed together with a blue shift (Fig. 1b). Without the targeting unit (Fig. 1b), NRK showed much smaller fluorescence enhancement and blue shift, suggesting low affinity of NRK to lipid membranes. Thus, PM-HZ favors binding of NRK to lipid membranes. To identify the formation of the hydrazone conjugate, the mixtures of NRK with LUVs containing PM-HZ were subjected to extraction with dichloromethane, followed by thin layer chromatography (TLC) and mass spectrometry analysis. According to the TLC (Fig. 1c), in the presence of PM-HZ, a new spot with small R_f value appeared, that could be assigned to a hydrazone conjugate containing highly polar and charged sulfonate group. The mass spectrum of this new TLC spot confirmed the presence of the desired conjugate (Fig. 1d). These results provide an evidence for the hydrazone formation between PM-HZ and NRK *in situ* at the lipid membranes. Chromatographic separation and further spectrophotometric analysis revealed that the extract from the reaction mixture in LUVs contained 65 mol% of the conjugate (Fig. S1†), indicating that the reaction equilibrium was shifted towards hydrazone conjugate. Similar experiments were also conducted for an *in situ* reaction of NRK with Mito-HZ in lipid vesicles, yielding 28 mol% of Mito-HZ hydrazone with NRK, which was identified by mass spectrometry (Fig. S1†). In case of LD-HZ, we performed an *in situ* reaction with NRK lipid nanoemulsions, which are oil-core/surfactant-shell nanostructures mimicking intracellular lipid droplets.⁶⁴ It was found that the reaction mixture contained 63 mol% of LD-HZ hydrazone with NRK, which was also identified by mass spectrometry (Fig. S1†). Thus, all three targeting hydrazide ligands can form hydrazones with NRK in corresponding lipid environment of membranes and nanoemulsion droplets. This reaction is probably favored by local apolar environment and high concentration of the reactive components in the lipid nanostructures, in line with the earlier studies on the hydrazone formation in lipid nanoemulsions.⁵⁸

Then, we performed cellular studies in order to evaluate the capacity of PM-HZ to induce accumulation of NRK in plasma membranes. First, HeLa cells were incubated with different concentrations of PM-HZ, followed by NRK addition. Starting from 5 μ M concentration of HZ-PM, a tendency of NRK accumulation in the plasma membranes was already observed





Scheme 1 Hydrazide derivatives for dynamic covalent targeting of organelles with Nile Red-ketone (NRK) dye and doxorubicin drug.

(Fig. S2†). This effect was even more obvious at higher concentrations, 20 and 100 μM . In the further experiments, to remove the excess PM-HZ that could eventually react with NRK

outside the cells, HeLa cells were washed after treatment with PM-HZ, and then incubated with NRK followed by confocal fluorescence microscopy. The fluorescence imaging using green

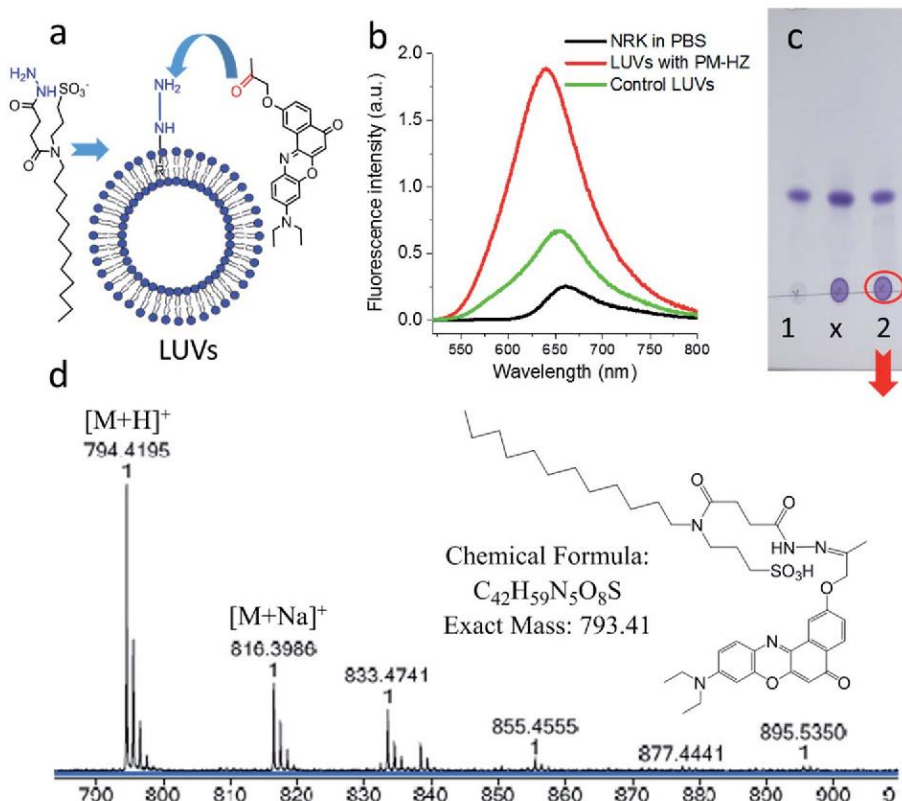


Fig. 1 Studies of *in situ* reaction of NRK with targeting hydrazide PM-HZ in LUVs composed of DOPC. PM-HZ (50 μM) was pre-incubated for 30 min with LUVs (1 mM), dialyzed to remove excess of PM-HZ and then NRK (15 μM) was added. (a) Scheme of a model reaction of NRK with PM-HZ in LUVs. (b) Fluorescence spectra of NRK (2 μM) in PBS, blank LUVs (10 μM) and dialyzed LUVs (10 μM) with PM-HZ. Excitation wavelength was 480 nm. (c) TLC result (DCM : MeOH = 95 : 5 as an eluent) of DCM extraction of NRK in blank LUVs and LUVs containing PM-HZ: 1 – control sample (with blank LUVs), x – cross point, 2 – reaction. (d) Mass identification of red circled point in (c).



and red channels was done in order to evaluate the solvatochromic response of Nile Red moiety on binding to lipid structures.^{12,26,65} In the control, NRK showed rather even distribution throughout the cell interior, in line with the previous work.⁵⁸ In contrast, the cells pretreated with PM-HZ showed significant enhancement of their plasma membrane fluorescence in both emission channels (Fig. 2 and S3†). The effect was clearly seen on the line profile across the plasma membrane, showing a sharp pick, which was not observed in the control cells (Fig. 2c). These observations were confirmed by colocalization with a membrane probe F2N12SM,⁶⁶ where the cell contour of the plasma membrane corresponded well to the signal from NRK in the presence of PM-HZ (Fig. S4†). Pearson's and Mander's correlation coefficient values were higher in the presence of the membrane targeting hydrazide (0.55 and 0.42, respectively) compared to control NRK (0.20 and 0.13, respectively) (Table S1†). Moreover, the fluorescence intensity ratio

from plasma membrane *versus* whole cell was significantly higher (2.06) compared to the control (0.88). Thus, hydrazide PM-HZ favored redistribution the dye ketone towards plasma membrane. In the merged two-color images, these plasma membrane structures appeared more greenish compared to yellow-orange intracellular parts. The color variation was further confirmed by the line profile (Fig. 2c), where the peak of the green channel was higher compared to the red one, being similar for other cellular compartments. The observed color change corresponds to lower polarity in the plasma membrane, which was systematically observed for different solvatochromic probes.^{12,67,68}

To verify the dynamic nature of our targeting approach, we first treated the cells with PM-HZ (20 μ M) and NRK and then washed the cells three times to remove NRK and PM-HZ from the extracellular medium and replaced it with new medium at neutral pH (7.4) or low pH (5.8). It was observed that at neutral

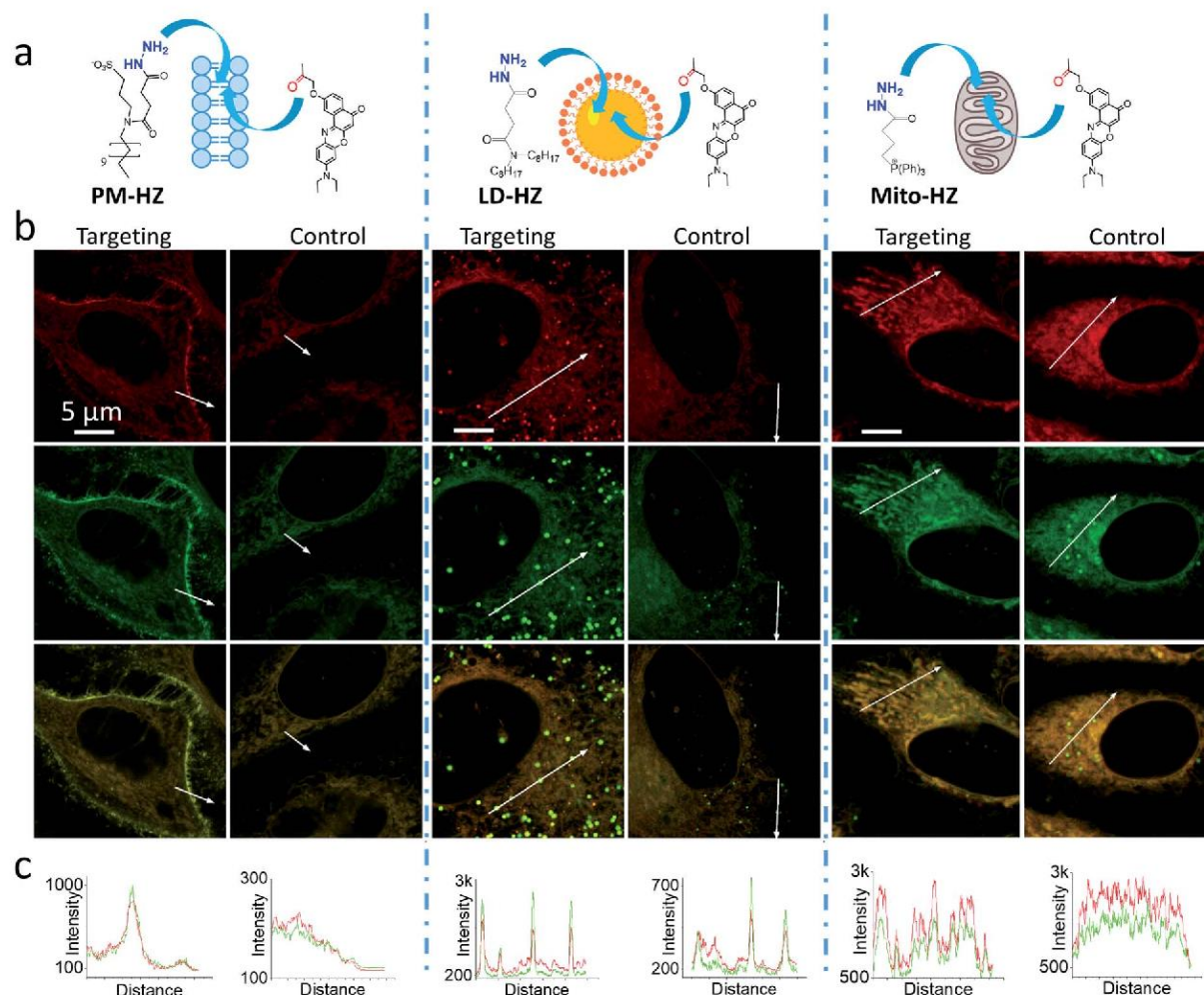


Fig. 2 (a) Targeting NRK dye to plasma membrane, lipid droplets and mitochondria by corresponding hydrazide ligands: PM-HZ, LD-HZ and Mito-HZ. (b) Confocal images at the red channel (600–670 nm, upper panels) and the green channel (550–600 nm, middle panels) for NRK emission and the merge (lower panels); excitation: 488 nm. (c) Plot profiles for the red and green channels from white arrows indicated in images. Targeting agent (100 μ M) was pre-incubated with cells for 30 min at 37 $^{\circ}$ C, followed by washing with PBS and then addition of NRK (1 μ M for PM-HZ, LD-HZ and 2.5 μ M for Mito-HZ) in Opti-MEM and incubation for 30 min at 37 $^{\circ}$ C. In controls, NRK was used directly without the targeting agent.



pH after washing, the signal from plasma membranes was still detectable (especially in the merged two-color images), but it was lower than before washing (Fig. S5†). At low pH, the effect was even stronger, so that the NRK distribution became the same as in the control without PM-HZ (Fig. S5†). Quantitative analysis of NRK co-localization with the plasma membrane marker F2N12SM (average fluorescence intensity ratio of plasma membrane *vs.* the whole cell as well as Pearson's and Mander's coefficients) confirmed the decrease in the localization of NRK in plasma membranes in the neutral pH medium after washing and the co-localization values further decreased after 1 h incubation (Table S2†). Moreover, the co-localization parameters were the lowest for the low pH (Table S2†). In all control experiments without PM-HZ, the colocalization parameters were low for all conditions, as expected (Fig. S5†). These results indicate that the targeting of NRK to plasma membranes is a reversible process. Indeed, washing out PM-HZ and NRK from the extracellular medium shifted the equilibrium toward hydrazone bond disruption, leading to NRK release into the medium and inside the cells, and, thus, decreased signal from the plasma membranes. Moreover, in the low pH medium after washing, the destabilization of the hydrazone bond led to nearly complete hydrolysis of the hydrazone and non-specific distribution of NRK within the cell, similar to the control without PM-HZ (Fig. S5†).

Next, we explored the possibility to target LDs in cells pre-treated with LD-HZ. In comparison to the control cells, those incubated with LD-HZ showed strong dot-shaped fluorescence, which was observed as much brighter dots and peaks of high intensity in the line profiles (Fig. 2b and c). These dots colocalized well with the near-infrared marker of LDs SMCy5.5,⁶⁹ which was also confirmed by the line profiles for the two dyes (Fig. S6†). For control cells, the signal from dots was much weaker, so that the colocalization with SMCy5.5 marker was less clear. The Pearson's and Mander's correlation coefficients were higher in the presence of LD-HZ (0.68 and 0.77, respectively) than that of control (0.52 and 0.26, respectively) (Table S1†). Moreover, the targeting hydrazide LD-HZ increased the ratio of mean fluorescence intensity of LDs/whole cell from 1.67 (control) to 4.46 (Table S1†). These results confirm that our system combining LD-HZ and NRK ensures selective dye accumulation in LDs, whereas for control NRK the partitioning into LDs is not efficient. The two-color images showed clear green pseudo-color of LDs, in contrast to the rest of the cytoplasm, in agreement with line profiles, where green emission was much stronger at the peaks corresponding to LDs (Fig. 2 and S6†). LDs are known to present much lower polarity of their lipid core, compared to any other lipid structures,^{59,60,67,70} which explains the dominant green emission of solvatochromic Nile Red moiety.

Finally, we tested our mitochondria-targeting hydrazide Mito-HZ in combination with NRK. In the presence of Mito-HZ, the characteristic mitochondrial staining could be identified in contrast to that of the control (Fig. 2b and S7†). The line profile across the cells revealed clear differences between control cells and those pre-treated with Mito-HZ (Fig. 2c). The observed structures colocalized with the mitochondria staining by

MitoTracker Deep Red FM 644/665, in contrast to the control cells stained only with NRK (Fig. S7†). However, the targeting effect was much weaker than that for LDs or plasma membranes, according to ratio of mean fluorescence intensity in mitochondria/whole cell (1.73 with Mito-HZ *vs.* 1.58 in the control), Pearson's correlation coefficient (0.75 with Mito-HZ *vs.* 0.65 in the control) and Mander's correlation coefficient (0.44 with Mito-HZ *vs.* 0.54 in the control) (Table S1†). The weaker mitochondria targeting is in line with the lower yield of hydrazone formation observed in models for Mito-HZ compared to other two targeting hydrazide ligands (see above). Moreover, we assume that some fluorescence from other cell organelles might overlap with fluorescence from mitochondria, which complicates the co-localization analysis. Thus, all three targeting hydrazides induced selective accumulation of a ketone-functionalized dye in specific cellular organelles. This implies the formation of dynamic covalent bond (hydrazone) with the ligand through an orthogonal reaction, which can provide sufficient driving force to direct originally non-specific dye to the targeted subcellular compartment.

Then, we explored a possibility to extend our dynamic covalent targeting concept to a drug molecule bearing ketone group, such as doxorubicin. The control cells incubated with doxorubicin (for 30 min) showed fluorescence all over the cytoplasm (Fig. 3b), in line with the previous studies (nuclear localization of doxorubicin is commonly observed in cells lines poorly resistant to this drug⁷¹).^{58,72,73} Remarkably, in the presence of PM-HZ, the intracellular fluorescence of doxorubicin changed drastically, showing preferential localization at the level of plasma membranes (Fig. 3a), similar to dye NRK. Line profiles across the cell membrane confirmed this observation (Fig. 3). Colocalization imaging with a membrane probe F2N12SM (Fig. S8†) confirmed the membrane targeting, while the colocalization analysis based on Pearson's and Mander's coefficients as well as the intensity ratio (plasma membrane/whole cell) showed significantly improved localization in the plasma membranes compared to control cells without PM-HZ (Table S1†).

In the presence of LD-HZ, doxorubicin displayed strong dotted fluorescence, which colocalized well with the marker of LDs SMCy5.5 according to the two-colour images and the corresponding line profiles (Fig. 4a). Thus, doxorubicin, which does not show any affinity to LDs in control cells (Fig. 4b), can be directed towards LDs using LD-HZ. The colocalization analysis based on Pearson's and Mander's coefficients as well as the intensity ratio (organelle/whole cell) confirmed drastically improved localization of doxorubicin in the lipid droplets compared to control cells without LD-HZ (Table S1†). Likewise, the capability of Mito-HZ to direct doxorubicin towards mitochondria was also tested. In the presence of Mito-HZ the characteristic mitochondrial staining could be identified, which could be seen from the line profiles of the images of targeted doxorubicin and MitoTracker Deep Red FM 644/665 (Fig. S9†). In contrast, control cells with doxorubicin did not show a clear colocalization with mitochondria (Fig. S9†). However, one should note that mitochondria targeting was much less specific compared to the plasma membrane and LDs targeting, which



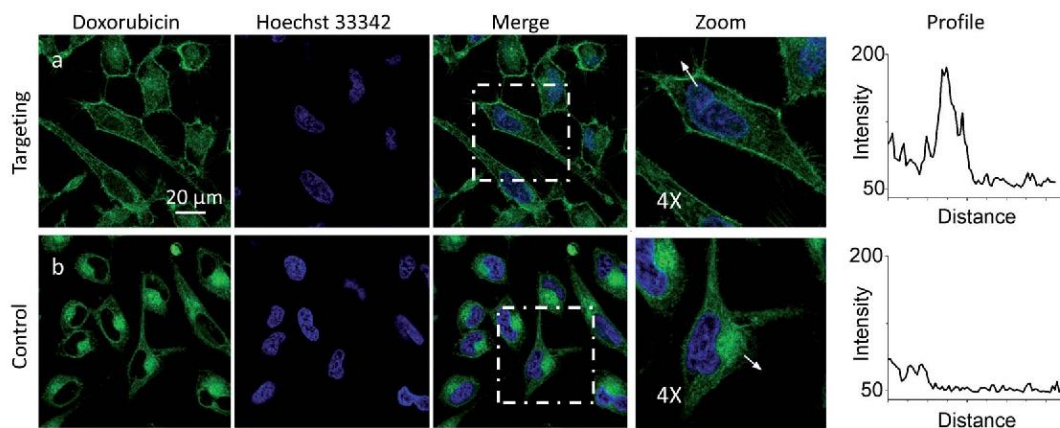


Fig. 3 Targeting doxorubicin to plasma membranes. Cells were pre-incubated for 10 min at 37 °C with (a) or without (b) PM-HZ (20 μM) followed by addition doxorubicin (1 μM) and incubation for 30 min at 37 °C. Condition for the green channel (doxorubicin imaging): excitation at 488 nm, emission filter at 520–650 nm. Condition for the blue channel (Hoechst 33342 imaging): excitation at 405 nm, emission filter at 420–480 nm. The line profiles (right panels) of the image in the green channel is indicated by white arrows in 4× magnified images.

was in line with the data using NRK dye. This was confirmed by only limited changes in the Pearson's and Mander's coefficients as well as the intensity ratio (mitochondria/whole cell) compared to control cells (Table S1†). Overall, these results show that our targeting hydrazides can tune intracellular localization of the ketone drug, so that dynamic covalent bonds provide a driving force for the repartitioning of the drug to the target organelle. It should be noted that it is the first time that intracellular localization of a drug can be tuned without its chemical pre-functionalization.

Previous works showed that Nile Red derivatives can be phototoxic after continuous illumination in wide-field fluorescence microscopy.⁷⁴ Therefore, NRK could be a suitable model to verify whether a PDT effect of the same dye can be tuned by targeting it to different organelles. To this end, cells pretreated with different targeting hydrazides were stained with NRK and

then illuminated in wide-field microscopy conditions in order to induce a photodamage. It should be noted that the mean fluorescence intensity of NRK in cells was at the similar level for all studied conditions, which ensured that the amount of internalized NRK was similar in all these cases (Fig. S10†). To monitor cell death, CellTox™ Green assay was used, which stains nucleus of dead cells. In case of PM-HZ, illuminated (+) area revealed strong green fluorescence from dead cells, in contrast to non-illuminated area with practically no signs of cell damage (Fig. 5a). Similar though smaller effects were observed for Mito-HZ (Fig. 5b). In sharp contrast, only few dead cells were observed in the illuminated area of either non-targeted NRK or LD-targeted NRK (Fig. 5c and d), indicating that these conditions provided much smaller phototoxic effects. The quantitative analysis of the CellTox™ Green fluorescence (Fig. 5e) in the large population of cells (Fig. S11†) confirmed the strongest

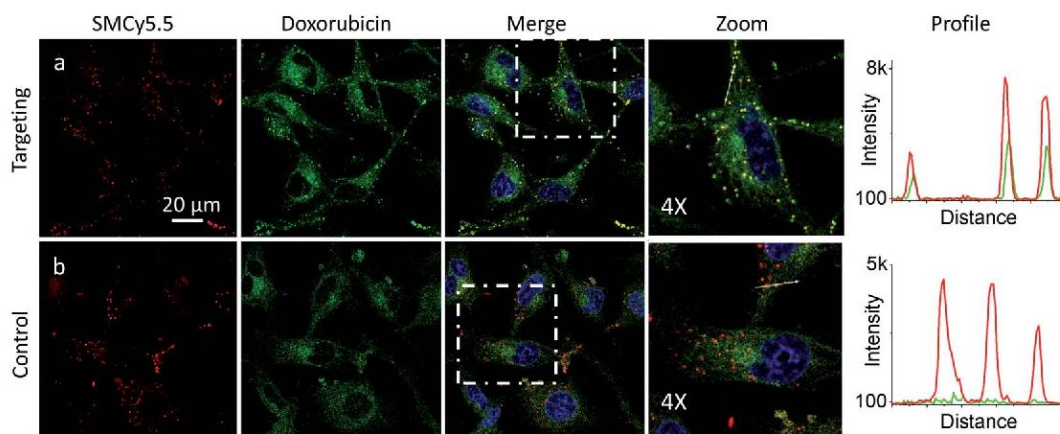


Fig. 4 Targeting doxorubicin to lipid droplets. Cells were pre-incubated for 10 min at 37 °C with (a) or without (b) LD-HZ (20 μM) followed by addition doxorubicin (1 μM) and incubation for 30 min at 37 °C. Conditions for red channel (lipid droplet marker SMCy5.5 imaging): excitation at 644 nm, emission filter at 650–800 nm; the green channel (doxorubicin imaging): excitation at 488 nm, emission filter at 520–650 nm; the blue channel (Hoechst 33342 imaging): excitation at 405 nm, emission filter at 420–480 nm. The line profiles (right panels) of the image in the green channel is indicated by white arrows in 4× magnified images.



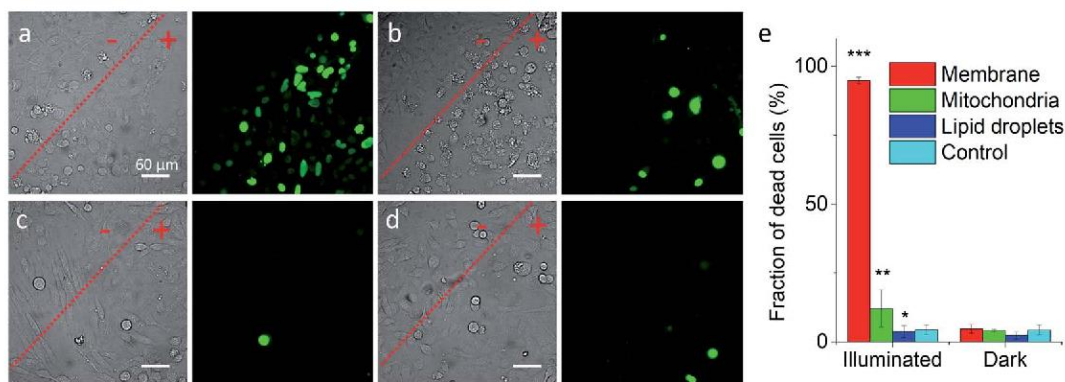


Fig. 5 Phototoxicity of targeted NRK dye evaluated by CellTox™ Green assay. Transmission (left panels) and CellTox™ Green fluorescence (right panels) of cells pretreated with (a) PM-HZ, (b) Mito-HZ and (c) LD-HZ at and (d) control. Targeting agent (100 μM) was pre-incubated with cells for 30 min at 37 °C, followed by washing with PBS and then addition of NRK (1 μM) in Opti-MEM and incubation for 30 min at 37 °C. Areas labelled as "+" were illuminated under microscope for 1 min at 550 nm, while "-" areas were not illuminated. Images were taken after incubation for 30 min with CellTox™ Green assay. (e) Phototoxicity analysis by using Hoechst-CellTox™ Green assay co-staining (based on data shown in Fig. S11†).

phototoxic effect for plasma membrane targeting (90% cell death) and less prominent effect for the mitochondria targeting, whereas the phototoxicity of non-targeted and LD-targeted NRK was negligible. In the bright-field images, detaching round cells were clearly observed for the membrane- and mitochondria-targeted NRK, whereas for control and LD-targeted NRK, the cell morphology did not change after the illumination.

In the time-lapse bright-field images, gradual morphology changes were observed only for cells with NRK targeted to plasma membrane and mitochondria (Fig. S12†): a formation of large membrane blebs together with gradual cell detachment in the former case and dense small bubbles at the surface of cells in the latter case. These morphological alternations indicate the cell damage, in line with the CellTox™ Green assay. Overall, these results show that phototoxic effects at the level of plasma membrane and mitochondria are much more important than at other membrane regions of the cells, in line with previous studies.^{15,18–21,75} Moreover, phototoxic damage in cell plasma membranes and mitochondria leads to different morphological changes of the cells, which shows that the phototoxicity profile can be finely tuned by the subcellular localization of the photosensitizer dye.

Conclusions

In conclusion, a concept of "dynamic covalent targeting" of organelles is proposed based on reversible covalent bond (hydrazone) formation in live cells, which allows tuning subcellular localization of the same molecule (a dye or a drug) and reveals organelle-dependent phototoxicity. Three hydrazides bearing organelle-targeting moieties have been developed, which enable localizing Nile Red-ketone dye and anti-cancer drug doxorubicin specifically in plasma membranes, mitochondria and LDs of live cells. To the best of our knowledge, this is the first method capable to target an unmodified drug molecule to any desired location inside the cells. It is important to note that the dynamic covalent targeting works on two

molecules of very different chemical structure (NRK and doxorubicin), which shows that the concept is rather universal for targeting ketone molecules. We also found that the same photosensitizer dye targeted to plasma membranes and mitochondria produced much stronger phototoxic effect compared to non-targeted or LDs-targeted dye. Thus, by localizing dye molecules in desired subcellular compartments, our approach provides fine tuning the dye phototoxicity, important for effective and precise photodynamic therapy. Moreover, capacity of the dynamic covalent targeting approach to provide specific localization to some drugs (*e.g.* doxorubicin) could enable optimizing their efficacy and better understanding their intracellular mechanisms. We should stress that reversible nature of dynamic covalent chemistry provides unique opportunities in the field of targeted drug delivery, where a non-functionalized drug can be localized in the target organelle and further released in a free form due to the dynamic equilibrium. Finally, we expect that this concept could be extended to other biologically active molecules and dynamic covalent bonds.

Data availability

The datasets supporting this article have been uploaded as part of the ESI.†

Author contributions

ASK proposed the concept and supervised the project. ASK and FL designed the experiments. FL performed and analyzed most of the experiments. DID, FL, and BA synthesized new molecules. ASK and FL wrote the manuscript. All authors contributed to preparation of the manuscript.

Conflicts of interest

The authors declare no competing financial interest.



Acknowledgements

This work was supported by the European Research Council ERC Consolidator grant BrightSens 648528, CNRS and University of Strasbourg. FL is supported from China Scholarship council (CSC). DID was supported by a fellowship from the Ministère de la Recherche (France). BA was supported by LabEx Chimie des Systèmes Complexes. Yosuke Niko is acknowledged for synthesis of NRK. PACSI and PIC platforms are acknowledged for assistance with NMR/mass spectrometry and confocal microscopy, respectively.

Notes and references

- N. M. Sakhrani and H. Padh, *Drug Des., Dev. Ther.*, 2013, **7**, 585–599.
- H. Zhu, J. Fan, J. Du and X. Peng, *Acc. Chem. Res.*, 2016, **49**, 2115–2126.
- W. Xu, Z. Zeng, J.-H. Jiang, Y.-T. Chang and L. Yuan, *Angew. Chem., Int. Ed.*, 2016, **55**, 13658–13699.
- D. Srikun, A. E. Albers, C. I. Nam, A. T. Iavarone and C. J. Chang, *J. Am. Chem. Soc.*, 2010, **132**, 4455–4465.
- P. Gao, W. Pan, N. Li and B. Tang, *Chem. Sci.*, 2019, **10**, 6035–6071.
- F. Hu and B. Liu, *Org. Biomol. Chem.*, 2016, **14**, 9931–9944.
- N. Wagner, M. Stephan, D. Höglinger and A. Nadler, *Angew. Chem., Int. Ed.*, 2018, **57**, 13339–13343.
- S. Kunjiappan, P. Pavadai, S. Vellaichamy, S. Ram Kumar Pandian, V. Ravishankar, P. Palanisamy, S. Govindaraj, G. Srinivasan, A. Premanand, M. Sankaranarayanan and P. Theivendren, *Drug Dev. Res.*, 2021, **82**, 309–340.
- N. M. Sakhrani and H. Padh, *Drug Des., Dev. Ther.*, 2013, **7**, 585–599.
- P. Gao, W. Pan, N. Li and B. Tang, *ACS Appl. Mater. Interfaces*, 2019, **11**, 26529–26558.
- S. Louzoun-Zada, Q. Z. Jaber and M. Fridman, *Angew. Chem., Int. Ed.*, 2019, **58**, 15584–15594.
- D. I. Danylchuk, P. H. Jouard and A. S. Klymchenko, *J. Am. Chem. Soc.*, 2021, **143**, 912–924.
- A. Goujon, A. Colom, K. Straková, V. Mercier, D. Mahecic, S. Manley, N. Sakai, A. Roux and S. Matile, *J. Am. Chem. Soc.*, 2019, **141**, 3380–3384.
- H. B. Xiao, P. Li, X. F. Hu, X. H. Shi, W. Zhang and B. Tang, *Chem. Sci.*, 2016, **7**, 6153–6159.
- Z. Y. Liu, H. Zou, Z. Zhao, P. F. Zhang, G. G. Shan, R. T. K. Kwok, J. W. Y. Lam, L. Zheng and B. Z. Tang, *ACS Nano*, 2019, **13**, 11283–11293.
- I. R. Calori, H. Bi and A. C. Tedesco, *ACS Appl. Bio Mater.*, 2021, **4**, 195–228.
- W. Lv, Z. Zhang, K. Y. Zhang, H. R. Yang, S. J. Liu, A. Q. Xu, S. Guo, Q. Zhao and W. Huang, *Angew. Chem., Int. Ed.*, 2016, **55**, 9947–9951.
- X. P. Li, Y. Zhao, T. Zhang and D. Xing, *Adv. Healthcare Mater.*, 2021, **10**, 23.
- J. Kim, O. A. Santos and J. H. Park, *J. Controlled Release*, 2014, **191**, 98–104.
- H. Cheng, R. R. Zheng, G. L. Fan, J. H. Fan, L. P. Zhao, X. Y. Jiang, B. Yang, X. Y. Yu, S. Y. Li and X. Z. Zhang, *Biomaterials*, 2019, **188**, 1–11.
- R. L. Wei, Y. S. Dong, Y. L. Tu, S. W. Luo, X. R. Pang, W. L. Zhang, W. Yao, W. J. Tang, H. K. Yang, X. H. Wei, X. Q. Jiang, Y. Y. Yuan and R. M. Yang, *ACS Appl. Mater. Interfaces*, 2021, **13**, 14004–14014.
- R. Wang, X. S. Li and J. Yoon, *ACS Appl. Mater. Interfaces*, 2021, **13**, 19543–19571.
- S. Y. Li, W. X. Qiu, H. Cheng, F. Gao, F. Y. Cao and X. Z. Zhang, *Adv. Funct. Mater.*, 2017, **27**, 1–11.
- P. Agostinis, K. Berg, K. A. Cengel, T. H. Foster, A. W. Girotti, S. O. Gollnick, S. M. Hahn, M. R. Hamblin, A. Juzeniene, D. Kessel, M. Korbelik, J. Moan, P. Mroz, D. Nowis, J. Piette, B. C. Wilson and J. Golab, *Ca-Cancer J. Clin.*, 2011, **61**, 250–281.
- M. Ethirajan, Y. Chen, P. Joshi and R. K. Pandey, *Chem. Soc. Rev.*, 2011, **40**, 340–362.
- D. I. Danylchuk, S. Moon, K. Xu and A. S. Klymchenko, *Angew. Chem., Int. Ed.*, 2019, **58**, 14920–14924.
- S. Takahashi, Y. Kagami, K. Hanaoka, T. Terai, T. Komatsu, T. Ueno, M. Uchiyama, I. Koyama-Honda, N. Mizushima, T. Taguchi, H. Arai, T. Nagano and Y. Urano, *J. Am. Chem. Soc.*, 2018, **140**, 5925–5933.
- A. Jiménez-Sánchez, E. K. Lei and S. O. Kelley, *Angew. Chem., Int. Ed.*, 2018, **57**, 8891–8895.
- Z. Yang, Y. He, J.-H. Lee, N. Park, M. Suh, W.-S. Chae, J. Cao, X. Peng, H. Jung, C. Kang and J. S. Kim, *J. Am. Chem. Soc.*, 2013, **135**, 9181–9185.
- J. M. Meinig, L. Fu and B. R. Peterson, *Angew. Chem., Int. Ed.*, 2015, **54**, 9696–9699.
- A. Borrmann and J. C. M. van Hest, *Chem. Sci.*, 2014, **5**, 2123–2134.
- N. K. Devaraj, *ACS Cent. Sci.*, 2018, **4**, 952–959.
- E. M. Sletten and C. R. Bertozzi, *Angew. Chem., Int. Ed.*, 2009, **48**, 6974–6998.
- J. M. Baskin, J. A. Prescher, S. T. Laughlin, N. J. Agard, P. V. Chang, I. A. Miller, A. Lo, J. A. Codelli and C. R. Bertozzi, *Proc. Natl. Acad. Sci. U. S. A.*, 2007, **104**, 16793–16797.
- T. W. Bumpus and J. M. Baskin, *Trends Biochem. Sci.*, 2018, **43**, 970–983.
- A. Keppler, S. Gendreizig, T. Gronemeyer, H. Pick, H. Vogel and K. Johnsson, *Nat. Biotechnol.*, 2003, **21**, 86–89.
- A. Gautier, A. Juillerat, C. Heinis, I. R. Corrêa, M. Kindermann, F. Beauflis and K. Johnsson, *Chem. Biol.*, 2008, **15**, 128–136.
- G. V. Los, L. P. Encell, M. G. McDougall, D. D. Hartzell, N. Karassina, C. Zimprich, M. G. Wood, R. Learish, R. F. Ohana, M. Urh, D. Simpson, J. Mendez, K. Zimmerman, P. Otto, G. Vidugiris, J. Zhu, A. Darzins, D. H. Klaubert, R. F. Bulleit and K. V. Wood, *ACS Chem. Biol.*, 2008, **3**, 373–382.
- K. Straková, J. López-Andarias, N. Jiménez-Rojo, J. E. Chambers, S. J. Marciniak, H. Riezman, N. Sakai and S. Matile, *ACS Cent. Sci.*, 2020, **6**, 1376–1385.



- 40 J. E. Chambers, M. Kubánková, R. G. Huber, I. López-Duarte, E. Avezov, P. J. Bond, S. J. Marciniak and M. K. Kuimova, *ACS Nano*, 2018, **12**, 4398–4407.
- 41 Y. H. Jin, C. Yu, R. J. Denman and W. Zhang, *Chem. Soc. Rev.*, 2013, **42**, 6634–6654.
- 42 J. M. Lehn, *Chem. Soc. Rev.*, 2007, **36**, 151–160.
- 43 S. P. Black, J. K. M. Sanders and A. R. Stefankiewicz, *Chem. Soc. Rev.*, 2014, **43**, 1861–1872.
- 44 P. T. Corbett, J. Leclaire, L. Vial, K. R. West, J. L. Wietor, J. K. M. Sanders and S. Otto, *Chem. Rev.*, 2006, **106**, 3652–3711.
- 45 D. K. Kolmel and E. T. Kool, *Chem. Rev.*, 2017, **117**, 10358–10376.
- 46 N. Roy, B. Bruchmann and J. M. Lehn, *Chem. Soc. Rev.*, 2015, **44**, 3786–3807.
- 47 M. J. Webber and R. Langer, *Chem. Soc. Rev.*, 2017, **46**, 6600–6620.
- 48 Y. Zhang and M. Barboiu, *Chem. Rev.*, 2016, **116**, 809–834.
- 49 S. Ulrich, *Acc. Chem. Res.*, 2019, **52**, 510–519.
- 50 Y. Y. Cheng, L. L. Zong, J. Lopez-Andarias, E. Bartolami, Y. Okamoto, T. R. Ward, N. Sakai and S. Matile, *Angew. Chem., Int. Ed.*, 2019, **58**, 9522–9526.
- 51 A. Fuertes, M. Juanes, J. R. Granja and J. Montenegro, *Chem. Commun.*, 2017, **53**, 7861–7871.
- 52 A. Bandyopadhyay, K. A. McCarthy, M. A. Kelly and J. Gao, *Nat. Commun.*, 2015, **6**, 6561.
- 53 W. Sheng, S. T. Nick, E. M. Santos, X. Ding, J. Zhang, C. Vasileiou, J. H. Geiger and B. Borhan, *Angew. Chem., Int. Ed.*, 2018, **57**, 16083–16087.
- 54 M. Kanamala, W. R. Wilson, M. M. Yang, B. D. Palmer and Z. M. Wu, *Biomaterials*, 2016, **85**, 152–167.
- 55 J. M. Priegue, I. Lostale-Seijo, D. Crisan, J. R. Granja, F. Fernandez-Trillo and J. Montenegro, *Biomacromolecules*, 2018, **19**, 2638–2649.
- 56 S. Aryal, C. M. J. Hu and L. F. Zhang, *ACS Nano*, 2010, **4**, 251–258.
- 57 Y. M. Zhao, F. Fay, S. Hak, J. M. Perez-Aguilar, B. L. Sanchez-Gaytan, B. Goode, R. Duivenvoorden, C. D. Davies, A. Bjorkoy, H. Weinstein, Z. A. Fayad, C. Perez-Medina and W. J. M. Mulder, *Nat. Commun.*, 2016, **7**, 11221.
- 58 F. Liu, Y. Niko, R. Bouchaala, L. Mercier, O. Lefebvre, B. Andreiuk, T. Vandamme, J. G. Goetz, N. Anton and A. Klymchenko, *Angew. Chem., Int. Ed.*, 2021, **60**, 6573–6580.
- 59 T. K. Fam, A. S. Klymchenko and M. Collot, *Materials*, 2018, **11**, 1768.
- 60 Y. Guo, K. R. Cordes, R. V. Farese Jr and T. C. Walther, *J. Cell Sci.*, 2009, **122**, 749–752.
- 61 O. Tacar, P. Sriamornsak and C. R. Dass, *J. Pharm. Pharmacol.*, 2013, **65**, 157–170.
- 62 C. F. Thorn, C. Oshiro, S. Marsh, T. Hernandez-Boussard, H. McLeod, T. E. Klein and R. B. Altman, *Pharmacogenet. Genomics*, 2011, **21**, 440–446.
- 63 A. S. Klymchenko, *Acc. Chem. Res.*, 2017, **50**, 366–375.
- 64 A. S. Klymchenko, F. Liu, M. Collot and N. Anton, *Adv. Healthcare Mater.*, 2021, **10**, 2001289.
- 65 O. A. Kucherak, S. Oncul, Z. Darwich, D. A. Yushchenko, Y. Arntz, P. Didier, Y. Mély and A. S. Klymchenko, *J. Am. Chem. Soc.*, 2010, **132**, 4907–4916.
- 66 R. Kreder, S. Oncul, O. A. Kucherak, K. A. Pyrshev, E. Real, Y. Mély and A. S. Klymchenko, *RSC Adv.*, 2015, **5**, 22899–22905.
- 67 Y. Niko, P. Didier, Y. Mely, G. Konishi and A. S. Klymchenko, *Sci. Rep.*, 2016, **6**, 9.
- 68 D. M. Owen, C. Rentero, A. Magenau, A. Abu-Siniyeh and K. Gaus, *Nat. Protoc.*, 2012, **7**, 24–35.
- 69 M. Collot, T. K. Fam, P. Ashokkumar, O. Faklaris, T. Galli, L. Danglot and A. S. Klymchenko, *J. Am. Chem. Soc.*, 2018, **140**, 5401–5411.
- 70 M. Collot, S. Bou, T. K. Fam, L. Richert, Y. Mély, L. Danglot and A. S. Klymchenko, *Anal. Chem.*, 2019, **91**, 1928–1935.
- 71 G. J. Schuurhuis, T. H. van Heijningen, A. Cervantes, H. M. Pinedo, J. H. de Lange, H. G. Keizer, H. J. Broxterman, J. P. Baak and J. Lankelma, *Br. J. Cancer*, 1993, **68**, 898–908.
- 72 F. Li, W.-l. Chen, B.-g. You, Y. Liu, S.-d. Yang, Z.-q. Yuan, W.-j. Zhu, J.-z. Li, C.-x. Qu, Y.-j. Zhou, X.-f. Zhou, C. Liu and X.-n. Zhang, *ACS Appl. Mater. Interfaces*, 2016, **8**, 32146–32158.
- 73 N. Bellance, F. Furt, S. Melser, C. Lalou, D. Thoraval, L. Maneta-Peyret, D. Lacombe, P. Moreau and R. Rossignol, *Int. J. Mol. Sci.*, 2020, **21**, 1317.
- 74 Z. Darwich, A. S. Klymchenko, O. A. Kucherak, L. Richert and Y. Mély, *Biochim. Biophys. Acta*, 2012, **1818**, 3048–3054.
- 75 A. P. Castano, T. N. Demidova and M. R. Hamblin, *Photodiagn. Photodyn. Ther.*, 2004, **1**, 279–293.



Electronic Supplementary Information

Dynamic covalent chemistry in live cells for organelle targeting and enhanced photodynamic action

Fei Liu,¹ Dmytro I. Danylchuk,¹ Bohdan Andreiuk,¹ Andrey S. Klymchenko^{1*}

¹ Laboratoire de Bioimagerie et Pathologies, UMR 7021 CNRS, ITI Chimie des Systèmes Complexes, Université de Strasbourg, 74 route du Rhin, 67401, Illkirch, France

*Corresponding author: andrey.klymchenko@unistra.fr

Experimental Section

Material and Methods

All starting materials for synthesis were purchased from Alfa Aesar or Sigma-Aldrich unless specifically mentioned. MitoTracker Deep Red FM 644/665 were purchased from Thermo Fisher. Nile Red Ketone (NRK),¹ lipid droplets marker SMCy5.5² and plasma membrane marker F2N12SM³ were synthesized as described before. CellTox™ Green assay (Cat.# G8741) was bought in Promega. Milli-Q water (Millipore) was used in all experiments. Synthesis and characterization of all new compounds, including membrane, lipid, and mitochondria targeting agents are described below. NMR spectra were recorded on a Bruker Avance III 400 MHz spectrometer. The following abbreviations are used in the presentation of the NMR data: s, singlet; brs, broad singlet; d, doublet; brd, broad doublet; dt, doublet of triplets; t, triplet; m, multiplet. Mass spectra were obtained using an Agilent Q-TOF 6520 mass spectrometer. Absorption spectra were recorded on Cary 5000 UV-visible spectrophotometer (Agilent). Fluorescence spectra were recorded on an Edinburg FS5 spectrofluorometer. All the spectra were corrected for the wavelength-dependent response function of the detector. Emission measurements were systematically done at rt. The confocal laser scanning microscopy was done by Leica Application Suite. Epi-fluorescence images were obtained from a microscope produced by Nikon Instruments Europe B.V. Cell images were processed using ImageJ 1.52a software (NIH, Bethesda, MD, USA).

In situ reaction in model lipid membranes

Preparation of large unilamellar vesicles (LUVs). A stock solution of dioleoylphosphatidylcholine (DOPC) in chloroform was placed into a round-neck flask, after which the solvent was evaporated in vacuo and phosphate buffer (20 mM, pH 7.4) was added. After all the solid was dissolved a suspension of multilamellar vesicles was extruded by using a Lipex Biomembranes extruder (Vancouver, Canada). The size of the filters was first 200 nm (7 passages) and thereafter 100 nm (10 passages). This generates monodisperse LUVs with a mean hydrodynamic diameter of 120 nm as measured by dynamic light scattering (DLS), using

Malvern Zetasizer Nano ZSP (Malvern, U.K.). The final DOPC concentration in the LUVs was calculated to be 1 mM.

Preparation of nanoemulsions (NEs)

Nanoemulsions were produced by spontaneous nanoemulsification according to protocols described previously.¹ Labrafac oil (Labrafac WL 1349® from Gattefossé, Saint Priest, France) (50 mg) was mixed with the surfactant Kolliphor ELP® (Sigma-Aldrich) (50 mg) in a sonication bath at 40 °C for 10 min. Then, the mixture was homogenized under magnetic stirring at 40 °C for 10 min up to complete homogenization. Finally, NEs were generated with the addition of ultrapure (Milli-Q) water (230 mg). The hydrodynamic diameter of NEs was 90 nm according to DLS.

Model study of *in situ* reactions in LUVs/NEs. 1 mL of LUVs (1 mM) in PBS were mixed with 5 µL of 10 mM stock solution (in DMSO) of membrane targeting compound PM-HZ and incubated for 30 min, then the excess of membrane targeting moiety was removed by dialysis using a dialysis membrane with molecular cut off weight of 14000 Da. Afterwards, 5 µL of 3 mM solution of NRK in DMSO were added and further incubated for 1h at r. t. Then, the mixture was extracted by 500 µL distilled water and 500 µL DCM, DCM phase was collected and concentrated *in vacuo*. The reaction was controlled using TLC by comparing with a control, which was prepared by directly mixing 100 µL of LUVs with 5 µL 3 mM (in DMSO) NRK, followed by the same extraction process. DCM:MeOH=95:5 was used as the eluent. The novel compound, identified by the different polarity in comparing to starting materials, was collected and subjected to mass spectrometry detection. Fluorescence spectra of NRK in LUVs in the presence of the membrane targeting hydrazine PM-HZ were recorded using the following sample preparation: 2 µM NRK in 1 mL in phosphate buffer (pH 7.4) were mixed with 10 µL of the LUVs with PM-HZ, prepared as mentioned above (after the dialysis) and incubated for 30 min. In the two control samples, 2 µM NRK in 1 mL in phosphate buffer were mixed or not with 10 µL of the LUVs (1 mM).

In order to estimate the yield of the hydrazone conjugate of PM-HZ, LD-HZ and Mito-HZ with NRK in LUVs/NEs, the following protocol was used. PM-HZ or Mito-HZ (20 µM) was incubated in 1 mL LUVs (containing 1 mM DOPC) for 20 min at r. t. LD-HZ (20 µM) was incubated in 1 mL NEs (containing 1 mM Labrafac oil) for 20 min at r. t. Then, NRK (10 µM) was added to these solutions and further incubated for 1h at r. t. Finally, the mixture was extracted by 1 mL ethyl acetate twice; the extract was evaporated in vacuum and then purified by TLC (DCM:MeOH=95:5 as an eluent). The formed fractions of NRK-PM-HZ conjugate (with higher polarity, low R_f), NRK-LD-HZ (with lower polarity, high R_f) and NRK-Mito-HZ (with higher polarity, low R_f) and NRK were collected and their absorbance was measured by dissolving in 1 mL MeOH. According to the absorbance of NRK and NRK-PM-HZ, NRK-LD-HZ or NRK-Mito-HZ, the reaction yields of the hydrazone formation were 65 mol%, 63 mol% and 28 mol% for NRK in-situ reaction with PM-HZ, LD-HZ and Mito-HZ, respectively.

Cell experiments

HeLa cells (ATCC® CCL-2) were grown in Dulbecco's modified Eagle's medium (DMEM, Gibco-Invitrogen), supplemented with penicillin (100 U/mL), 1% glycan (100 U/mL) and 10% FBS at 37 °C in a humidified atmosphere containing 5% CO₂. HeLa cells (ATCC) were then seeded on 36 mm ibidi coverslips at 30,000 cell per well in this DMEM medium with overnight. The DMEM medium was firstly removed and the cells were washed with PBS for three times. Then, medium was changed to Opti-MEM containing or not (in case of control) 100 µM of targeting hydrazides: LD-HZ for lipid droplets, PM-HZ for plasma membrane or Mito-HZ for mitochondria. The cells were incubated at 37 °C in a humidified atmosphere containing 5% CO₂ for 30 min. Then, after washing the cells gently once with PBS, the medium was changed to Opti-MEM containing 1 µM NRK (except 2.5 µM for mitochondria) and further incubated for 30 min at room temperature followed by fluorescence imaging. In the case of protocol without washing out the targeting molecule, the cells were seeded into labtek (8 well chambered coverslips) at 4000 cells per well in this DMEM medium and left overnight. The DMEM medium was then removed and the cells were washed with PBS for three times. The Opti-MEM medium (200 µL) containing certain concentration (1, 5, 20, 100 µM) of HZ-PM was added to HeLa cells. The cells were incubated for 10 min at r.t. followed by addition of NRK (1 µM) and further incubation for 30 min before imaging.

For all co-localization experiments, the cells were seeded into LabTek (8 well chambered coverslips) at 4000 cells per well in the DMEM medium and left overnight. The DMEM medium was then removed and the cells were washed with PBS for three times. Cells were pre-incubated with Opti-MEM medium (200 µL) containing or not (in cases of control) 20 µM corresponding targeting moieties of PM-HZ, LD-HZ or Mito-HZ for 10 min at 37 °C followed by addition of NRK or doxorubicin at 1 µM concentration and further incubated for 30 min. In case of co-localization in plasma membranes, F2N12SM (400 nM) was added after the cells were treated with Mito-HZ and NRK/doxorubicin and incubated for 15 min before imaging. For LDs labeling, LDs marker SMCy5.5 (1 µM) was added to the cells, incubated for 3h at 37 °C before adding targeting hydrazine LD-HZ and NRK/doxorubicin. For mitochondria labeling, MitoTracker Deep Red FM 644/665 (200 nM) was added after the cells were treated with Mito-HZ and NRK/doxorubicin and further incubated for 5 min at 37 °C. Finally, the corresponding medium was changed to Opti-MEM followed by fluorescence imaging. In cases of nucleus staining, Hoechst 33342 (10 µg/mL) in Opti-MEM was used to stain cell nucleus over 1 h and washed with PBS once before all the processes.

For reversibility analysis of reaction of NRK with PM-HZ at plasma membrane interface, the cells in LabTek were pre-incubated with Opti-MEM medium (200 µL) containing or not (in cases of control) 20 µM PM-HZ for 10 min at 37 °C followed by addition of 1 µM NRK and further incubated for 30 min at 37 °C. For experiments with different pH (short incubation time), the cells were washed with PBS three times and the medium was changed to Opti-MEM (pH 7.4) or to phosphate-acetate buffer (pH 5.8). For long incubation in Opti-MEM (pH 7.4), after washing with PBS three times, cell medium was changed to Opti-MEM medium (200 µL) and the cells were incubated for 1 h at 37 °C. For each experimental condition, just before imaging the cells were incubated for 5 min at 37 °C with reference plasma membrane probe F2N12SM (400 nM).³

Fluorescence imaging of NRK was done with the excitation wavelength at 488 nm, and fluorescence emission was collected at two different spectral channels: 550-600 nm and 600-670 nm. In the colocalization measurements with LDs marker SMCy5.5, for NRK channel, excitation wavelength was set at 488 nm and emission wavelength was collected in the range of 550-600 nm. For doxorubicin channel, the excitation wavelength was at 488 nm and fluorescence emission was collected in range of 520-650 nm (images of for membrane and mitochondria targeting were collected over average of 20 frames for this channel due to low brightness of doxorubicin). For the SMCy5.5 and MitoTracker Deep Red FM 644/665 channel, the excitation wavelength was set at 635 nm and the emission wavelength was collected in the range of 650-800 nm.

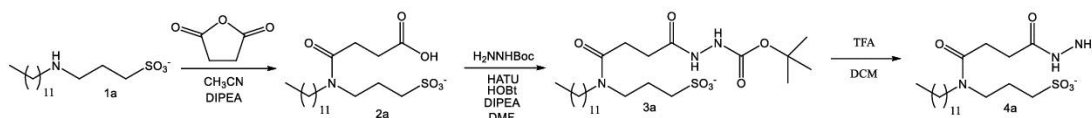
Colocalization analysis was conducted in two ways. The first way was by calculating Pearson's and Mander's correlation coefficients. This was conducted by using an ImageJ plugin named "Just Another Colocalisation Plugin (JACoP)". A certain threshold for both Green and Red channels was applied to select the ROI area for the calculation of Pearson's and Mander's correlation coefficients. The second way was to calculate the ratio of the mean fluorescence intensity from organelle areas versus the whole cells. The organelle areas were selected by using fluorescence image of corresponding reference markers, F2N12SM for plasma membrane, SMCy5.5 for lipid droplet or Mito Tracker Deep Red FM for mitochondria. Cell selection and calculation of the mean fluorescence intensity were done using ImageJ.

Phototoxicity study

HeLa cells (ATCC® CCL-2) were grown in Dulbecco's modified Eagle's medium (DMEM, Gibco-Invitrogen), supplemented with penicillin (100 U/mL), 1% glycan (100 U/mL) and 10 % FBS at 37 °C in a humidified atmosphere containing 5% CO₂. HeLa cells (ATCC) were then seeded on 36 mm coverslips at 30,000 cell per well in this DMEM medium with overnight. The DMEM medium were first removed and washed with PBS for three times before changing the medium to Opti-MEM (as control) or Opti-MEM containing PM-Hz, Mito-HZ or LD-HZ (100 µM), then the cells were incubated at 37 °C in a humidified atmosphere containing 5% CO₂ for 30 min. After that the cell were washed with PBS and the medium was changed to Opti-MEM containing 1 µM of NRK, followed by an incubation for 30 min at r. t. To understand PDT effect when NRK is targeted to different cell organelles, we used CellTox™ Green, a nucleus maker for monitoring cell death induced by membrane disruption. After targeting NRK to cell organelles with corresponding ligands, the dishes with cells were washed once with PBS and subjected to illumination with excitation of 550 nm (50% LED source power) continuously over 1 min followed by changing the medium to 1 mL CellTox™ Green assay containing 12 µg/mL Hoechst nucleus staining agent and incubated for 30 min. The transmission and fluorescence (CellTox™ Green channel) images were taken before and after illumination using 20x air objective Nikon CFI Plan Apo, NA = 0.75 (for data in Figure 3) or 10x air objective Nikon Plan Fluor NA = 0.3 (for data in Figure S5); excitation: 470 nm, emission filter: 531/40 nm for CellTox™ Green channel and excitation: 405 nm, emission filter: 475/50 nm for Hoechst 33342 channel. To observe the cell morphology change induced by phototoxicity, cell images (both bright field and epi-fluorescence channel (4% power, 300 ms

integration period) with excitation of 550 nm and filter of 600/50 nm) were firstly taken before the application of high source power. Then video was prepared by taking images of the bright field transmission channel and epi-fluorescence channel (source power: 30% for lipid droplets, plasma membrane and their controls; 50 % for mitochondria and its control) and short integration period (30 ms) continuously for 30 slices over 10 min. After the video recording, images were taken in dic channel (300 ms) and epi channel (4% power, 300 ms integration period). This cellular imaging studies were done using epi-fluorescence mode with a Nikon Ti-E inverted microscope, equipped with CFI Plan Apo $\times 60$ oil (numerical aperture = 1.4) objective, and a Hamamatsu Orca Flash 4 sCMOS camera.

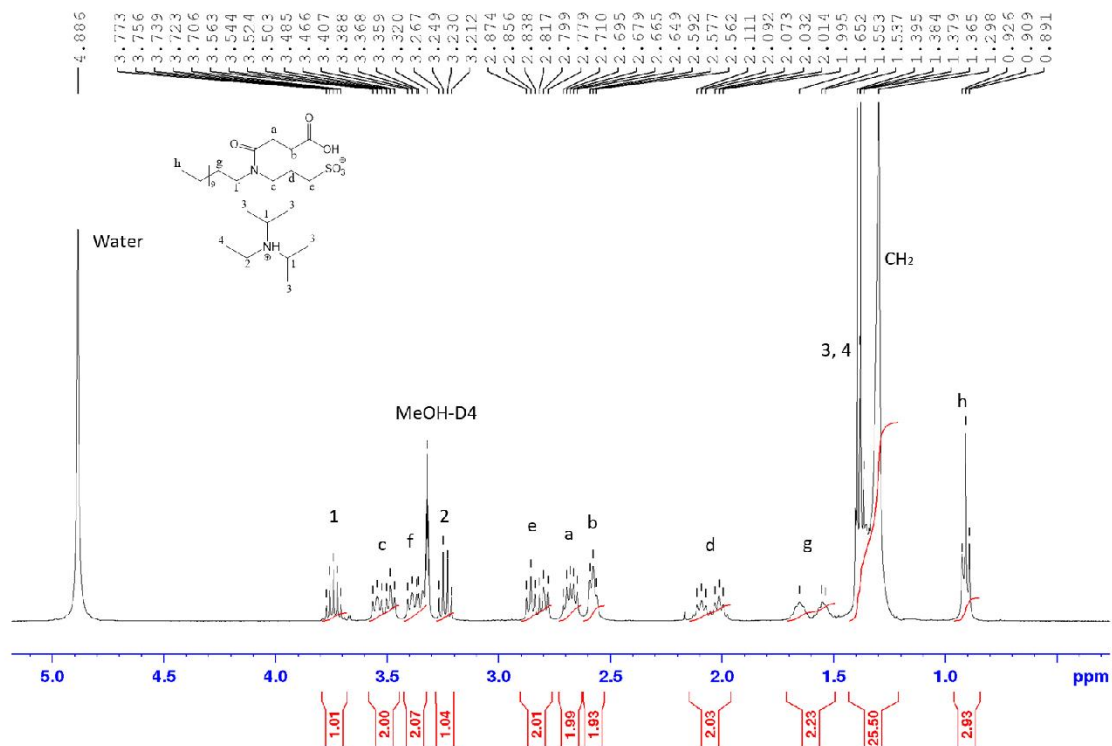
Synthesis of targeting hydrazides



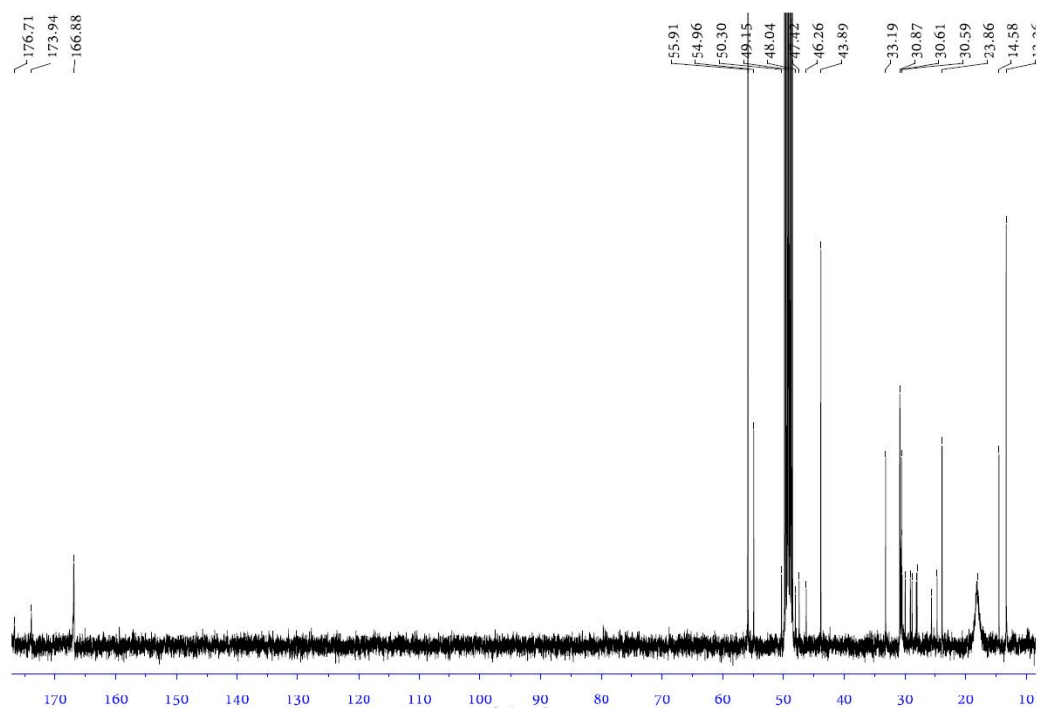
Scheme S1. Synthesis route for PM-HZ (**4a**).

Compound **1a** was prepared as described previously.⁴

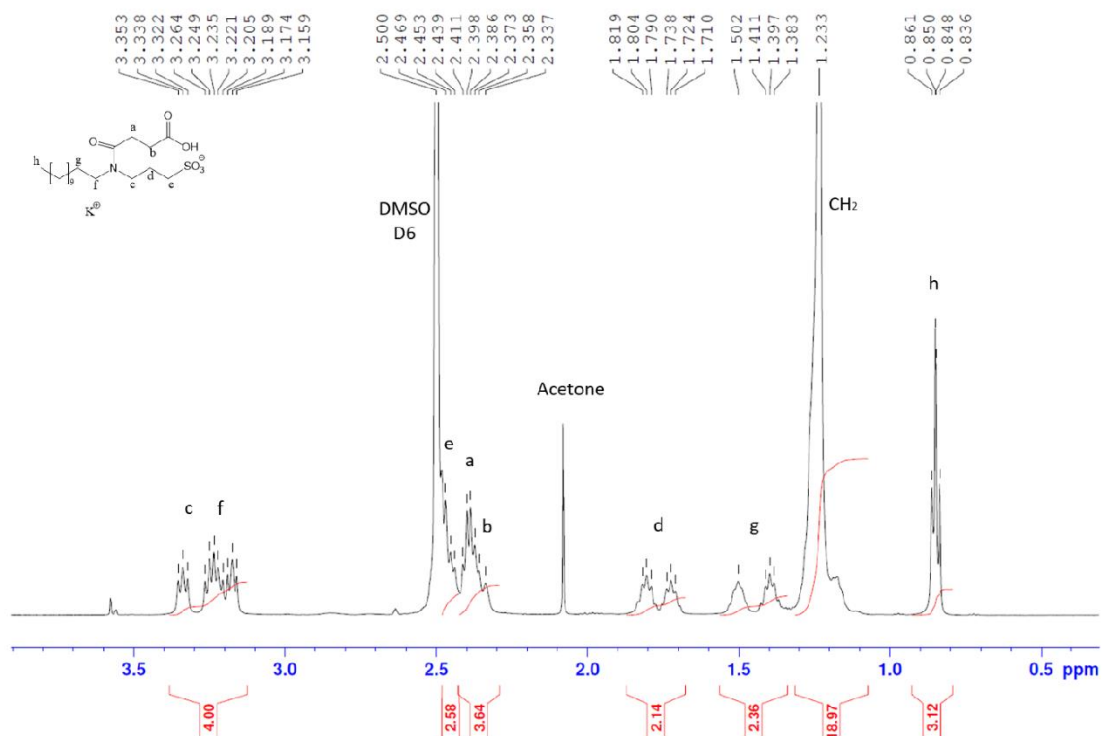
Compound 2a. 400 mg of compound **1a** were dissolved in 7 mL of dry CH_3CN together with 589 mg (3.5 equiv., 794 μL) of DIPEA. After that, a solution of 196 mg (1.5 eq.) of succinic anhydride in 3 mL of dry CH_3CN was added dropwise and the resulting mixture was stirred for 12h (control by TLC) under Ar atmosphere. After the reaction the solvent was evaporated *in vacuo* and the crude product was purified by column chromatography (SiO_2 , $\text{DCM}:\text{MeOH}:\text{HCOOH}$ 80:20:2). Yield: 550 mg as a colourless solid (DIPEA salt is present, its signals are not presented). ^1H NMR (400 MHz, $\text{MeOH}-d_4$) δ ppm 3.49 (2H, dt), 3.36 (2H, dt), 2.86 (2H, dt), 2.68 (2H, m), 2.58 (2H, t), 2.06 (2H, m), 1.60 (2H, brd), 1.30 (18 H, brs), 0.81 (3H, t). Splitting of d, f, g was due to presence of amide rotamers, which disappeared under high temperature. ^{13}C NMR (400 MHz, $\text{MeOH}-d_4$) δ ppm 176.70, 173.94, 166.88, 55.91, 54.96, 50.30, 49.15, 48.04, 47.42, 46.26, 43.89, 33.19, 30.87, 30.71, 30.61, 30.59, 30.50, 30.00, 29.16, 28.88, 28.21, 28.06, 25.58, 24.66, 23.86, 18.11, 17.85, 14.58, 13.26. Chemical Formula: $[\text{C}_{19}\text{H}_{36}\text{N}_3\text{O}_6\text{S}^-]$ m/z (M) calc. 406.2263 MS for m/z $[\text{M}^-+2\text{H}^+]^+$ found 408.2432.



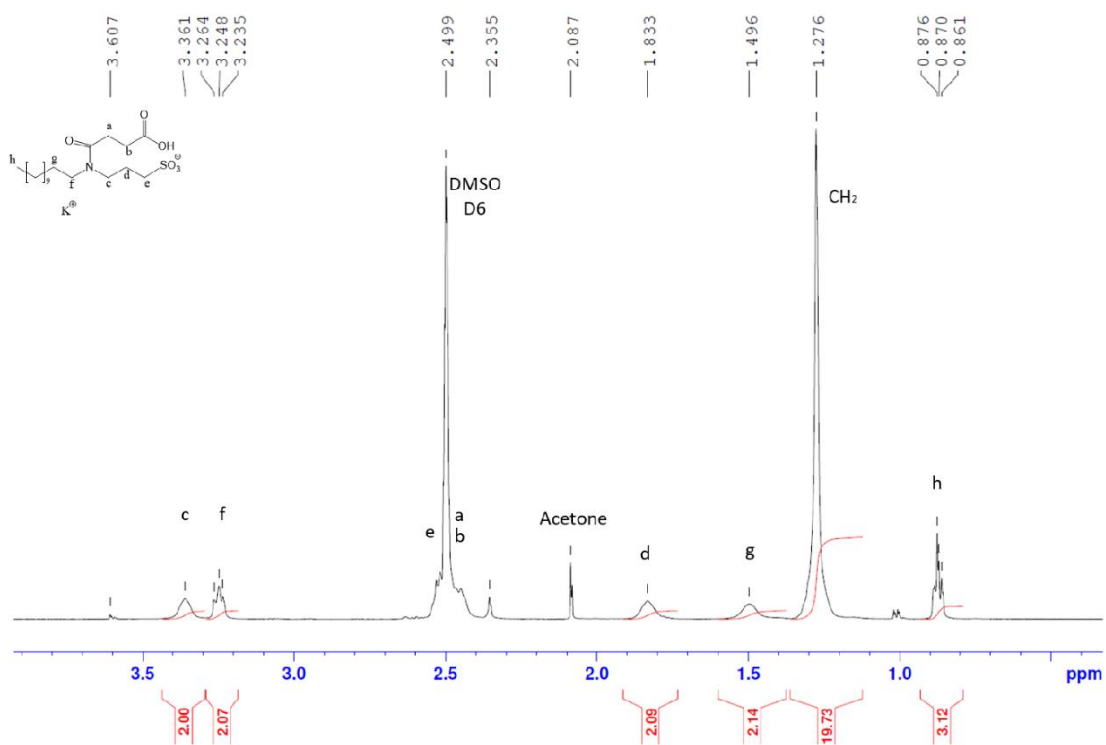
¹H-NMR spectrum of **2a** in MeOH-D₄.



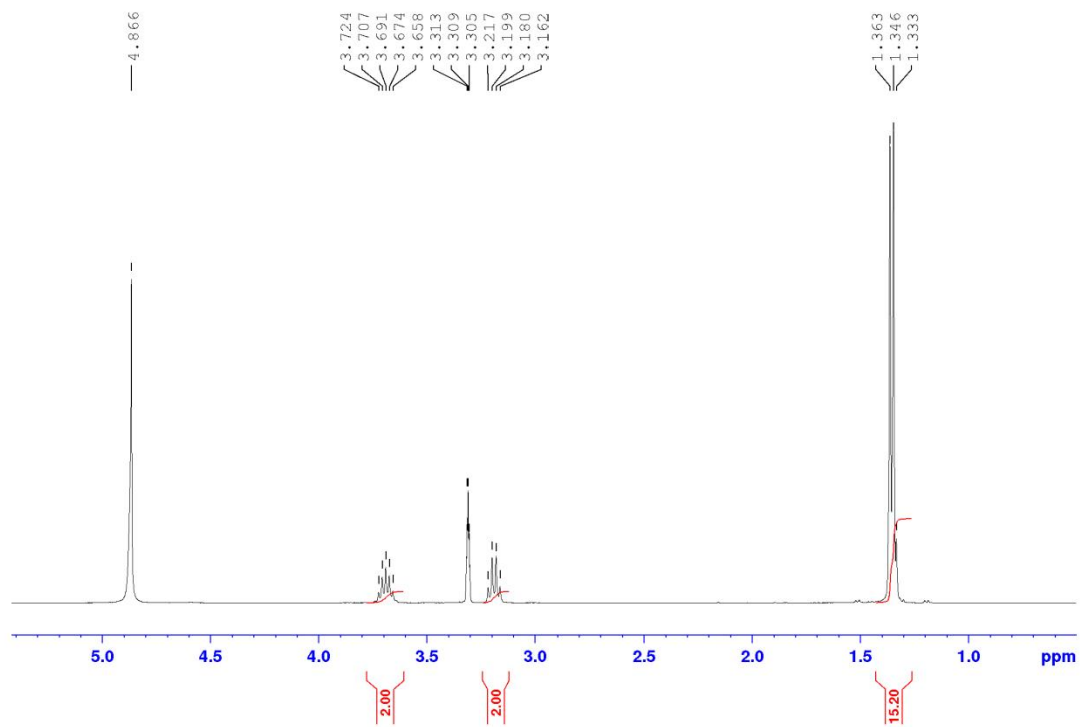
¹³C-NMR spectrum of **2a** in MeOH-D₄.



^1H -NMR spectrum of **2a** in DMSO (D6) under room temperature after ion exchange of protonated DIPEA with K^+ ion.

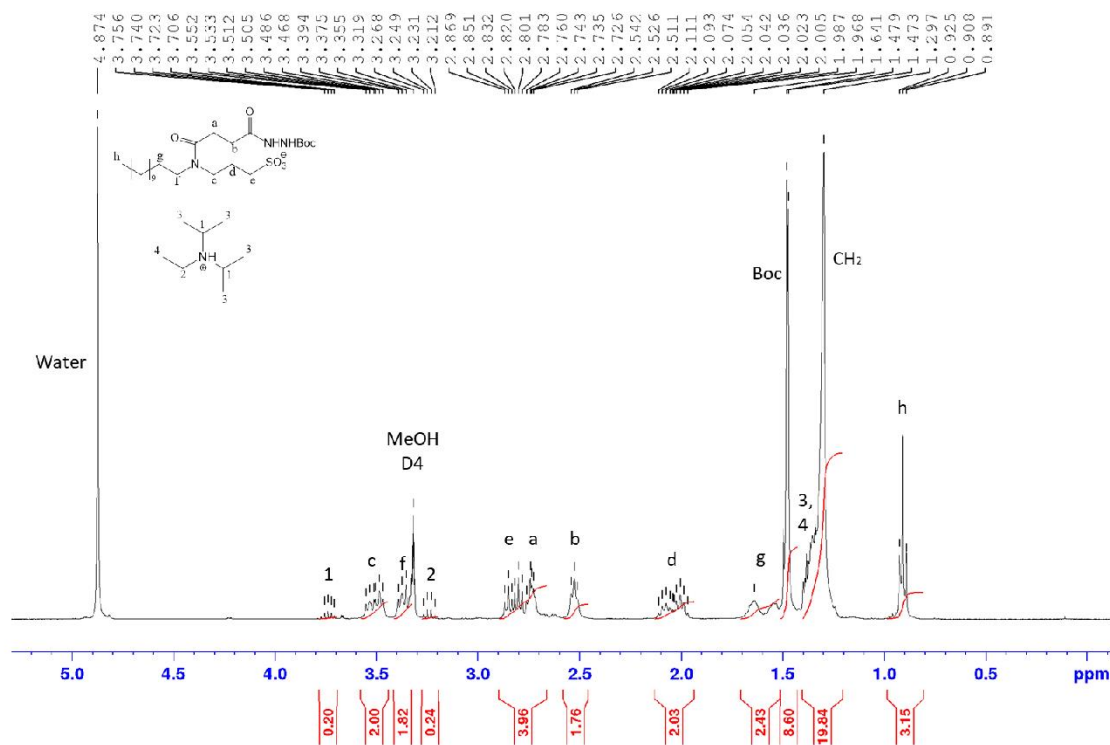


^1H -NMR spectrum of **2a** under high temperature (375 K) after ion exchange of protonated DIPEA with K^+ ion in DMSO (6d).

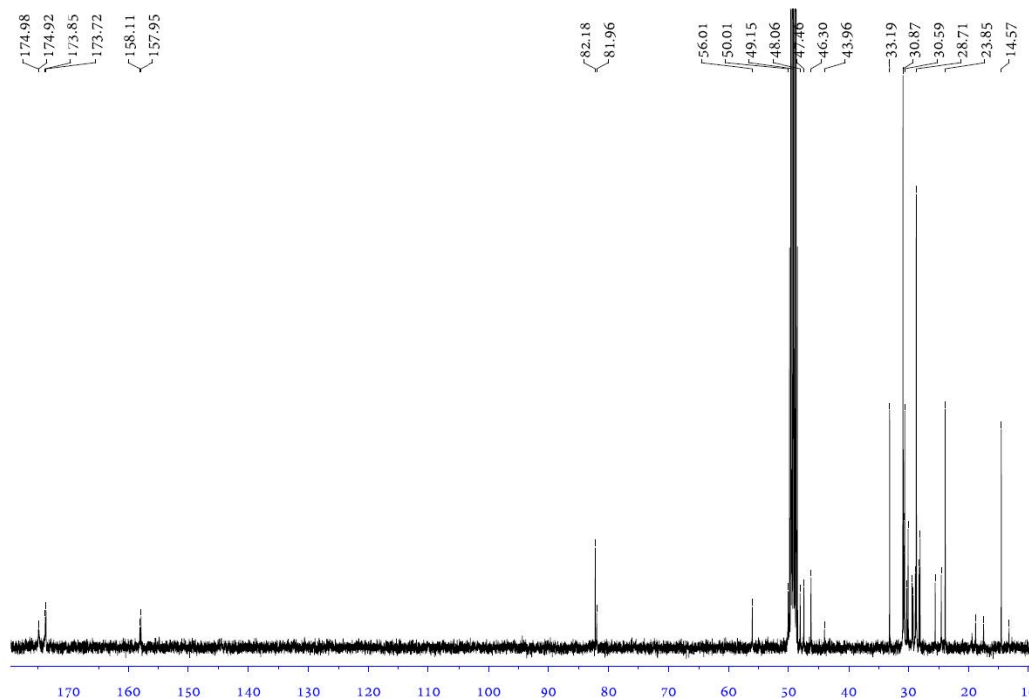


^1H -NMR spectrum of protonated N,N-diisopropylethylamine (DIPEA) in TFA in MeOH-D₄.

Compound 3a. 200 mg of compound **2a** were dissolved in 3 mL of dry DMF together with 238 mg (1.5 eq.) of HATU, 28 mg (0.5 eq.) of HOBt and 215 mg (4 eq., 291 μ L) of DIPEA under Ar atmosphere. After 5 minutes, a solution of 83 mg (1.5 eq.) of tert-Butyl carbazate in 1.5 mL of dry DMF was added and the mixture was stirred for 24h (control by TLC) under Ar atmosphere. After the reaction the solvent was evaporated *in vacuo* and the crude product was purified by column chromatography (SiO₂, DCM:MeOH 80:20, redone twice). Yield: 165 mg as a colourless solid (DIPEA salt is present, its signals are not presented). ¹H NMR (400 MHz, MeOH-D₄) δ ppm 3.50 (2H, dt), 3.37 (2H, dt), 2.82 (2H, dt), 2.74 (2H, m), 2.53 (2H, t), 2.05 (2H, m), 1.60 (2H, brd), 1.47 (9H, m), 1.30 (18H, brs), 0.91 (3H, t). ¹³C NMR (400 MHz, MeOH-D₄) δ ppm 174.98, 174.92, 173.85, 173.72, 158.11, 157.95, 82.18, 81.96, 56.01, 50.01, 49.15, 48.06, 47.46, 46.30, 43.96, 33.19, 30.87, 30.71, 30.64, 30.59, 30.26, 30.04, 29.39, 29.23, 28.87, 28.71, 28.25, 28.09, 25.62, 24.50, 23.85, 18.89, 17.45, 14.57. HRMS for Chemical Formula: [C₂₄H₄₆N₃O₇S⁻] m/z (M) calc. 520.3056, found 520.3051.

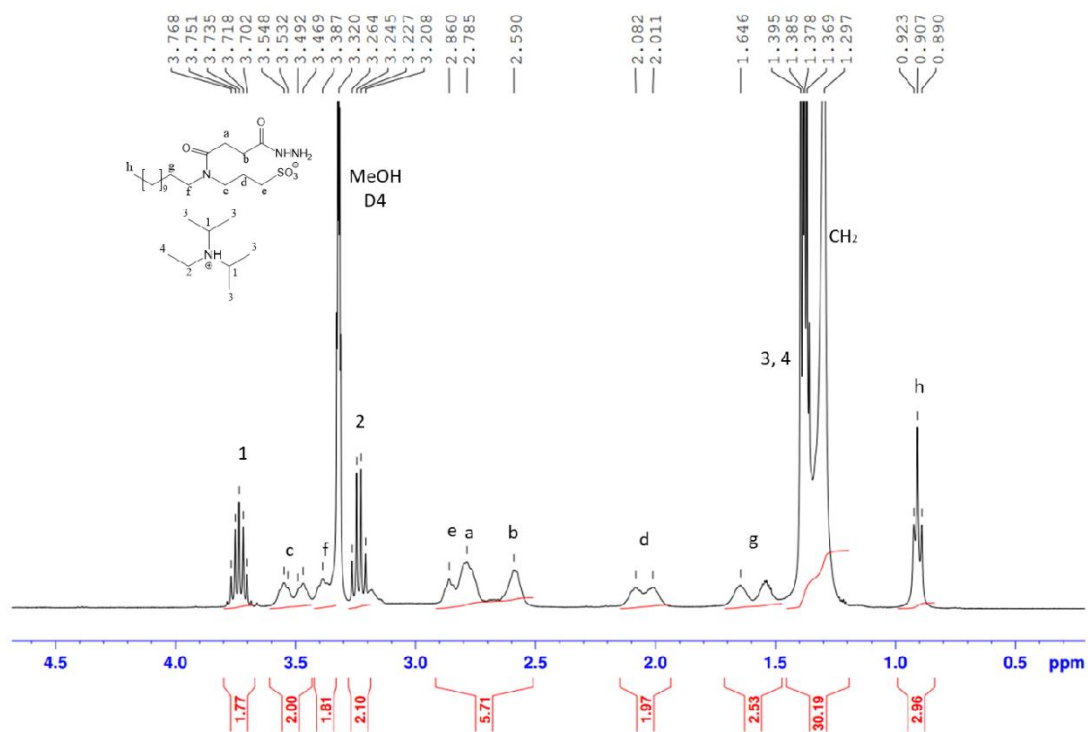


¹H-NMR spectrum of **3a** in MeOH-D₄.

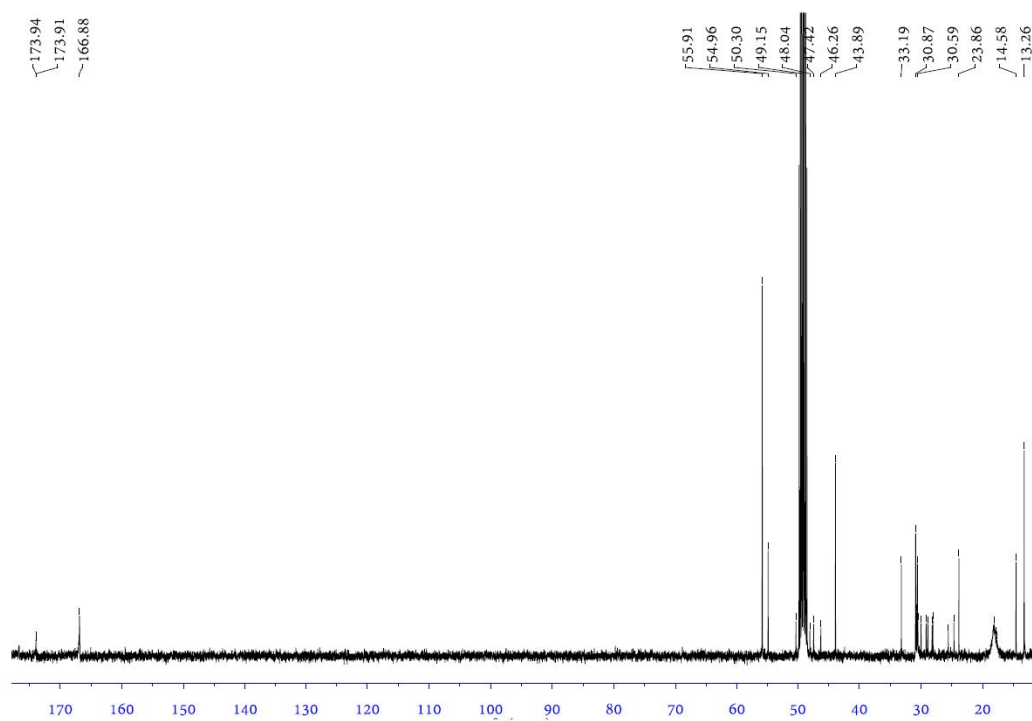


^{13}C -NMR spectrum of **3a** in MeOH-D₄.

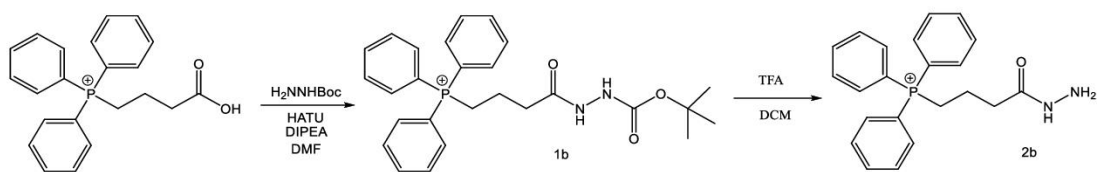
Compound 4a (PM-HZ). To the solution of **3a** (165 mg, 0.31 mmol) in DCM (5 mL), TFA (5 mL) and 1 drop of MiliQ water were added and stirred at room temperature for 2 h. After confirming the reaction completely proceeded with TLC, the solvents were evaporated under reduced pressure, and then the residue was dissolved in MeOH and evaporated 3 times to remove TFA and give desired product **4a** as a colorless solid (153 mg) (DIPEA salt is present, its signals are not presented). ^1H NMR (400 MHz, MeOH-D₄) δ ppm 3.51 (2H, brd), 3.39 (2H, brs), 2.80 (4H, m), 2.59 (2H, brs), 2.04 (2H, brd), 1.59 (2H, brd), 1.30 (18H, brs), 0.91 (3H, t). ^{13}C NMR (400 MHz, MeOH-D₄) δ ppm 173.94, 173.91, 166.88, 55.91, 54.96, 50.30, 49.15, 48.04, 47.42, 46.26, 43.89, 33.19, 30.87, 30.71, 30.61, 30.59, 30.50, 30.00, 29.16, 28.88, 28.21, 28.06, 25.58, 24.66, 23.86, 18.11, 17.85, 17.67, 14.58, 13.26. HRMS for Chemical Formula: $[\text{C}_{19}\text{H}_{38}\text{N}_3\text{O}_5\text{S}^-]$ m/z (M) calc. 420.2532, found 420.2534.



¹H-NMR spectrum of **4a** in MeOH-D₄.

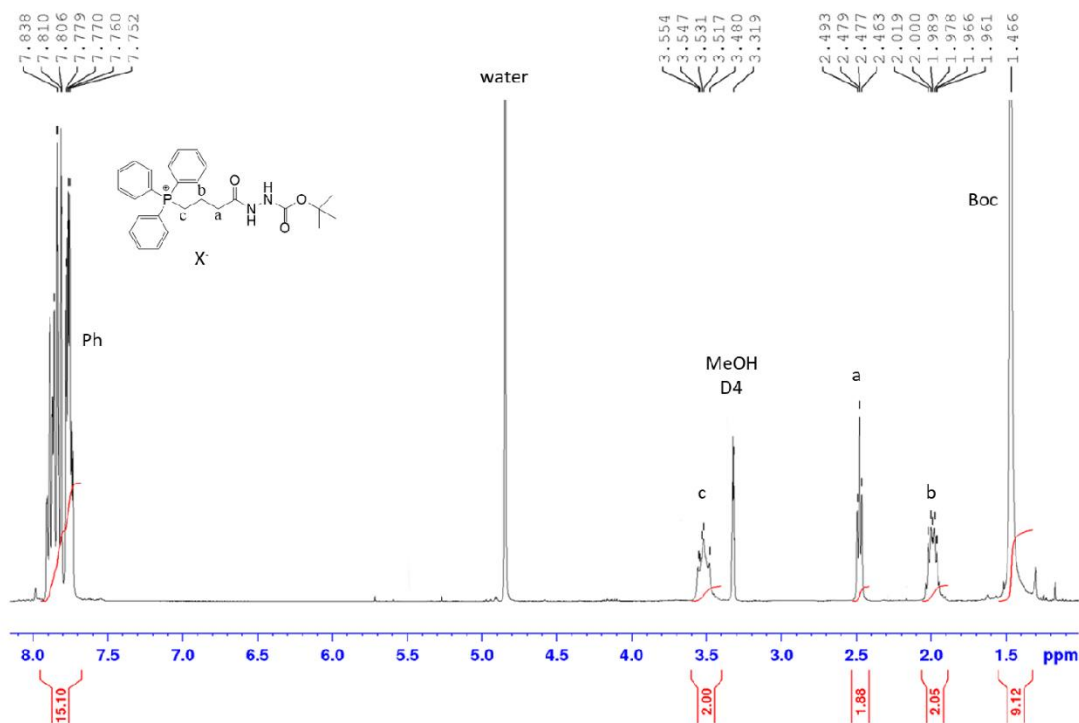


¹³C-NMR spectrum of **4a** in MeOH-D₄.

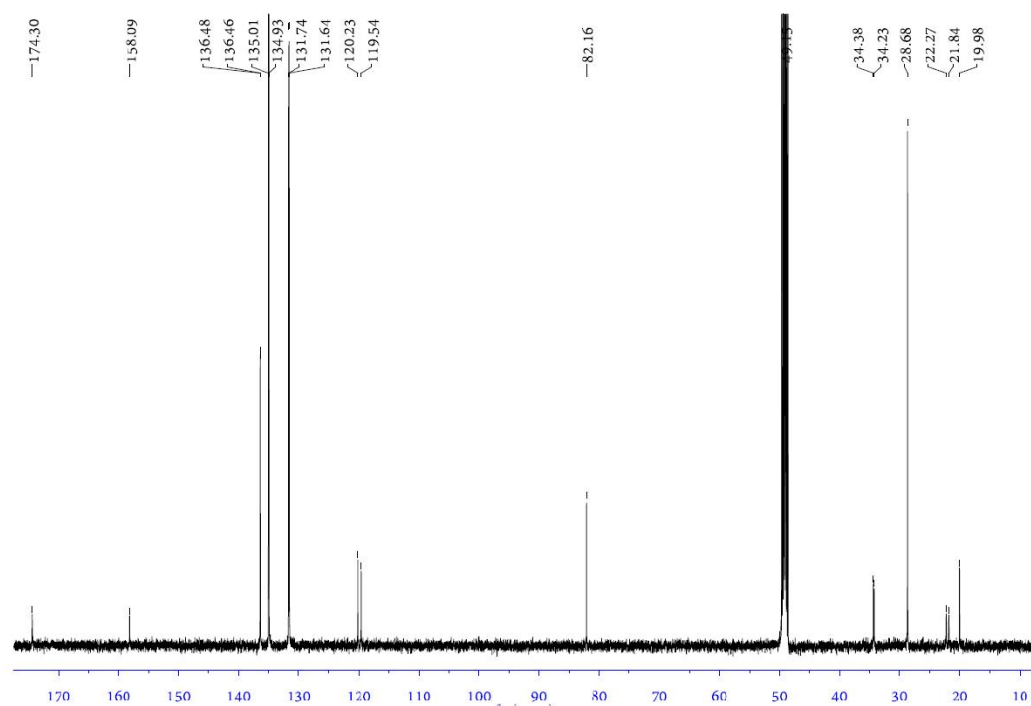


Scheme S2. Synthesis route for Mito-HZ (**2b**).

Compound 1b. 500 mg of (3-carboxypropyl)triphenylphosphonium bromide were dissolved in 8 mL of dry DMF together with 465 mg (1.05 eq.) of HATU and 450 mg (3 eq., 610 μL) of DIPEA. After 5 minutes, a solution of 161 mg (1.05 eq.) of tert-Butyl carbazate in 2 mL of dry DMF was added and the mixture was stirred for 24h (control by TLC) under Ar atmosphere. After the reaction the solvent was evaporated *in vacuo*, then the solid residue was dissolved in MeOH and precipitated with Et₂O, filtered and washed with Et₂O (redone twice). After that, the solid residue was dissolved in DCM, washed with water (x2) and brine, dried over Na₂SO₄ and the solvent was evaporated *in vacuo*. The crude product was purified by gradient column chromatography (SiO₂, DCM:MeOH 90:10 to 80:20). Yield: 70 mg as a colourless solid. ¹H NMR (400 MHz, MeOH-D₄) δ ppm 7.81 (15H, m), 3.54 (2H, t), 2.48 (2H, t), 1.99 (2H, m), 1.47 (9H, s). ¹³C NMR (400 MHz, MeOH-D₄) δ ppm 174.30, 158.09, 136.48, 136.46, 135.01, 134.93, 131.74, 131.64, 120.23, 119.54, 82.16, 49.15, 34.38, 34.23, 28.68, 22.27, 21.84, 19.98. HRMS for Chemical Formula: [C₂₇H₃₂N₂O₃P⁺] m/z (M) calc. 463.2151, found 463.2657.

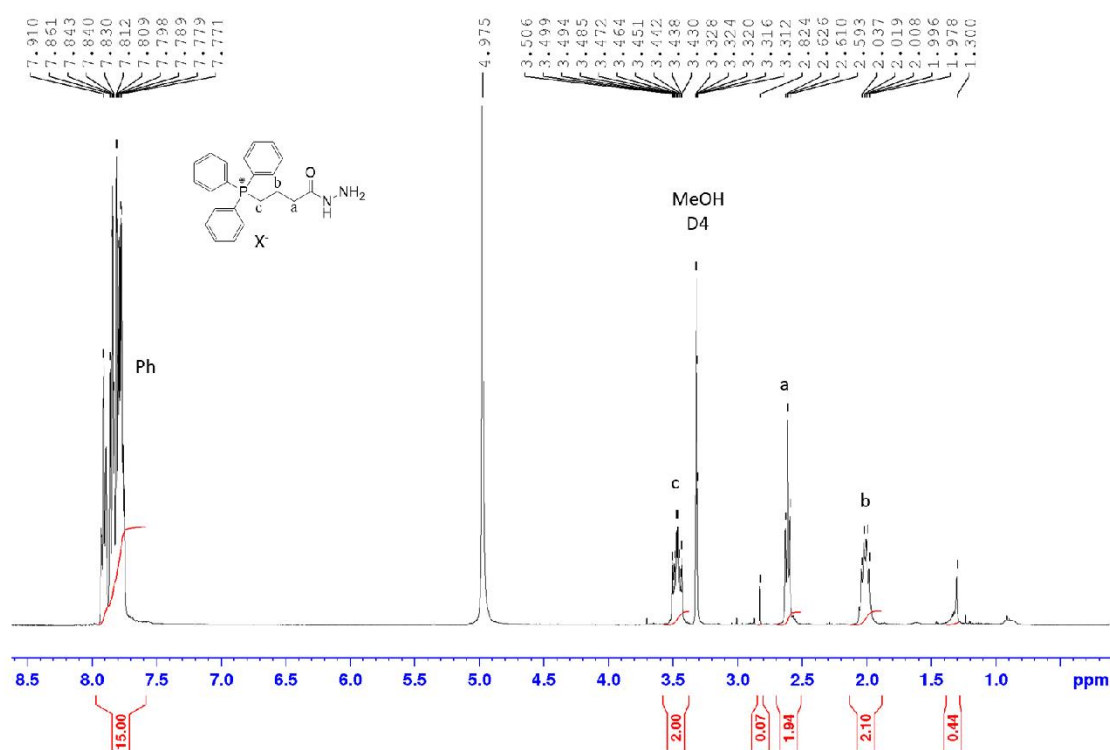


¹H-NMR spectrum of **1b** in MeOH-D₄.

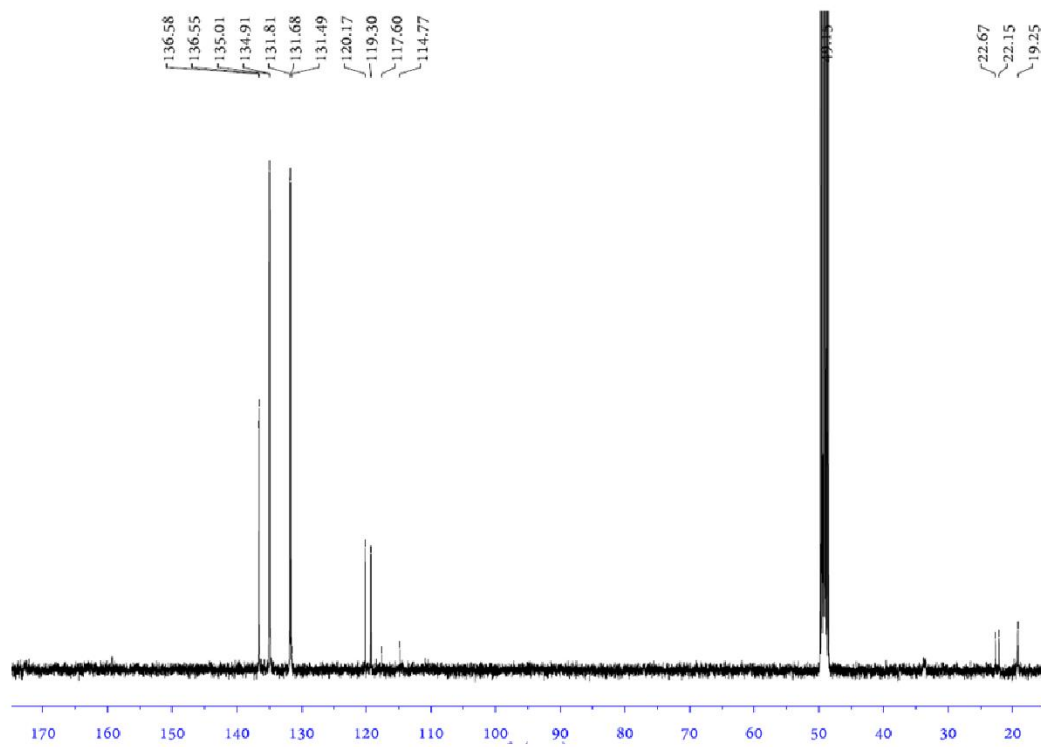


^{13}C -NMR spectrum of **1b** in MeOH-D₄.

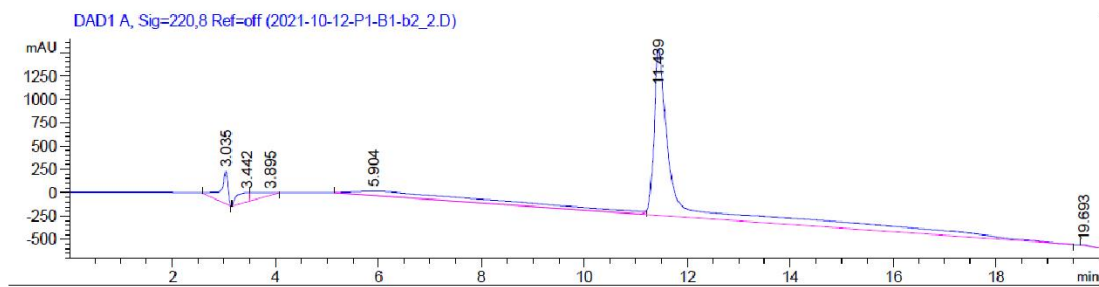
Compound 2b (Mito-HZ). To the solution of **1b** (70 mg, 0.15 mmol) in DCM (2 mL), TFA (2 mL) and 1 drop of MiliQ water were added and stirred at room temperature for 2 h. After confirming the reaction completely proceeded with TLC, the solvents were evaporated under reduced pressure, and then the residue was dissolved in MeOH and evaporated 3 times to remove TFA and give desired product **4a** as a colorless solid (54 mg). ^1H NMR (400 MHz, MeOH-D₄) δ ppm 7.83 (15H, m), 3.47 (2H, m), 2.61 (2H, t), 2.01 (2H, pentet). ^{13}C NMR (400 MHz, MeOH-D₄) δ ppm 136.58, 136.55, 135.01, 134.91, 131.81, 131.68, 131.49, 120.17, 119.30, 117.60, 114.77, 49.15, 22.67, 22.15, 19.25. HRMS for Chemical Formula: $[\text{C}_{22}\text{H}_{24}\text{N}_2\text{OP}^+]$ m/z (M) calc. 363.1626, found 363.2060. This compound was further characterized by RP-HPLC by using C4 column (diameter 4.6 mm, length 250 mm, 5 μM pore size) at flow rate of 1 mL/min, 45 $^\circ\text{C}$, 50% /50% of water/acetonitrile on an Agilent 1290 Infinity II LC System.



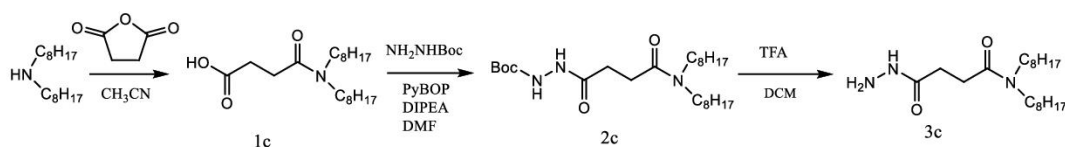
^1H -NMR spectrum of **2b** MeOH-D₄.



^{13}C -NMR spectrum of **2b** MeOH-D₄.

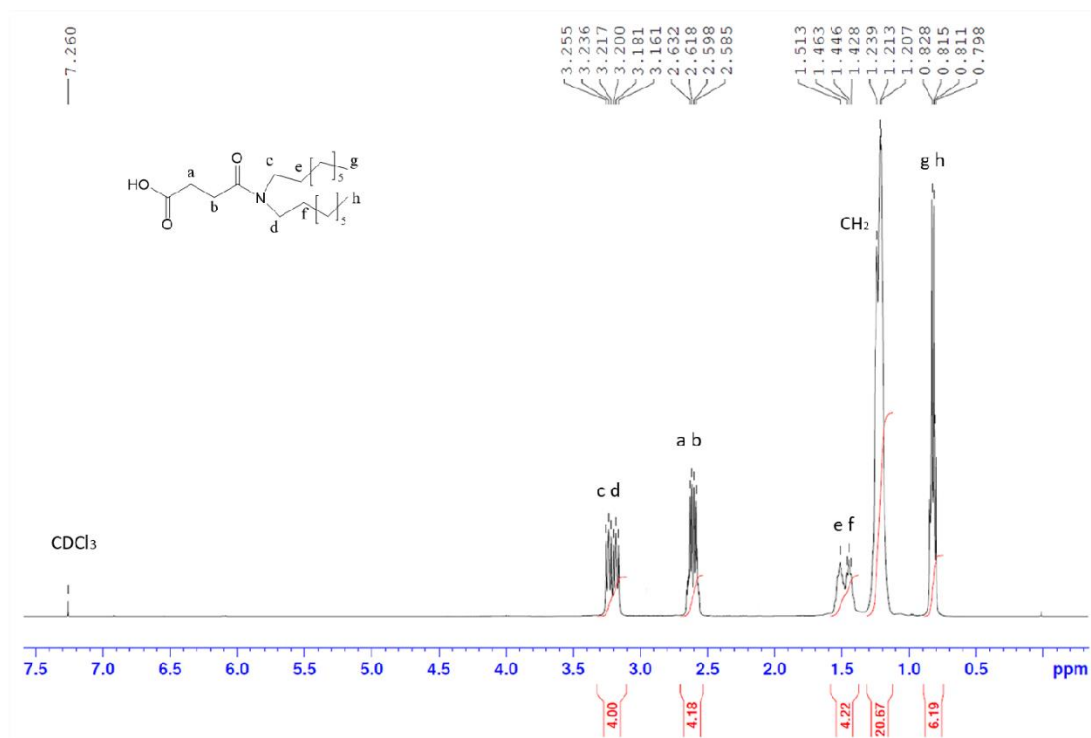


RP-HPLC profile of **2b**.

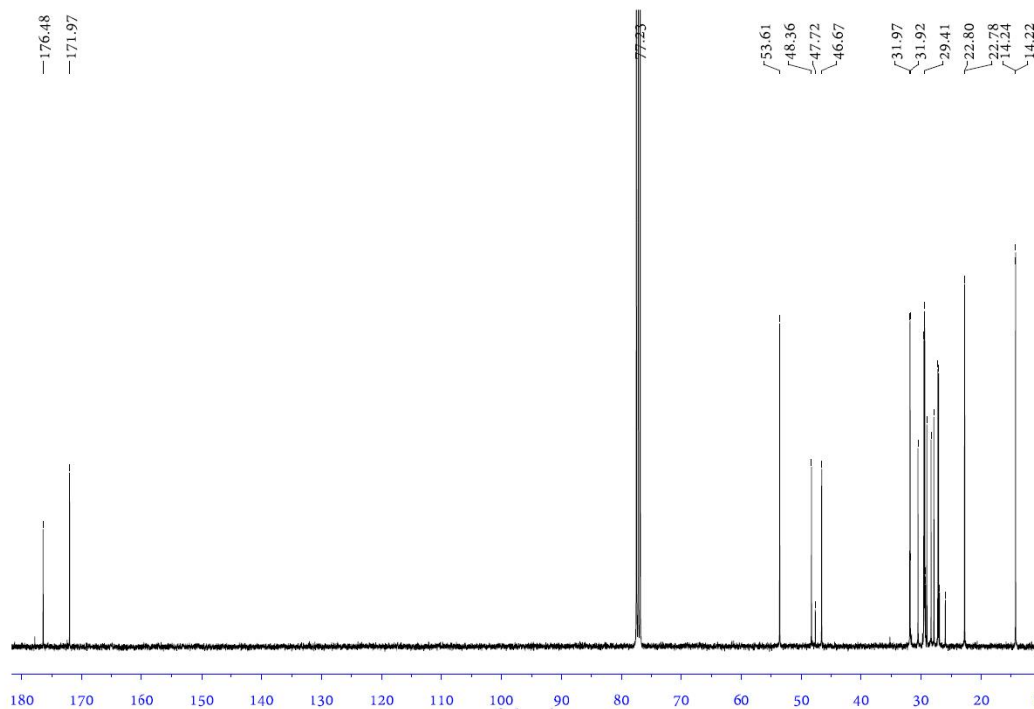


Scheme S3. Synthesis route for LD-HZ (**3c**).

Compound 1c. To the solution of succinic anhydride (192 mg, 1.92 mmol) in THF (20 mL) was added 1,1-Dioctylamine (250 mg, 1.04 mmol), then mixture was refluxed overnight under argon atmosphere. The solvent was evaporated in vacuo, then resulting residue was purified by recrystallization from dioxane to give desired product as a colorless solid (243 mg, 68 %). ^1H NMR (400 MHz, CDCl_3) δ ppm 3.23 (2H, t), 3.18 (2H, t), 2.62 (2H, m), 2.59 (2H, m), 1.51 (2H, m), 1.45 (2H, m), 1.21 (20H, m), 0.81 (6H, m). ^{13}C NMR (400 MHz, CDCl_3) δ ppm 176.48, 171.97, 77.23, 53.61, 48.36, 47.72, 46.67, 31.97, 31.92, 31.90, 30.48, 29.53, 29.46, 29.41, 29.36, 29.30, 29.24, 29.02, 28.33, 27.86, 27.21, 27.08, 26.94, 25.97, 22.80, 22.78, 14.24, 14.22. HRMS for Chemical Formula $[\text{C}_{20}\text{H}_{39}\text{NO}_3]^-$ m/z (M) calc. 341.2929, found m/z for $[\text{M}^- + 2\text{Na}^+ - \text{H}^+]^+$ 386.3101.

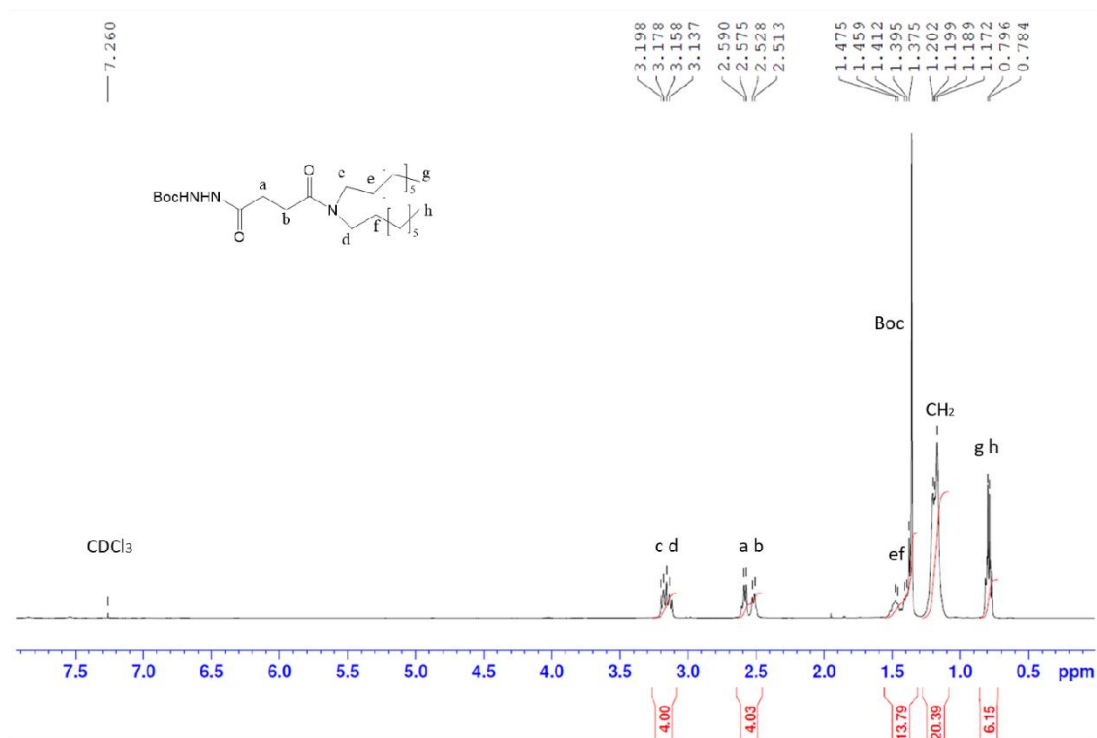


^1H -NMR spectrum of **1c** in CDCl_3 .

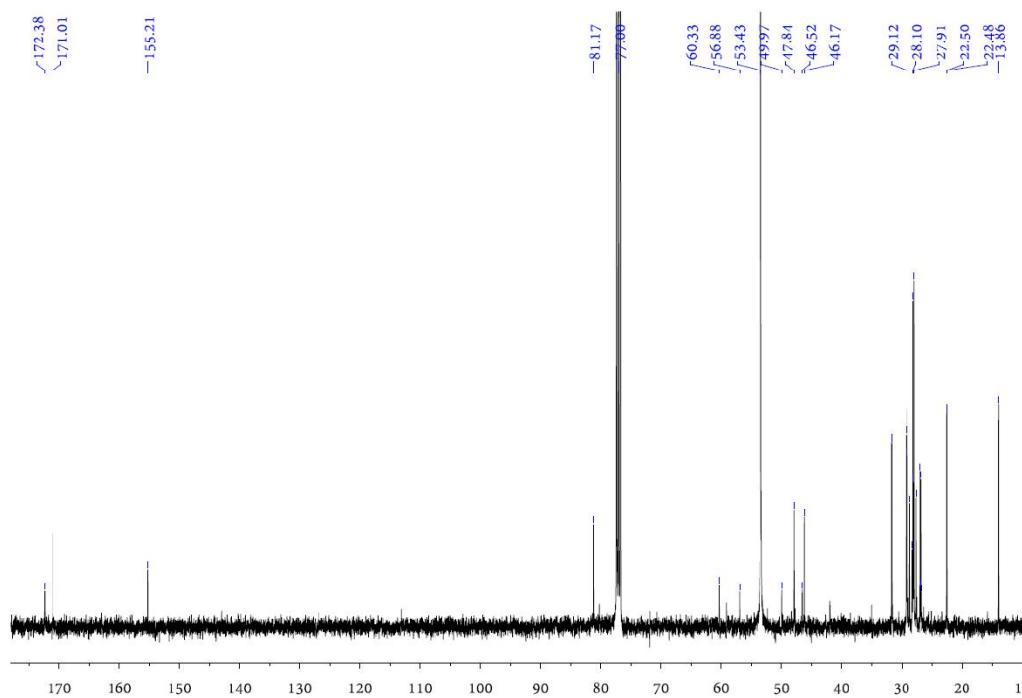


^{13}C -NMR spectrum of **1c** in CDCl_3 .

Compound 2c. To the solution of **1c** (243 mg, 0.71 mmol) in DMF (10 mL), tert-butylcarbazate (159 mg 1.21 mmol), PyBOP (630 mg, 1.21 mmol), and DIPEA (1.11 mL, 6.4 mmol (9 eq)) were added and stirred at room temperature overnight under argon atmosphere. The solvent was evaporated in vacuo, then resulting residue was purified by flash column chromatography on silica gel (eluent EtOAc/Hepane 50:50) to give desired product as a colorless solid (163 mg, yield 50%). ^1H NMR (400 MHz, CDCl_3) δ ppm 3.17 (4H, m), 2.58 (2H, m), 2.51 (2H, m), 1.3-1.5 (13H, m), 1.20 (20H, m), 0.79 (6H, m). ^{13}C NMR (400 MHz, CDCl_3) δ ppm 172.38, 171.01, 155.21, 81.17, 77.00, 60.33, 56.88, 53.43, 49.97, 47.84, 46.52, 46.17, 31.68, 31.63, 29.26, 29.17, 29.12, 29.07, 28.67, 28.23, 28.10, 28.04, 27.91, 27.60, 26.94, 26.87, 26.79, 26.73, 22.50, 22.48, 13.86. HRMS for Chemical Formula $[\text{C}_{20}\text{H}_{39}\text{NO}_3]^-$ m/z (M) calc 455.3723, found m/z for $[\text{M}+\text{Na}^+]^+$ 478.4062.

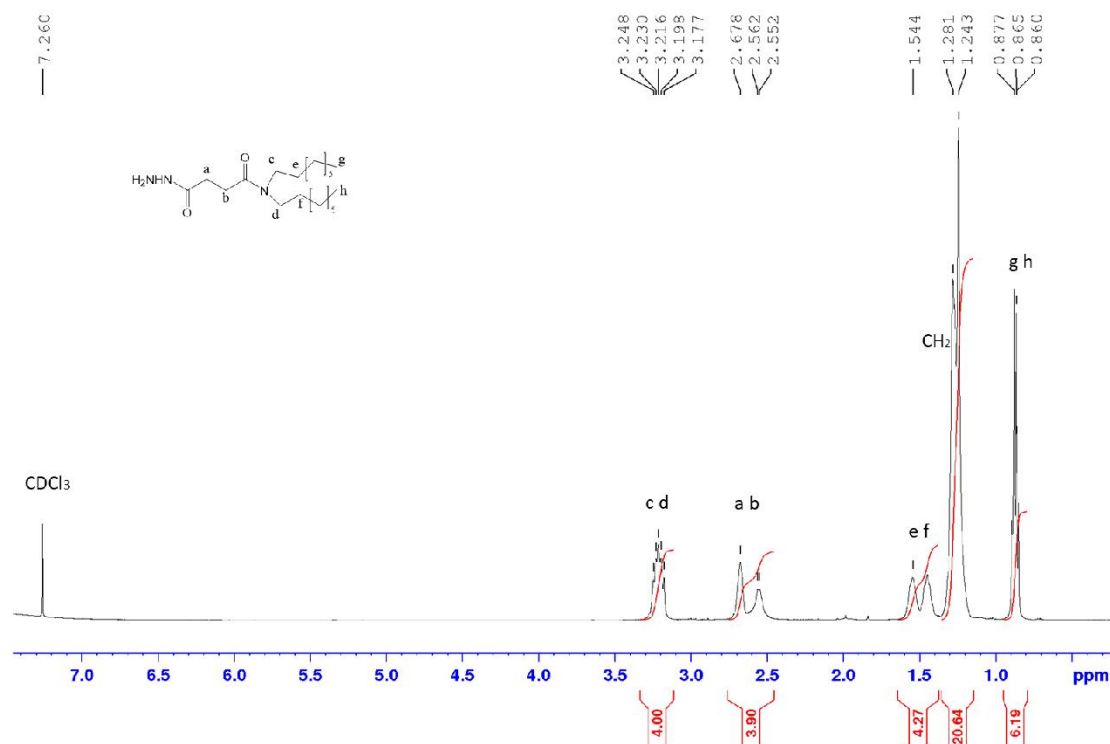


^1H -NMR spectrum of **2c** in CDCl_3 .

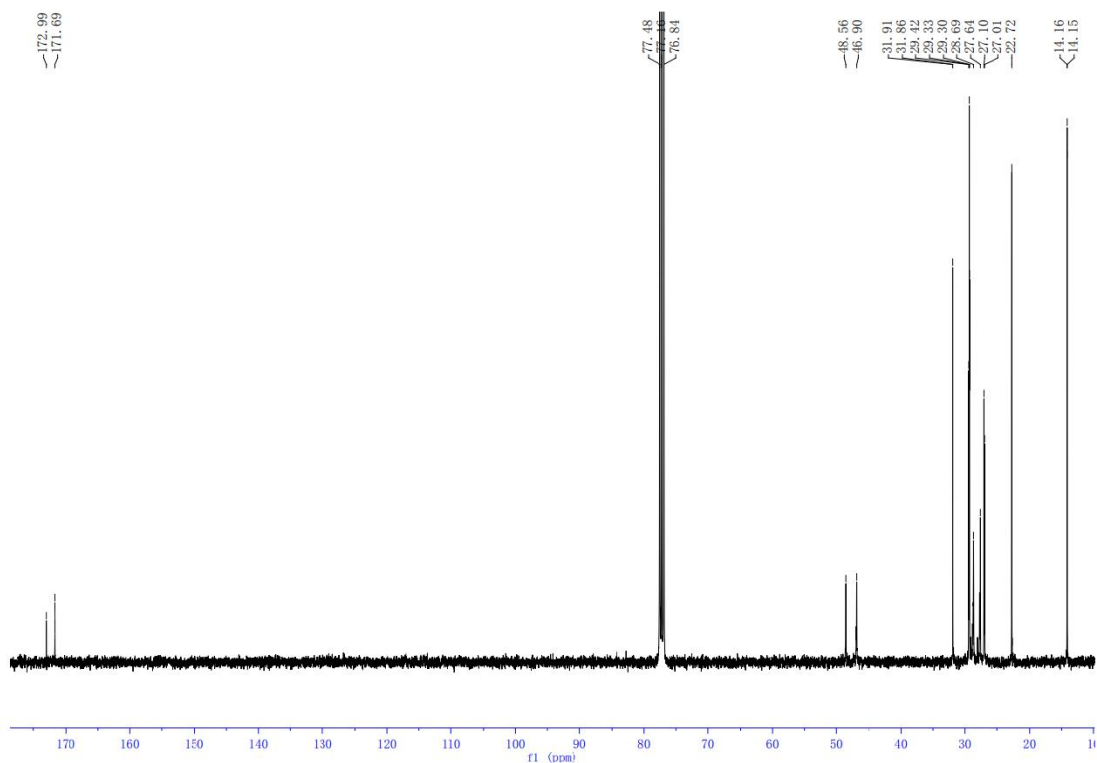


^{13}C -NMR spectrum of **2c** in CDCl_3 .

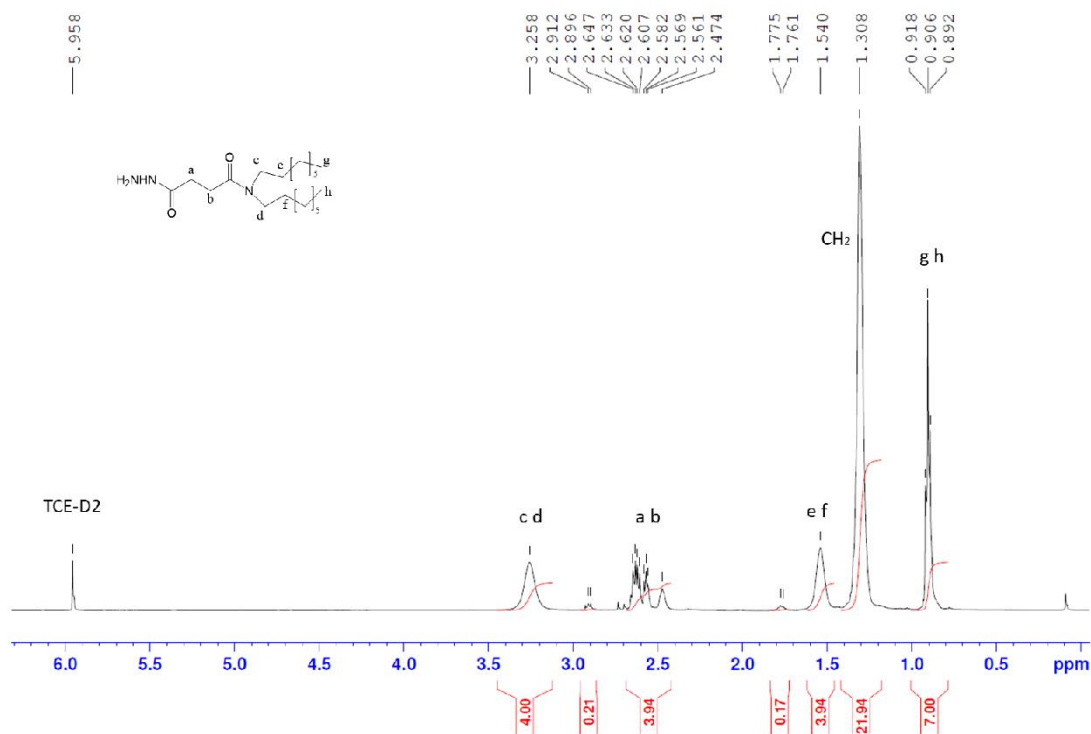
Compound 3c (LD-HZ). To the solution of **2c** (163 mg, 0.48 mmol) in DCM (10 mL), TFA (10 mL) and 2 drops of MiliQ water were added and stirred at room temperature for 2 h. After confirming the reaction completely proceeded with TLC, the solvents were evaporated under reduced pressure, and then the residue was dissolved in MeOH and evaporated 3 times to remove TFA and give desired product **3c** as a colorless solid (158 mg). ^1H NMR (400 MHz, CDCl_3) δ ppm 3.22 (4H, m), 2.68 (2H, brs), 2.56 (2H, brs), 1.50 (4H, brd), 1.26 (20H, m), 0.87 (6H, t). Splitting of protons of c, d and e, f were due to presence of amide rotamers; the splitting disappeared under high temperature. ^{13}C NMR (400 MHz, CDCl_3) 172.99, 171.69, 77.48, 77.16, 76.84, 48.56, 46.90, 31.91, 31.86, 29.42, 29.33, 29.30, 28.69, 27.64, 27.10, 27.01, 22.72, 14.16, 14.15. 3HRMS for Chemical Formula: $[\text{C}_{20}\text{H}_{41}\text{N}_3\text{O}_2]$ m/z calc. 355.3199, found m/z ($\text{M}+\text{Na}^+$) 378.3163.



^1H -NMR spectrum of **3c** in CDCl_3 .



^{13}C -NMR spectrum of **3c** in CDCl_3 .



^1H -NMR spectrum of **3c** at high temperature (379 K) in trichloroethylene (TCE- D_2). Additional minor peaks appear probably due to partial degradation of **3c** at high temperature.

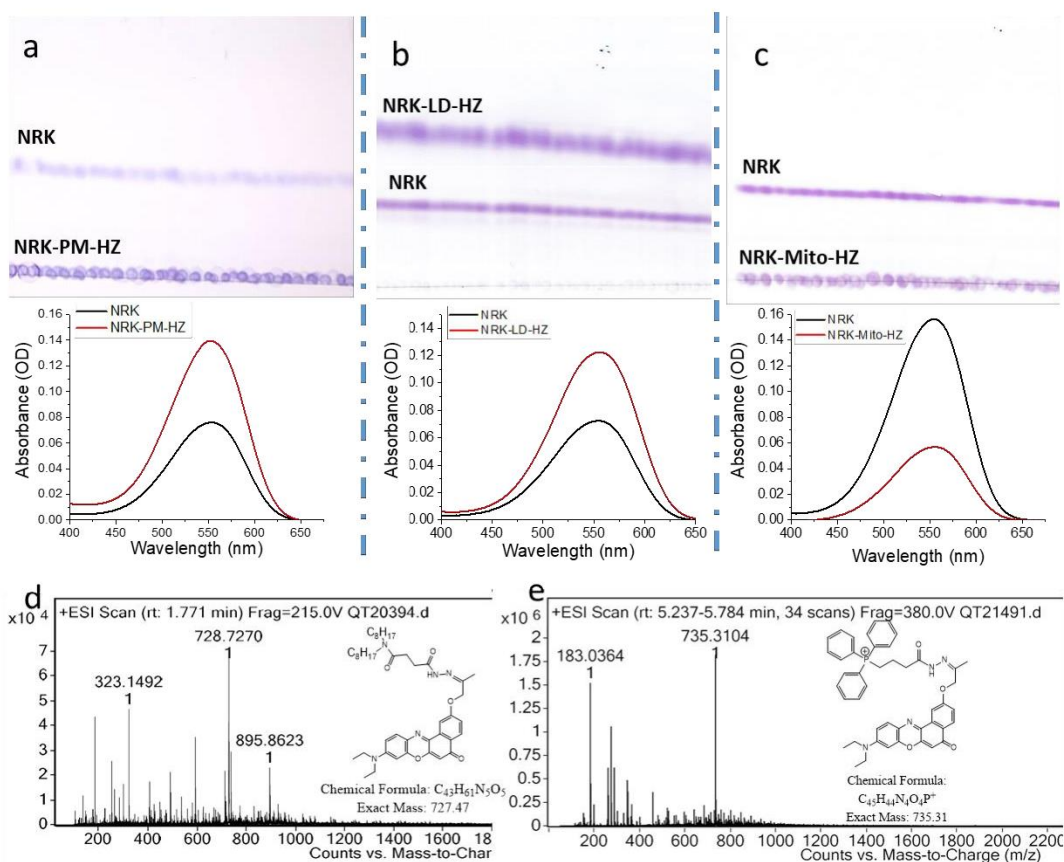


Fig. S1. (a-c) Upper panels: Photos of thin layer chromatography (TLC) plates for purification (DCM:MeOH=95:5 as eluent) of the extracts from the *in situ* reactions of NRK (10 μ M) with (a) PM-HZ (20 μ M) in LUVs (1 mM DOPC); (b) LD-HZ (20 μ M) in nanoemulsion (1 mM Labrafac oil); (c) Mito-HZ (20 μ M) in LUVs (1 mM DOPC). (a-c) Upper panels: absorption spectra of NRK and the conjugates NRK-PM-HZ (a), NRK-LD-HZ (b) and NRK-Mito-HZ (c) in methanol after TLC purification. (d) Mass data for NRK-LD-HZ conjugate collected from TLC band with higher R_f (b). (e) Mass for NRK-Mito-HZ conjugate collected from TLC band with lower R_f (c).

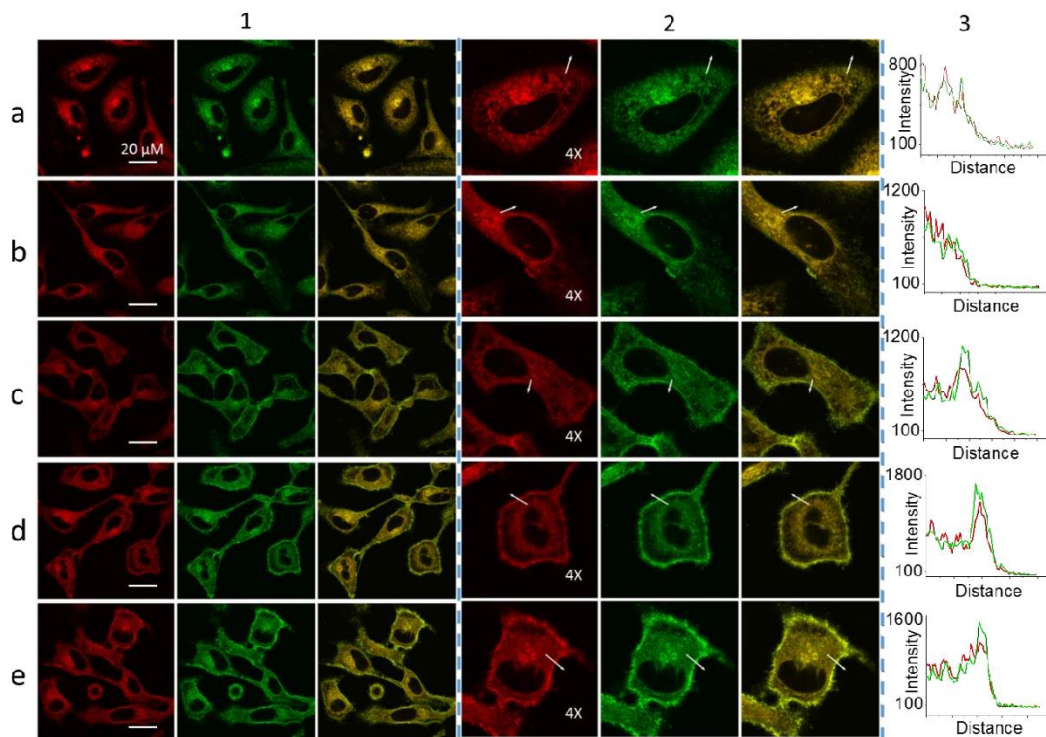


Fig. S2. Targeting NRK to plasma membrane with HZ-PM at different concentrations: 0 μM (a); 1 μM (b); 5 μM (c); 20 μM (d); 100 μM (e) following non-wash protocol. (1) Confocal images recorded in the red channel (excitation: 488 nm, emission filter: 600~670 nm) and green channel (excitation: 488nm, emission filter: 550~600 nm). (2) Corresponding zoomed (4x) images of (1). (3) Plot profile of red and green channel from white arrows indicated in images (2). Targeting agent was pre-incubated with cells followed by addition of NRK (1 μM).

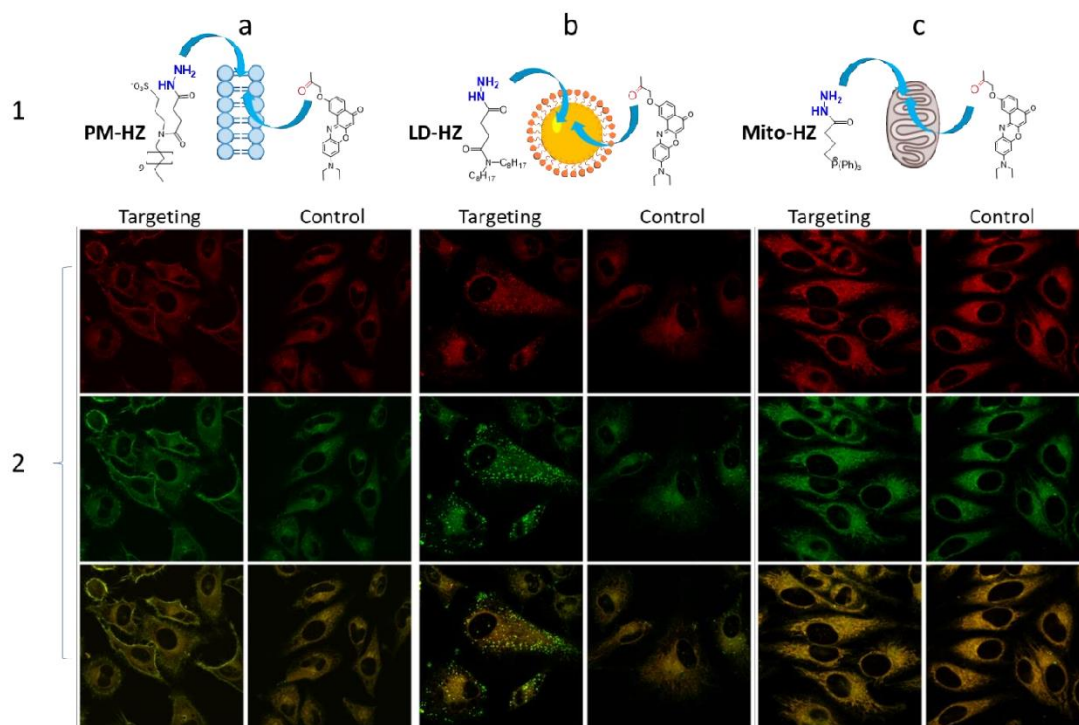


Fig. S3. Targeting NRK dye to (a) plasma membrane, (b) lipid droplets and (c) mitochondria by corresponding hydrazide ligands. (1) General scheme of targeting mechanism; (2) confocal images under condition for red channel: excitation 488 nm, emission filter of 600-670 nm; condition for green channel: excitation 488nm, emission filter of 550-600 nm. Targeting agent was pre-incubated with cells followed by washing and then addition of NRK (1 μ M). In controls, NRK was used directly without the targeting agent. Zoomed images are given in Fig. 2.

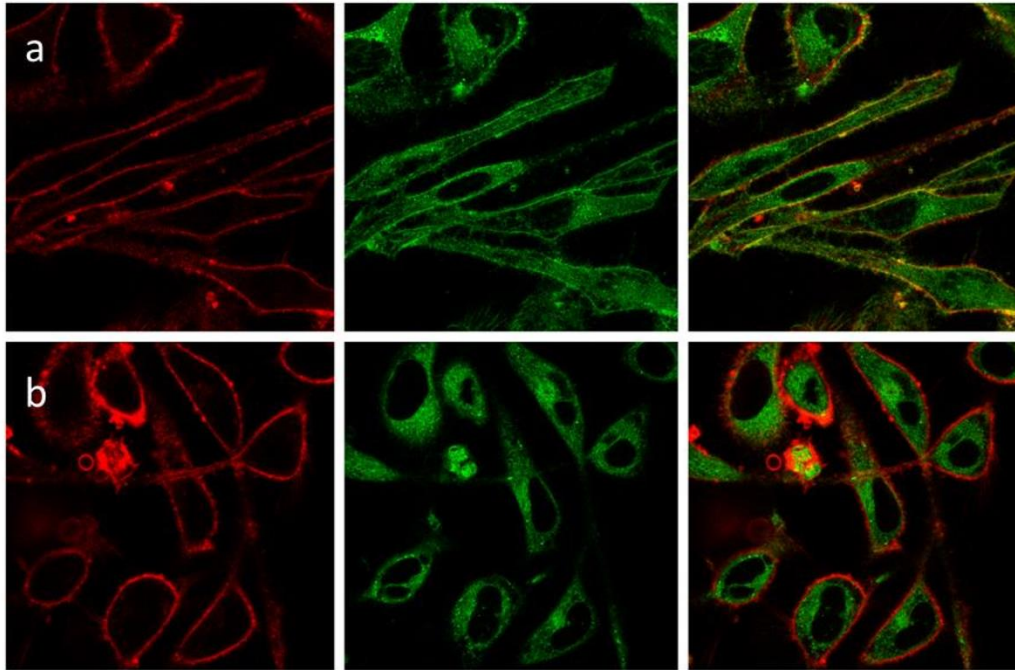
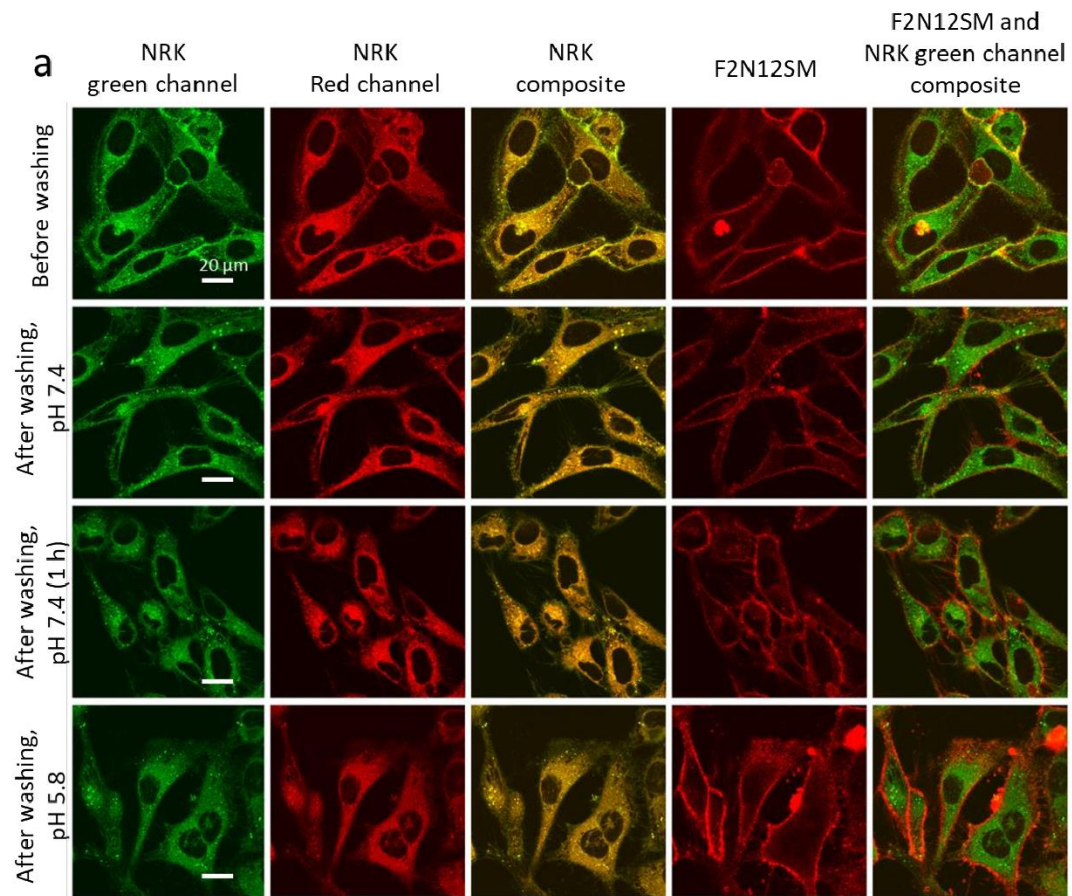


Fig. S4. Targeting NRK to plasma membranes and colocalization with membrane probe F2N12SM. Cells were pre-incubated for 10 min at 37 °C with (a) or without (b) PM-HZ (20 μM) followed by addition NRK (1 μM) and incubation for 30 min at 37 °C. Membrane staining by 400 nM F2N12SM is shown in red. Imaging conditions: for NRK, 488 nm excitation, emission filter of 550-600 nm, for F2N12SM, 405 nm excitation, emission filter of 420-480 nm.



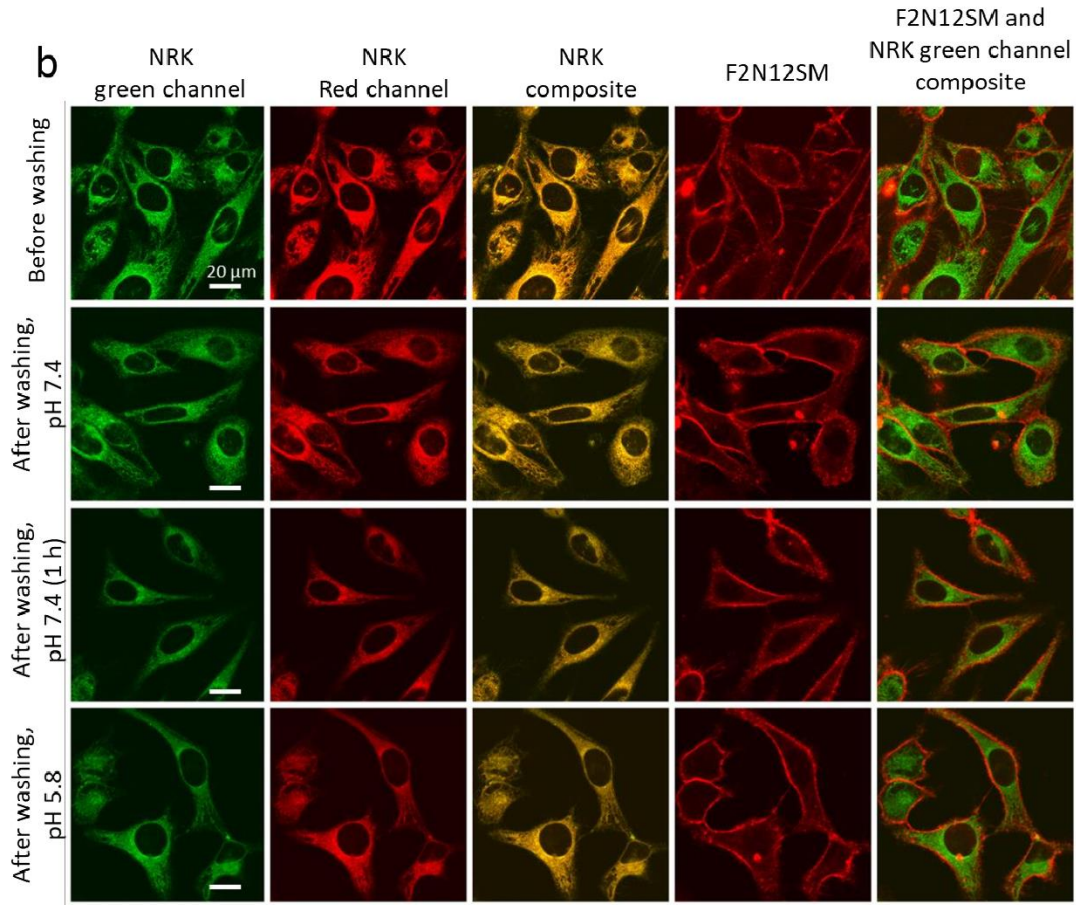


Fig. S5. Testing reversibility of NRK targeting to plasma membrane by PM-HZ in HeLa cells at neutral and low pH after washing. Plasma membranes were stained by F2N12SM. (a) NRK (1 μ M) targeted to HeLa cells pretreated with PM-HZ (20 μ M). (b) Controls treated with NRK (1 μ M) without PM-HZ. Images were taken in Opti-MEM (pH 7.4) before washing, in Opti-MEM (pH 7.4) after washing with PBS, after long incubation (1 h) in Opti-MEM (pH 7.4) and in pH 5.8 phosphate-acetate buffer. For all four conditions before imaging, the cells were incubated for 5 min at 37 $^{\circ}$ C with plasma membrane probe F2N12SM (400 nM). Imaging conditions for the NRK red channel: excitation 488 nm, emission filter 600-670 nm; for NRK green channel: excitation 488nm, emission filter 550-600 nm; for F2N12SM: excitation 405 nm, emission filter 420-480 nm.

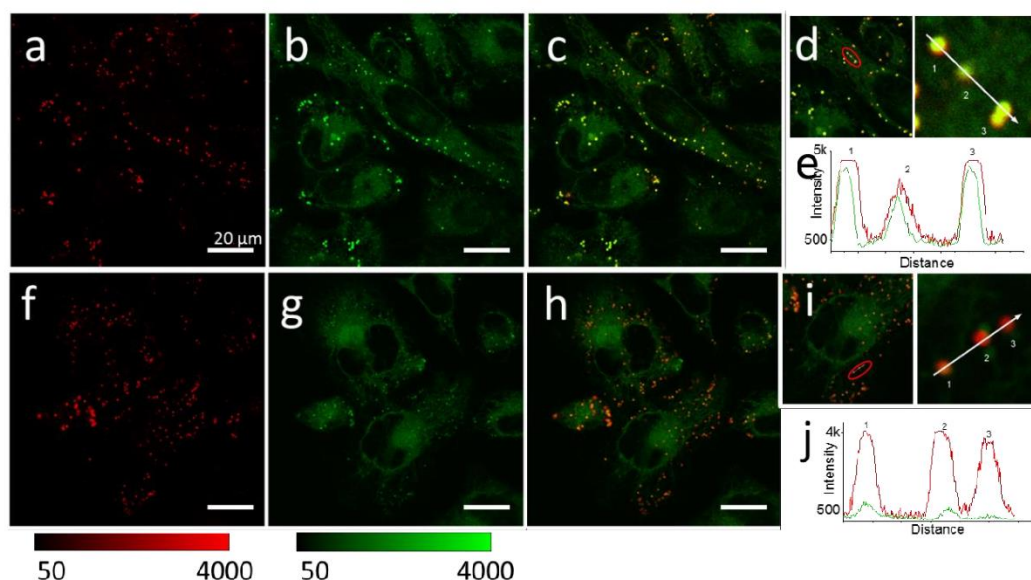


Fig. S6. Targeting of NRK (1 μ M) to lipid droplets by LD-HZ (20 μ M) identified by colocalization with SMCy5.5. Condition for red channel (a and f) for imaging of SMCy5.5: excitation at 644 nm, emission filter at 650-800 nm; condition for green channel (b and g): excitation at 488nm, emission filter at 550-600 nm. (c) NRK-SMCy5.5 colocalization in cells preloaded with lipid droplets targeting agent LD-HZ (overlay of a and b). (d) The selected area of (c) where the line profile analysis was performed. (e) The line profile of fluorescence intensity from (d) in SMCy5.5 channel (Red) and NRK channel (Green). (h) NRK-SMCy5.5 colocalization of control cells without LD-HZ (overlay of f and g). (i) The selected area of (h) where the line profile analysis was performed. (j) The line profile of fluorescence intensity from (i) in SMCy5.5 channel (Red) and NRK channel (Green).

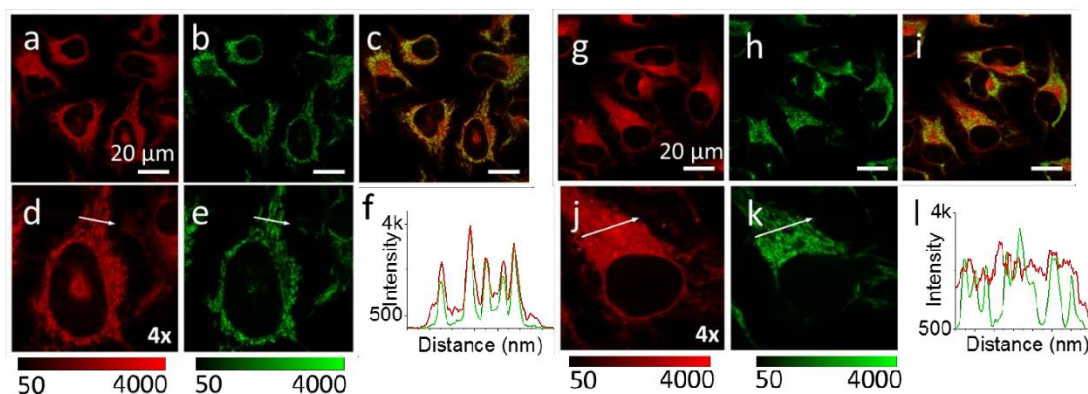


Fig. S7. Targeting NRK to mitochondria by NH-Mito identified by colocalization with MitoTracker Deep Red FM 644/665. Cells were pre-incubated for 10 min at 37 °C with (a-f) or without (g-l) Mito-HZ (20 μ M), followed by cell wash with PBS and addition NRK (1 μ M) and incubation for 30 min at 37 °C. Condition for red (MitoTracker Deep Red FM 644/665) channel (a,d,g,j): excitation at 635 nm, emission filter at 650-800 nm; condition for green (NRK) channel (b,e,h,k): excitation at 488 nm, emission filter at 550-600 nm. (c) NRK-MitoTracker Deep Red FM 644/665 colocalization in cells preloaded with mitochondria targeting agent Mito-HZ (overlay of a and b). (i) NRK- MitoTracker Deep Red FM 644/665 colocalization in control cells without Mito-HZ (overlay of g and h). (d, e) Selected area from (a, b) where the line profile analysis was performed; (j, k) selected area from (g, h) where the line profile analysis was performed. (f) Histogram of fluorescence intensity indicated by the white arrow in (d) and (e); (l) histogram of fluorescence intensity indicated by the white arrow in (j) and (k).

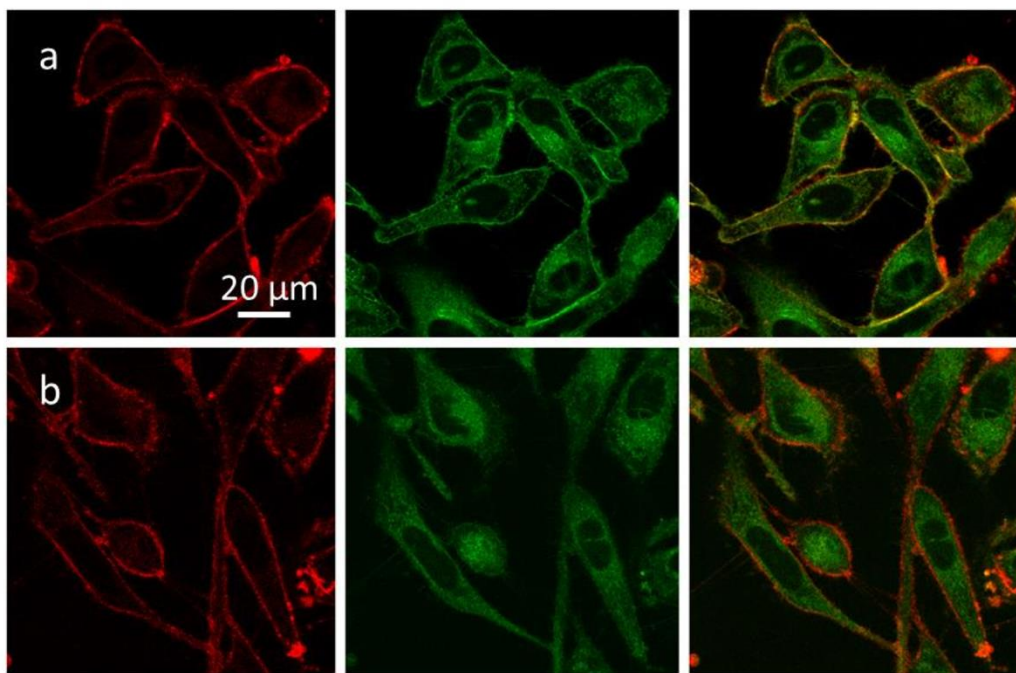


Fig. S8. Targeting doxorubicin to plasma membranes by PM-HZ and co-localization with the membrane probe F2N12SM. Confocal image of membrane co-localization of 1 μ M Doxorubicine (green) by PM-HZ (20 μ M) with 400 nM F2N12SM (red). (a) Targeting with PM-HZ and (b) control cells. Imaging condition: for NRK, 488 nm excitation, filter of 550-600 nm, for F2N12SM, 405 nm excitation, filter of 420 nm-480 nm.

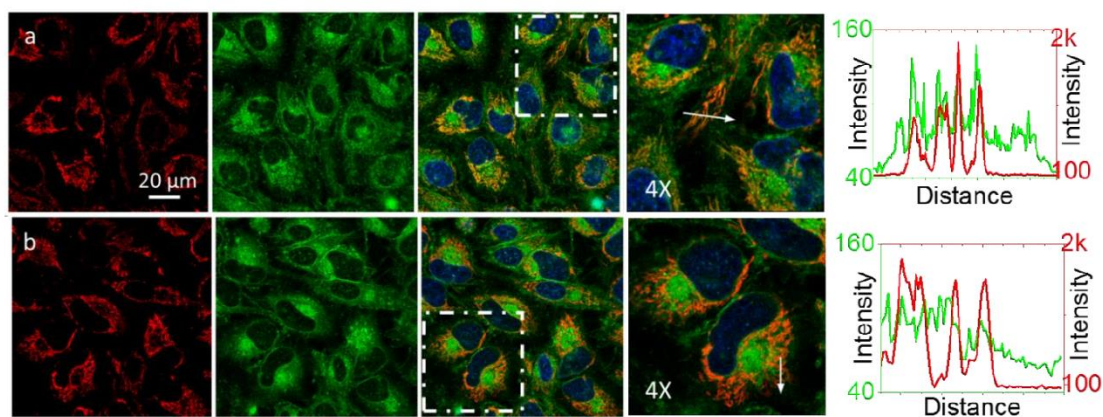


Fig. S9. Targeting doxorubicin to mitochondria by Mito-HZ. Cells were pre-incubated for 10 min at 37 °C with (a) or without (b) Mito-HZ (20 μ M) followed by addition doxorubicin (1 μ M) and incubation for 30 min at 37 °C. Conditions for red channel (MitoTracker Deep Red FM): excitation at 644 nm, emission filter at 650-800 nm; the green channel (doxorubicin imaging): excitation at 488 nm, emission filter at 520-650 nm; the blue channel (Hoechst 33342 imaging): excitation at 405 nm, emission filter at 420-480 nm. The line profiles (right panels) of the image in the green channel is indicated by white arrows in 4x magnified images.

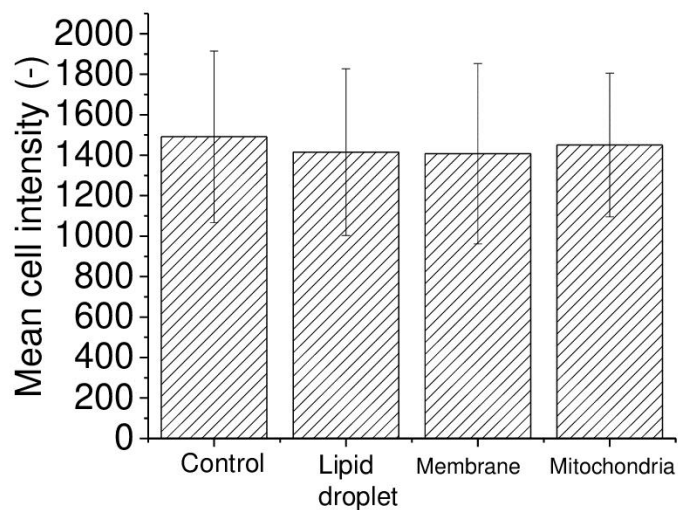


Fig. S10. Calculation of mean fluorescence intensity for cells used for the PDT experiments: control, LDs targeting (with LD-HZ), plasma membrane targeting (with PM-HZ), mitochondria targeting (with Mito-HZ). Mean fluorescence intensity was calculated for ~300 cells for each condition. Errors are standard deviation of the mean. Cells were selected by using ImageJ cell finding plugin.

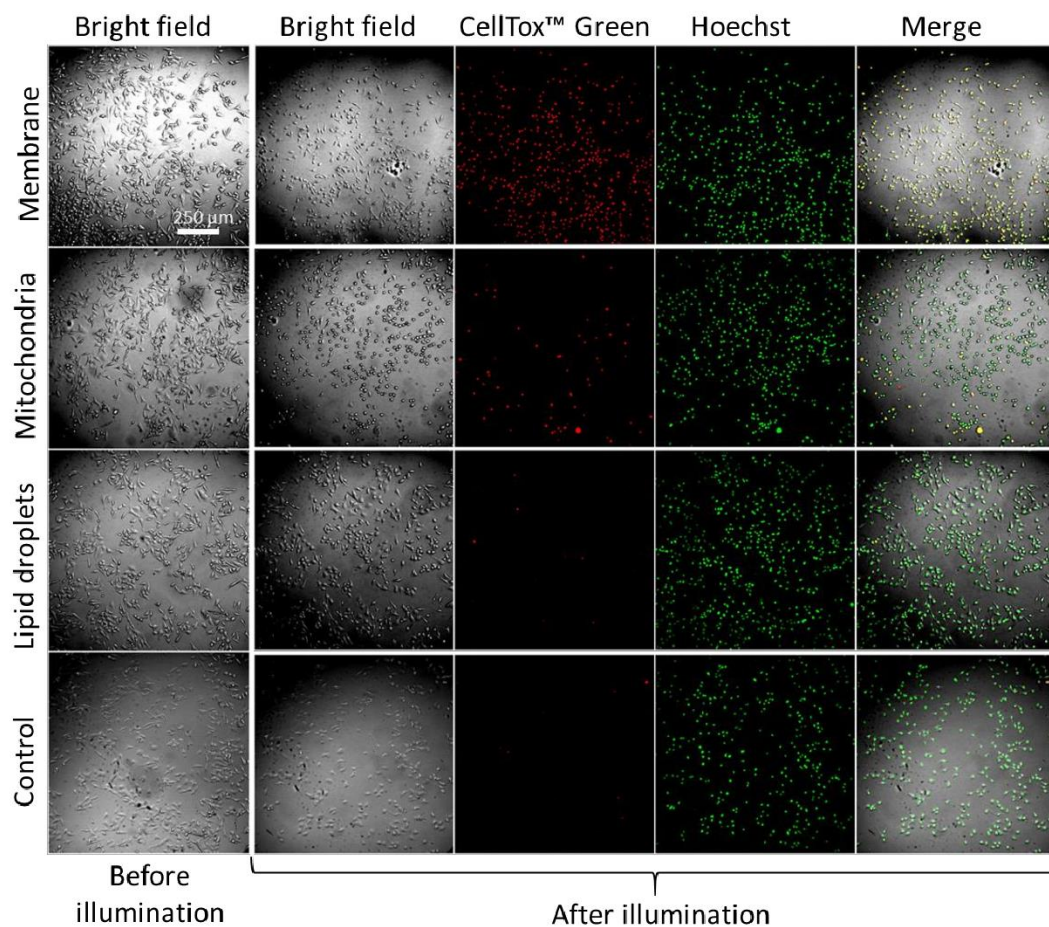


Fig. S11. Phototoxicity of NRK targeted to different organelles (plasma membranes with PM-HZ, mitochondria with Mito-HZ and lipid droplets with LD-HZ), evaluated using cell death staining agent CellTox™ Green (in Red) co-stained with nucleus staining agent Hoechst33342 (in Green). Transmission (bright field) and merged images are also shown. The cells were illuminated under microscope for 1 min at 550 nm. Images were taken after incubation for 30 min with CellTox™ Green assay.

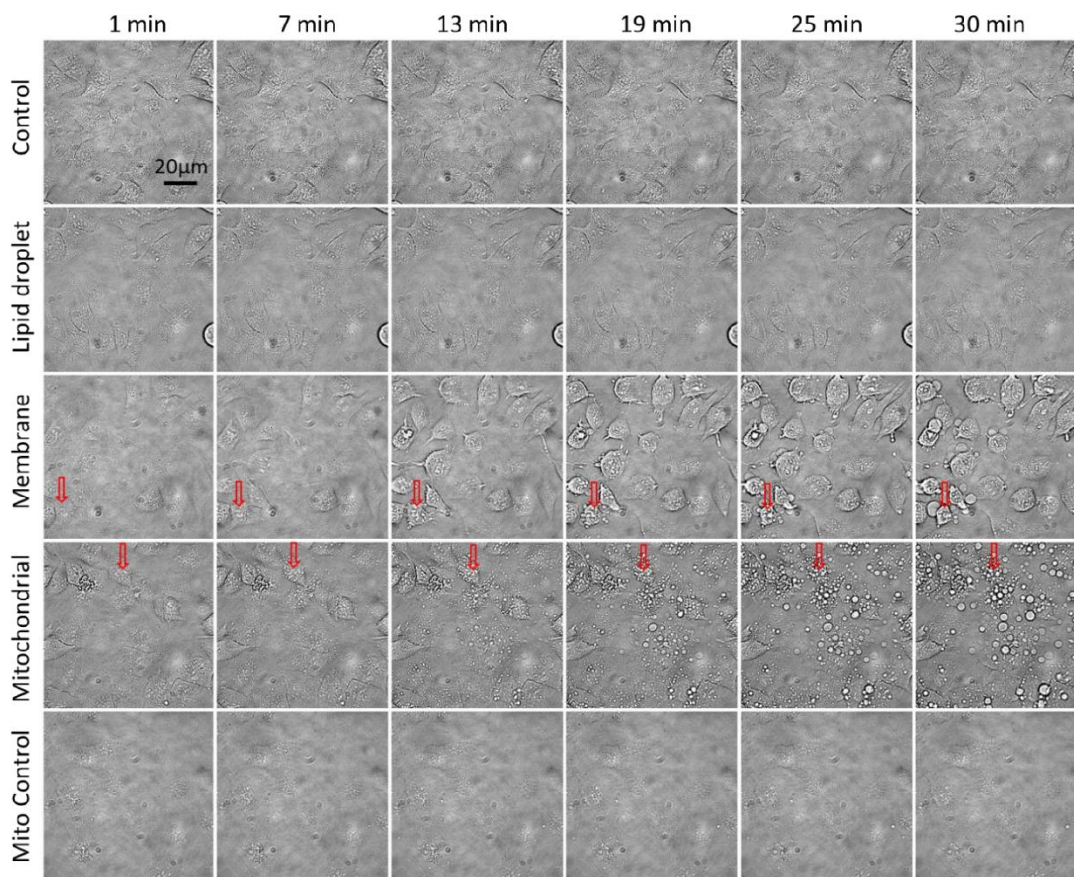


Fig. S12. Phototoxicity study based on cell morphology changes due to excitation of NRK targeted to lipid droplets, plasma membrane and mitochondria by the corresponding targeting agents. Bright-field images were taken every 1 min after excitation at 550 nm for 300 ms using high illumination power (30% for lipid droplets and plasma membrane and its control; 50 % for mitochondria and its control), images were selected for display at indicated periods of 1 min, 7 min. Red arrows show example of cells undergoing the morphological change.

Table S1. Colocalization analysis for targeting of NRK and doxorubicin (Dox) to plasma membranes, lipid droplets and mitochondria by PM-HZ, LD-HZ and Mito-HZ, respectively.^a

Sample Parameter	Plasma membranes				Lipid droplets				Mitochondria			
	NRK		Dox		NRK		Dox		NRK		Dox	
	Control	Target	Control	Target	Control	Target	Control	Target	Control	Target	Control	Target
Intensity ratio (Organelle/cell)	0.88±0.11	2.06±0.35	1.02±0.23	1.50±0.23	1.67±0.32	4.46±0.60	1.98±0.048	8.45±0.25	1.58±0.12	1.73±0.39	1.46±0.12	1.52±0.085
Pearson's correlation coefficient	0.20±0.038	0.55±0.01	0.21±0.042	0.52±0.068	0.52±0.026	0.68±0.041	0.16±0.034	0.58±0.068	0.65±0.036	0.75±0.028	0.34±0.018	0.38±0.026
Mander's correlation coefficient	0.13±0.033	0.42±0.001	0.21±0.042	0.35±0.074	0.26±0.068	0.77±0.081	0.04±0.029	0.57±0.068	0.54±0.034	0.44±0.11	0.31±0.071	0.30±0.082

^a 15 cells were analysed per condition.

Table S2. Colocalization analysis for reversibility of NRK labelling of plasma membranes with PM-HZ with respect to reference dye F2N12SM.^a

Experiment Parameter	Targeting group				Control group			
	Before washing	After washing, pH 7.4	After washing, pH 7.4 (1 h)	After washing, pH 5.8	Before washing	After washing, pH 7.4	After washing, pH 7.4 (1 h)	After washing, pH 5.8
Intensity ratio (Organelle/cell)	1.71±0.12	1.28±0.10	1.10±0.021	0.85±0.02	0.86±0.010	0.80±0.11	1.10±0.019	0.85±0.016
Pearson's correlation coefficient	0.49±0.045	0.32±0.075	0.32±0.064	0.22±0.030	0.14±0.11	0.16±0.072	0.25±0.064	0.19±0.023
Mander's correlation efficiency	0.55±0.056	0.53±0.065	0.42±0.028	0.36±0.037	0.21±0.033	0.18±0.022	0.30±0.053	0.19±0.056

^a 15 cells were analysed per condition.

References

1. F. Liu, Y. Niko, R. Bouchaala, L. Mercier, O. Lefebvre, B. Andreiuk, T. Vandamme, J. G. Goetz, N. Anton and A. Klymchenko, *Angew. Chem. Int. Ed.*, 2021, **60**, 6573-6580.
2. M. Collot, T. K. Fam, P. Ashokkumar, O. Faklaris, T. Galli, L. Danglot and A. S. Klymchenko, *J. Am. Chem. Soc.*, 2018, **140**, 5401-5411.
3. R. Kreder, S. Oncul, O. A. Kucherak, K. A. Pyrshev, E. Real, Y. Mély and A. S. Klymchenko, *RSC Adv.*, 2015, **5**, 22899-22905.
4. D. I. Danylchuk, S. Moon, K. Xu and A. S. Klymchenko, *Angew. Chem. Int. Ed.*, 2019, **58**, 14920-14924.

3-PART 3. Conclusions and Perspectives

The aim of my Ph.D. project was development of novel concepts for drug delivery and uptake using *in situ* chemical reactions in lipid nanomaterials, with particular interest in dynamic covalent chemistry in nanoemulsions.

The first part of my work presented a novel approach, the so-called “drug sponge”, of drug encapsulation in NEs. Dynamic covalent chemistry was exploited to achieve the reversible *in situ* cargo loading in NEs. Since most drugs have moderate lipophilicity, modifying them with a highly lipophilic moiety with the use of a dynamic covalent bond would increase the stability of the cargo (that can be a drug or a contrast agent) against leakage from the oil core. In this project, we revisited the prodrug strategy and proposed to directly generate the generation of a prodrug conjugate *in situ* inside of the oil core of NEs. We designed a highly lipophilic hydrazide (LipoHD) capable of forming a hydrazone bond with a cargo (fluorescent dye and doxorubicin drug) bearing ketone group. Lipid NEs loaded with LipoHD were able to spontaneously accumulate cargo ketones within hours. Due to the sensitivity of the hydrazone bond to pH, the drug sponge system is stable in neutral pH, but releases its cargo (drug) in the intact form under low pH, which is important for the controlled release in the tumor microenvironment. Firstly, we studied models to characterize the *in situ* reaction process: two ketone compounds were used, one was a Nile Red dye derivative named NRK and another was doxorubicin, an anti-tumor drug. Förster Resonance Energy Transfer (FRET) technique was exploited for real-time investigation of the *in situ* reaction process, due to high sensitivity of FRET to donor-acceptor distance. Consequently, encapsulating F888 (as the donor for NRK) or Cy5 TPB (as the acceptor for doxorubicin) allowed monitoring the progression of *in situ* reaction by the increase in the FRET signal. Then, the same technique was also used for the model study of the cargo release under low pH. FRET signals decreased after applying low pH to NEs encapsulated with NRK-LipoHD with F888 (or Dox-LipoHD with Cy5 TPB). This drug-sponge system was validated in a cancer cell line, where it showed the efficient capability of extraction of free ketone cargos (NRK/doxorubicin) from cells and pH-controlled release of dye/drug cargos into the cells. Cytotoxicity of LipoHD NCs loaded with doxorubicin was studied in four cell lines after 48h incubation, and it was found similar to free doxorubicin. The therapeutic potential of drug-sponge NCs loaded with doxorubicin was demonstrated for xenografted tumors

(D2A1 and MDA cells) in mice. Interestingly, an experiment on model skin showed that the functional NEs (containing LipoHD) could extract free ketone cargos (NRK/doxorubicin) from lipid-rich skin adipose tissue, implying new possibilities in detoxification from toxins and excess of used drugs.

In the second part of my work, we extended our drug-sponge concept to dynamic imine bonds for designing functional NEs for pH-controlled release and *in situ* uptake. A lipophilic reactive capture molecule bearing two long alkyl chains and an amine group (LipoAmine) was encapsulated inside the NEs droplets. Here, we monitored the *in situ* reaction using a push-pull fluorescent dye bearing an aldehyde group (PA) as a model compound. We found that the imine bond formation was accompanied by a blue shift, resulting from the change in the push-pull dye system after the formation of imine bond. At low pH, the red shift was observed due to the dye release process. Remarkably, the reduction product of PA-LipoAmine from the *in situ* reaction was successfully identified from TLC-mass spectrometry. The pH-controlled release of PA in cells experiment showed that the imine bond containing NEs was stable in neutral pH, while the release of PA was observed in an acidic environment. The LipoAmine-loaded NEs also showed the capability to extract PA from pre-stained cells and chicken skin surfaces. Finally, cytotoxicity studies showed that the LipoAmine-loaded NEs could extract a toxic aldehyde (4-hydroxynonenal) from the cells and thus increase cell viability in the presence of this toxic compound, showing the potential of this approach for the detoxification. Importantly, in this case we achieved delivery and capture aldehyde molecules using a lipophilic amine compound, which is much less toxic than a hydrazide.

Next, we challenged to achieve the ultimate goal of NCs, *i.e.* to realize the active targeting of tumor cells. In this work, we used *in situ* reaction technique to prepare targeted NEs. Cholesterol bearing a carbonate group was synthesized as capturing moiety for amine species and encapsulated inside NEs. We encapsulated this reactive cholesterol (NPC-Chol) in NEs and showed that it was capable to react *in situ* with model amine compound ethanolamine. Next, we designed a Biotin-PEG3000-lysine linker, where the two amino groups of lysine are expected to react *in situ* with NPC-Chol. Latter would serve as an anchor to fix the linker to the oil droplet, while PEG3000 would expose biotin at the NEs surface. These biotinylated NEs loaded with a fluorescent dye were capable of binding to the Neutravidin on the glass surface, which was evidenced by fluorescence microscopy. Interestingly, these NEs were also capable of binding to Cy5-streptavidin and showed nice co-localization on the electrophoresis gel. After proving the strong affinity of biotinylated NEs to

avidin-based proteins, biotinylated NEs were successfully targeted to the plasma membrane of SKBr3 cells. This was achieved through the direct assembly of biotin-Neutravidin-biotinylated antibody (cetuximab) sandwich structure on the cell surface by sequential additions with washing at each step. Then, antibody NEs with the same sandwich structure were formulated. However, unpurified antibody NEs did not show strong affinity to SKBr3 cells. Size exclusion chromatography profile of Biotinylated NEs with Cy5-streptavidin showed good separation of fractions of Cy5-streptavidin-Biotinylated NEs from excess of Cy5-streptavidin, which suggest it as an efficient method for the purification of NEs with biotin-avidin conjugations. After being purified with this technique, antibody NEs showed nice targeting efficacy to SKBr3 cells. Antibody-NEs conjugates obtained in this way showed potential for drug active targeting delivery at cellular level. Thus, we developed a “green” method of functionalization of NEs with an antibody, where the conjugation takes place *in situ* using biocompatible non-toxic components, such as cholesterol, amino acid, biotin, PEG and proteins. Therefore, we can consider it as promising approach for development of non-toxic targeted green nanocarriers.

Finally, the last part of work expanded the application of *in situ* reaction on biological lipid structures to organelles, for the purpose of targeting an unmodified drug molecule to specific desired location inside the cells. We developed three different targeting moieties bearing hydrazide moiety to target ketone compounds to plasma membrane, lipid droplet and mitochondria. Firstly, we studied models to characterize the *in situ* reaction process with ketone derivative of Nile Red, NRK. Hydrazide conjugates with NRK were identified by mass spectra from mixtures of *in situ* reaction carried out in NEs (mimicking lipid droplets and mitochondria) and LUVs (mimicking plasma membrane). The yield of three conjugates were 65 mol% (for NRK-PM-HZ), 63 mol% (for NRK-LD-HZ), and 28 mol% (for NRK-Mito-HZ), respectively according to extraction results. To show the universality of the approach to target free ketone containing drugs to specific organelles, *in situ* reaction of hydrazide groups with two structurally different ketone groups, NRK and doxorubicin, was further explored in cells by confocal imaging. Confocal images showed the presence of the targeting hydrazide groups favors co-localization of the tested ketone groups of dyes or drugs with respect to reference organelle targeting probes, which validated organelle targeting approach. It is interesting to note that this approach is also capable of releasing the unmodified drug under low pH, due to the pH sensitivity of hydrazide bond, based on confocal imaging results. We also found that NRK was much more phototoxic when it was targeted was

targeted plasma membrane and mitochondria, probably because these organelles are particularly sensitive to photo-oxidative stress. Thus, our approach could tune the phototoxicity of a photosensitizer due to specific targeting to different organelles, which can be important to improve efficiency of photodynamic therapy (PDT).

Overall, the obtained results showed that nano-droplets in combination with dynamic covalent chemistry could be used as a powerful tool in the field of drug delivery. Several points could be addressed from the total four projects of the present work. Based on the first two projects we can conclude that *in situ* reaction using dynamic covalent chemistry could be considered as a green and universal way for the encapsulation and release of cargoes (especially drugs) with moderate lipophilicity. Here, we should mention several key advantages of this approach compared to classical prodrug approach. First, drugs could be encapsulated in a direct and simply way, avoiding prodrug synthesis and purification. Second, drugs could be released in their original form, thus avoiding issues about the effectiveness of the released drug compared with the prodrug approach, where drug is released in its chemically modified form. Third, this approach allows exactly the opposite processes: extract toxic compounds from cells and tissues, which could be applied in the future for detoxification *in vivo*. Therefore, we named this drug encapsulation and release system as “drug sponge”. One should also note that this is an universal approach that could be applied theoretically to any drug with reactive groups compatible with dynamic covalent chemistry. For now, only two types of dynamic covalent chemistry, based on imine and hydrazone, were investigated. We believe that this approach could also extended to other types of dynamic covalent reactions. From the antibody NEs project, we can conclude that *in situ* reaction could be applied for the formulation of biotinylated NEs. This process could also be considered as a universal method for the modification of NEs surface. Surface modification of NEs remains a huge challenge until now, because ligands attached to amphiphiles can easily desorb from the particle present in a liquid phase. Very high hydrophobicity is expected to stabilize the ligand on NEs surface. Moreover, the biotin group could be replaced with other functional groups for different types of conjugation. For the developed NEs covered with biotin-Neutravidin could be applied for any antibody of interest by after its biotinylation. By using NEs as probe/drug carrier modified with targeting antibodies, we expect to obtain a powerful “green” nano-platform for the targeted imaging and drug delivery in biomedical applications, especially against cancer. From the last project of my thesis, we can conclude that the application of *in situ* reactions is not limited to

Conclusions and Perspectives

nanoemulsions, but can be extended organelles of living cells. To date, this is the first method capable of targeting a drug to specific organelles of live cells without its initial chemical modification. The result indicated the universality of approach by targeting two structurally different molecular with ketones (NRK and doxorubicin). Potentially, the approach could also be used for targeting any other drug molecule with ketone group. This enables specific cellular localization of some drugs (doxorubicin) or photosensitizers, which is important for understanding their intracellular mechanisms and PDT effects. In the meantime, this organelle-targeting approach could be expanded to other type of dynamic covalent bonds.

4- PART 4. Materials and Methods

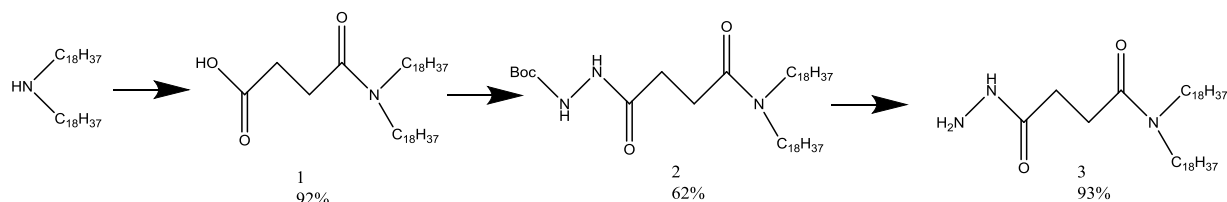
4.1- Materials

All starting materials for synthesis were purchased from Alfa Aesar, Sigma-Aldrich or TCI Europe, unless specifically mentioned. Labrafac Lipophile WL 1349 (LabrafacWL[®]), composed of medium-chain triglycerides and caprylic/capric triglyceride, was obtained from Gattefossé (Saint Priest, France). Cremophor ELP was from BASF (Ludwigshafen, Germany). Acetic acid (>99.0%, Sigma-Aldrich), Sodium phosphate monobasic (>99.0%, Sigma-Aldrich), sodium phosphate dibasic dihydrate (>99.0%, Sigma-Aldrich) and acetic acid were used to prepare 20 mM phosphate buffers at various pH. Borate buffer was prepared from 25 mM sodium tetraborate, 25 mM NaCl, and 1 mM EDTA at pH 8.1 or 8.4. Phosphate-buffer saline (PBS) was 140 mM NaCl and 12 mM sodium phosphate at pH 7.4. Sodium azide 0.5% (w/v) was prepared by dissolving 5 mg of sodium azide in 1 mL of water. Solutions of tris(2-carboxyethyl) phosphine hydrochloride (TCEP) 10 mM (2.87 g/mL) were prepared in borate buffer. pH 8.5 phosphate buffer was prepared by dissolving 3.5 g of dipotassium hydrogen phosphate and 4.5 g of sodium chloride in 500 mL of water. Adjusted the pH with a mixture of equal volumes of dilute phosphoric acid and water. DiD oil (1,1'-dioctadecyl-3,3,3',3'-tetramethylindodicarbocyanine perchlorate) (Cy5) were purchased from ThermoFisher Scientific. 4'-dioctylamino-3-octyloxyflavone (F888), SMCy5.5 and PA were synthesized as described before ^[45,123,361]. Milli-Q water (Millipore) was used in all experiments, obtained through a MilliQ filtration system (Millipore, Saint-Quentin-en-Yvelines, France). Foetal bovine serum (FBS) was acquired from Lonza (Verviers, Belgium) and Gibco-Invitrogen (Grand Island, USA). Culture reagents were obtained from Sigma (St. Louis, USA), Lonza (Verviers, Belgium) and Gibco-Invitrogen (Grand Island, USA). Erbitux 5 mg/mL (cetuximab) was obtained from Merck Serono (Biberach, Germany).

4.2- Methods

4.2.1- Synthesis and chemical characterization

4.2.1.1- Synthesis of chemicals related to “drug sponge” projects

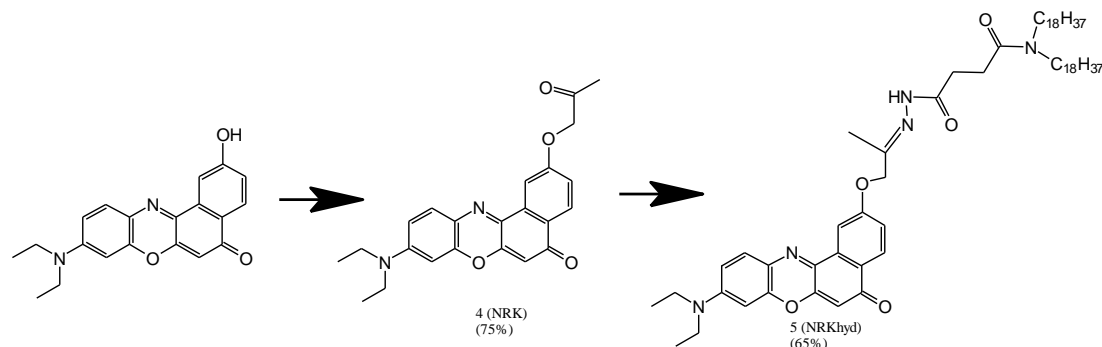


Compound 1. To the solution of succinic anhydride (192 mg, 1.92 mmol) in THF (20 mL) was added dioctadecylamine (500 mg, 0.96 mmol), then mixture was refluxed overnight under argon atmosphere. The solvent was evaporated in vacuo, then resulting residue was purified by recrystallization from dioxane to give desired product as a colorless solid (550 mg, 92%). ¹H NMR (400 MHz, CDCl₃) δ ppm 11.72 (1H, bs), 3.34 (4H, t), 3.19 (4H, t), 1.56 (4H, bs), 1.24 (60H, bs), 0.86 (6H, t). MS for [C₄₀H₇₉NO₃ – H⁺][–] m/z (M-1) calc. 620.61, found 620.60.

Compound 2. To the solution of **1** (500 mg, 0.080 mmol) in DMF (10 mL), tert-butylcarbazate (159 mg 1.21 mmol), PyBOP (630 mg, 1.21 mmol), and DIPEA (1.11 mL, 6.4 mmol (8 eq)) were added and stirred at room temperature overnight under argon atmosphere. The solvent was evaporated in vacuo, then resulting residue was purified by flash column chromatography on silica gel (eluent EtOAc/Hepane 50:50) to give desired product as a colorless solid (365 mg, yield 62%). ¹H NMR (400 MHz, CDCl₃) δ ppm 8.14 (1H, bs), 6.36 (1H, bs), 3.29 (2H, t), 3.21 (2H, t), 2.68 (2H, t), 2.58 (2H, t), 1.53 (13H, bs), 1.20 (60H, bs), 0.88 (6H, t). MS for [C₄₅H₈₉N₃O₄+H]⁺ m/z (M+1) calc. 736.69, found 736.69.

Compound 3 (LipoHD). To the solution of **2** (350 mg, 0.48 mmol) in DCM (10 mL), TFA (10 mL) and 2 drops of MiliQ water were added and stirred at room temperature for 2 h. After confirming the reaction completely proceeded with TLC, the solvents were evaporated under reduced pressure, and then the residue was dissolved in MeOH and evaporated 3 times to remove TFA and give desired product **3** as a colorless solid (362 mg). ¹H NMR (400 MHz, CDCl₃) δ ppm

7.77 (1H, bs), 3.27 (2H, t), 3.16 (2H, t), 2.65 (2H, t), 2.49 (2H, t), 1.50 (4H, bd), 1.24 (60H, bs), 0.84 (6H, t). MS for Chemical Formula: $[C_{40}H_{81}N_3O_2+H]^+$ m/z (M+1) calc. 636.63, found 636.63.



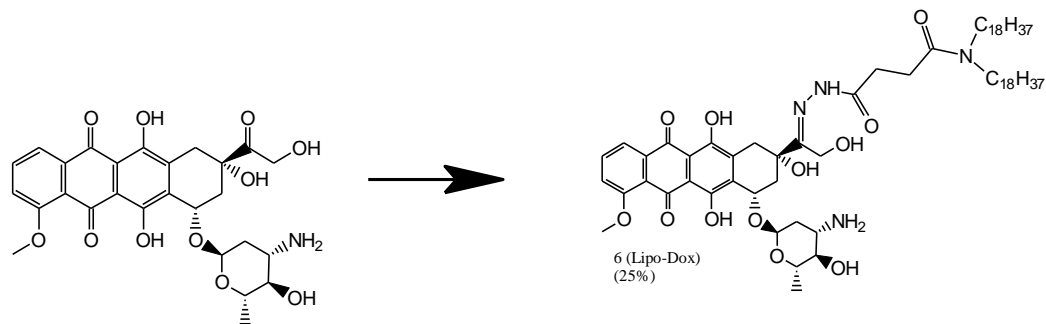
Compound 4 (NRK).

To the solution of 2-hydroxy-Nile Red (150 mg, 0.45 mmol), potassium carbonate (310 mg, 2.24), catalytic amount of potassium iodide in DMF (10 mL), (159 mg 1.21 mmol), chloroacetone (160 μ L, 2.24 mmol) was added and stirred at 100 $^{\circ}$ C for 3 h under argon atmosphere. The solvent was evaporated in vacuo, then resulting residue was washed by brine. The organic layer was dried over MgSO_4 , filtered and evaporated in vacuo. The residue was purified by flash column chromatography on silica gel (eluent DCM/MeOH = 98:2) to give desired product as a violet solid (132 g, yield 75%). ^1H NMR (500 MHz, CDCl_3) 8.24-8.22 (d, J =10.4 Hz, 1H), 7.99-7.96 (d, J =3.6 Hz, 1H), 7.21-7.18 (q, J =11.6 Hz, 1H), 6.66-6.63 (q, J =10.8 Hz, 1H), 6.43-6.42 (d, J =2.8 Hz, 1H), 6.28 (s, 1H), 4.74 (s, 1H), 3.46-3.43 (q, J =24.3 Hz, 4 H), 2.36 (s, 3 H), 1.27-1.24 (t, J =13.9 Hz, 6H). MS (ESI $^{+}$) calc. 391.16 $\text{C}_{23}\text{H}_{22}\text{N}_2\text{O}_4\text{H}$ ($\text{M}+\text{H}$) $^{+}$, 391.164 observed.

Compound 5 (Lipo-NRK).

To the solution of **LipoHD** (30 mg, 0.077 mmol), in EtOH (2 mL), **NRK** (115 mg 0.15 mmol), triethylamine (22 μ L, 0.15 mmol) was added and refluxed for 3 h under argon atmosphere. The solvent was evaporated in vacuo, then resulting residue was purified by puriflash HPLC (eluent DCM/MeOH = 98:2 to 96:4) to give desired product as a violet solid (50 mg, yield 65%). ^1H NMR (500 MHz, CDCl_3) 8.69 (s, 1H), 8.63 (d, J = 7.0 Hz, 1H), 8.39 (s, 1H), 7.73-7.70 (d, J =8.1 Hz, 1H), 7.08-7.06 (d, J =9.3 Hz, 1H), 6.51 (s, 1 H), 6.20-6.19 (d, J = 8.1 Hz, 1H), 6.10 (s, 1H), 4.3 (s, 1H), 3.44 – 3.39 (m, J = 29.1 Hz, 3H), 3.30-3.22 (m, J = 33.7 Hz, 1H), 3.08-3.04 (m, J = 19.8 Hz,

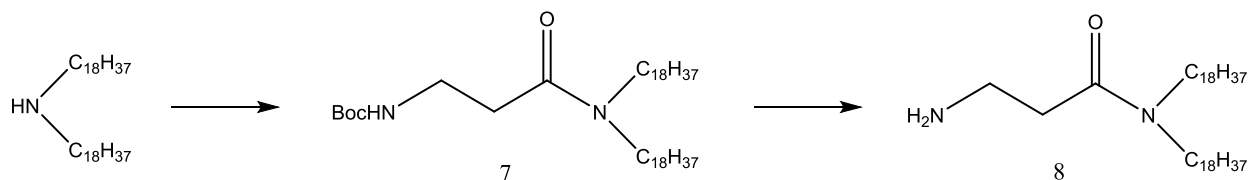
2H), 2.82 – 2.68 (q, $J = 47.7$ Hz, 5H), 2.54-2.39 (m, $J = 57.0$ Hz, 1H), 1.89 (s, 1H), 1.63-1.48 (m, $J=67.5$ Hz, 4 H), 0.94-0.90 (t, $J = 12.8$ Hz, 6H), 0.78- 0.74 (t, $J=12.4$ Hz, 6H), 1.36-1.25 (m, $J=47.7$ Hz, 63 H). MS (ESI⁺) calc. 1009 C₆₃H₁₀₁N₅O₅H (M+H)⁺; 1008.79 observed, 1008.78 cal.



Synthesis of Compound 6 (Lipo-Dox)

To the solution of doxorubicine/hydrochloride (40 mg, 0.069 mmol), in MeOH (45 mL) and DCM (5 mL), compound **3** (57 mg 0.09 mmol), TFA (50 μ L) was added and stirred overnight under argon atmosphere. The solvent was evaporated in vacuo, then resulting residue was purified by flash column chromatography on silica gel (eluent DCM/MeOH/triethylamine = 85:14: 1) to give desired product as a red solid (45 mg, yield 25%).

¹H NMR (500 MHz, CDCl₃) 8.01 (m, $J = 8.0$ Hz, 1H), 7.74 (m, $J = 7.7$ Hz, 1H), 7.35 (m, $J = 7.4$ Hz, 1H), 5.49 (s, 1H), 5.26 (s, 1H), 4.75 - 4.57 (m, $J=4.7$ Hz, 2H), 4.05 (d, $J = 4.1$ Hz, 4H), 3.48 (s, 1H), 3.38 – 3.18 (m, $J = 3.3$ Hz, 6H), 3.18 – 2.89 (m, $J = 3.0$ Hz, 3H), 2.79 - 2.61 (m, $J= 2.7$ Hz, 2H), 2.52 (d, $J = 2.52$ Hz, 1H), 2.37 – 2.12 (m, $J = 2.2$ Hz, 1H), 1.81 - 1.64 (m, $J = 1.7$ Hz, 2H), 1.55 (d, $J = 1.6$ Hz, 4H), 1.27 (s, 63 H), 0.89 (t, $J = 0.9$ Hz, 6H). MS (ESI⁺) calc. 1162 C₈₇H₁₁₀N₄O₁₃H (M+H)⁺; observed, 1161.8.



Compound 7

To the solution of Boc- β -Ala-OH 190 mg (1.1 mmol) in DMF (10 mL) was added dioctadecylamine (388 mg, 0.062 mmol), PyBOP (500 mg, 0.96 mmol), and DIPEA (1.11 mL, 6.4 mmol (6 eq)) were added and stirred at room temperature overnight under argon atmosphere. The solvent was evaporated in vacuo, the resulting residue was purified by flash column chromatography on silica gel (eluent EtOAc/Hepane 50:50) to give desired product as a colorless solid (268 mg, yield 75%).

^1H NMR (400 MHz, CDCl_3) 5.36 (s, 1H), 3.41 (p, $J=11.3$, 6.0, 2H), 3.30 - 3.21 (t, 2H), 3.20 - 3.11 (t, 2H), 2.48 (t, $J=5.5$, 2H), 1.50 (m, $J=6.7$, 6H), 1.42 (s, 9H), 1.25 (s, 64H), 0.87 (t, $J=6.9$, 6H). ^{13}C NMR (101 MHz, CDCl_3) δ 170.42, 77.32, 77.21, 77.01, 76.69, 48.03, 46.24, 36.63, 31.93, 29.71, 29.66, 29.63, 29.59, 29.56, 29.52, 29.36, 29.27, 28.63, 27.56, 27.06, 26.89, 22.69, 14.10. MS (ESI+) cal. 692.68 $\text{C}_{44}\text{H}_{88}\text{N}_2\text{O}_3$ and 715.68 ($\text{M}+\text{Na}$) $^+$, observed, 715.6702.

Compound 8 (LipoAmine)

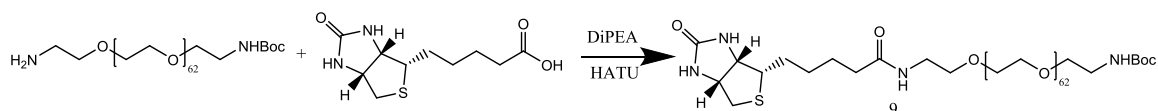
To the solution of **7** (268 mg, 0.39 mmol) in DCM (5 mL), TFA (5 mL) and 2 drops of MiliQ water were added and stirred at room temperature for 2 hours. After confirming the reaction completely proceeded with TLC, the solvents were evaporated under reduced pressure, and then the residue was dissolved in MeOH and evaporated 3 times to remove TFA and give desired product **3** as a colorless solid (214 mg).

^1H NMR (400 MHz, CDCl_3) 3.60 (s, 1H), 3.34-3.20 (m, 4H), 3.21-3.10 (t, 2H), 2.74 (s, 2H), 1.63-1.42 (m, 4H), 1.25 (s, 64H), 0.88 (t, $J=6.9$, 6H). ^{13}C NMR (101 MHz, CDCl_3) δ 170.58, 77.48, 77.36, 77.16, 76.84, 48.18, 46.39, 36.79, 32.08, 29.87, 29.82, 29.78, 29.74, 29.71, 29.68, 29.52, 29.42, 28.78, 27.72, 27.21, 27.05, 22.84, 14.26. MS (ESI+) calc. 592.63 $\text{C}_{39}\text{H}_{80}\text{N}_2\text{O}$ and 593.63 ($\text{M}+\text{H}$) $^+$, observed, 593.6339.

4.2.1.2- Synthesis of chemicals related NEs functionalization project

Compound 9

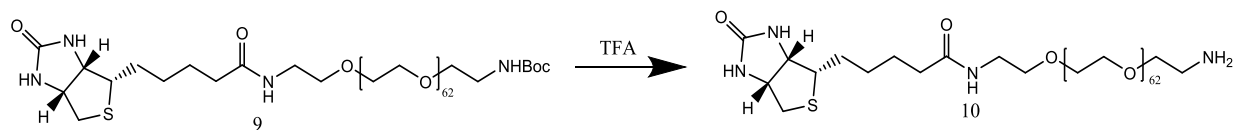
To a solution of PEG3000 amine (100 mg, 0.033 mmol) and biotin (24 mg, 0.1 mmol) in DMF, HATU (30 mg, 0.079 mmol) and TEA (60 μ L) were added. The reaction mixture was stirred under 40 °C overnight. The resulting solution was then concentrated in vacuum and purified by dialysis in water (dialysis membrane molecular cut off weight: 2000 Da). After dialysis, 110 mg product in the form of light-yellow lipid was obtained after evaporation.



^1H NMR (400 MHz, MeOH 4D) δ 4.37 (d, 1H), 4.21 (d, 1H), 3.46 (s, ~268H), 3.32 – 3.24 (m, 2H), 3.32 – 3.23 (m, 2H), 3.11-3.07 (m, 2H), 2.85 – 2.74 (m, 2H), 2.59 (d, 1H), 2.06 (d, 2H), 1.51 (dd, 7.3 Hz, 2H), 1.28 (s, 9H).

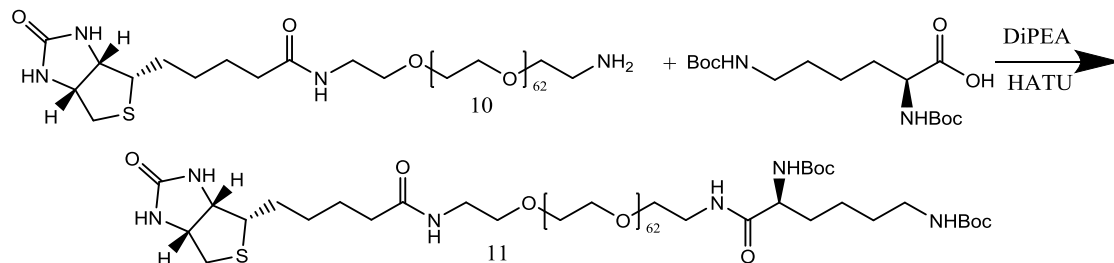
Compound 10

Compound **9** (110 mg) was vigorously stirred in 20% TFA/DCM solution for 3 h. The reaction solution was then concentrated and dried in vacuum to afford compound **2** (93 mg) as light-yellow lipid.



^1H NMR (400 MHz, MeOD) δ 4.42-4.39 (q, 1H), 4.23-4.21 (q, 1H), 3.54 (m, ~268H), 3.36-3.35 (t, 2H), 3.23-3.25 (t, 2H), 3.14-3.09 (m, 3H), 2.86-2.81 (q, 1H), 2.63-2.60 (d, 1H), 2.14-2.10 (t, 2H), 1.69-1.46 (m, 4H), 1.38-1.42 (t, 2H).

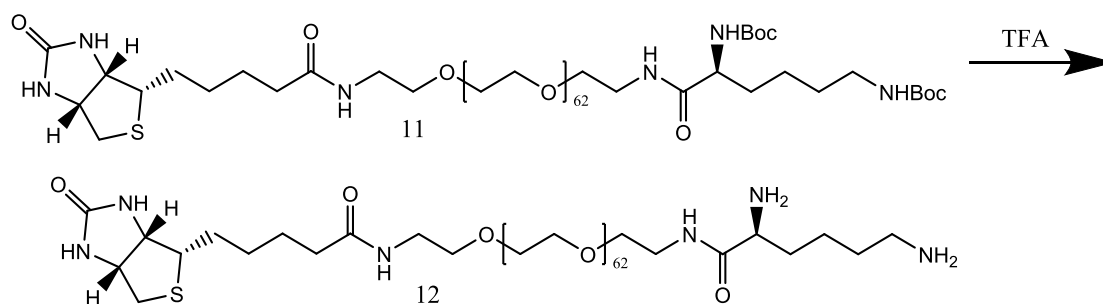
Compound 11



To a solution of **10** (50 mg, 0.016 mmol) and Boc-lysine-OH (12 mg, 0.05 mmol) in DMF, HATU (15 mg, 0.04 mmol) and TEA (30 μ L) were added. The reaction mixture was stirred under 40 °C overnight. The resulting solution was then concentrated in vacuum and purified by dialysis in water (dialysis membrane molecular cut off weight: 2000 Da). After dialysis, 53 mg product in the form of colorless lipid was obtained after evaporation.

^1H NMR (400 MHz, MeOH, 4D) δ 4.51-4.47 (q, 1H), 4.33-4.30 (q, 1H), 4.01-3.95 (m, 1H), 3.79-3.34 (m, ~272 H), 3.26-3.21 (d, 2H), 3.04-3.01 (t, 3H), 2.96-2.91 (q, 1H), 2.73-2.70 (d, 1H), 2.24-2.20 (t, 2H), 1.79-1.55 (m, 8H), 1.49-1.39 (m, 22H).

Compound 12



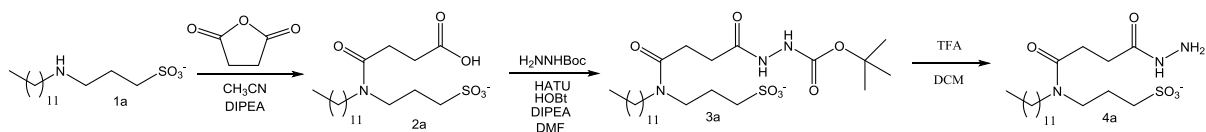
Compound 11 (53 mg) was vigorously stirred in 1 mL 20% TFA/DCM solution for 3 h. The reaction solution was then concentrated and dried in vacuum to afford compound **4** (46 mg) as light-yellow lipid.

^1H NMR (400 MHz, MeOD) δ 4.54-4.51 (d, 1H), 4.35-4.32 (d, 1H), 4.0-3.97 (t, 1H), 3.75 – 3.41 (m, ~200 H), 3.24-3.21 (m, 1H), 3.15-3.05 (t, 2H), 2.98-2.93 (dd, 1H), 2.75-2.72 (d, 1H), 2.27-2.23 (t, 2H), 1.94-1.92 (q, 2H), 1.91-1.60 (m, 6H), 1.59-1.45 (q, 2H), 1.39-1.37 (m, 2H).

di-ion and tri-ion $\text{C}_{144}\text{H}_{286}\text{N}_6\text{O}_{66}$ (3187.92) Mass detected: 1617.70 and 1086.09 (calc.: $(\text{M}+2\text{Na}^+)/2=1616.96$ and $(\text{M}+3\text{Na}^+)/3=1085.64$).

Synthesis of NPC-Chol was done as described elsewhere^[364].

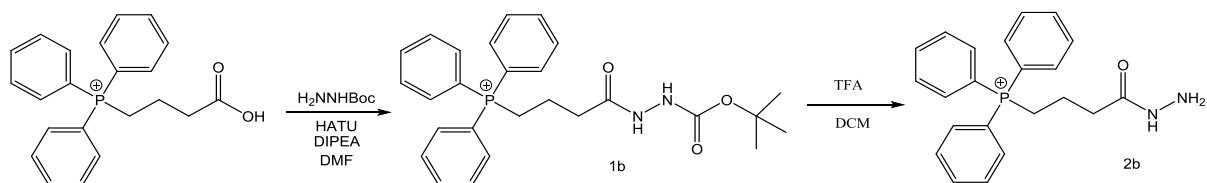
4.2.1.3- Synthesis of targeting hydrazide compounds



Compound **1a** was prepared as described previously [33].

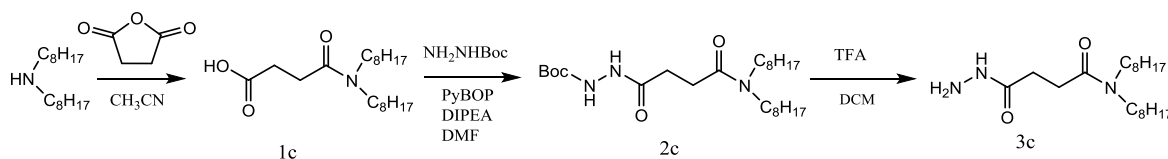
Compound 2a. 400 mg of compound **1a** were dissolved in 7 mL of dry CH₃CN together with 589 mg (3.5 equiv., 794 μ L) of DIPEA. After that, a solution of 196 mg (1.5 eq.) of succinic anhydride 3 mL of dry CH₃CN was added dropwise and the resulting mixture was stirred for 12h (control by TLC) under Ar atmosphere. After the reaction the solvent was evaporated *in vacuo* and the crude product was purified by column chromatography (SiO₂, DCM:MeOH:HCOOH 80:20:2).Yield: 550 mg as a colourless solid (DIPEA salt is present, its signals are not presented). ¹H NMR (400 MHz, MeOH-D₄) δ ppm 3.49 (2H, dt), 3.36 (2H, dt), 2.86 (2H, sext), 2.68 (2H, pentet), 2.58 (2H, t), 2.06 (2H, dpentet), 1.65 (2H, dpentet), 1.30 (18 H, bs), 0.89 (3H, t). Splitting of d, f, g was due to presence of amide rotamers, which disappeared under high temperature. ¹³C NMR (400 MHz, MeOH-D₄) δ ppm 176.70, 173.94, 166.88, 55.91, 54.96, 50.30, 49.15, 48.04, 47.42, 46.26, 43.89, 33.19, 30.87, 30.71, 30.61, 30.59, 30.50, 30.00, 29.16, 28.88, 28.21, 28.06, 25.58, 24.66, 23.86, 18.11, 17.85, 14.58, 13.26. Chemical Formula: [C₁₉H₃₆N₃O₆S⁻] m/z (M) calc. 406.2263MS for m/z [M⁻+2H⁺]⁺ found 408.2432.**Compound 3a.** 200 mg of compound **2a** were dissolved in 3 mL of dry DMF together with 238 mg (1.5 eq.) of HATU, 28 mg (0.5 eq.) of HOBt and 215 mg (4 eq., 291 μ L) of DIPEA under Ar atmosphere. After 5 minutes, a solution of 83 mg (1.5 eq.) of tert-Butyl carbazate in 1.5 mL of dry DMF was added and the mixture was stirred for 24h (control by TLC) under Ar atmosphere. After the reaction the solvent was evaporated *in vacuo* and the crude product was purified by column chromatography (SiO₂, DCM:MeOH 80:20, redone twice).Yield: 165 mg as a colourless solid (DIPEA salt is present, its signals are not presented). ¹H NMR (400 MHz, MeOH-D₄) δ ppm 3.50 (2H, dt), 3.37 (2H, dt), 2.82 (2H, dt), 2.74 (2H, pentet), 2.52 (2H, t), 2.05 (2H, dpentet), 1.64 (2H, dpentet), 1.47 (9H, ts), 1.30 (18H, bs), 0.91 (3H, t). ¹³C NMR (400 MHz, MeOH-D₄) δ ppm 174.98, 174.92, 173.85, 173.72, 158.11, 157.95, 82.18, 81.96, 56.01, 50.01, 49.15, 48.06, 47.46, 46.30, 43.96, 33.19, 30.87, 30.71, 30.64, 30.59, 30.26, 30.04, 29.39, 29.23, 28.87, 28.71, 28.25, 28.09, 25.62, 24.50, 23.85, 18.89, 17.45, 14.57. HRMS for Chemical Formula: [C₂₄H₄₆N₃O₇S⁻] m/z (M) calc. 520.3056, found 520.3051.

Compound 4a (PM-HZ). To the solution of **3a** (165 mg, 0.31 mmol) in DCM (5 mL), TFA (5 mL) and 1 drop of MiliQ water were added and stirred at room temperature for 2 h. After confirming the reaction completely proceeded with TLC, the solvents were evaporated under reduced pressure, and then the residue was dissolved in MeOH and evaporated 3 times to remove TFA and give desired product **4a** as a colorless solid (153 mg) (DIPEA salt is present, its signals are not presented). ^1H NMR (400 MHz, MeOH- D_4) δ ppm 3.53 (2H, dt), 3.39 (2H, dt), 2.80 (4H, m), 2.59 (2H, pentet), 2.06 (2H, dpentet), 1.65 (2H, dpentet), 1.30 (18H, bs), 0.91 (3H, t). ^{13}C NMR (400 MHz, MeOH- D_4) δ ppm 173.94, 173.91, 166.88, 55.91, 54.96, 50.30, 49.15, 48.04, 47.42, 46.26, 43.89, 33.19, 30.87, 30.71, 30.61, 30.59, 30.50, 30.00, 29.16, 28.88, 28.21, 28.06, 25.58, 24.66, 23.86, 18.11, 17.85, 17.67, 14.58, 13.26. HRMS for Chemical Formula: $[\text{C}_{19}\text{H}_{38}\text{N}_3\text{O}_5\text{S}^-]$ m/z (M) calc. 420.2532, found 420.2534.



Compound 1b. 500 mg of (3-carboxypropyl)triphenylphosphonium bromide were dissolved in 8 mL of dry DMF together with 465 mg (1.05 eq.) of HATU and 450 mg (3 eq., 610 μL) of DIPEA. After 5 minutes, a solution of 161 mg (1.05 eq.) of tert-Butyl carbazate in 2 mL of dry DMF was added and the mixture was stirred for 24h (control by TLC) under Ar atmosphere. After the reaction the solvent was evaporated *in vacuo*, then the solid residue was dissolved in MeOH and precipitated with Et_2O , filtered and washed with Et_2O (redone twice). After that, the solid residue was dissolved in DCM, washed with water (x2) and brine, dried over Na_2SO_4 and the solvent was evaporated *in vacuo*. The crude product was purified by gradient column chromatography (SiO_2 , DCM:MeOH 90:10 to 80:20). Yield: 70 mg as a colourless solid. ^1H NMR (400 MHz, MeOH- D_4) δ ppm 7.82 (15H, m), 3.52 (2H, t), 2.48 (2H, t), 1.99 (2H, q), 1.47 (9H, s). ^{13}C NMR (400 MHz, MeOH- D_4) δ ppm 174.30, 158.09, 136.48, 136.46, 135.01, 134.93, 131.74, 131.64, 120.23, 119.54, 82.16, 49.15, 34.38, 34.23, 28.68, 22.27, 21.84, 19.98. HRMS for Chemical Formula: $[\text{C}_{27}\text{H}_{32}\text{N}_2\text{O}_3\text{P}^+]$ m/z (M) calc. 463.2151, found 463.2657.

Compound 2b (Mito-HZ). To the solution of **1b** (70 mg, 0.15 mmol) in DCM (2 mL), TFA (2 mL) and 1 drop of MiliQ water were added and stirred at room temperature for 2 h. After confirming the reaction completely proceeded with TLC, the solvents were evaporated under reduced pressure, and then the residue was dissolved in MeOH and evaporated 3 times to remove TFA and give desired product **4a** as a colorless solid (54 mg). ^1H NMR (400 MHz, MeOH- D_4) δ ppm 7.83 (15H, m), 3.47 (2H, t), 2.61 (2H, t), 2.01 (2H, q). ^{13}C NMR (400 MHz, MeOH- D_4) δ ppm 136.58, 136.55, 135.01, 134.91, 131.81, 131.68, 131.49, 120.17, 119.30, 117.60, 114.77, 49.15, 22.67, 22.15, 19.25. HRMS for Chemical Formula: $[\text{C}_{22}\text{H}_{24}\text{N}_2\text{OP}^+]$ m/z (M) calc. 363.1626, found 363.2060. This compound was further characterized by RP-HPLC by using C4 column (diameter 4.6 mm, length 250 mm, 5 μM pore size) at flow rate of 1 mL/min, 45 $^\circ\text{C}$, 50% /50% of water/acetonitrile on an Agilent 1290 Infinity II LC System.



Compound 1c. To the solution of succinic anhydride (192 mg, 1.92 mmol) in THF (20 mL) was added 1,1-Dioctylamine (250 mg, 1.04 mmol), then mixture was refluxed overnight under argon atmosphere. The solvent was evaporated in vacuo, then resulting residue was purified by recrystallization from dioxane to give desired product as a colorless solid (243 mg, 68 %). ^1H NMR (400 MHz, CDCl_3) δ ppm 3.20 (4H, t), 2.62 (4H, t), 1.50 (4H, bs), 1.21 (20H, bs), 0.82 (6H, t). ^{13}C NMR (400 MHz, CDCl_3) δ ppm 176.48, 171.97, 77.23, 53.61, 48.36, 47.72, 46.67, 31.97, 31.92, 31.90, 30.48, 29.53, 29.46, 29.41, 29.36, 29.30, 29.24, 29.02, 28.33, 27.86, 27.21, 27.08, 26.94, 25.97, 22.80, 22.78, 14.24, 14.22. HRMS for Chemical Formula $[\text{C}_{20}\text{H}_{39}\text{NO}_3^-]$ m/z (M) calc. 341.2929, found m/z for $[\text{M}^- + 2\text{Na}^+ - \text{H}^+]^+$ 386.3101.

Compound 2c. To the solution of **1c** (243 mg, 0.71 mmol) in DMF (10 mL), tert-butylcarbazate (159 mg 1.21 mmol), PyBOP (630 mg, 1.21 mmol), and DIPEA (1.11 mL, 6.4 mmol (9 eq)) were added and stirred at room temperature overnight under argon atmosphere. The solvent was evaporated in vacuo, then resulting residue was purified by flash column chromatography on silica gel (eluent EtOAc/Hepane 50:50) to give desired product as a colorless solid (163 mg, yield 50%). ^1H NMR (400 MHz, CDCl_3) δ ppm 3.22 (4H, t), 2.58 (4H, t), 1.46 (13H, ms), 1.20 (20H, bs), 0.78

(6H, t). ^{13}C NMR (400 MHz, CDCl_3) δ ppm 172.38, 171.01, 155.21, 81.17, 77.00, 60.33, 56.88, 53.43, 49.97, 47.84, 46.52, 46.17, 31.68, 31.63, 29.26, 29.17, 29.12, 29.07, 28.67, 28.23, 28.10, 28.04, 27.91, 27.60, 26.94, 26.87, 26.79, 26.73, 22.50, 22.48, 13.86. HRMS for Chemical Formula $[\text{C}_{20}\text{H}_{39}\text{NO}_3]^+$ m/z (M) calc. 455.3723, found m/z for $[\text{M}+\text{Na}^+]^+$ 478.4062. **Compound 3c (LD-HZ)**. To the solution of **2c** (163 mg, 0.48 mmol) in DCM (10 mL), TFA (10 mL) and 2 drops of MilliQ water were added and stirred at room temperature for 2 h. After confirming the reaction completely proceeded with TLC, the solvents were evaporated under reduced pressure, and then the residue was dissolved in MeOH and evaporated 3 times to remove TFA and give desired product **3c** as a colorless solid (158 mg). ^1H NMR (400 MHz, CDCl_3) δ ppm 3.22 (2H, t), 2.68 (2H, t), 2.56 (2H, t), 1.50 (4H, bd), 1.24 (20H, bs), 0.87 (6H, t). Splitting of protons of c, d and e, f were due to presence of amide rotamers; the splitting disappeared under high temperature. ^{13}C NMR (400 MHz, CDCl_3) 172.99, 171.69, 77.48, 77.16, 76.84, 48.56, 46.90, 31.91, 31.86, 29.42, 29.33, 29.30, 28.69, 27.64, 27.10, 27.01, 22.72, 14.16, 14.15. 3HRMS for Chemical Formula: $[\text{C}_{20}\text{H}_{41}\text{N}_3\text{O}_2]$ m/z calc. 355.3199, found m/z ($\text{M}+\text{Na}^+$) 378.3163.

4.2.2- Instruments

4.2.2.1- Spectroscopy

Absorption spectra were recorded on a Cary 4000 Scan ultraviolet–visible spectrophotometer (Varian). Emission spectra were recorded on a FluoroMax-4 spectrofluorometer (Horiba Jobin Yvon) or Edinburgh FS5 spectrofluorometer equipped with a thermostated cell compartment, respectively. For standard recording of fluorescence spectra, the emission was collected 10 nm after the excitation wavelength. All the spectra were corrected from the lamp fluctuations and wavelength-dependent response of the detector. NMR spectra were recorded on a Bruker Avance III 400 MHz spectrometer. Mass spectra were obtained using an Agilent Q-TOF 6520 mass spectrometer. All error bars correspond to standard deviation of the mean. Statistical analysis was based on the one-tailed T-test, using Microsoft Excel.

4.2.2.2- Dynamic light scattering and zeta potential measurements

The hydrodynamic diameters and polydispersity index (PDI) of the NEs were measured, in triplicate, by dynamic light scattering (DLS) along with zeta potential measurement using a

Malvern Zetasizer Nano ZS instrument (Malvern Instruments, Orsay, France), equipped with a helium–neon laser (4 mW) operating at 633 nm, with a scatter angle of 173° and the temperature maintained at 25 °C. Measurements of zeta potentials were performed under similar dilution conditions (60 µL in 1 mL, 5mM NaCl), to ensure the comparability between the different samples.

4.2.2.3- Microscopy

The confocal laser scan images were recorded with Leica Application Suite. Epi-fluorescence images were obtained from a microscope produced by Nikon Instruments Europe B.V. Cell images were processed using ImageJ 1.52a software (NIH, Bethesda, MD, USA). Transmission and fluorescence images were taken using Nikon Ti-E inverted microscope, equipped with CFI Plan Apo ×60 oil (numerical aperture = 1.4), 20x air objective Nikon CFI Plan Apo, NA = 0.75 or 10x air objective Nikon Plan Fluor NA = 0.3 and a Hamamatsu Orca Flash 4 sCMOS camera.

4.2.2.4- 3D printing

Form 3, 3D printer (Formlabs) was used for 3D printing. Stent prototype (1cm width, 3 cm height) that mimics the vascular medical stents was designed with FreeCAD parametric 3D modeler software (STL file is available upon request). Clear V4 resin (Formlabs) was used for 3D printing. After the 3D printing, polymer stents were rinsed with isopropyl alcohol to get rid of the excess resin and exposed under UV light for 30 minutes.

4.2.3- Preparation of NEs

4.2.3.1- General protocol for cargo-loaded nanoemulsions (NEs) formulation

All NEs used in present studies were produced by spontaneous nanoemulsification, the cargo (dyes, LipoHD, LipoAmine or NPC-Chol) were dissolved in LabrafacWL[®] (50 mg) and homogenized under magnetic stirring at 40 °C for 10 mins. Then, the surfactant Cremophor ELP[®] (also called Kolliphor ELP[®]) was added (50 mg), and the mixture was homogenized under magnetic stirring at 40 °C for 10 min up to complete homogenization. Finally, NEs were generated with the addition of ultrapure (Milli-Q) water (230 mg) and shaking at 1400 rpm.

4.2.3.2- Preparation of NEs (for chapter 2.1)

NEs for drug sponge study were produced by following process: the cargo (dyes, LipoHD and/or Pro-NRK) were dissolved in LabrafacWL[®] (50 mg). In order to prepare NEs containing different portions of cargoes, they were firstly dissolved fully into labrafac WL[®] (50mg) and homogenized under magnetic stirring at 40 °C for 10 mins. Then, the surfactant Cremophor ELP[®] (also called Kolliphor ELP[®]) was added (50 mg), and the mixture was homogenized under magnetic stirring at 40 °C for 10 min up to complete homogenization. Finally, NEs were generated with the addition of ultrapure (Milli-Q) water (230 mg). Stability of loading and pH-controlled release.

4.2.3.3- Preparation of NEs (for chapter 2.2)

LipoAmine containing NEs were prepared in the following sequence: firstly dissolve 3 mg LipoAmine in 50 μ L DCM, then, 50 mg of both LabrafacWL[®] and surfactant Cremophor ELP[®] (also called Kolliphor ELP[®]) was added, the mixture was homogenized and homogenized under magnetic stirring at 40 °C for 10 min, followed by DCM evaporation under vacuum. Finally, NEs were generated with the addition of ultrapure (Milli-Q) water (230 μ L) mixed by a thermo-shaker at the speed of 1400 r/min under 40 °C. For *in situ* reaction, 30 μ L of this LipoAmine NEs was used to react with 5 μ L PA (3 mM) in 1 mL ultrapure (Milli-Q) water under 40 °C. The molar ratio of LipoAmine to PA was calculated to be 30 to 1. Control group was conducted by mixing 30 μ L empty NEs with 5 μ L PA (3 mM). The reaction was monitored by fluorescence spectrum under the excitation wavelength of 380 nm and 420 nm, end point was indicated by the total blue shift of the absorption spectrum (4 hours).

4.2.3.4- Preparation of NEs (for chapter 2.3)

NPC-Chol containing NEs were produced by following process: the cargo (3 mg NPC-Chol and certain percentage of dyes, 1% of Cy5.5-TPB, 1% of DiD-TPB, 1 % of DiI-TPB or 1 % of Cy5.5-TPB in cases of dye-loaded NEs) were dissolved in Vitamin E acetate (50 mg) and placed in sonication bath at 40 °C for 10 min. Then, the surfactant Kolliphor ELP[®] was added (50 mg), and the mixture was homogenized under magnetic stirring (400 rpm) under 40 °C for 10 min to complete homogenization. Finally, NEs were generated by addition of 40 °C ultrapure (Milli-Q) water (230 μ L) on a heat-shaker (1400 rpm, 40 °C).

4.2.3.4.1- Preparation of NEs with biotin surface (Biotin-NEs)

In situ reaction of NPC-Chol (3 mg) loaded NEs (330 mg) with (or without for control) 50 mg biotin-PEG-lysine were conducted by mixing them to final volume of 1 mL by pH 8.5 buffer and vortexing at speed of 500 rpm over 24 hours under 40 °C. After reaction, 5 µL ethanolamine were added. The mixture was incubated further for 4 hours to consume the excess NPC-Chol. Absorbance scans were checked after reaction and after adding ethanolamine in order to calculate the reaction ratio. Neutralized (control) NEs group was prepared by mixing NPC-Chol (3 mg) loaded NEs with excess of ethanolamine to final volume of 1 mL of pH 8.5 buffer. Dialysis using membrane (Mw 14 000 Da) in Milli-Q water was conducted in the end, to remove the side product nitrophenol.

4.2.3.4.2- Functionalization of NEs with antibody surface

DiD-TPB (1% in oil) loaded Biotinylated-NEs were mixed with Neutravidin (67 µM) and incubated in room temperature for 3 h. Then, the mixture was added by biotinylated cetuximab (33 µM) and incubated in room temperature for 5 hours. After this process, the sample was subjected to size exclusion purification.

4.2.3.4.3- Size exclusion chromatography

Sephacryl S-300 High Resolution resin (in ethanol) was used for the size exclusion purification of NEs functionalized with an antibody. Column loading and was performed as listed in the instruction of the provider. Briefly, the resin was filled in 1.5 cm diameter (30 cm) column, then, ethanol was flowed by pH 7.4 PBS buffer at speed of 150 cm/h for 3 column volumes. Then, the tap of the column was closed and placed still overnight. Then, 100 µL of sample was loaded to the column and eluted at speed of 150 cm/h, fractions were collected by Fraction Collector Frac-920 (2 mL/fraction).

4.2.3.5- Preparation of liposomes (for chapter 2.4)

A stock solution of lipid(s) composed of DOPC (dioleoylphosphatidylcholine) in chloroform was placed into a round-neck flask, after which the solvent was evaporated in vacuo and phosphate

buffer (20 mM, pH 7.4) was added. After all solids were dissolved in PBS, a suspension of multilamellar vesicles was extruded by using a Lipex Biomembranes extruder (Vancouver, Canada). The size of the filters was first 0.2 μm (7 passages) and thereafter 0.1 μm (10 passages). This generates monodisperse LUVs (Large Unilamellar Vesicle) with a mean diameter of 0.12 μm as measured with a Zetasizer NanoZS (Malvern Instruments, Orsay, France). The final DOPC concentration in the LUVs was calculated to be 1 mM.

4.2.4- pH dependent cargo release

4.2.4.1- pH dependent release of Lipo-NRK

In order to prove that LipoHD modified NRK (Lipo-NRK) is more lipophilic and resistant to leakage than NRK, the conjugate was first synthesized chemically and used for the release model study. For NRK and Lipo-NRK release model study, five formulations were prepared: NRK with and without F888, Lipo-NRK with and without F888 and F888 alone. The concentration of each dye in labrafacWL[®] was 10 mM. The condition for testing the dye stability in the presence of empty NEs was created by mixing 100 μL 100 times diluted dye-loaded NEs (by mixing 10 μL NEs with 990 μL distilled water) with 10-fold excess of blank NEs (10 μL), which acted as the acceptor medium for the released dyes. The pH dependent release of LipoNRK was conducted by using buffers of ranging pH from pH 5 to pH 7.4 prepared by mixing different portion of acetate buffer (pH 4) with phosphate buffer (pH 7.4) during mixing with 10-fold excess of blank particles. Fluorescence of the sample was tested at several time points (5, 10, 15, 30, 60, 120, 240 and 480 min). Fluorescence intensity ratio of F888 and NRK (taken at 453 and 603 nm, respectively) under the excitation wavelength of 405 nm was measured. All the spectra were corrected by subtracting the blank corresponding to the empty NEs.

2.2.4.2- Lipo-Dox NEs pH dependent release study

To monitor the pH-controlled release of Dox, we used FRET technique similar to that used for Nile Red derivative NRK. Cy5/Lipo-Dox NEs were prepared by *in situ* reaction of NEs containing 90 mM LipoHD and 0.95 mM of DiD (Cy5) in LabrafacWL[®] for 6 h and for dialysis to remove unreacted Dox. The obtained Cy5/Lipo-Dox NEs were mixed with 10-fold excess of blank nano-droplets and the emission spectra were recorded as a function of time at a range of pHs from pH 5

to pH 7.4 prepared by pH 7.4 (phosphate buffer) and pH 4 (acetate buffer). Finally, in order to test the compatibility with cell experiments media, PBS with pH 7.4 and pH 5 adjusted with acetic acid as well as 10% serum were also tested in similar manner. Fluorescence intensity ratio of Cy5 and Dox (peaks at 670 and 600 nm, respectively) under the excitation at 520 nm was measured.

4.2.4.3- pH dependent release of PA-LipoAmine

100 μ L of PA-LipoAmine NEs (formed after 4 hours of *in situ* reaction under 40 °C) was mixed with 10 μ L empty NEs as PA acceptor in 1 mL pH adjusted phosphate buffer with pH of 4, 6, 7.4. Emission scan under the excitation wavelength of 380 nm was used to monitor the degradation process on time points of 1 min, 15 min, 30 min, 60 min and 120 min.

4.2.5- In situ reaction study

4.2.5.1- In situ formation of Lipo-NRK detected by FRET

To evaluate the *in situ* reaction inside NEs, NRK was used as a model drug. 300 μ L of NEs prepared from LabrafacWL[®] containing LipoHD (90 mM) and Kolliphor ELP[®] was mixed with 12.6 μ L of 47 mM NRK and 300 μ L of pH 4 acetate buffer and reacted for 6 h (rt). Then, the emulsion was extracted by 600 μ L dichloromethane. TLC was used to examine the content in the organic phase compared with pure Lipo-NRK. Dichloromethane:MeOH=95:5 was used as the mobile phase for TLC. With the help of F888 as energy donor, the reaction was monitored by the FRET efficiency between F888, the FRET donor, and NRK, the acceptor. NEs prepared from LabrafacWL[®] containing F888 (10 mM) and LipoHD (90 mM) were used for the reaction. NEs prepared from LabrafacWL[®] containing only F888 (10 mM) were used as a control. The reaction was initiated by adding 300 μ L of pH 4 acetate buffer along with 12.6 μ L of 47 mM NRK. The reaction was diluted at different time points by mixing 10 μ L of the reacted solution with 990 μ L of pH 7.4 phosphate buffer. Then 100 μ L of this diluted solution was mixed with 10 μ L empty NEs and 880 μ L milliQ water, and the emission spectrum was measured under the excitation wavelength of 405 nm. The fluorescence intensity ratio of peak at 450 and 600 nm was calculated from the spectrum. All the spectra were corrected from the blank by subtracting the corresponding spectrum of empty NEs.

4.2.5.2- In situ formation of Lipo-Dox conjugate detected by FRET

Doxorubicine (Dox), an anti-tumor drug, was also tested by this *in situ* pro-drug formation system. Similarly, 300 mL of NEs prepared from LabrafacWL[®] containing LipoHD (90 mM) were mixed with 300 μ L acetate buffer (pH 4) along with 10 μ L of Dox-HCl (150 mM). In the control experiment NEs without LipoHD were used. The mixtures were vortexed for 24 h at 37 °C. The resulting solutions were dialyzed in 500 mL of 0.1 M NaHCO₃ for 24 h. After the dialysis, encapsulation efficiencies were tested based on the absorbance at 500 nm of the NEs solution before and after dialysis using 100 fold diluted reaction solution. Afterwards, NEs containing 90 mM LipoHD and 0.95 mM of DiD (Cy5) in LabrafacWL[®] were prepared to monitor the reaction by FRET. To start the reaction, 10 μ L of 150 mM Dox-HCl solution in DMSO were added to 330 μ L of NEs along with 300 μ L pH 4 buffer, control was conducted with NEs containing only 0.95 mM of Cy5 in LabrafacWL[®]. To study the *in situ* reaction kinetics, the reaction at different time points was quenched with 100 fold of phosphate buffer (pH 7.4). Then, 100 μ L of this diluted solution were mixed with 10 μ L of empty NEs and 980 μ L milliQ water. The reaction was examined by measuring the fluorescence intensity ratio of Cy5 and Dox at 670 and 600 nm, respectively, under the excitation wavelength of 520 nm. After the reaction, the mixture underwent dialysis for 24 hours. UV absorption was used to determine the encapsulation ratio of Dox in the form of Lipo-Dox. NEs with the same concentration of Cy5 but without LipoHD were used as a control in the same protocol above. the same concentration of Cy5 with the reaction group after dialysis was prepared.

4.2.5.3- Identification of formed PA-LipoAmine

The reacted NEs (30 μ L LipoAmine NEs reacted with 5 μ L 3 mM PA in 1 mL Milli-Q water) were mixed with excess of NaBH₄ (1.2 mg) for 2 hours to reduce the formed proton sensitive imine into stable amine. Control groups (30 μ L Empty NEs added by 5 μ L 3 mM PA in 1 mL Milli-Q water) were treated with the same reduction process. After this process, samples before and after the reduction were extracted by DCM and distilled water. The organic phase was collected for TLC analysis (DCM:MeOH = 9:1). The novel blue point, which appeared in the PA-LipoAmine reduced extraction, was collected and extracted by MeOH and sent for mass analysis for the identification of the reduced product of PA-LipoAmine.

4.2.5.4- Identification of in situ reaction product of NPC-Chol with ethanolamine

100 μ L of NPC-Chol containing NEs were added (or not for control) by 5 μ L (50 times excess) ethanolamine and added by pH 8.5 Phosphate buffer to final volume of 500 μ L, Reaction was conducted in a heat-shaker vortexed at speed of 500 rpm over 6 hours under 40 °C. Absorption scan of 100 times diluted solution was checked after the reaction of reaction and control group. For the reaction group, the resulting solution was dialyzed (Membrane cut off size of 14 KDa) in Milli-Q water for 24 hours with changing of medium every 8 hours. After this process, the solution was extracted by 500 μ L DCM by centrifugation. Organic phase was examined by mass spectrometry.

4.2.6- Preparing of Antibody NEs (for chapter 2.3)

4.2.6.1- Conjugation of Abs with biotin Experiment General Remarks

Conjugation experiments were carried out in the Eppendorf, DNA low-binding tube 1.5 mL at atmospheric pressure at room temperature unless otherwise stated. All buffer solutions were prepared with deionised water and filter-sterilised prior to use. Borate buffer was prepared from 25 mM sodium tetraborate, 25 mM NaCl, and 1 mM EDTA at pH 8.1 or 8.4. Phosphate-buffer saline (PBS) was 140 mM NaCl and 12 mM sodium phosphate at pH 7.4. Sodium azide 0.5% (w/v) was prepared by dissolving 5 mg of sodium azide in 1 mL of water. Ultrapure DMF (analytical reagent grade) was purchased from Fischer Chemical. Solutions of tris(2-carboxyethyl) phosphine hydrochloride (TCEP) 10 mM (2.87 g/mL) were prepared in borate buffer. pH 8.5 phosphate buffer was prepared by dissolving 3.5 g of dipotassium hydrogen phosphate and 4.5 g of sodium chloride in 500 mL of water. pH was adjusted with diluted phosphoric acid. Ultrafiltration was carried out in vivaspin 500 polyethersulfone (PES) membrane concentrator with a molecular weight cut-off (MWCO) of 50 kDa or 100 kDa. Centrifugation was carried out on an Eppendorf mini spin operating at 12 000 rpm at room temperature. cetuximab is a chimeric IgG1 full length antibody directed against EGFR overexpresses in SKBr3 cells. The antibody was obtained from ERBITUX as 5 mg/mL solution (ERBITUX). Concentration of antibody was determined by UV-vis

absorbance ($\epsilon_{280} = 210,000 \text{ M}^{-1} \text{ cm}^{-1}$ for cetuximab mAb), adjusted to $33 \mu\text{M}$ (5.0 mg/mL) and stored as aliquots at 4°C .

4.2.6.2- Conjugation of cetuximab with biotin-NHS ester

The antibody-biotin conjugate was prepared through a modification of a reported protocol^[365]. cetuximab ($32 \mu\text{M}$, $500 \mu\text{L}$) was prepared in the sodium carbonate buffer pH 8.4. Next, biotin-NHS ester was prepared in DMSO (100 mM , $5 \mu\text{L}$) and added to the cetuximab. The reaction was incubated at r.t. overnight, rotating at 240 rpm . Afterwards, excess reagent was removed by ultrafiltration (50 kDa MWCO) with PBS to afford the modified antibody-biotin in PBS. Afterward, sodium azide 0.5% (w/v) was added to make the final concentration of 0.05% (w/v) for conservation; this agent was removed by ultrafiltration (50 kDa) before each use.

4.2.6.3- Conjugation of cetuximab-biotin with streptavidin-Cy5

Firstly, absorbance of Cy5-streptavidin ($17 \mu\text{M}$, $35 \mu\text{L}$, 0.60 nmol) in PBS buffer (1 mL) was tested. Then, the cetuximab-biotin ($33 \mu\text{M}$, $3 \mu\text{L}$, 0.010 nmol) in PBS buffer (20 mM , pH 7.4) was added Cy5-streptavidin ($17 \mu\text{M}$, $35 \mu\text{L}$, 0.60 nmol) in PBS buffer (1 mL). The reaction was incubated at 24°C in a shaker 450 rpm for 2 h . Afterwards, excess reagent was removed by ultrafiltration (100 kDa MWCO) with PBS. Absorbance was measured before and after the process of ultrafiltration.

4.2.6.4- Determination of fluorophore to antibody ratio (FAR)

UV-vis spectra measurements were recorded on a Cary 4000 Scan UV-visible spectrophotometer (Varian) operating at room temperature. Sample buffer was used as blank for baseline correction. Calculation of Cy5, antibody ratio (FAR) follows the formula presented below with $\epsilon_{\text{cetuximab}} = 210,000 \text{ M}^{-1} \cdot \text{cm}^{-1}$ for cetuximab, $\epsilon_{653} = 250,000 \text{ M}^{-1} \cdot \text{cm}^{-1}$ for Cyanine-5 and 0.03 as a correction factor (cf₂₈₀) of the dye absorption at 280 nm . According to the absorbance spectra of Cy5-streptavidin, $\text{Abs}_{657} = 0.57$, $\text{Abs}_{280} = 0.34$. Based on the equation $\text{Abs}_{657} = n \cdot c_{\text{strep}} \cdot \epsilon_{\text{Cy5}}$ number of Cy5 per streptavidin was calculated as 3.9 . The absorbance of streptavidin at 280 nm was corrected to 0.32 using the equation $\text{Abs}_{280\text{strep}} = \text{Abs}_{280} - \text{Abs}_{657} \cdot \text{cf}_{280}$. According to the equation $\text{Abs}_{280\text{strep}} = c_{\text{strep}} \cdot \epsilon_{\text{strep}}$, the extinction coefficient of streptavidin (ϵ_{strep}) was calculated as $550,000 \text{ M}^{-1} \cdot \text{cm}^{-1}$. After filtration, according to the equation $\text{Abs}_{657} = 3.9 \cdot c_{\text{strep}} \cdot \epsilon_{\text{Cy5}}$, the concentration of streptavidin

was calculated to be 238 nM. Then, according to the equation of $Ab_{s280strep} + Ab_{s280cetuximab} = Ab_{s280} - Ab_{s657} * cf_{280}$, $Ab_{s280strep} = c_{strep} * \epsilon_{strep}$ and $Ab_{s280Cetuximab} = c_{strep} * \epsilon_{cetuximab}$. The concentration of cetuximab was calculated as 92.1 nM, slightly decreased from the original 100 nM, this is probably due to slight precipitation during the ultrafiltration process. $FAR = c_{strep} / c_{cetuximab} = 2.8$.

4.2.6.5- Biotin NEs immobilization protocol

8 well LabTek® chambers were washed 3 times with PBS and incubated with 200 µL BSA-Biotin (0.5 mg/mL) for 5 min. Then, BSA-Biotin was removed, the chambers were washed 3 times with PBS and replaced by 200 µL of 30000, 100000 and 300000 times diluted Biotin-NEs and neutralized (control) NEs (300 nM). Then, the NEs were incubated in darkness under room temperature for 30 min. For biotin block group, 200 µL of biotin (0.5 mg/mL) were added and incubated for 30 min and washed with PBS 3 times before adding 200 µL of Biotin-NEs and further incubated for 30 min. All samples were washed with Milli-Q water 2 times with PBS before final measurement.

4.2.6.6- Electrophoresis

The electrophoresis was performed on 0.5% agarose gel in trisacetate EDTA (TAE). 12 µL of each solution was added into the wells and subjected to electrophoresis for 30 -60 min at 125 V in darkness. The gels were analyzed with a gel imager (LAS 4000) using two different channels. Cy5-Streptavidin was monitored by excitation at 630 nm and with an emission filter at 670 nm, FWHM 10 nm. DiI-TPB loaded NEs were monitored by excitation at 540 nm and using a bandpass emission filter at 570 nm. The exposure time for each picture was set at 10 sec. The images were processed and analyzed by using ImageJ software.

4.2.6.6- Identification of biotinylated NEs conjugation with Cy5-streptavidin To perform gel electrophoresis, the following solutions were prepared: (1) Cy5-streptavidin (9 µM); (2) Biotinylated-NEs (max biotin concentration of 8 µM) + Cy5-streptavidin (9 µM); (3) Control NEs (750 times diluted) + Cy5-streptavidin (9 µM); (4) biotinylated-NEs (maximum biotin concentration of 8 mM) + free biotin (200 mM)+Cy5-Streptavidin (9 µM); (5) Biotinylated-NEs (750 times diluted, max biotin concentration of 8 µM); (6) Control NEs (NPC-Chol containing NEs neutralized by ethanolamine, 750 times diluted); and (7) biotinylated-NEs (maximum biotin concentration of 8 mM) + free biotin (200 mM) .

4.2.6.7- Evaluation of size exclusion for the purification of functional NEs

Conjugation of biotinylated-NEs loaded by DiI-TPB (1%) with Cy5-streptavidin (5 eq by volume, 17 μ M) was conducted in room temperature for 5 h. In the control NEs, biotinylated-NEs were substituted by the same volume of neutralized and dialyzed NEs (loaded with 1 wt.% DiI-TPB and 3 mg NPC-Chol, neutralized by excess of ethanolamine and dialyzed with membrane cut off size of 14 KDa). The two samples were subjected to size exclusion chromatography (see above), then, several fractions were checked by fluorescence spectroscopy (at Cy3 channel and Cy5 channel, respectively) and gel electrophoresis. For Cy3 channel, excitation was conducted under wavelength of 520 nm, emission was collected in the wavelength range of 550-750 nm, while for Cy5 channel, excitation was conducted under wavelength of 620 nm, emission was collected in the wavelength range of 650-750 nm.

4.2.7- Cell experiments

4.2.7.1- General protocol for cell culture

HeLa cells (ATCC) or SKBr3 cells(ATCC HTB-30) were grown in Dulbecco's modified Eagle's medium supplemented with 10% fetal calf serum (FCS), 1% antibiotic solution (penicillin streptomycin, Gibco-Invitrogen) and 1% L-glutamine (GIBCO BRL, Life Technologies) at 37°C in a humidified atmosphere containing 5% CO₂. Cells plated on a 75 cm² flask at a density of 10⁶ cells/flask were harvested at 80 % confluence with trypsin-EDTA (Sigma).

4.2.7.2- Cell experiments for chapter 2.1

4.2.7.2.1- Cell imaging

Hela cells (ATCC) were seeded on 12 mm coverslips at 30,000 cell per well in DMEM medium with penicillin (100 U/mL), 1% glycan (100 U/mL) and 10 % FBS overnight. The pH of PBS was adjusted with 1 M acetic acid and 1 M disodium phosphate to 5 and 7.4, respectively. Solution of F888/Lipo-NRK NEs (10 mM each in labrafacWL[®]) or Cy5/Lipo-Dox NEs (sample from *in situ* reaction) pre-diluted 100-times in milliQ water (100 μ L) was added to PBS of a given pH to a final volume of 1 mL, corresponding to 1000-times total dilution of NEs. The cells were washed 3 times

with PBS and then the medium was replaced with a diluted solution of NEs at corresponding pH. Control NEs, containing F888/NRK or DiD/Dox, were also used in PBS medium at pH 7.4 and pH 5 to check the release of free NRK and Dox in cells. Cell imaging were conducted at two different time points: 1 min and 30 min. For both time points, the samples were imaged after washing with PBS. All cellular imaging studies were done using epi-fluorescence mode with a Nikon Ti-E inverted microscope, equipped with CFI Plan Apo $\times 60$ oil (numerical aperture = 1.4) objective, and a Hamamatsu Orca Flash 4 sCMOS camera. For Lipo-NRK and NRK imaging, the excitation wavelength was 550 nm, and emission was detected through 600/50 nm filter. For Lipo-Dox and Dox imaging, the excitation wavelength was 470 nm, and emission was detected through 531/40 nm filter. In the colocalization studies, F888 was detected using 390 nm excitation and 470 nm detection filter, whereas DiD was detected using 640 nm excitation and 705/80 nm detection filter. The *in situ* extraction of molecules from cells was done as follows. Briefly, cells were first incubated with 15 μ M of Dox or 1 μ M of NRK (concentration determined by the absorption spectrum) for 30 minutes in the cell culture medium. Afterwards, cells were washed with PBS once, the fluorescence images were checked to ensure all the groups of cells were stained with similar amount of Dox and NRK (data not shown). Then, the medium was changed to 100-times diluted LipoHD NEs (above mentioned) in PBS medium. Control group was treated with empty NEs (the same dilution) in PBS, and the PBS buffer without NEs was used as blank control. Images were acquired immediately after the changing of medium defined as time point 1 min (<1 min) and after 1 hour for Dox and NRK *in situ* uptake study. After imaging, mean intensity from each cell for NRK and Dox channels was analyzed excluding nucleus (the center black part of each cells). The obtained values are the mean fluorescence intensity from ~ 15 cells. To study the extraction media, HeLa cells were first stained with 1 μ M of NRK for 30 min, washed with PBS and then treated with different extraction media (1 mL): 100-fold diluted LipoHD NCs, blank NCs or PBS. The extraction media were collected after 1, 5, 15, 30 and 60 min of incubation with HeLa cells to examine the emission spectrum (each condition was

done in triplicate). For PBS group, 100-times diluted LipoHD NCs were added to the extraction solution to ensure the comparable measuring condition for NRK. To quantify NRK concentration in the extraction media, the calibration curve of peak fluorescence intensity vs NRK concentration was built after measuring fluorescence spectra of LipoHD NCs (100-fold dilution) with increasing concentration of NRK. For estimating the total amount of NRK accumulated in HeLa cells, the

emission spectra of the 1 μ M of NRK (1 mL), used for cell staining, was measured before and after cell staining in the presence of 100-times diluted LipoHD NCs. To provide chemical identification of Lipo-NRK conjugates in the extract, NRK-stained HeLa cells were treated with the LipoHD NCs for 60 min. Then, the medium was collected and the extraction by dichloromethane was performed. The presence of Lipo-NRK in the extract studied by TLC (Dichloromethane:MeOH = 95:5) using as references pure Lipo-NRK and a the in-situ reaction mixture of NRK with LipoHD NCs extracted by dichloromethane (see above the protocol for the in-situ reaction). Finally, the Lipo-NRK from the same dichloromethane extract (cell medium with LipoHD NCs) was also identified by mass spectrometry.

4.2.7.2.2- Cytotoxicity study

Cytotoxicity of empty NEs, LipoHD loaded NEs, free doxorubicin and NEs loaded Lipo-Dox (Dox-LipoHD) were compared on 4 cancer cell lines (D2A1, 4T1, Hela and MDA-MB-231). The MTS cytotoxicity assay was used, which is based on the reduction of the MTS tetrazolium compound by viable mammalian cells to generate a colored formazan dye. The formazan dye is quantified by measuring the absorbance at 490-500 nm. Briefly, tumor cells (D2A1, 4T1, MDA-MB-231 or Hela cells) were seeded at 5000 cell per well in a 96 wells plate. After 24h, the medium was removed and replaced by drug-containing (Lipo-Dox NPCs or Dox alone) medium (DMEM). To study time-dependent effect, HeLa cells were incubated for 12, 24 and 48 hours. For other three cell lines, incubation was done for 48 hours. After incubation, the medium was removed and replaced with MTS containing medium (0.5 mg/mL). 6 After 4h of incubation, absorbance was read at 490-500 nm. The values of absorbance corresponding to cell viability was normalized to 100% of the non-treated control cells.

4.2.7.3- Cell experiments for chapter 2.2

4.2.7.3.1- pH dependent release from PA-LipoAmine NEs

Hela cells (ATCC[®] CCL-2) were seeded on 35 mm ibidi dish (40000/dish) with glass bottom and coverslips in DMEM medium with penicillin (100 U/mL), 1% glycan (100 U/mL) and 10 % FBS at 37 °C in a humidified atmosphere containing 5% CO₂ overnight. The cells were washed 3 times with PBS and then the medium was changed to 50 times diluted solution of PA-LipoAmine NEs

(containing 300 nM PA-LipoAmine) of pH 6 and 7.4. Control group containing 300 nM PA in pH 7.4 and pH 6 PBS medium was also prepared to test the release of free PA in cells. Cell imaging were acquired after washing at 1 min and 30 min.

4.2.7.3.2- Cellular in situ uptake of PA by LipoAmine NPs

The *in situ* extraction of PA from cells was done as following. Cells were first incubated with 600 nM of PA for 30 min in Opti-Mem. Afterwards, cells were washed with PBS, fluorescence images were checked to ensure all the groups of cells were stained with similar amount of PA (before application of NEs). Then, the medium was changed to 200-times diluted LipoAmine NEs in PBS medium. Control group was treated with 200-times diluted empty NEs in PBS, finally, PBS buffer without NEs was used as blank control. Video was acquired immediately after the changing of medium by taking 30 frames over 30 min for PA *in situ* uptake study. Images avoiding the video recording area were also taken to compare PA fluorescence intensity from cells. After imaging, mean intensity from each cell for PA channel was analyzed excluding nucleus (the center black part of each cells). The obtained values are the mean fluorescence intensity from 15 cells. For PA imaging, the excitation wavelength was 470 nm, and emission was detected through 531/40 nm filter.

To study the extraction media, the extraction media were collected to examine the emission spectrum (in triplicates). For PBS group, 200-times diluted empty NEs were added to the extraction solution to ensure the comparable measurement condition for PA. To quantify PA or PA-LipoAmine concentration in the extraction media, the calibration curve based on peak fluorescence intensity of PA or PA-LipoAmine in solutions of a gradient dilution of PA or PA-LipoAmine (15 μ M) NEs. For estimating the total amount of PA accumulated in HeLa cells, the emission spectra of PA staining solution were measured before and after cell staining in the presence of 200-times diluted NEs. Excitation wavelength were set at 420 nm and 380 nm for efficient PA or PA-LipoAmine excitation, respectively.

4.2.7.3.3- Cytotoxicity assay

In order to test the capability of LipoAmine loaded NEs to uptake toxic compounds in or exposed to cells, 4-hydroxynonenal, a toxic compound with great biological importance with reactive

aldehyde group was chosen for the potential of the de-toxic ability of this functional NEs by uptaking this toxic compound. WST-1 assay was used to test cell viability in this experiment. Briefly, 96-well plate and 6-well plate was seeded with Hela cells (5000 cells/well and 30000 cells/well, respectively) overnight, washed by PBS twice before changing to PBS containing testing samples. The toxicity of 4-hydroxynonenal was tested under different concentration of 4-Hydroxynonenal (0, 2, 5, 10, 20, 40 μM) in PBS. Afterward, 20 μM 4-hydroxynonenal were used for the testing of de-toxicity potential of LipoAmine containing NEs or empty NEs (as control) at different concentrations (0-10%). The toxicity of NEs (empty or with LipoAmine) were also tested in PBS. After adding PBS containing testing samples, cells were incubated for 4 hours, before being washed with PBS twice and changed the medium to WST-1 containing cell culture medium (5 μL /200 μL for 96-well plate and 25 μL /1000 μL for 6-well plate). Then, the cells were incubated for 30 min. For 96 well plates, the absorbance at 440 nm were tested under a micro-plate reader, each condition had 6 replicates, vitality were calculated in according to UV absorbance data. Statistics analysis including the calculating of derivation and significance between two set of data were conducted using Origin.

4.2.7.4- Cell experiments for chapter 2.3

4.2.7.4.1- Specific targeting by NEs using sequential staining protocol

4000 cells per well of cells was later split on 8 well LabTek® with coverlid and incubated over 2 days for imaging experiments. The first experiment was conducted in the following order to observe the capability of Biotinylated-NEs to attach on cell surface with Neutravidin surface. Before the experiment, cell nucleus was stained with Hoechst 33342 (20 μM in Opti-Mem). For the experiment, firstly, cells were incubated with (or without for controls) biotinylated antibody (60 pM in Opti-Mem) for 30 min, then washed with PBS to remove excess of biotinylated antibody. After this, the medium was changed (or not for biotin NEs control) to Neutravidin (80 pM in Opti-Mem) and further incubated for 30 min and washed with PBS to remove excess Neutravidin. Finally, cells were incubated with 100 times diluted biotinylated NEs (with 1% of DiD TPB, maximum biotin concentration of 20 μM) and incubated on ice for 1 hour. Before imaging, cell membrane was stained with WGA (5 $\mu\text{g}/\text{mL}$) over 5 min.

4.2.7.4.2- Specific targeting of antibody-NEs to SKBr 3 cells

4000 cells per well of cells was later split on 8 well LabTeK® with coverlid and incubated over 2 days for imaging experiments. After washing with PBS for 3 times, cells were directly incubated with purified NEs functionalized with cetuximab (1% DiD TPB, 100 μ L mixed with 100 μ L Opti-Mem, estimated with same concentration as before according to fluorescence from DiD), or Biotinylated NEs (1% DiD, 100 times diluted). The incubation was conducted on ice for 3 hours. Before imaging, cell membrane was stained with WGA-Alexa488 (5 μ g/mL) over 5 min.

4.2.7.5- Cell experiment (for chapter 2.4)

4.2.7.5.1- Cell imaging

Hela cells (ATCC) were then seeded on 36 mm ibidi® coverslips at 30,000 cell per well in this DMEM medium with overnight. The DMEM medium was firstly removed and the cells were washed with PBS for three times. Then, medium was changed to Opti-MEM containing or not (in case of control) 100 μ M of targeting hydrazide compounds: LD-HZ for lipid droplets, PM-HZ for plasma membrane or Mito-HZ for mitochondria. The cells were incubated at 37 °C in a humidified atmosphere containing 5% CO₂ for 30 min. Then, after washing the cells gently once with PBS, the medium was changed to Opti-MEM containing 1 μ M NRK (except 2.5 μ M for mitochondria) and further incubated for 30 min at room temperature followed by fluorescence imaging. In the case of protocol without washing out the targeting molecule, the cells were seeded into labtek (8 well chambered coverslips) at 4000 cells per well in this DMEM medium and left overnight. The DMEM medium was then removed and the cells were washed with PBS for three times. The Opti-MEM medium (200 μ L) containing certain concentration (1, 5, 20, 100 μ M) of HZ-PM was added to HeLa cells. The cells were incubated for 10 min at r.t. followed by addition of NRK (1 μ M) and further incubation for 30 min before imaging.

For all co-localization experiments, the cells were seeded into LabTek (8 well chambered coverslips) at 4000 cells per well in the DMEM medium and left overnight. The DMEM medium was then removed and the cells were washed with PBS for three times. Cells were pre-incubated with Opti-MEM medium (200 μ L) containing or not (in cases of control) 20 μ M corresponding targeting moieties of PM-HZ, LD-HZ or Mito-HZ for 10 min at 37 °C followed by addition of

NRK or doxorubicin at 1 μ M concentration and further incubated for 30 min. In case of co-localization in plasma membranes, F2N12SM (400 nM) was added after the cells were treated with Mito-HZ and NRK/doxorubicin and incubated for 15 min before imaging. For LDs labeling, LDs marker SMCy5.5 (1 μ M) was added to the cells, incubated for 3h at 37 °C before adding targeting hydrazine LD-HZ and NRK/doxorubicin. For mitochondria labeling, MitoTracker Deep Red FM 644/665 (200 nM) was added after the cells were treated with Mito-HZ and NRK/doxorubicin and further incubated for 5 min at 37 °C. Finally, the corresponding medium was changed to Opti-MEM followed by fluorescence imaging. In cases of nucleus staining, Hoechst 33342 (10 μ g/mL) in Opti-MEM was used to stain cell nucleus over 1 h and washed with PBS once before all the processes.

For reversibility analysis of reaction of NRK with PM-HZ at plasma membrane interface, the cells in LabTek® were pre-incubated with Opti-MEM medium (200 μ L) containing or not (in cases of control) 20 μ M PM-HZ for 10 min at 37 °C followed by addition of NRK or doxorubicin at 1 μ M concentration and further incubated for 30 min. For washing group, the cells were washed with PBS over 3 times and changed the medium to Opti-Mem. For long incubation group, after washing with PBS, cell medium was changed to Opti-MEM medium (200 μ L) and further incubated over 1 h. F2N12SM (400 nM) was used as membrane co-localization probe, cells were incubated with this probe over 5 min before imaging for each groups.

Fluorescence imaging of NRK was done with the excitation wavelength at 488 nm, and fluorescence emission was collected at two different spectral channels: 550-600 nm and 600-670 nm. In the colocalization measurements with LDs marker SMCy5.5, for NRK channel, excitation wavelength was set at 488 nm and emission wavelength was collected in the range of 550-600 nm. For doxorubicin channel, the excitation wavelength was at 488 nm and fluorescence emission was collected in range of 520-650 nm (images of for membrane and mitochondria targeting were collected over average of 20 frames for this channel due to low brightness of doxorubicin). For the SMCy5.5 and MitoTracker Deep Red FM 644/665 channel, the excitation wavelength was set at 635 nm and the emission wavelength was collected in the range of 650-800 nm.

Colocalization analysis was conducted in two ways. The first way was by calculating Pearson's and Mander's correlation coefficients. This was conducted by using an ImageJ plugin named "Just

Another Colocalisation Plugin (JACoP)". A certain threshold for both Green and Red channels was applied to select the ROI area for the calculation of Pearson's and Mander's correlation coefficients. The second way was to calculate the ratio of the mean fluorescence intensity from organelle areas versus the whole cells. The organelle areas were selected by using fluorescence image of corresponding reference markers, F2N12SM for plasma membrane, SMCy5.5 for lipid droplet or Mito Tracker Deep Red FM for mitochondria. Cell selection and calculation of the mean fluorescence intensity were done using ImageJ.

4.2.7.5.2- Phototoxicity study

Hela cells (ATCC) were then seeded on 36 mm coverslips at 30,000 cell per well in this DMEM medium with overnight. The DMEM medium were first removed and washed with PBS for three times before changing the medium to Opti-MEM (as control) or Opti-MEM containing PM-Hz, Mito-HZ or LD-HZ (100 μ M), then the cells were incubated at 37 °C in a humidified atmosphere containing 5% CO₂ for 30 min. After that the cell were washed with PBS and the medium was changed to Opti-MEM containing 1 μ M of NRK, followed by an incubation for 30 min at r. t. To understand PDT effect when NRK is targeted to different cell organelles, we used CellTox™ Green, a nucleus maker for monitoring cell death induced by membrane disruption. After targeting NRK to cell organelles with corresponding ligands, the dishes with cells were washed once with PBS and subjected to illumination with excitation of 550 nm (50% LED source power) continuously over 1 min followed by changing the medium to 1 mL CellTox™ Green assay containing 12 μ g/mL Hoechst nucleus staining agent and incubated for 30 min. The transmission and fluorescence (CellTox™ Green channel) images were taken before and after illumination using 20x air objective Nikon CFI Plan Apo, NA = 0.75 (for data in Figure 3) or 10x air objective Nikon Plan Fluor NA = 0.3 (for data in Figure S5); excitation: 470 nm, emission filter: 531/40 nm for CellTox™ Green channel and excitation: 405 nm, emission filter: 475/50 nm for Hoechst 33342 channel. To observe the cell morphology change induced by phototoxicity, cell images (both bright field and epi-fluorescence channel (4% power, 300 ms integration period) with excitation of 550 nm and filter of 600/50 nm) were firstly taken before the application of high source power. Then video was prepared by taking images of the bright field transmission channel and epi-fluorescence channel (source power: 30% for lipid droplets, plasma membrane and their controls; 50 % for mitochondria and its control) and short integration period (30 ms) continuously

for 30 slices over 10 min. After the video recording, images were taken in DIC channel (300 ms) and epi channel (4% power, 300 ms integration period). This cellular imaging studies were done using epi-fluorescence mode with a Nikon Ti-E inverted microscope, equipped with CFI Plan Apo $\times 60$ oil (numerical aperture = 1.4) objective, and a Hamamatsu Orca Flash 4 sCMOS camera.

4.2.8- Experiment with adipose tissue from chicken skin

4.2.8.1- General protocol for preparing chicken skin

A serial of specially cut chicken skin circles (5 mm or 3 cm diameter) was washed with ethanol for 3 times to remove oil on the surface, followed by washing 3 times with water to remove ethanol.

4.2.8.2- Adipose tissue from chicken skin experiment (for chapter 2.1)

Chicken skin was immersed into aqueous solutions of 5 μM NRK or 45 μM Dox for 10 min. Then, the chicken skin tissue was washed with PBS once. The wet skin then was evenly spread in wells of a Lab-Tek[®] chamber, and the fluorescence images were acquired. Then, the medium was changed to 100-times diluted LipoHD NEs in PBS medium (300 μL). Control group was treated with blank NEs (300 μL , the same dilution) in PBS, and the PBS buffer (300 μL) without NEs was used as a control. Fluorescence images were acquired immediately after changing the medium, defined as time point 1 min (<1 min). Then the skins with the buffers were removed into a 1.5 mL Eppendorf[®] tube and shaken for 30 min at speed of 600 r/min on a ThermoMixer at RT. Later on, skins were again flatly spread on the Lab-Tek[®] wells for the fluorescence microscopy measurements. Fluorescence imaging was done by the Nikon microscope (see above) using Nikon 20x air objective (Nikon CFI Plan Apo, NA = 0.75). For Dox and NRK imaging, the excitation wavelength was 550 nm, and emission was detected through 600/50 nm filter. After the imaging, mean intensity for NRK and Dox channels was analyzed by selecting the center area (same size) of each images (3 images for each condition).

4.2.8.3- Adipose tissue from chicken skin experiment (for chapter 2.2)

The wet skin was then evenly spread on a 150 mm plastic plate with epidermis side on the top. Then our 3D printed funnel with diameter of 25 mm was pressed on the skin tissue and incubated

with 2 mL PA (3 μ M) for 30 min, then medium were removed and washed with PBS, then image was taken under UV lamp (excitation 254 nm), followed by taking fluorescence images of the epidermis side. Then, a funnel with diameter of 15 mm was pressed on the central PA-stained area on epidermis side, then, the device was loaded with 100-times diluted LipoAmine NEs in PBS medium (2 mL). Control group was treated with empty NEs (2 mL, the same dilution) in PBS, and only PBS buffer (2 mL) as empty control. After 6 hours, solutions were removed, image was taken under UV lamp (excitation 254 nm), fluorescence images (epidermis side) were acquired immediately. Extracted medium was also imaged under UV lamp (excitation 365 nm). Fluorescence imaging was done by the Nikon microscope (see above) using Nikon 10x air objective (Nikon CFI Plan Apo, NA = 0.75). For PA imaging, the excitation wavelength was 470 nm, and emission was detected through 531/40 nm filter. After the imaging, mean intensity for PA channels was analyzed of each image (3 images for each condition).

4.2.9- *In vivo* mice experiments (for chapter 2.1)

All mice were housed and handled according to the guidelines of INSERM and the ethical committee of Alsace, France (CREMEAS), under the APAFIS agreement number 12780-2017122016498879. For all experiments, 8 weeks-old female Rj:NMRI Foxn1 nu/nu mice were purchased from Janvier Labs. 2 millions of D2A1 or MDA-MB-231 stably expressing Luciferase cells were diluted in 50 μ L of PBS and injected subcutaneously in the back of 8-week-old female Rj:NMRI Foxn1nu/nu mice. When tumors reached a tumor volume of \pm 0.5 cm³ (measured with a caliper using the following formula (width² \times length)/2 (mm³)), mice were randomized in 4 groups of 8 mice and subjected to the 4 different treatments: PBS, Doxorubicin, LipoHD NEs or Lipo-Dox NEs (prepared *in situ* as described above by incubating LipoHD NEs with Dox at pH 4, followed by dialysis of the reaction mixture to remove excess of Dox). Final Dox loading in this formulation was 0.7 % with respect to oil. Before the injection, the nanoemulsion was diluted twice in PBS. Mice received the treatments by *i.v.* injection through the retro-orbital sinus, 2 times per weeks (alternating eyes at each round) of 100 μ L corresponding solution. For free Dox and Lipo-Dox formulations, the single injection dose of Dox was the same (51 μ g corresponding to \sim 2.5 mg/kg). Tumor growth was tracked two times/week either by caliper measurement (D2A1) or by *in vivo* bioluminescence imaging (MDA-MB-231). For bioluminescence imaging, mice were anesthetized with isoflurane and subjected to *i.v.* injection

of 166 $\mu\text{g/g}$ of a luciferin solution (Perkin Elmer). Imaging was done 5 min upon injection on a IVIS Illumina LT (Perkin Elmer). Photon counts(photon/second/ cm^2/sr) were analyzed using Living Image software 4.5 (Perkin Elmer).

References

- [1] H. Maeda, H. Nakamura, J. Fang, *Adv. Drug Deliv. Rev.* **2013**, *65*, 71.
- [2] S. D. Perrault, W. C. W. Chan, *Proc. Natl. Acad. Sci. U. S. A.* **2010**, *107*, 11194.
- [3] J. Fang, T. Akaike, H. Maeda, *Apoptosis* **2004**, *9*, 27.
- [4] Y. Matsumura, H. Maeda, *Cancer Res.* **1986**, *46*, 6387.
- [5] K. N. Sugahara, T. Teesalu, P. P. Karmali, V. R. Kotamraju, L. Agemy, O. M. Girard, D. Hanahan, R. F. Mattrey, E. Ruoslahti, *Cancer Cell* **2009**, *16*, 510.
- [6] L. D. Leserman, J. Barbet, F. Kourilsky, J. N. Weinstein, *Nature* **1980**, *288*, 602.
- [7] G. Prévot, M. Duonor-Cérutti, M. Larivière, J. Laroche-Traineau, M. J. Jacobin-Valat, P. Barthélémy, G. Clofent-Sanchez, S. Crauste-Manciet, *Data Br.* **2017**, *15*, 824.
- [8] N. Kamaly, Z. Xiao, P. M. Valencia, A. F. Radovic-Moreno, O. C. Farokhzad, *Chem. Soc. Rev.* **2012**, *41*, 2971.
- [9] X. Wang, S. Li, Y. Shi, X. Chuan, J. Li, T. Zhong, H. Zhang, W. Dai, B. He, Q. Zhang, *J. Control. Release* **2014**, *193*, 139.
- [10] A. Loureiro, E. Nogueira, N. G. Azoia, M. P. Sárria, A. S. Abreu, U. Shimanovich, A. Rollett, J. Härmark, H. Hebert, G. Guebitz, et al., *Colloids Surfaces B Biointerfaces* **2015**, *135*, 90.
- [11] I. K. Park, Y. J. Kim, K. M. Huh, Y. K. Lee, *Funct. Sens. Mater.* **2010**, *93–94*, 324.
- [12] S. J. Yang, J. W. Chen, F. H. Lin, T. H. Young, P. J. Lou, M. J. Shieh, *Biomed. Eng. BASIS Commun.* **2010**, *22*, 9.
- [13] R. I. El-Gogary, N. Rubio, J. T.-W. Wang, W. T. Al-Jamal, M. Bourgognon, H. Kafa, M. Naeem, R. Klippstein, V. Abbate, F. Leroux, et al., *ACS Nano* **2014**, *8*, 1384.
- [14] A. Karageorgis, S. Dufort, L. Sancey, M. Henry, S. Hirsjarvi, C. Passirani, J. P. Benoit, J. Gravier, I. Texier, O. Montigon, et al., *Sci. Rep.* **2016**, *6*, 1.
- [15] S. Christian, J. Pilch, M. E. Akerman, K. Porkka, P. Laakkonen, E. Ruoslahti, *J. Cell Biol.* **2003**, *163*, 871.
- [16] R. Pasqualini, E. Koivunen, R. Kain, J. Lahdenranta, M. Sakamoto, A. Stryhn, R. A. Ashmun, L. H. Shapiro, W. Arap, E. Ruoslahti, *Cancer Res.* **2000**, *60*, 722.
- [17] W. Arap, R. Pasqualini, E. Ruoslahti, *Science* **1998**, *279*, 377.
- [18] L. Wei, X.-Y. Guo, T. Yang, M.-Z. Yu, D.-W. Chen, J.-C. Wang, *Int. J. Pharm.* **2016**, *510*, 394.
- [19] J. M. Kagan, A. M. Sanchez, A. Landay, T. N. Denny, *For. Immunopathol. Dis. Therap.* **2015**, *6*, 57.
- [20] A. M. Sochaj, K. W. Swiderska, J. Otlewski, *Biotechnol. Adv.* **2015**, *33*, 775.
- [21] Y. J. Cao, C. F. Yu, K. L. Wu, X. C. Wang, D. Liu, Z. R. Tian, L. J. Zhao, X. X. Qi, A. Loredó, A. N. Chung, et al., *Theranostics* **2021**, *11*, 9107.
- [22] J. Hamzehalipour Almaki, R. Nasiri, A. Idris, M. Nasiri, F. A. Abdul Majid, D. Losic, *J. Mater. Chem. B* **2017**, *5*, 7369.
- [23] B. Dorjsuren, B. Chaurasiya, Z. Ye, Y. Liu, W. Li, C. Wang, D. Shi, C. E. Evans, T. J. Webster, Y. Shen,

- Int. J. Nanomedicine* **2020**, *15*, 8201.
- [24] X. Lin, A. O'Reilly Beringhs, X. Lu, *AAPS J.* **2021**, *23*, 43.
 - [25] P. Zhang, L. Hu, Q. Yin, Z. Zhang, L. Feng, Y. Li, *J. Control. Release* **2012**, *159*, 429.
 - [26] H. He, Y. Li, X.-R. Jia, J. Du, X. Ying, W.-L. Lu, J.-N. Lou, Y. Wei, *Biomaterials* **2011**, *32*, 478.
 - [27] Y. Li, H. He, X. Jia, W.-L. Lu, J. Lou, Y. Wei, *Biomaterials* **2012**, *33*, 3899.
 - [28] M. Marcinkowska, E. Sobierajska, M. Stanczyk, A. Janaszewska, A. Chworos, B. Klajnert-Maculewicz, *Polymers (Basel)*. **2018**, *10*, 1.
 - [29] M. F. Attia, N. Anton, J. Wallyn, Z. Omran, T. F. Vandamme, *J. Pharm. Pharmacol.* **2019**, *71*, 1185.
 - [30] H. Zhu, J. Fan, J. Du, X. Peng, *Acc. Chem. Res.* **2016**, *49*, 2115.
 - [31] N. M. Sakhrani, H. Padh, *Drug Des. Devel. Ther.* **2013**, *7*, 585.
 - [32] S. Biswas, V. P. Torchilin, *Adv. Drug Deliv. Rev.* **2014**, *66*, 26.
 - [33] D. I. Danylchuk, S. Moon, K. Xu, A. S. Klymchenko, *Angew. Chemie Int. Ed.* **2019**, *58*, 14920.
 - [34] D. I. Danylchuk, P. H. Jouard, A. S. Klymchenko, *J. Am. Chem. Soc.* **2021**, *143*, 912.
 - [35] L. B. Chen, *Annu. Rev. Cell Biol.* **1988**, *4*, 155.
 - [36] M. F. Ross, G. F. Kelso, F. H. Blaikie, A. M. James, H. M. Cocheme, A. Filipovska, T. D. Ros, T. R. Hurd, R. A. J. Smith, M. P. Murphy, *Biokhimiya* **2005**, *70*, 273.
 - [37] R. G. Kurumbail, A. M. Stevens, J. K. Gierse, J. J. McDonald, R. A. Stegeman, J. Y. Pak, D. Gildehaus, J. M. Miyashiro, T. D. Penning, K. Seibert, et al., *Nature* **1996**, *384*, 644.
 - [38] H. Zhang, J. Fan, J. Wang, S. Zhang, B. Dou, X. Peng, *J. Am. Chem. Soc.* **2013**, *135*, 11663.
 - [39] H. Wang, Z. He, Y. Yang, J. Zhang, W. Zhang, W. Zhang, P. Li, B. Tang, *Chem. Sci.* **2019**, *10*, 10876.
 - [40] S. Li, L. Huang, *Gene Ther.* **2000**, *7*, 31.
 - [41] H. Zhang, J. Fan, H. Dong, S. Zhang, W. Xu, J. Wang, P. Gao, X. Peng, *J. Mater. Chem. B* **2013**, *1*, 5450.
 - [42] A. Goujon, A. Colom, K. Straková, V. Mercier, D. Mahecic, S. Manley, N. Sakai, A. Roux, S. Matile, *J. Am. Chem. Soc.* **2019**, *141*, 3380.
 - [43] S. Ghosh, S. Nandi, C. Ghosh, K. Bhattacharyya, *ChemPhysChem* **2016**, *17*, 2818.
 - [44] N. Wagner, M. Stephan, D. Höglinger, A. Nadler, *Angew. Chemie Int. Ed.* **2018**, *57*, 13339.
 - [45] M. Collot, T. K. Fam, P. Ashokkumar, O. Faklaris, T. Galli, L. Danglot, A. S. Klymchenko, *J. Am. Chem. Soc.* **2018**, *140*, 5401.
 - [46] A. Kumari, S. K. Yadav, S. C. Yadav, *Colloids Surfaces B Biointerfaces* **2010**, *75*, 1.
 - [47] D. Arora, S. Jaglan, *Trends Food Sci. Technol.* **2016**, *54*, 114.
 - [48] A. Saneja, C. Nehate, N. Alam, P. N. Gupta, *undefined* **2016**, 229.
 - [49] Y.-L. Lo, K.-H. Sung, C.-C. Chiu, L.-F. Wang, *Mol. Pharm.* **2013**, *10*, 664.
 - [50] V. M. Platt, F. C. Szoka, *Mol. Pharm.* **2008**, *5*, 474.
 - [51] M. Talelli, M. Barz, C. J. F. Rijcken, F. Kiessling, W. E. Hennink, T. Lammers, *Nano Today* **2015**, *10*,

- 93.
- [52] C. Deng, Y. Jiang, R. Cheng, F. Meng, Z. Zhong, *Nano Today* **2012**, 7, 467.
- [53] S. C. Owen, D. P. Y. Chan, M. S. Shoichet, *Nano Today* **2012**, 7, 53.
- [54] K. Madaan, S. Kumar, N. Poonia, V. Lather, D. Pandita, *J. Pharm. Bioallied Sci.* **2014**, 6, 139.
- [55] B. Noriega-Luna, L. A. Godínez, F. J. Rodríguez, A. Rodríguez, G. Zaldívar-Lelo De Larrea, C. F. Sosa-Ferreyra, R. F. Mercado-Curiel, J. Manríquez, E. Bustos, *J. Nanomater.* **2014**, 2014, 507273.
- [56] J. D. K. Twibanire, T. B. Grindley, *Polymers (Basel)*. **2012**, 4, 794.
- [57] T. R. Hoare, D. S. Kohane, *Polymer (Guildf)*. **2008**, 49, 1993.
- [58] S. Ladet, L. David, A. Domard, *Nature* **2008**, 452, 76.
- [59] C. Luo, J. Sun, B. Sun, Z. He, *Trends Pharmacol. Sci.* **2014**, 35, 556.
- [60] X. Pang, X. Yang, G. Zhai, *Expert Opin. Drug Deliv.* **2014**, 11, 1075.
- [61] M. Chang, F. Zhang, T. Wei, T. Zuo, Y. Guan, G. Lin, W. Shao, *J. Drug Target.* **2016**, 24, 475.
- [62] B. Ozpolat, A. K. Sood, G. Lopez-Berestein, *Adv. Drug Deliv. Rev.* **2014**, 66, 110.
- [63] R. Tenchov, R. Bird, A. E. Curtze, Q. Zhou, *ACS Nano* **2021**, 15, 16982.
- [64] W. Mehnert, K. Mäder, *Adv. Drug Deliv. Rev.* **2001**, 47, 165.
- [65] S. Nasirizadeh, B. Malaekhe-Nikouei, *J. Drug Deliv. Sci. Technol.* **2020**, 55, 101458.
- [66] R. H. Müller, K. Mäder, S. Gohla, *Eur. J. Pharm. Biopharm.* **2000**, 50, 161.
- [67] R. V. Tikekar, N. Nitin, *Soft Matter* **2011**, 7, 8149.
- [68] S. M. Jafari, D. J. McClements, *Nanoemulsions : Formulation, Applications, and Characterization*, n.d.
- [69] N. Anton, T. F. Vandamme, *Pharm. Res.* **2011**, 28, 978.
- [70] Y. Singh, J. G. Meher, K. Raval, F. A. Khan, M. Chaurasia, N. K. Jain, M. K. Chourasia, *J. Control. Release* **2017**, 252, 28.
- [71] S. Akram, X. Wang, T. F. Vandamme, M. Collot, A. U. Rehman, N. Messaddeq, Y. Mély, N. Anton, *Langmuir* **2019**, 35, 2313.
- [72] T. Sheth, S. Seshadri, T. Prileszky, M. E. Helgeson, *Nat. Rev. Mater.* **2020**, 5, 214.
- [73] F. Perche, V. P. Torchilin, *J. Drug Deliv.* **2013**, 2013, 1.
- [74] L. Sercombe, T. Veerati, F. Moheimani, S. Y. Wu, A. K. Sood, S. Hua, *Front. Pharmacol.* **2015**, 6, 286.
- [75] I. D. Raut, R. C. Doijad, S. K. Mohite, *Int. J. Pharm. Sci. Res.* **2018**, 9, 862.
- [76] A. Saneja, D. R. Dubey, N. Alam, V. Khare, N. P. Gupta, *Curr. Cancer Drug Targets* **2014**, 14, 419.
- [77] S. Weber, A. Zimmer, J. Pardeike, *Eur. J. Pharm. Biopharm.* **2014**, 86, 7.
- [78] R. Chen, S. Wang, J. Zhang, M. Chen, Y. Wang, *Drug Deliv.* **2015**, 22, 666.
- [79] S. Kumar, A. Singhal, U. Narang, S. Mishra, P. Kumari, *Curr. Med. Chem.* **2020**, 27, 6015.
- [80] J. Fan, S. Wang, W. Sun, S. Guo, Y. Kang, J. Du, X. Peng, *AIChE J.* **2018**, 64, 835.

- [81] K. Khoshnevisan, M. Daneshpour, M. Barkhi, M. Gholami, H. Samadian, H. Maleki, *J. Drug Target.* **2018**, *26*, 525.
- [82] S. Bagheri, M. Yasemi, E. Safaie-Qamsari, J. Rashidiani, M. Abkar, M. Hassani, S. A. Mirhosseini, H. Kooshki, *Artif. Cells, Nanomedicine, Biotechnol.* **2018**, *46*, 462.
- [83] S. Thambiraj, S. Hema, D. R. Shankaran, *Mater. Today Proc.* **2018**, *5*, 16763.
- [84] M. Fuller, H. Whiley, I. Koper, *SN Appl. Sci.* **2020**, *2*, 1022.
- [85] I. Rajendran, H. Dhandapani, R. Anantanarayanan, R. Rajaram, *RSC Adv.* **2015**, *5*, 51055.
- [86] M. A. Sanzhakov, V. A. Kudinov, K. K. Baskaev, G. E. Morozovich, D. S. Stepanova, T. I. Torkhovskaya, Y. A. Tereshkina, E. I. Korotkevich, E. G. Tikhonova, *Biomed. Pharmacother.* **2021**, *142*, 111985.
- [87] R. M. Reilly, *J. Nucl. Med.* **2007**, *48*, 1039 LP.
- [88] A. Kiran, G. K. Kumari, P. T. Krishnamurthy, *J. Drug Deliv. Sci. Technol.* **2020**, *59*, 101892.
- [89] E. Pérez-Herrero, A. Fernández-Medarde, *Eur. J. Pharm. Biopharm.* **2015**, *93*, 52.
- [90] E. Kianfar, *J. Supercond. Nov. Magn.* **2021**, *34*, 1709.
- [91] P. Periyathambi, T. Hemalatha, *Mater. Lett.* **2021**, *294*, 129763.
- [92] I. Belyanina, O. Kolovskaya, S. Zamay, A. Gargaun, T. Zamay, A. Kichkailo, *Molecules* **2017**, *22*, 975.
- [93] J. G. Croissant, Y. Fatieiev, N. M. Khashab, *Adv. Mater.* **2017**, *29*, 1604634.
- [94] M. Manzano, M. Vallet-Regi, *Adv. Funct. Mater.* **2020**, *30*, 1902634.
- [95] T.-T. Le, A. K. Elzhry Elyafi, A. R. Mohammed, A. Al-Khattawi, *Pharmaceutics* **2019**, *11*, 269.
- [96] T. S. Anirudhan, A. S. Nair, *J. Mater. Chem. B* **2018**, *6*, 428.
- [97] R. N. S. Aresteanu, A. Borodetsky, H. Azhari, I. S. Weitz, *Nanotechnology* **2021**, *32*, 055705.
- [98] Z. Al-Ahmady, K. Kostarelos, *Chem. Rev.* **2016**, *116*, 3883.
- [99] Y. Bai, F.-Y. Xie, W. Tian, *Chinese J. Polym. Sci.* **2018**, *36*, 406.
- [100] Z. Zhang, D. Zhang, L. Wei, X. Wang, Y. Xu, H. W. Li, M. Ma, B. Chen, L. Xiao, *Colloids Surfaces B Biointerfaces* **2017**, *159*, 905.
- [101] Y. Guo, Y. Zhang, J. Ma, Q. Li, Y. Li, X. Zhou, D. Zhao, H. Song, Q. Chen, X. Zhu, *J. Control. Release* **2018**, *272*, 145.
- [102] A. Hervault, N. T. K. Thanh, *Nanoscale* **2014**, *6*, 11553.
- [103] R. Bouchaala, N. Anton, H. Anton, T. Vandamme, J. Vermot, D. Smail, Y. Mély, A. S. Klymchenko, *Colloids Surfaces B Biointerfaces* **2017**, *156*, 414.
- [104] M. Mathiyazhakan, C. Wiraja, C. Xu, *Nano-micro Lett.* **2018**, *10*, 10.
- [105] M. X. Hu, B. H. Zhu, H. F. Zhou, L. Qiao, J. M. Fan, Y. Q. Du, F. Chang, S. Y. Yu, *Inorg. Chem. Commun.* **2020**, *119*, 108093.
- [106] L. Xu, L. Qiu, Y. Sheng, Y. Sun, L. Deng, X. Li, M. Bradley, R. Zhang, *J. Mater. Chem. B* **2018**, *6*, 510.
- [107] G. Ma, W. Lin, Z. Yuan, J. Wu, H. Qian, L. Xu, S. Chen, *J. Mater. Chem. B* **2017**, *5*, 935.

- [108] R. Grillo, J. Gallo, D. G. Stroppa, E. Carbó-Argibay, R. Lima, L. F. Fraceto, M. Bañobre-López, *ACS Appl. Mater. Interfaces* **2016**, *8*, 25777.
- [109] S. Kondaveeti, A. T. S. Semeano, D. R. Cornejo, H. Ulrich, D. F. S. Petri, *Colloids Surfaces B Biointerfaces* **2018**, *167*, 415.
- [110] C. W. Chen, W. J. Syu, T. C. Huang, Y. C. Lee, J. K. Hsiao, K. Y. Huang, H. P. Yu, M. Y. Liao, P. S. Lai, *J. Mater. Chem. B* **2017**, *5*, 5774.
- [111] M. Gu, X. Wang, T. B. Toh, E. K.-H. Chow, *Drug Discov. Today* **2018**, *23*, 1043.
- [112] M. Chen, C. T. Jafvert, *Environ. Sci. Nano* **2018**, *5*, 1350.
- [113] Y. Nagasaki, T. Yaguchi, T. Matsumura, T. Yoshitomi, Y. Ikeda, A. Ueda, A. Hirayama, *Biomater. Sci.* **2014**, *2*, 522.
- [114] D. Stamopoulos, P. Bouziotis, D. Benaki, C. Kotsovassilis, P. N. Ziropiannis, *Nephrol. Dial. Transplant.* **2008**, *23*, 3234.
- [115] S. Wang, D. Wang, Y. Duan, Z. Zhou, W. Gao, L. Zhang, *Adv. Mater.* **2022**, *34*, DOI 10.1002/adma.202107719.
- [116] Y. Chen, Y. Zhang, J. Zhuang, J. H. Lee, L. Wang, R. H. Fang, W. Gao, L. Zhang, *ACS Nano* **2019**, *13*, 7209.
- [117] N. Anton, T. F. Vandamme, *Int. J. Pharm.* **2009**, *377*, 142.
- [118] D. J. McClements, *Soft Matter* **2012**, *8*, 1719.
- [119] M. Yao, H. Xiao, D. J. McClements, *Annu. Rev. Food Sci. Technol.* **2014**, *5*, 53.
- [120] M. Kumar, R. S. Bishnoi, A. K. Shukla, C. P. Jain, *Prev. Nutr. Food Sci.* **2019**, *24*, 225.
- [121] C. Lovelyn, A. A. Attama, *J. Biomater. Nanobiotechnol.* **2011**, *02*, 626.
- [122] K. Pathak, S. Pattnaik, K. Swain, in *Nanoemulsions Formul. Appl. Charact.*, Elsevier Inc., **2018**, pp. 415–433.
- [123] A. S. Klymchenko, E. Roger, N. Anton, H. Anton, I. Shulov, J. Vermot, Y. Mely, T. F. Vandamme, *RSC Adv.* **2012**, *2*, 11876.
- [124] X. Li, N. Anton, G. Zuber, *Adv. Drug Deliv. Rev.* **2014**, *76*, 116.
- [125] N. Anton, F. Hallouard, M. F. Attia, T. F. Vandamme, Springer, Cham, **2016**, pp. 273–300.
- [126] A. Prokop, V. Wissing, *Intracellular Delivery III Market Entry Barriers of Nanomedicines*, **2016**.
- [127] X. Li, N. Anton, G. Zuber, M. Zhao, N. Messaddeq, F. Hallouard, H. Fessi, T. F. Vandamme, *Biomaterials* **2013**, *34*, 481.
- [128] S. Martin, R. G. Parton, *Nat. Rev. Mol. Cell Biol.* **2006**, *7*, 373.
- [129] Y. Guo, K. R. Cordes, R. V Farese, T. C. Walther, *J. Cell Sci.* **2009**, *122*, 749.
- [130] D. Sobot, S. Mura, S. O. Yesylevskyy, L. Dalbin, F. Cayre, G. Bort, J. Mougin, Di. Desmaële, S. Lepetre-Mouelhi, G. Pieters, et al., *Nat. Commun.* **2017**, *8*, 15678.
- [131] K. K. Ng, J. F. Lovell, G. Zheng, *Acc. Chem. Res.* **2011**, *44*, 1105.
- [132] Y.-Z. Du, S.-N. Li, Y.-L. Feng, D.-L. Yu, F.-Q. Hu, H. Yuan, S. He, S. P. Jiang, X.-Y. Lu, *Int. J. Nanomedicine* **2013**, *8*, 3141.

- [133] S. Anuchapreeda, Y. Fukumori, S. Okonogi, H. Ichikawa, *J. Nanotechnol.* **2012**, 2012, 1.
- [134] Y. Y. Hwang, K. Ramalingam, D. R. Bienek, V. Lee, T. You, R. Alvarez, *Antimicrob. Agents Chemother.* **2013**, 57, 3568.
- [135] V. Ghosh, A. Mukherjee, N. Chandrasekaran, *Colloids Surfaces B Biointerfaces* **2014**, 114, 392.
- [136] K. A. Abd-Elsalam, A. R. Khokhlov, *Appl. Nanosci.* **2015**, 5, 255.
- [137] T. K. Vyas, A. Shahiwala, M. M. Amiji, *Int. J. Pharm.* **2008**, 347, 93.
- [138] S. Al-Edresi, S. Baie, *Int. J. Pharm.* **2009**, 373, 174.
- [139] D. S. Bernardi, T. A. Pereira, N. R. Maciel, J. Bortoloto, G. S. Viera, G. C. Oliveira, P. A. Rocha-Filho, *J. Nanobiotechnology* **2011**, 9, 44.
- [140] D. Bera, D. Lahiri, A. Nag, *J. Food Eng.* **2006**, 74, 542.
- [141] V. K. Pawar, S. B. Panchal, Y. Singh, J. G. Meher, K. Sharma, P. Singh, H. K. Bora, A. Singh, D. Datta, M. K. Chourasia, *J. Control. Release* **2014**, 196, 295.
- [142] B. Ozturk, S. Argin, M. Ozilgen, D. J. McClements, *Food Chem.* **2015**, 188, 256.
- [143] J. M. Morais Diane, J. Burgess, *Int. J. Pharm.* **2014**, 465, 455.
- [144] X. Wang, N. Anton, P. Ashokkumar, H. Anton, T. K. Fam, T. Vandamme, A. S. Klymchenko, M. Collot, *ACS Appl. Mater. Interfaces* **2019**, 11, 13079.
- [145] M. S. Ali, M. S. Alam, N. Alam, M. R. Siddiqui, *Iran. J. Pharm. Res. IJPR* **2014**, 13, 1125.
- [146] B. Sharif Makhmalzadeh, S. Torabi, A. Azarpanah, *Iran. J. Pharm. Res. IJPR* **2012**, 11, 47.
- [147] X. Wang, Y. Jiang, Y.-W. Wang, M.-T. Huang, C.-T. Ho, Q. Huang, *Food Chem.* **2008**, 108, 419.
- [148] A. Azeem, M. Rizwan, F. J. Ahmad, Z. Iqbal, R. K. Khar, M. Aqil, S. Talegaonkar, *AAPS PharmSciTech* **2009**, 10, 69.
- [149] Y.-J. Jo, Y.-J. Kwon, *Food Sci. Biotechnol.* **2014**, 23, 107.
- [150] V. Polychniatou, C. Tzia, *J. Am. Oil Chem. Soc.* **2014**, 91, 79.
- [151] C. Jadhav, V. Kate, S. A. Payghan, *J. Nanostructure Chem.* **2015**, 5, 107.
- [152] K. J. Scheller, S. J. Williams, A. J. Lawrence, B. Jarrott, E. Djouma, *MethodsX* **2014**, 1, 212.
- [153] C. Brüsewitz, A. Schendler, A. Funke, T. Wagner, R. Lipp, *Int. J. Pharm.* **2007**, 329, 173.
- [154] W. Wu, W. He, Y. Tan, Z. Tian, L. Chen, F.-Q. Hu, W. Wu, *Int. J. Nanomedicine* **2011**, 6, 521.
- [155] P. G. Maher, M. A. Fenelon, Y. Zhou, M. Kamrul Haque, Y. H. Roos, *J. Food Sci.* **2011**, 76, C1108.
- [156] A. Ali, G. Mekhloufi, N. Huang, F. Agnely, *Int. J. Pharm.* **2016**, 500, 291.
- [157] J. Combrinck, A. Otto, J. Du Plessis, *AAPS PharmSciTech* **2014**, 15, 588.
- [158] N. Rapoport, D. A. Christensen, A. M. Kennedy, K.-H. Nam, *Ultrasound Med. Biol.* **2010**, 36, 419.
- [159] V. V. Erramreddy, S. Ghosh, *Langmuir* **2014**, 30, 11062.
- [160] S. Uluata, E. A. Decker, D. J. McClements, *Food Biophys.* **2016**, 11, 52.
- [161] M. Kanamaru, Y. Einaga, *Polymer (Guildf)*. **2002**, 43, 3925.
- [162] S. Hirsjärvi, S. Dufort, J. Gravier, I. Texier, Q. Yan, J. Bibette, L. Sancey, V. Josserand, C. Passirani, J.

- P. Benoit, et al., *Nanomedicine Nanotechnology, Biol. Med.* **2013**, *9*, 375.
- [163] N. T. Huynh, C. Passirani, P. Saulnier, J. P. Benoit, *Int. J. Pharm.* **2009**, *379*, 201.
- [164] M. Adamczak, G. Para, C. Simon, P. Warszyński, *J. Microencapsul.* **2013**, *30*, 479.
- [165] J. Zhuang, M. Ying, K. Spiekermann, M. Holay, Y. Zhang, F. Chen, H. Gong, J. H. Lee, W. Gao, R. H. Fang, et al., *Adv. Mater.* **2018**, *30*, 1804693.
- [166] M. F. Attia, S. M. Dieng, M. Collot, A. S. Klymchenko, C. Bouillot, C. A. Serra, M. Schmutz, M. Er-Rafik, T. F. Vandamme, N. Anton, *Macromol. Biosci.* **2017**, *17*, 1600471.
- [167] R. Vecchione, G. Iaccarino, P. Bianchini, R. Marotta, F. D'aulia, V. Quagliariello, A. Diaspro, P. A. Netti, *Small* **2016**, *12*, 3005.
- [168] M. Y. Koroleva, E. V Yurtov, *Russ. Chem. Rev.* **2012**, *81*, 21.
- [169] N. Anton, T. F. Vandamme, in *Handb. Nanoparticles*, Springer International Publishing, Cham, **2015**, pp. 93–116.
- [170] K. S. Pafiti, E. Loizou, C. S. Patrickios, L. Porcar, *Macromolecules* **2010**, *43*, 5195.
- [171] T. Tadros, P. Izquierdo, J. Esquena, C. Solans, *Adv. Colloid Interface Sci.* **2004**, *108–109*, 303.
- [172] N. Anton, S. Akram, T. F. Vandamme, in *Nanoemulsions Formul. Appl. Charact.*, Elsevier Inc., **2018**, pp. 77–100.
- [173] H.-S. Peng, D. T. Chiu, *Chem. Soc. Rev.* **2015**, *44*, 4699.
- [174] K. Li, B. Liu, *Chem. Soc. Rev.* **2014**, *43*, 6570.
- [175] A. Vollrath, S. Schubert, U. S. Schubert, *J. Mater. Chem. B* **2013**, *1*, 1994.
- [176] A. Reisch, A. S. Klymchenko, *Small* **2016**, *12*, 1968.
- [177] H. Zhou, Y. Yue, G. Liu, Y. Li, J. Zhang, Q. Gong, Z. Yan, M. Duan, *Nanoscale Res. Lett.* **2010**, *5*, 224.
- [178] V. N. Kilin, H. Anton, N. Anton, E. Steed, J. Vermot, T. F. Vandamme, Y. Mely, A. S. Klymchenko, *Biomaterials* **2014**, *35*, 4950.
- [179] R. Bouchaala, L. Mercier, B. Andreiuk, Y. Mély, T. Vandamme, N. Anton, J. G. Goetz, A. S. Klymchenko, *J. Control. Release* **2016**, *236*, 57.
- [180] I. Texier, M. Goutayer, A. Da Silva, L. Guyon, N. Djaker, V. Josserand, E. Neumann, J. Bibette, F. Vinet, *J. Biomed. Opt.* **2009**, *14*, 054005.
- [181] P. A. Jarzyna, T. Skajaa, A. Gianella, D. P. Cormode, D. D. Samber, S. D. Dickson, W. Chen, A. W. Griffioen, Z. A. Fayad, W. J. M. Mulder, *Biomaterials* **2009**, *30*, 6947.
- [182] A. Jacquart, M. Kéramidas, J. Vollaie, R. Boisgard, G. Pottier, E. Rustique, F. Mittler, F. P. Navarro, J. Boutet, J.-L. Coll, et al., *J. Biomed. Opt.* **2013**, *18*, 101311.
- [183] A. Gianella, P. A. Jarzyna, V. Mani, S. Ramachandran, C. Calcagno, J. Tang, B. Kann, W. J. R. Dijk, V. L. Thijssen, A. W. Griffioen, et al., *ACS Nano* **2011**, *5*, 4422.
- [184] J. Gravier, F. P. Navarro, T. Delmas, F. Mittler, A.-C. Couffin, F. Vinet, I. Texier, *J. Biomed. Opt.* **2011**, *16*, 096013.
- [185] J. A. Rochira, M. V. Gudheti, T. J. Gould, R. R. Laughlin, J. L. Nadeau, S. T. Hess, *J. Phys. Chem. C* **2007**, *111*, 1695.

- [186] D. R. Larson, H. Ow, H. D. Vishwasrao, A. A. Heikal, U. Wiesner, W. W. Webb, *Chem. Mater.* **2008**, *20*, 2677.
- [187] G. Sun, M. Y. Berezin, J. Fan, H. Lee, J. Ma, K. Zhang, K. L. Wooley, S. Achilefu, *Nanoscale* **2010**, *2*, 548.
- [188] F. Würthner, T. E. Kaiser, C. R. Saha-Möller, *Angew. Chemie Int. Ed.* **2011**, *50*, 3376.
- [189] A. Reisch, P. Didier, L. Richert, S. Oncul, Y. Arntz, Y. Mély, A. S. Klymchenko, *Nat. Commun.* **2014**, *5*, 4089.
- [190] L. D. Lavis, R. T. Raines, *ACS Chem. Biol.* **2008**, *3*, 142.
- [191] K. Zyabrev, A. Doroshenko, E. Mikitenko, Y. Slominskii, A. Tolmachev, *European J. Org. Chem.* **2008**, *2008*, 1550.
- [192] A. O. Gerasov, M. P. Shandura, Y. P. Kovtun, *Dye. Pigment.* **2008**, *77*, 598.
- [193] A. O. Gerasov, M. P. Shandura, Y. P. Kovtun, *Dye. Pigment.* **2008**, *79*, 252.
- [194] A. O. Gerasov, K. V. Zyabrev, M. P. Shandura, Y. P. Kovtun, *Dye. Pigment.* **2011**, *89*, 76.
- [195] M. K. Kuimova, *Phys. Chem. Chem. Phys.* **2012**, *14*, 12671.
- [196] M. A. Haidekker, E. A. Theodorakis, *Org. Biomol. Chem.* **2007**, *5*, 1669.
- [197] S. Snipstad, S. Hak, H. Baghirov, E. Sulheim, Y. Mørch, S. Lélou, E. von Haartman, M. Bäck, K. P. R. Nilsson, A. S. Klymchenko, et al., *Cytom. Part A* **2017**, *91*, 760.
- [198] D. J. McClements, Y. Li, *Adv. Colloid Interface Sci.* **2010**, *159*, 213.
- [199] K. Ahmed, Y. Li, D. J. McClements, H. Xiao, *Food Chem.* **2012**, *132*, 799.
- [200] S. A. Abouelmagd, B. Sun, A. C. Chang, Y. J. Ku, Y. Yeo, *Mol. Pharm.* **2015**, *12*, 997.
- [201] R. Bouchaala, L. Richert, N. Anton, T. F. Vandamme, S. Djabi, Y. Mély, A. S. Klymchenko, *ACS Omega* **2018**, *3*, 14333.
- [202] U. Bazylińska, R. Skrzela, K. Szczepanowicz, P. Warszyński, K. A. Wilk, *Soft Matter* **2011**, *7*, 6113.
- [203] S. Bhargava, J. J. H. Chu, S. Valiyaveetil, *ACS Omega* **2018**, *3*, 7663.
- [204] Y. Wen, W. Zhang, X. Zhu, J. Zhang, L. Wang, *Energy* **2018**, *158*, 537.
- [205] Y. Qiu, H. Hu, D. Zhao, J. Wang, H. Wang, Q. Wang, H. Peng, Y. Liao, X. Xie, **2019**, DOI 10.1016/j.polymer.2019.02.063.
- [206] S. W. Morton, X. Zhao, M. A. Quadir, P. T. Hammond, *Biomaterials* **2014**, *35*, 3489.
- [207] Y. Zhao, I. Van Rooy, S. Hak, F. Fay, J. Tang, C. D. L. Davies, M. Skobe, E. A. Fisher, A. Radu, Z. A. Fayad, et al., *ACS Nano* **2013**, *7*, 10362.
- [208] J. Gravier, L. Sancey, S. Hirsjärvi, E. Rustique, C. Passirani, J. P. Benoît, J. L. Coll, I. Texier, *Mol. Pharm.* **2014**, *11*, 3133.
- [209] B. T. Bajar, E. S. Wang, S. Zhang, M. Z. Lin, J. Chu, *Sensors (Switzerland)* **2016**, *16*, 1.
- [210] E. L. Elson, *Biophys. J.* **2011**, *101*, 2855.
- [211] D. Wöll, *RSC Adv.* **2014**, *4*, 2447.
- [212] T. Liedl, S. Keller, F. C. Simmel, J. O. Rädler, W. J. Parak, *Small* **2005**, *1*, 997.

- [213] B. L. Sanchez-Gaytan, F. Fay, S. Hak, A. Alaarg, Z. A. Fayad, C. Pérez-Medina, W. J. M Mulder, Y. Zhao, *Angew Chem Int Ed Engl* **2017**, *56*, 2923.
- [214] S. K. Patel, M. J. Patrick, J. A. Pollock, J. M. Janjic, *J. Biomed. Opt.* **2013**, *18*, 101312.
- [215] E.-H. Lee, J.-K. Kim, J.-S. Lim, S.-J. Lim, *Colloids Surfaces B Biointerfaces* **2015**, *136*, 305.
- [216] M. Goutayer, S. Dufort, V. Josserand, A. Royère, E. Heinrich, F. Vinet, J. Bibette, J. L. Coll, I. Texier, *Eur. J. Pharm. Biopharm.* **2010**, *75*, 137.
- [217] J. Choi, E. Rustique, M. Henry, M. Guidetti, V. Josserand, L. Sancey, J. Boutet, J.-L. Coll, *Int. J. Pharm.* **2017**, *532*, 677.
- [218] A. Saito, S. Yamamoto, R. Ochi, K. Inoue, S. Hadano, S. Watanabe, T. Nakayama, Y. Niko, *Bull. Chem. Soc. Jpn.* **2020**, *93*, 568.
- [219] M. Attia, M. I. Swasy, R. Akasov, F. Alexis, D. C. Whitehead, *ACS Appl. Bio Mater.* **2020**, acsabm.0c00567.
- [220] E. Belcastro, A. U. Rehman, L. Remila, S.-H. Park, D. S. Gong, N. Anton, C. Auger, O. Lefebvre, J. G. Goetz, M. Collot, et al., *Nanomedicine Nanotechnology, Biol. Med.* **2021**, 102379.
- [221] G. Sahay, D. Y. Alakhova, A. V. Kabanov, *J. Control. Release* **2010**, *145*, 182.
- [222] A. Vollrath, A. Schallon, C. Pietsch, S. Schubert, T. Nomoto, Y. Matsumoto, K. Kataoka, U. S. Schubert, *Soft Matter* **2013**, *9*, 99.
- [223] S. Patel, J. Kim, M. Herrera, A. Mukherjee, A. V Kabanov, G. Sahay, **2019**, DOI 10.1016/j.addr.2019.08.004.
- [224] S. D. Conner, S. L. Schmid, *Nature* **2003**, *422*, 37.
- [225] O. Harush-Frenkel, E. Rozentur, S. Benita, Y. Altschuler, *Biomacromolecules* **2008**, *9*, 435.
- [226] Y. Luo, Z. Teng, T. T. Y. Wang, Q. Wang, *J. Agric. Food Chem.* **2013**, *61*, 7621.
- [227] H. S. Ribeiro, J. M. M. Guerrero, K. Briviba, G. Rechkemmer, H. P. Schuchmann, H. Schubert, *J. Agric. Food Chem.* **2006**, *54*, 9366.
- [228] Y. Fan, Y. Zhang, W. Yokoyama, J. Yi, *Nanomaterials* **2017**, *7*, 349.
- [229] J. Zheng, Y. Li, M. Song, X. Fang, Y. Cao, D. J. McClements, H. Xiao, *Food Res. Int.* **2014**, *62*, 98.
- [230] J. Yi, Y. Li, F. Zhong, W. Yokoyama, *Food Hydrocoll.* **2014**, *35*, 19.
- [231] A. C. Anselmo, M. Zhang, S. Kumar, D. R. Vogus, S. Menegatti, M. E. Helgeson, S. Mitragotri, *ACS Nano* **2015**, *9*, 3169.
- [232] X. Yi, X. Shi, H. Gao, *Phys. Rev. Lett.* **2011**, *107*, 098101.
- [233] M. Herant, V. Heinrich, M. Dembo, *J. Cell Sci.* **2005**, *118*, 1789.
- [234] M. Coelho, N. Maghelli, I. M. Tolić-Nørrelykke, *Integr. Biol.* **2013**, *5*, 748.
- [235] M. Pawlicki, H. A. Collins, R. G. Denning, H. L. Anderson, *Angew. Chemie - Int. Ed.* **2009**, *48*, 3244.
- [236] P. G. Bush, D. L. Wokosin, A. C. Hall, *Front. Biosci.* **2007**, *12*, 2646.
- [237] H. M. Kim, B. R. Cho, *Chem. Rev.* **2015**, *115*, 5014.
- [238] S. Hou, C. Johnson, K. Welscher, *Molecules* **2019**, *24*, 2826.

- [239] M. Dahan, S. Lévi, C. Luccardini, P. Rostaing, B. Riveau, A. Triller, *Science* (80-.). **2003**, 302, 442.
- [240] Y. Wang, R. Hu, G. Lin, I. Roy, K.-T. Yong, *ACS Appl. Mater. Interfaces* **2013**, 5, 2786.
- [241] M. U. Zahid, L. Ma, S. J. Lim, A. M. Smith, *Nat. Commun.* **2018**, 9, 1.
- [242] E. Genin, Z. Gao, J. A. Varela, J. Daniel, T. Bsaibess, I. Gosse, L. Groc, L. Cognet, M. Blanchard-Desce, *Adv. Mater.* **2014**, 26, 2258.
- [243] J. Yu, C. Wu, S. P. Sahu, L. P. Fernando, C. Szymanski, J. McNeill, *J. Am. Chem. Soc.* **2009**, 131, 18410.
- [244] A. Reisch, D. Heimbürger, P. Ernst, A. Runser, P. Didier, D. Dujardin, A. S. Klymchenko, *Adv. Funct. Mater.* **2018**, 28, 1805157.
- [245] C. B. Arechabala, C. Coiffard, P. Rivalland, LJM, *J. Appl. Toxicol.* **1999**, 19, 163.
- [246] H. Yoon, X. Zhang, M. Kang, G. Kim, S. Shin, S. Baek, B. Lee, S. Hong, J. Kim, K. Hong, et al., *Int. J. Mol. Sci.* **2018**, 19, 280.
- [247] C. Vater, A. Adamovic, L. Ruttensteiner, K. Steiner, P. Tajpara, V. Klang, A. Elbe-Bürger, M. Wirth, C. Valenta, *Int. J. Pharm.* **2019**, 566, 383.
- [248] S. K. Ko, X. Chen, J. Yoon, I. Shin, *Chem. Soc. Rev.* **2011**, 40, 2120.
- [249] V. Hyenne, S. Ghoroghi, M. Collot, J. Bons, G. Follain, S. Harlepp, B. Mary, J. Bauer, L. Mercier, I. Busnelli, et al., *Dev. Cell* **2019**, 48, 554.
- [250] F. J. Verweij, V. Hyenne, G. Van Niel, J. G. Goetz, *Trends Cell Biol.* **2019**, 29, 770.
- [251] B. S. Schuster, L. M. Ensign, D. B. Allan, J. S. Suk, J. Hanes, *Adv. Drug Deliv. Rev.* **2015**, 91, 70.
- [252] S. K. Lyons, *Cancer J. (United States)* **2015**, 21, 152.
- [253] L. Yuan, W. Lin, K. Zheng, L. He, W. Huang, *Chem. Soc. Rev* **2013**, 42, 622.
- [254] S. A. Hilderbrand, R. Weissleder, *Curr. Opin. Chem. Biol.* **2010**, 14, 71.
- [255] H. Kobayashi, M. Ogawa, R. Alford, P. L. Choyke, Y. Urano, *Chem. Rev.* **2010**, 110, 2620.
- [256] S. Luo, E. Zhang, Y. Su, T. Cheng, C. Shi, *Biomaterials* **2011**, 32, 7127.
- [257] Z. Guo, S. Park, J. Yoon, I. Shin, *Chem. Soc. Rev.* **2014**, 43, 16.
- [258] R. van der Meel, E. Sulheim, Y. Shi, F. Kiessling, W. J. M. Mulder, T. Lammers, *Nat. Nanotechnol.* **2019**, 14, 1007.
- [259] M. Z. El-Readi, M. A. Althubiti, *J. Nanomater.* **2019**, 2019, 4927312.
- [260] J. Yang, R. Zhang, D. C. Radford, J. Kopeček, *J. Control. Release* **2015**, 218, 36.
- [261] Y. Zhao, F. Fay, S. Hak, J. Manuel Perez-Aguilar, B. L. Sanchez-Gaytan, B. Goode, R. Duivenvoorden, C. de Lange Davies, A. Bjørkøy, H. Weinstein, et al., *Nat. Commun.* **2016**, 7, 11221.
- [262] a. L. Lainé, J. Gravier, M. Henry, L. Sancey, J. Béjaud, E. Pancani, M. Wiber, I. Texier, J. L. Coll, J. P. Benoit, et al., *J. Control. Release* **2014**, 188, 1.
- [263] M. A. Radicchi, J. V. de Oliveira, A. C. P. Mendes, D. M. de Oliveira, L. A. Muehlmann, P. C. Morais, R. B. Azevedo, J. P. F. Longo, *J. Mater. Chem. B* **2018**, 6, 7306.
- [264] J. Mérian, R. Boisgard, X. Decleves, B. Thezé, I. Texier, B. Tavitian, *J. Nucl. Med.* **2013**, 54, 1996.

- [265] A. S. Klymchenko, F. Liu, M. Collot, N. Anton, *Adv. Healthc. Mater.* **2021**, *10*, 2001289.
- [266] W. Zhang, Y. Jin, **n.d.**
- [267] B. L. Miller, *Dyn. Comb. Chem. Drug Discov. Bioorganic Chem. Mater. Sci.* **2009**, *1*.
- [268] S. J. Rowan, S. J. Cantrill, G. R. L. Cousins, J. K. M. Sanders, J. F. Stoddart, *Angew. Chemie Int. Ed.* **2002**, *41*, 898.
- [269] F. Schaufelberger, O. Ramström, *Chem. - A Eur. J.* **2015**, *21*, 12735.
- [270] Y. Jin, C. Yu, R. J. Denman, W. Zhang, *Chem. Soc. Rev.* **2013**, *42*, 6634.
- [271] A. Kurpanik, M. Matussek, G. Szafraniec-Gorol, M. Filapek, P. Lodowski, B. Marcol-Szumilas, W. Ignasiak, J. G. Malecki, B. Machura, M. Malecka, et al., *Chem. Eur. J.* **2020**, *26*, 12150.
- [272] G. Gao, X. Han, N. Sowan, X. Zhang, P. K. Shah, M. Chen, C. N. Bowman, J. W. Stansbury, *ACS Macro Lett.* **2020**, *9*, 713.
- [273] F. Li, X. Xu, Y. Liang, Y. Li, M. Wang, F. Zhao, X. Wang, Y. Sun, W. Chen, *Nanoscale* **2021**, *13*, 4774.
- [274] G. Deng, F. Li, H. Yu, F. Liu, C. Liu, W. Sun, H. Jiang, Y. Chen, *ACS Macro Lett.* **2012**, *1*, 275.
- [275] L. Imbernon, E. K. Oikonomou, S. Norvez, L. Leibler, *Polym. Chem.* **2015**, *6*, 4271.
- [276] M. Pepels, I. Pilot, B. Klumperman, H. Goossens, *Polym. Chem.* **2013**, *4*, 4955.
- [277] J. Han, T. Liu, S. Zhang, C. Hao, J. Xin, B. Guo, J. Zhang, *Ind. Eng. Chem. Res.* **2019**, *58*, 6466.
- [278] R. Gu, K. Flidrova, J.-M. Lehn, *J. Am. Chem. Soc.* **2018**, *140*, 5560.
- [279] N. Wilhelms, S. Kulchat, J. M. Lehn, *Helv. Chim. Acta* **2012**, *95*, 2635.
- [280] S. Huang, X. Kong, Y. Xiong, X. Zhang, H. Chen, W. Jiang, Y. Niu, W. Xu, C. Ren, *Eur. Polym. J.* **2020**, *141*, 110094.
- [281] J. Xu, Y. Liu, S. hui Hsu, *Molecules* **2019**, *24*, 1.
- [282] Y. Jin, A. Zhang, Y. Huang, W. Zhang, *Chem. Commun.* **2010**, *46*, 8258.
- [283] G. C. Vougioukalakis, R. H. Grubbs, *Chem. Rev.* **2010**, *110*, 1746.
- [284] X. Li, B. Lin, H. Li, Q. Yu, Y. Ge, X. Jin, X. Liu, Y. Zhou, J. Xiao, *Appl. Catal. B Environ.* **2018**, *239*, 254.
- [285] A. Franconetti, P. Domínguez-Rodríguez, D. Lara-García, R. Prado-Gotor, F. Cabrera-Escribano, *Appl. Catal. A Gen.* **2016**, *517*, 176.
- [286] S. F. Amarante, M. A. Freire, D. T. S. L. Mendes, L. S. Freitas, A. L. D. Ramos, *Appl. Catal. A Gen.* **2017**, *548*, 47.
- [287] X. Chen, M. A. Dam, K. Ono, A. Mal, H. Shen, S. R. Nutt, K. Sheran, F. Wudl, *Science (80-.).* **2002**, *295*, 1698.
- [288] J. Zhao, R. Xu, G. Luo, J. Wu, H. Xia, *J. Mater. Chem. B* **2016**, *4*, 982.
- [289] S. Ulrich, *Acc. Chem. Res.* **2019**, *52*, 510.
- [290] Q. Zhang, Y. Gong, X.-J. Guo, P. Zhang, C.-F. Ding, *ACS Appl. Mater. Interfaces* **2018**, *10*, 34840.
- [291] M. Podgórski, N. Spurgin, S. Mavila, C. N. Bowman, *Polym. Chem.* **2020**, *11*, 5365.
- [292] R. Larsson, Z. Pei, O. Ramström, *Angew. Chemie - Int. Ed.* **2004**, *43*, 3716.

- [293] L. D. Solid, L. W. Hrubesh, H. M. Chan, J. L. Grenestedt, M. P. Harmer, H. S. Caram, S. K. Roy, P. T. Handbook, B. Raton, M. F. Ashby, et al., **2011**, 965.
- [294] P. T. Corbett, J. Leclaire, L. Vial, K. R. West, J.-L. Wietor, J. K. M. Sanders, S. Otto, *Chem. Rev.* **2006**, *106*, 3652.
- [295] J.-C. Lai, J.-F. Mei, X.-Y. Jia, C.-H. Li, X.-Z. You, Z. Bao, *Adv. Mater.* **2016**, *28*, 8277.
- [296] S. Wang, X. Xing, X. Zhang, X. Wang, X. Jing, *J. Mater. Chem. A* **2018**, *6*, 10868.
- [297] S. W. Kantor, W. T. Grubb, R. C. Osthoff, *J. Am. Chem. Soc.* **1954**, *76*, 5190.
- [298] P. Zheng, T. J. McCarthy, *J. Am. Chem. Soc.* **2012**, *134*, 2024.
- [299] S. Ji, W. Cao, Y. Yu, H. Xu, *Angew. Chemie Int. Ed.* **2014**, *53*, 6781.
- [300] S. Ji, W. Cao, Y. Yu, H. Xu, *Adv. Mater.* **2015**, *27*, 7740.
- [301] S. Ji, J. Xia, H. Xu, *ACS Macro Lett.* **2016**, *5*, 78.
- [302] W. Qin, S. Long, M. Panunzio, S. Biondi, *Molecules* **2013**, *18*, 12264.
- [303] Z. Zhang, C. He, X. Chen, *Mater. Chem. Front.* **2018**, *2*, 1765.
- [304] M. A. Khomutov, S. Mandal, J. Weisell, N. Saxena, A. R. Simonian, J. Vepsalainen, R. Madhubala, S. N. Kochetkov, *Amino Acids* **2010**, *38*, 509.
- [305] P. E. Farahani, S. M. Adelmund, J. A. Shadish, C. A. DeForest, *J. Mater. Chem. B* **2017**, *5*, 4435.
- [306] K. Imato, H. Otsuka, *Polymer (Guildf)*. **2018**, *137*, 395.
- [307] T. Takarada, M. Maeda, *Bull. Chem. Soc. Jpn.* **2013**, *86*, 547.
- [308] Á. Martínez-Castañeda, H. Rodríguez-Solla, C. Concellón, V. del Amo, *Org. Biomol. Chem.* **2012**, *10*, 1976.
- [309] B. C. Norris, C. W. Bielawski, *Macromolecules* **2010**, *43*, 3591.
- [310] M. Holler, N. Allenbach, J. Sonet, J. F. Nierengarten, *Chem. Commun.* **2012**, *48*, 2576.
- [311] P. Vongvilai, O. Ramström, *J. Am. Chem. Soc.* **2009**, *131*, 14419.
- [312] X. Wang, K. S. K. Lin, J. C. C. Chan, S. Cheng, *J. Phys. Chem. B* **2005**, *109*, 1763.
- [313] J. Otera, *Chem. Rev.* **1993**, *93*, 1449.
- [314] P. A. Fernandes, M. J. Ramos, *Chem. - A Eur. J.* **2004**, *10*, 257.
- [315] C. F. H. Allen, J. O. Fournier, W. J. Humphlett, *Can. J. Chem.* **1964**, *42*, 2616.
- [316] C. E. Hoyle, A. B. Lowe, C. N. Bowman, *Chem. Soc. Rev.* **2010**, *39*, 1355.
- [317] D. P. Nair, M. Podgórski, S. Chatani, T. Gong, W. Xi, C. R. Fenoli, C. N. Bowman, *Chem. Mater.* **2014**, *26*, 724.
- [318] B. T. Worrell, S. Mavila, C. Wang, T. M. Kontour, C.-H. Lim, M. K. McBride, C. B. Musgrave, R. Shoemaker, C. N. Bowman, *Polym. Chem.* **2018**, *9*, 4523.
- [319] Y. L. Fang, X. S. Du, Y. X. Jiang, Z. L. Du, P. T. Pan, X. Cheng, H. B. Wang, *ACS Sustain. Chem. Eng.* **2018**, *6*, 14490.
- [320] W. G. Skene, J.-M. P. Lehn, *Proc. Natl. Acad. Sci. U. S. A.* **2004**, *101*, 8270 LP.

- [321] P. Zhao, J. Xia, M. Cao, H. Xu, *ACS Macro Lett.* **2020**, *9*, 163.
- [322] W. Zou, J. Dong, Y. Luo, Q. Zhao, T. Xie, *Adv. Mater.* **2017**, *29*, 1606100.
- [323] W. Luo, Y. Zhu, J. Zhang, J. He, Z. Chi, P. W. Miller, L. Chen, C.-Y. Su, *Chem. Commun.* **2014**, *50*, 11942.
- [324] T.-P. Huynh, H. Haick, *Adv. Mater.* **2016**, *28*, 138.
- [325] M. Wang, Y. Chen, R. Khan, H. Liu, C. Chen, T. Chen, R. Zhang, H. Li, *Colloids Surfaces A Physicochem. Eng. Asp.* **2019**, *567*, 139.
- [326] L. Zhou, M. Chen, Y. Guan, Y. Zhang, *Polym. Chem.* **2014**, *5*, 7081.
- [327] M. Rizwan, A. E. G. Baker, M. S. Shoichet, *Adv. Healthc. Mater.* **2021**, *10*, e2100234.
- [328] H. Wang, D. Zhu, A. Paul, L. Cai, A. Enejder, F. Yang, S. C. Heilshorn, *Adv. Funct. Mater.* **2017**, *27*, 1605609.
- [329] M. Dong, W. Zheng, Y. Chen, Y. Xianyu, B. Ran, Z. Qian, X. Jiang, *Anal. Chem.* **2018**, *90*, 9148.
- [330] M. Gao, P. An, H. Rao, Z. Niu, X. Xue, M. Luo, X. Liu, Z. Xue, X. Lu, *Analyst* **2020**, *145*, 1279.
- [331] J. Wang, Y. Wang, H. Chen, H. Xu, W. Wang, L. Bai, *Sensors Actuators B Chem.* **2018**, *258*, 998.
- [332] J. Wang, D. Yang, M. Chen, B. Liu, H. Chen, H. Xu, W. Wang, L. Bai, *Anal. Methods* **2018**, *10*, 526.
- [333] G. Hanson, B. Hanson, *Comb. Chem. High Throughput Screen.* **2008**, *11*, 505.
- [334] H. Ao, H. Feng, X. Huang, M. Zhao, Z. Qian, *J. Mater. Chem. C* **2017**, *5*, 2826.
- [335] X. Fu, L. Hosta-Rigau, R. Chandrawati, J. Cui, *CHEMPR* **2018**, *4*, 2084.
- [336] F. Gong, N. Yang, X. Wang, Q. Zhao, Q. Chen, Z. Liu, L. Cheng, *Nano Today* **2020**, *32*, 100851.
- [337] P. Chakma, D. Konkolewicz, *Angew. Chemie* **2019**, *131*, 9784.
- [338] Y. Zhang, Y. Qi, S. Ulrich, M. Barboiu, O. Ramström, *Mater. Chem. Front.* **2020**, *4*, 489.
- [339] P. L. Bedard, D. M. Hyman, M. S. Davids, L. L. Siu, *Lancet* **2020**, *395*, 1078.
- [340] Y. Tao, S. Liu, Y. Zhang, Z. Chi, J. Xu, *Polym. Chem.* **2018**, *9*, 878.
- [341] W. Xu, Y. Hong, A. Song, J. Hao, *Colloids Surfaces B Biointerfaces* **2020**, *185*, 110567.
- [342] L. Xiong, Q. Luo, Y. Wang, X. Li, Z. Shen, W. Zhu, *Chem. Commun.* **2015**, *51*, 14644.
- [343] F. Zhan, W. Chen, Z. Wang, W. Lu, R. Cheng, C. Deng, F. Meng, H. Liu, Z. Zhong, *Biomacromolecules* **2011**, *12*, 3612.
- [344] X. Zhang, T. Zhang, X. Ma, Y. Wang, Y. Lu, D. Jia, X. Huang, J. Chen, Z. Xu, F. Wen, *Asian J. Pharm. Sci.* **2020**, *15*, 605.
- [345] G. Li, M. Pei, P. Liu, *Mater. Sci. Eng. C* **2020**, *110*, 110653.
- [346] G. Yilmaz, E. Guler, C. Geyik, B. Demir, M. Ozkan, D. Odaci Demirkol, S. Ozcelik, S. Timur, C. R. Becer, *Mol. Syst. Des. Eng.* **2018**, *3*, 150.
- [347] T. Zhang, Y. Wang, X. Ma, C. Hou, S. Lv, D. Jia, Y. Lu, P. Xue, Y. Kang, Z. Xu, *Biomater. Sci.* **2020**, *8*, 473.
- [348] H. Liu, X. Shi, D. Wu, F. Kahsay Khshen, L. Deng, A. Dong, W. Wang, J. Zhang, *ACS Appl. Mater. Interfaces* **2019**, *11*, 19700.

- [349] D. Ding, Q. Zhu, *Mater. Sci. Eng. C* **2018**, 92, 1041.
- [350] L. Gui, X.-H. Zhang, Z.-Y. Qiao, H. Wang, *ChemNanoMat* **2020**, 6, 1138.
- [351] G. Gasparini, S. Matile, *Chem. Commun.* **2015**, 51, 17160.
- [352] Q. Laurent, R. Martinent, B. Lim, A.-T. Pham, T. Kato, J. López-Andarias, N. Sakai, S. Matile, *JACS Au* **2021**, 1, 710.
- [353] J. H. Lu, H. Wang, Z. Y. Tian, Y. Q. Hou, H. Lu, *J. Am. Chem. Soc.* **2020**, 142, 1217.
- [354] L. H. Qian, J. Q. Fu, P. Y. Yuan, S. B. Du, W. Huang, L. Li, S. Q. Yao, *Angew. CHEMIE-INTERNATIONAL Ed.* **2018**, 57, 1532.
- [355] Y. Asami, K. Yoshioka, K. Nishina, T. Nagata, T. Yokota, *Drug Discov. Ther.* **2016**, 10, 256.
- [356] C. Bouillon, Y. Bessin, F. Poncet, M. Gary-Bobo, P. Dumy, M. Barboiu, N. Bettache, S. Ulrich, *J. Mater. Chem. B* **2018**, 6, 7239.
- [357] T. M. Allen, *Science (80-.)*. **2004**, 303, 1818.
- [358] A. Kumari, R. Singla, A. Guliani, S. K. Yadav, *EXCLI J.* **2014**, 13, 265.
- [359] S. Mura, D. T. Bui, P. Couvreur, J. Nicolas, *J. Control. Release* **2015**, 208, 25.
- [360] D. Irby, C. Du, F. Li, *Mol. Pharm.* **2017**, 14, 1325.
- [361] Y. Niko, P. Didier, Y. Mely, G. I. Konishi, A. S. Klymchenko, *Sci. Rep.* **2016**, 6, 1.
- [362] Z. Liu, H. Zou, Z. Zhao, P. Zhang, G.-G. Shan, R. T. K. Kwok, J. W. Y. Lam, L. Zheng, B. Z. Tang, *ACS Nano* **2019**, 13, 11283.
- [363] I. R. Calori, H. Bi, A. C. Tedesco, *ACS Appl. Bio Mater.* **2021**, 4, 195.
- [364] M. Vangala, G. P. Shinde, *BEILSTEIN J. Org. Chem.* **2016**, 12, 2086.
- [365] S.-Y. Mao, *Methods Mol. Biol.* **2010**, 588, 49.

List of Publications

= equal contribution; * = correspondence

= equal contribution; * = correspondence

1) Klymchenko, Andrey S.#*, Fei Liu#, Mayeul Collot, and Nicolas Anton. 2021. “Dye-Loaded NEs: Biomimetic Fluorescent NCs for Bioimaging and Nanomedicine.” *Advanced Healthcare Materials* 10(1):2001289.

2) Liu, Fei, Dmytro I. Danylchuk, Bohdan Andreiuk, and Andrey S. Klymchenko*. 2022. “Dynamic Covalent Chemistry in Live Cells for Organelle Targeting and Enhanced Photodynamic Action.” *Chemical Science*.

3) Liu, Fei#, Yosuke Niko#, Redouane Bouchaala, Luc Mercier, Olivier Lefebvre, Bohdan Andreiuk, Thierry Vandamme, Jacky G. Goetz, Nicolas Anton, and Andrey Klymchenko*. 2021. “Drug-Sponge Lipid Nanocarrier for in Situ Cargo Loading and Release Using Dynamic Covalent Chemistry.” *Angewandte Chemie International Edition* 202014259.

4) Chow, Renee Wei-Yan, Hajime Fukui, Wei Xuan Chan, Kok Soon Justin Tan, Stéphane Roth, Anne-Laure Duchemin, Nadia Messaddeq, Hiroyuki Nakajima, Fei Liu, Nathalie Faggianelli-Conrozier, Andrey S. Klymchenko, Yap Choon Hwai, Naoki Mochizuki, and Julien Vermot*. 2022. “Cardiac Forces Regulate Zebrafish Heart Valve Delamination by Modulating Nfat Signaling.” *PLOS Biology* 20(1):e3001505.

List of Conferences

- 1) Liu, Fei, Yosuke Niko, Redouane Bouchaala, Luc Mercier, Olivier Lefebvre, Bohdan Andreiuk, Thierry Vandamme, Jacky G. Goetz, Nicolas Anton, and Andrey Klymchenko. Journée du campus d'Illkirch (JCI), Strasbourg, France April 19, 2021. (Oral presentation)
- 2) Liu, Fei, Dmytro I. Danylchuk, Yosuke Niko, Redouane Bouchaala, Luc Mercier, Olivier Lefebvre, Bohdan Andreiuk, Thierry Vandamme, Jacky G. Goetz, Nicolas Anton, and Andrey Klymchenko. 2nd International Conference of Lipid Droplet and Oleosomes, Strasbourg, France December 2-3, 2021. (Oral presentation)

In situ reactions in lipid nanostructures for bioimaging and therapy

Résumé

La chimie covalente dynamique a montré un énorme potentiel d'application dans le domaine de l'administration de médicaments. L'objectif de ce travail de doctorat est d'utiliser la chimie covalente dynamique comme outil pour trouver de nouvelles voies d'administration de médicaments. Les deux premières études concernent la conception d'un système de nano-émulsions fonctionnelles capable de libérer des médicaments/colorants utilisant une cétone libre (aldéhyde) avec contrôle du pH et de les encapsuler par réaction in situ directement dans le noyau gras des nano-émulsions. Sur la base de ce concept, d'extraction de médicaments/colorants de la peau de poulet et de désintoxication cellulaire in vitro ont également été tentées. La troisième étude est consacrée au développement d'une méthodologie universelle basée sur la réaction de modification des nano-émulsions in situ avec une surface d'anticorps pour cibler les cellules cancéreuses. Enfin une dernière étude porte sur une nouvelle technique consistant à diriger des médicaments/colorants cétoniques libres vers des organites spécifiques et voir l'influence des effets PDT.

Mots clés : Administration de médicaments; Chimie covalente dynamique; Nano-émulsions; Libre médicaments avec contrôle; Désintoxication; Extraction; Diriger des médicaments

Résumé en anglais

Dynamic covalent chemistry showed huge application potential in the field of drug delivery, this Ph.D. work aims to use dynamic covalent chemistry as a tool for finding novel ways of drug delivery. The first two studies concern the designing of a functional nano-emulsions system that is capable of releasing free ketone (aldehyde) drug/dyes under low pH and encapsulating them through in situ reaction directly in the oil core of nano-emulsions. Based on the concept, extraction of dyes/drugs from chicken skin, and in vitro cell detoxification were also attempted. The third study concerns the development of a universal methodology based on in situ reaction for functionalization nano-emulsions with antibody surfaces for targeting cancer cells. The last study is dedicated to a novel technique of directing free ketone dyes/drugs to specific organelles for enhanced PDT effects.

Keywords : Drug delivery ; Dynamic covalent chemistry ; Nano-emulsions; Controlled release; Detoxification; Extraction; Drug targeting